

Extrusion Printing of Carbon Nanotube Inks,  
from Rheology to Electronics

by

Crystal E. Owens

B.S.E., Mechanical Engineering, Duke University (2015)  
S.M., Mechanical Engineering, Massachusetts Institute of Technology (2017)

Submitted to the Department of Mechanical Engineering  
in partial fulfillment of the requirements for the degree of

Doctor of Philosophy in Mechanical Engineering

at the

MASSACHUSETTS INSTITUTE OF TECHNOLOGY

June 2023

© Crystal E. Owens. All rights reserved.

The author hereby grants to MIT a nonexclusive, worldwide, irrevocable,  
royalty—free license to exercise any and all rights under copyright,  
including to reproduce, preserve, distribute and publicly display copies  
of the thesis, or release the thesis under an open—access license.

Authored by .....  
Crystal E. Owens  
Department of Mechanical Engineering  
June 29, 2023

Certified by .....  
Gareth H. McKinley  
School of Engineering Professor of Teaching Innovation  
Thesis Supervisor

Co-certified by .....  
A. John Hart  
Professor of Mechanical Engineering  
Thesis Co-Supervisor

Accepted by .....  
Nicolas Hadjiconstantinou  
Graduate Officer Department of Mechanical Engineering

# Extrusion Printing of Carbon Nanotube Inks, from Rheology to Electronics

by

Crystal E. Owens

Submitted to the Department of Mechanical Engineering on June 29, 2023  
in partial fulfillment of the requirements for the degree of  
Doctor of Philosophy in Mechanical Engineering

## ABSTRACT

Printed electronics rely on the deposition of conductive liquid-based inks into continuous lines and films, typically on polymeric substrates. Among candidate conductive fillers for use in electronic inks, carbon nanotubes (CNTs) have high conductivity, low density, processability at ambient temperatures, and intrinsic mechanical flexibility, showing their potential to serve as a material of choice in the manufacturing of electronics. However, printed CNT structures have been limited to date in electrical conductivity by manufacturing constraints, typically necessitating nonconductive modifiers to render ink suitable for extrusion, as well as by imperfect CNT quality and low concentration. The goal of this thesis is to surpass the limitations of current manufacturing processes using CNTs in ad-hoc mixtures, and instead to explore printing and electronic properties in relation to CNT-based solution composition and rheology in order to lay the framework for intelligent, fit-for-purpose ink design. In Part One, a short overview of CNT ink rheology is presented, particularly focusing on elastoviscoplastic yield stress behavior, observing scaling laws for flow behavior, and denoting rheometric signatures of ink phase, solution quality, and printability. With further attention to rheometry, a modified vane tool is introduced that has an optimized fractal cross section to improve measurements of this class of slip-prone yield stress fluids.

In Part Two, printing methods and ink designs are developed in coordination to realize three demonstrations of CNT artifact production in 2D and 3D shapes, with the objective in all cases of maximizing electrical performance while attaining “good enough” geometric resolution. By using an aqueous CNT ink with moderate yield stress (2 Pa) for feature fidelity and considering wetting interactions between the ink and a substrate, the printing of thin CNT lines onto paper and polymer substrates is achieved to create flexible electronics, exhibiting conductivity up to 10 kS/m and specific conductivity tailorable from 0.004 to 140 S.m<sup>2</sup>/kg. As a demonstration of the process, printed lines serve as interconnects to power embedded LEDs while flexing; as contact sensors; and as interdigitated capacitors for liquid imbibition. Next, taking inspiration from wet fiber-spinning processes, a method of extruding CNT inks into a coagulating liquid bath of non-solvent is

introduced, generating rapidly solidifying, lightweight fibers with specific conductivity up to 7,000 S.m<sup>2</sup>/kg, comparable with copper (6,600 S.m<sup>2</sup>/kg), and conductivity up to 200 kS/m. Harnessing a fluid mechanical coiling instability observed during immersed printing, extensible CNT coils for strain sensing are produced. Third, a family of inks is created with yield stress in the range of 500 Pa and CNT concentrations around 15% to print arrays of cold cathode field electron emitters with freestanding miniature conical shapes having sub-100-micrometer tip diameters onto addressable gridpoints of a PCB. By modifying the ink further to increase extensional viscosity, individual 100-micrometer-scale freestanding cylinders are fabricated that surpass state-of-the-art CNT field emission performance.

Finally, in Part Three, to overcome fundamental limitations of the conductivity of CNT-based macrostructures, a method is developed to enhance the conductivity of existing CNT structures using copper electrodeposition. By understanding the role of CNT wettability for homogeneous nucleation of metal, CNT-copper composites are formed with final conductivity up to 2,000 kS/m for a lightweight composite with density less than 0.8 g/cm<sup>3</sup>, yielding a specific conductivity of 2,500 S.m<sup>2</sup>/kg. The contributions presented in this thesis provide the means to develop new electronics using CNT-based conductors, and guidelines drawn from the properties of yield stress fluids apply more broadly to the design of solution-processable conductive inks.

Thesis Supervisor: Gareth H. McKinley

Title: School of Engineering Professor of Teaching Innovation

Thesis Co-supervisor: A. John Hart

Title: Professor of Mechanical Engineering

## Table of Contents (Clickable Links)

Table of Contents (Clickable Links).....	4
Acknowledgments .....	9
List of Figures with Captions (Clickable Links).....	11
List of Tables with Captions (Clickable Links).....	26
<b>Chapter 1. Project Introduction.....</b>	<b>27</b>
1.1. Manufacturing of electronics across length scales .....	27
1.2. New performance needs.....	28
1.3. Aims of this thesis .....	29
1.4. Contribution and funding statements .....	30
1.5. How to read this thesis .....	31
<b>Part I: Carbon Nanotubes in Solution and Their Rheology .....</b>	<b>32</b>
<b>Chapter 2. Rheology of Carbon Nanotube Solutions and Implications for Printing Functional Items</b>	<b>33</b>
2.1. Abstract.....	33
2.2. Background .....	34
2.3. Data sources and methods .....	35
2.4. Carbon nanotube ink rheology .....	36
2.4.1. Concentration thresholds .....	36
2.4.2. Experimental rheology of CNTs.....	40
2.4.3. Shear yield stress and shear modulus.....	42
2.4.4. Structure at rest: shear modulus and yield strain.....	47
2.4.5. Shear-thinning index.....	48
2.4.6. Consistency index.....	49
2.5. Implications for 3D printability .....	50
2.6. Conclusions and Perspective.....	52
<b>Chapter 3. Improved Rheometry of Yield Stress Fluids Using Bespoke Fractal 3D Printed Vanes....</b>	<b>54</b>
3.1. Abstract.....	54
3.2. Introduction to yield stress fluids and measurement challenges.....	55
3.3. Theory of yield stress flow behavior .....	59
3.3.1. Rheology of yield stress fluids.....	59
3.3.2. Torque-shear stress and rotation rate-shear rate relations for the vane geometry .....	60
3.4. Generalized torque-to-stress conversion relations for vane geometries.....	64
3.5. Design and 3D printing of vanes and rheometer tools .....	68

3.5.1.	A. Design of vane for stereolithography .....	68
3.5.2.	Design of the coupling for attachment to the rheometer .....	71
3.5.3.	3D-printed cup with textured wall.....	72
3.6.	Experimental validation: rheological measurements vs tool design .....	74
3.6.1.	A. Measurements of viscous oils.....	74
3.6.2.	B. Measurement of a simple yield stress fluid.....	77
3.6.3.	Direct comparison of torque/stress conversion factors with models .....	80
3.6.4.	Start-up of steady shear flow.....	81
3.7.	Conclusion and Perspective on Rheometric Tool Choice .....	87
3.8.	Appendix .....	90
3.8.1.	Full field stress distribution around N-bladed vane.....	90
3.8.2.	Fractal design .....	91
3.8.3.	Occluded Area Fraction (OAF) of a vane.....	92
3.8.4.	Printing and qualifying a new geometry .....	95
<b>Chapter 4.</b>	<b>On Oreology, the fracture and flow of “milk’s favorite cookie®” .....</b>	<b>97</b>
4.1.	Abstract.....	97
4.2.	Introduction .....	98
4.3.	Understanding shear stress and strain in sandwich cookie flow.....	103
4.4.	Results.....	105
4.4.1.	Fracture of creme.....	105
4.4.2.	Dependence of fracture on flavor, rotation rate, and creme “stuf” level .....	107
4.4.3.	Mapping creme failure in a box .....	108
4.4.4.	Creme distribution control and predictability .....	110
4.4.5.	Creeping flow causing delayed yielding under constant stress (horeology) .....	112
4.4.6.	The influence of milk.....	114
4.4.7.	Design of the mechanical Oreometer .....	115
4.5.	Moreology: conclusions and future work.....	117
4.6.	Materials and Methods.....	119
<b>Part II: Manufacturing with Carbon Nanotubes .....</b>		<b>120</b>
<b>Chapter 5.</b>	<b>Two-dimensional extrusion additive manufacturing.....</b>	<b>121</b>
5.1.	Abstract.....	121
5.2.	Introduction .....	122
5.2.1.	Survey of current applications and inks.....	122
5.3.	Experimental Methods.....	124

5.4.	Ink and Printing Process Development .....	126
5.4.1.	Formulation and Rheology of Aqueous CNT Ink .....	126
5.5.	Direct-Write Extrusion of CNT Ink .....	129
5.6.	Control of Conductivity During Printing .....	131
5.7.	Ink-Substrate Interactions for Impermeable Substrates .....	133
5.8.	Application of Printed CNTs to Flexible Conductors, Circuits, and Sensors .....	137
5.8.1.	Conformal and Extensible Circuit Elements .....	137
5.8.2.	Interactive Touch Sensor .....	138
5.8.3.	A Capacitive Fluid Sensor .....	140
5.9.	Benchmarking the Conductivity and Flexibility Achieved by Direct-Write CNT Printing .....	142
5.10.	Conclusions .....	144
5.11.	Appendix .....	145
5.11.1.	Time-Dependent Rheology of CNT inks .....	145
5.11.2.	Evidence of Isotropic CNT Arrangement .....	146
5.11.3.	Calculating Conductivity of Constituent CNTs .....	147
5.11.4.	Influence of Concentration on Feature Size .....	149
5.11.5.	Comparison of Commercial CNT Inks .....	149
5.11.6.	Mechanical Testing of CNT Prints .....	150
5.11.7.	Predictive Model for Width of Printed Lines .....	151
5.11.8.	Monitoring drying time of printed CNT traces .....	154
5.11.9.	Influence of the Substrate on Minimum Printing Resolution .....	155
5.11.10.	Conductivity of CNT Lines for Repeated Bending Cycles .....	156
5.11.11.	Contact Resistance Measurements of CNT Traces .....	159
5.11.12.	Fluid Sensor Used For Droplet Impact .....	162
<b>Chapter 6.</b>	<b>Immersed extrusion of high-conductivity carbon nanotube threads and extensible coils using an anti-solvent bath .....</b>	<b>164</b>
6.1.	Abstract .....	164
6.2.	Introduction .....	165
6.3.	Materials & Methods .....	167
6.4.	Submerged Nozzle Printing Process .....	168
6.5.	CNT Ink Rheometry .....	171
6.6.	Classification and Measurement of Printed Threads .....	172
6.6.1.	Printing regimes .....	172
6.6.2.	Diameter and conductivity of continuous threads .....	173

6.7.	Regime 3: Coil printing.....	176
6.7.1.	Printing control of coiling structures .....	176
6.7.2.	Extensibility and Piezoresistivity of Printed Coils .....	179
6.8.	Perspective.....	181
6.9.	Conclusions .....	181
<b>Chapter 7. Fabrication of columnar field emitters by pointwise deposition and fluidic shaping of carbon nanotubes .....</b>		<b>183</b>
7.1.	Abstract.....	183
7.2.	Introduction .....	183
7.2.1.	Background .....	183
7.3.	Fabrication by static stretch-printing.....	185
7.4.	Field emission theory .....	188
7.5.	Field emission properties.....	189
7.6.	Discussion.....	189
7.7.	Conclusions .....	191
7.8.	Materials and Methods.....	191
<b>Chapter 8. Automating the 3D-printing of carbon nanotube field emitter arrays for high-current performance 192</b>		
8.1.	Abstract.....	192
8.2.	Materials and Methods.....	193
8.3.	Design of First Printing Method: direct deposition.....	193
8.4.	Design of Second Printing Method .....	194
8.4.1.	Ink design for extensibility .....	194
8.5.	Field emission results.....	197
8.6.	Conclusions .....	197
<b>Chapter 9. Individually addressable, 3d-printed carbon nanotube field emitter arrays for large-area vacuum electronics .....</b>		<b>198</b>
9.1.	Abstract.....	198
9.2.	Introduction .....	199
9.3.	Methods.....	199
9.3.1.	Device Design .....	199
9.3.2.	CNT Ink Preparation .....	200
9.4.	Field Emission Results .....	202
9.5.	Discussion and Conclusion .....	204
9.6.	Appendix: Field emission properties of mound-like emitters .....	205

<b>Part III: Path to a Copper-Carbon Nanotube Composite .....</b>	<b>206</b>
<b>Chapter 10. Process design for a copper-CNT composite for improved electrical performance .....</b>	<b>207</b>
10.1. Abstract .....	207
10.2. Introduction .....	208
10.3. Materials and Methods.....	209
10.4. Controlling Cu-CNT material composition by electrodeposition .....	209
10.5. Microscopic view and theory .....	213
10.6. Tuning wettability of electrolyte solutions .....	214
10.6.1. Cu-CNT Percolation .....	215
10.7. Integration into planar spiral inductor.....	216
10.8. Recommended Future Steps.....	<b>Error! Bookmark not defined.</b>
10.9. Conclusions .....	217
<b>Chapter 11. Conclusions and Recommendations for Further Work.....</b>	<b>218</b>
11.1. Research summary.....	218
11.2. Synthesizing a perspective on ink design rules to create flexible vs freestanding structures..	222
11.3. Recommendations for future work .....	224
<b>Bibliography .....</b>	<b>227</b>



## Acknowledgments

Thank you to everyone who has supported me during my time at MIT. Thank you first to leaders and mentors, older students and postdocs who gracefully served as role models for me early on and at the end, particularly Brian, Hangbo, Yu, Sanha, Pablo, Jonathan, George, Aoyi, Justin, Laurel, and Isaac. Thank you to late-night lab buddies in the HML, HML visitors and people always with a kind word in the HML kitchen, especially Anoop, Jianyi, Igor, Pavani, Dominico, Afzal, Yasmin, Mohua, and Lani. Particularly special thanks also to Anoop, Afzal, Joshua, Eric, and sometimes WolframAlpha (and ChatGPT) for late-night math help when equations were giving me trouble. Thanks to Olek for help with electronics, and to the whole Printing Cluster in Mechanosynthesis for brilliant feedback, cool suggestions, and freely-given help on research progress; it's communities like these that make groundbreaking research not only possible, but a lot of fun.

I would like to particularly thank Alex Kashkin and Megan Creighton, along with Jon and Luis, for help reviving the field emission project after much heartache...without your scientific insight and energy it would never have been possible, nor nearly as enjoyable, to get real results from the research ideas we started with.

Thanks to Maytee C, my partner in crime organizing MERE just for one year, then getting wrapped up into it again for our second year during COVID, it was fun to make something new with you. And thanks to Noam, Nicole, Ippolyti, and April for all the fun times strategizing and planning with our advising working group, and Prof. Gallant for behind-the-scenes support in our efforts.

Thanks to all the friends in our SidPac Breakfast clubs with Naveen, Zoey, Alex, Avi, Dan, and more, and midnight walks and book clubs with the same group, and sometimes Anzo, Max, Mark, Martín, and many others. Thanks Zoey for organizing so many social events that have been convenient to go to. Thanks Conley for always being there when I need to call and talk about something besides work.

Thanks to the many UROPs in our lab for inspiring me to approach research with a more creative view: Myles, Mandy, Philip, Siena, Joy,Carolynn, Helen, Anupama, Jay, Cody, Max, Aquila, and Andrew (and I hope I didn't miss anyone). Myles, Helen, and Cody, I hope grad school is still going ok. And congrats also to Dr. Kurfess (you even beat me to graduation!). And thanks to Ugo, Korine, Vrad, Dr. López, and very especially Wyatt for continued support and cheering me on. It means a lot.

I'd like to also remember Prof Swan, who ought to still be with us. Many thanks for his careful and apt feedback in joint group meetings, from him and from his students Kyle and Mary. Excelsior! Onwards and upwards. And many thanks to our SuperGroup meetings also with so many people and diverse ideas with all the lab members working with Profs. Doyle and Qi.

Thanks to Sarah, my roommate for the last two years, for giving me space to write. And to Pika, our feline roommate of the last several months, for always making sure I take time to play.

And anyone I forgot to mention. I promise I haven't forgotten you, I've just lost track of everyone in the last moments of writing my thesis. Drop me a line.

Thank you everyone.

Detailed acknowledgments for funding and assistance in the lab for work included in this thesis are included in **Chapter 1.4**. Other collaborators are not forgotten! But there are too many to list right now.

## List of Figures with Captions (Clickable Links)

**Figure 2.4-1:** Stick plot. Based on the well-known Graessley diagram for polymers [47] and using insight from polymer dynamics literature of rigid rods [48], this chart delineates regimes of CNT solutions based on volume concentration,  $\phi$ , from 0.001 to 1 (0.1% to 100%) and aspect ratio AR, the ratio of the length L to diameter d, from 1 to 1,000. With increase in either property, isotropic suspensions travel from dilute, to semidilute, to concentrated, two-phasic including liquid crystalline (LC) and isotropic, and finally fully liquid crystalline regimes. A vertical line at  $\phi=0.1$  marks the boundary of the semidilute regime if rods are aligned. The boundary for the semidilute regime is increased for flexible materials.

**Figure 2.4-2:** CNT ink rheology for long CNTs in aqueous suspension. Shear stress  $\sigma$  as a function of shear rate  $\dot{\gamma}$  for an array of CNT concentrations spanning the maximum measured extent in our lab in concentration and shear rate.

**Figure 2.4-3:** Nondimensionalized CNT flow curves for long CNTs in aqueous suspension. Nondimensionalized shear stress per yield stress  $\sigma_y$  as a function of shear rate nondimensionalized by solvent viscosity  $\eta_s$  per yield stress  $\sigma_y$ . Two grey lines indicate reference curves from [36] for short CNTs (—) and long CNTs (- -) in epoxy.

**Figure 2.4-4:** CNT ink rheology for a series of inks as a function of concentration. Aspect ratios are approximately <6200, 6400, 76, 1168, and 80 following the legend order (or data order from left to right). Power laws are 2.1, 2.7, 3.9, 3.3, and 5.1 in the same order.

**Figure 2.4-5:** Rheometry in action. a) A 0.7% CNT ink appears as a liquid, flowing into channels confined on a square gridded sandpaper, and having apparent curvature due to surface tension around the rheometer upper disk for fluid measurement. b) A high-concentration ink shows self-supporting behavior at a distance from the blot, appearing more as a solid. When confined between rheometer plates before testing, the structure retains a fine grooved texture inscribed by the sandpaper. c) Rheology measurement failure

**Figure 2.4-6:** CNT data on rheology map for data shown in **Figure 2.4-4**. Data all falls above the concentrated region and can extend into the liquid crystalline region.

**Figure 2.4-7:** CNT ink yield stress vs aspect ratio times volume fraction for data shown in **Figure 2.4-4**. Data collapse into two distinct populations, one within the concentrated regime ( $\phi AR > 1$ ) and one within the liquid crystalline regime ( $\phi AR > 7.8$ ). Both populations fit independently to a power law of  $\approx 2.7$ .

**Figure 2.4-8:** CNT ink yield stress vs aspect ratio times volume fraction for data shown in **Figure 2.4-4**. Data collapse into two one population when aspect ratio is based on the persistence length of  $\approx 500$  nm for a diameter of  $\approx 1.5$  nm. Both populations seen in **Figure 2.4-7** now fall within the concentrated regime and fit again to a master power law of 2.7.

**Figure 2.4-9:** Linear elasticity of CNT solutions showing (a) elastic shear modulus and (b) yield strain as a function of CNT concentration.

**Figure 2.4-10:** Modulus variation of CNT solutions as a function of volume fraction times aspect ratio, showing multiple behaviors.

**Figure 2.4-11:** CNT ink shear thinning index as a function of CNT mass concentration.

**Figure 2.4-12:** CNT ink shear thinning index, same as in **Figure 2.4-11** but plotted by concentration in percent volume fraction to show separation of data due to different solvent densities.

**Figure 2.4-13:** CNT ink yield stress vs consistency index for aqueous ink with long CNTs.

**Figure 2.5-1:** CNT ink printability. The shear modulus is plotted vs the yield stress, and a benchmark empirical threshold of 3D printability for ceramics [69], [70].

**Figure 2.5-2:** Interactions between mechanics and yield stress  $\sigma_y$ .

**Figure 2.5-3:** Interactions between feature radius and yield stress  $\sigma_y$ . Thresholds based on gravity (horizontal lines) and yield stress (descending lines) are shown. Inset schematics show representative morphologies compared to a dashed outline showing a droplet with size set by the capillary length. The accessible region is above the threshold lines, shaded here in grey.

**Figure 3.3-1.** (a) Schematic of a 4-arm vane ( $N = 4$ ) inserted halfway (for illustrative purposes only) into a cup of yield stress material (blue) for measurement. As the vane rotates, the shearing of material exerts a torque on the vane that is measured by the rheometer. (b) The local stress decays radially from the cylinder of material cut by the vane, out to a radius  $R_v$  where  $\sigma(r) = \sigma_y$ . Inside the vane boundary  $r < R_v$ , material ideally moves as a solid plug guided by the vane arms, and the radial velocity  $v(r)$  decays from  $v = \Omega R_v$  at the edge of the vane to  $v = 0$  at  $r = R_y$ , although the velocity profile is expected to deviate from an axisymmetric path, especially if the vane has few arms. (c) The shear stress field in the sheared region of fluid decays from a wall shear stress  $\sigma_w$  at  $r = R_v$  to the yield stress  $\sigma_y$  at a critical radius  $R_y$ , beyond which material is unyielded. The shear rate  $\dot{\gamma}(r)$  of material elements also decays to zero at  $R_y$ .

**Figure 3.4-1.** (a) Analytical contour plot of the shear stress field for a Newtonian fluid calculated using equations (A1-A3) around a 4-armed vane in an unbounded domain, normalized by  $\mu\Omega$  as a representative scale for the viscous stress. Strong dipolar stress concentrations are present at each vane tip. Progressively smoother profiles form around 12 and 24-armed vanes. Profiles are all  $N$ -fold azimuthally periodic, approaching an axisymmetric Couette flow in the limit  $N \rightarrow \infty$  (b) The azimuthal shear stress profile  $\sigma_{r\theta}(\theta)$  as a function of angle  $\theta/N$  between two neighboring vane tips for a family of vanes with increasing number of arms, calculated at a constant radius of  $r = 1.05R_v$ . The first vane arm is located at  $\theta=0$ . The stress initially increases sharply due to the stress dipole, and then decreases between arms. (c) Profiles for  $0 < \theta < \pi/2$  for the same vanes in (b), shifted vertically for clarity. The y-axis labels indicate the number of arms. (d) A series of vane designs considered in the present chapter, along with the number of vane arms  $N$ , the occluded area fraction (OAF) displaced by the solid vane compared to an equivalent circle, and a comparison of the area occluded by the vane compared to the corresponding area of a vane with  $N$  straight arms (denoted OAFN).

**Figure 3.5-1.** a) A complete vane design for the case of a finite 3-generation Bethe lattice with  $N = 24$  contact points at  $\mathbf{r} = \mathbf{R}_v$  and (b) the printed vane mounted on a DHR-3 rheometer spindle. The mounting design (A) allows us to directly connect the spindle coupling to the chosen vane geometry. A  $45^\circ$  transition angle and otherwise straight cylindrical features allows the vane to be printed via stereolithography without supports, building vertically from the vane end first, which is the upper surface in the 3D printer tray shown in (c). An oblique view shows smooth sidewalls despite the presence of visible stacked layers (d). This is because of the chosen printing orientation. (e) The input fractal shape design and a photograph of the fabricated part on end. (f) An optical micrograph of one edge of the printed design shows the  $\sim 200\mu\text{m}$  feature resolution achieved with 3D printing.

**Figure 3.5-2.** (a) The DHR and AR-G2 family of controlled stress rheometers have a loose threaded “draw rod” extending through the drag cup motor housing and sensing head (outlined in blue), with (b) a spindle (highlighted red) that aligns the geometry to the axis of rotation of the rheometer. (c) An on-end view of the as-designed coupling and (d) a photograph of the 3D-printed part, which has a loose interference fit ( $50\mu\text{m}$  overlap) on the spindle for radial positioning, and locks in place axially using the spindle M4 screw with a threaded nut insert. (e) Computer drawing of the press-fit M4 nut that connects the part to the rheometer. The knurled bottom surface holds it in place within a centered hole in the printed vane.

**Figure 3.5-3.** (a) A 3D-printed cup featuring a textured inner wall to prevent slip. Lower arms clip onto the standard Peltier plate base, and the cup walls disassemble from the base via a threaded mating feature for ease of cleaning out thick yield stress materials from within the ribbed surface texture. The inset shows the crenelated ribs around the outer surface, which have 1 mm width and side length, and 2 mm spacing. (b) The assembled cup mounted onto a Peltier plate base, filled with mayonnaise, and (c) the disassembled cup with material still inside, and (d) a cleaned and disassembled cup and base.

**Figure 3.6-1:** a) Measured viscosity of a viscous Newtonian silicone oil ( $1.0 \text{ Pa}\cdot\text{s}$ ) measured using several 3D printed vanes (including regular  $N = 3$  and  $N = 4$  arm vanes plus a 24-armed fractal vane and a ribbed cylinder (see Appendix C for details)), and (b) an expanded view of  $1 < \dot{\gamma} < 10 \text{ s}^{-1}$ . (c) Viscosity values measured for each geometry compared to the reference measurement made with a cone-and-plate geometry, with the mean percent difference labeled, averaged for three or more measurements for the shear rates in (b). (d) Measured viscosity of a lower viscosity Newtonian silicone oil ( $\mu = 0.010 \text{ Pa}\cdot\text{s}$ ) measured by several 3D printed vanes ( $N = 3, 6, 10, 24$ -arm fractal, and 24-arm ribbed cylinder). Data is shown with lines indicating mean values and clouds of similar color representing the standard deviation from three or more repeated measurements. At low shear rates  $\dot{\gamma} < 2 \text{ s}^{-1}$ , machine limitations of torque sensing caused noise. At high shear rates  $\dot{\gamma} \geq 20 \text{ s}^{-1}$ , secondary flow cause the torque to increase due to inertial effects, with the effect delayed to higher  $\dot{\gamma}$  for vanes with more arms. For shear rates of  $2 < \dot{\gamma} < 10 \text{ s}^{-1}$ , the viscosity was approximately constant for all vanes, and so results are inter-compared in this region. (e) Enlarged view of the region within  $2 < \dot{\gamma} < 10 \text{ s}^{-1}$  together with percentage error. (f) Measurement range shown for each geometry compared to the reference measurement made with a cone-and-plate geometry, with the mean percent difference labeled, averaged for three or more measurements over the range of shear rates shown in (e).

**Figure 3.6-2:** Comparison of vane performance when measuring the flow curve of a Carbopol-based hair gel, a simple (non-thixotropic) yield stress fluid. a) Raw torque vs rotation rate for a range of 3D printed vanes (cylinder, vanes with  $N = 3, 4, 12, 24$  arms), and (b) shear rate conversion factor from equation (7). (c) Final flow curve of shear stress-shear rate after converting stress via equation (11), compared to the cone-plate reference curve (black filled circles). (d) For stress converted via the  $N$ -dependent equation (12), most data falls on top of the true curve. The exceptions are for the sparse 3-armed vane, and the cylinder which experiences slip at low shear rates. (e,g) The error in the vane data compared to cone and plate reference is shown, along with an error cloud (grey shaded region) showing error from three repeated cone-and-plate measurements of the Carbopol microgel. (caption continued on next page)

(f, h) Mean error and the range of error for each vane for three repeated measurements, averaged along the entire curve, where the mean percent error is labeled. The background grey bar shows the range of repeated cone-and-plate reference measurements. The error from the cylinder is represented for both the entire curve including slip (light purple bar) as well as for the partial curve without slip at higher shear rates (dark purple bar). Computing the sample stress using the  $N$ -dependent expression (h) leads to the lowest overall error for all vanes (excluding the 3-armed vane) with  $<1\%$  mean error for the fractal and 4-armed vanes, indicating the universal applicability of this conversion expression (equation (12)).

**Figure 3.6-3.** The optimal torque conversion factors calculated from experimental data for three different fluids were compared with the torque conversions factors computed using the two expressions in equations (11) and (12) for a series of  $N$ -armed vanes. Separately, we also show the conversion factor expected for a Couette “bob” (cylinder) with  $N \rightarrow \infty$ .

**Figure 3.6-4.** Transient yielding behavior of a Carbopol-based hair gel shows simple yield stress behavior in start-up of steady shear flow tests using a fractal vane ( $N = 24$ ). (a) A series of shear rates were applied, with 1,000-2,000 s per step, to understand the transient response of the Carbopol. (b) For all imposed rates, the Carbopol shows an initial elastic response followed by plastic yielding at a constant terminal flow stress. (c) When the data are plotted using the apparent strain  $\theta = \Omega t$  rather than the experimental step time on the abscissa, they superimpose, revealing a consistent material response. In all cases, the material elastically deforms until it yields at a critical apparent strain  $\theta_y \approx 0.2$  rad and immediately plateaus at an almost constant value of the stress. The inset shows an optical micrograph of the material microstructure.

**Figure 3.6-5.** Yielding behavior of mayonnaise (a thixotropic jammed oil-in-water emulsion) measured with a 24-arm fractal vane. A start-up of steady shear test at a constant rotation rate  $\Omega = 1.6 \times 10^{-4}$  rad/s was performed after a sequence of pre-conditioning at a shear rate of  $0.1 \text{ s}^{-1}$  followed by a waiting time  $tw$ . An inset image in (a) shows an optical micrograph of the material microstructure. (b) A fractional model with a single Scott Blair element was used to describe the viscoelastic material response for times  $tw < t < t_{peak}$ . Up until 100 s, the quasi-modulus  $G^*$  increases and the exponent  $\alpha$  decreases rapidly, indicating stronger and more solid-like behavior arising from restructuration. For waiting times  $tw > 100$  s, changes in the viscoelastic solid properties were more gradual while (c) the magnitude of the stress overshoot began to increase more rapidly, indicating a complex multiscale reformation of the microstructure between tests.

**Figure 3.6-6.** Yielding behavior of a carbon black-based battery slurry measured with a 24-arm fractal vane. The sample permanently degraded with each yielding event, instead of fully recovering, and the stress overshoot decreased with each repeated trial. The inset image shows an optical micrograph of the material microstructure.

**Figure 3.7-1.** Competing factors affect choice of the rheometric test fixture, *i.e.*, vane, bob, or an intermediate structure. Relative merits are shown with a graded performance scale from excellent (blue) to poor (white). General design criteria include slip mitigation, consideration of sample volume displaced by the vanes, stress homogeneity, recirculation of fluid, and manufacturability. Schematics of these main sources of error for 4-arm vanes and cylindrical bobs are shown above, together with photographs of the 4-arm and 24-arm vanes.

**Figure 3.8-1.** Coordinate system of  $(\xi, \varphi)$  used here for a vane of thickness  $t \ll R_v$ . (b) An example of the local dipolar stress field evaluated around a vane tip for a vane with  $N = 4$  arms.

**Figure 3.8-2.** Designs of the fractal vane geometries analyzed here and subsequently 3D printed. (Left) A finite Bethe lattice with  $Z = 4$  central branches and  $G = 2$  generations. (Right) Lattices with 3 center branches and 2, 3, and 4 generations. The occluded area fraction (OAF) defined in equation (13) are labeled for each design. The values of occluded area fraction are calculated assuming a constant vane thickness of  $t = 0.13R_v$ .

**Figure 3.8-3.** Optimal shapes connecting a center point to  $N$  equidistant points on the outside of a circle (solved for using a Steiner Tree algorithm [130]).

**Figure 3.8-4.** (a) Comparison of the Occluded Area Fraction (OAF) for a series of designs of vanes (see equations C2, C3, and (13) in the main text), versus the number of arms,  $N$ . (b) Comparison of the occluded area for the local optimum shape (as determined by Steiner optimization) as compared to a set of fractal designs such as those shown in **Figure 3.8-2**.

**Figure 3.8-5.** Comparison of four designs of an 8-armed vane using the optimum Steiner tree, straight arms, a fractal structure with  $120^\circ$  angled branches, and a ribbed cylinder. The occluded area fraction (OAF) is calculated for a vane thickness of  $t/R_v = 0.13$ .

**Figure 3.8-6.** Measured runout for six coupling methods or inserts.

**Figure 3.8-7.** Effect of runout, or eccentricity of rotation of the spindle, on torque measurement, calculated as equation 1C4 in [150]. Lines mark the measured runout for the commercial TA vane and press-fit nut, which give  $\lesssim 2\%$  error in torque.

**Figure 4.2-1:** (a) What happens when you twist an Oreo? (b) Eventually it splits into two parts, exposing the creme. (c, d) We observed that in a typical failure profile for Oreos from newly opened boxes, the creme most often tends to remain on one side, “Wafer 1,” with a consistent orientation per box. In this case, Wafer 1 faces to the left side of the upright box for a standard size package of regular Oreos. The creme occasionally splits between sides, often due to defects or small fractures in one or both wafers. (e) This is consistent for cookies with different creme level, with a strong bias towards wafers facing one

side of the box rather than the other, facing left for Regular, right for Double, and up for Mega (where rows are oriented vertically rather than horizontally) in standard size packages.

**Figure 4.3-1:** (a) A cookie is mounted for testing on parallel plate fixtures of a laboratory rheometer and adhered to the metal plates by a low-temperature thermoplastic adhesive. (b) The sandwich cookie is a layered composite with two solid wafers enclosing a central cream layer. When one wafer is rotated relative to the other, the creme deforms in torsion. (c) The resulting velocity field within the creme is a function of applied rotation rate, material height, and radius from the center. In this figure, red colors indicate kinematic properties and blue colors indicate geometric properties.

**Figure 4.4-1.** When the cookie is rotated on the rheometer at a constant speed of 0.1 rad/s, the shear stress is measured and plotted (a) on linear axes and (b) on logarithmic axes. The results show three mechanical regimes: (1) a linear elastic response, (2) a stress maximum indicating material plasticity and yielding, and (3) structural breakdown of cookie integrity, typically due to creme delamination from the top wafer (Wafer 2). Results are shown for  $n \geq 4$  repeats of cookies from two separate boxes purchased a week in advance (red solid lines) and the day of the trial (black dash-dotted lines) with the average line for each box shown in bold for clarity. Annotations indicate the failure stress  $\sigma_f$ , failure strain  $\gamma_f$ , and slope corresponding to the linear elastic shear modulus  $G = \sigma/\gamma$  at low strains for the mean red curve.

**Figure 4.4-2:** The material mechanics are extracted to compare values between boxes. We use box plots (naturally) to visualize the comparative distributions of (a) failure stress  $\sigma_f$ , (b) failure strain  $\gamma_f$ , and (c) linear elastic shear modulus  $G = \sigma/\gamma$  at low strains. While systematic differences in the measured attributes are visible for all three parameters, only the reported values of failure stress and linear elastic modulus are statistically different ( $p < 0.05$ ) between boxes.

**Figure 4.4-3:** (a, b) Creme failure tests were repeated for different rotation rates, and our tests revealed a rate dependence, with the faster rotation requiring higher stress and strain. At the highest speed only, 10 rad/s (about 370 rotations per minute, as fast as a typical ceiling fan rotates), the wafer tended to break along with the creme, as shown in the inset to b of the cookie post-failure but still mounted on the rheometer. The dashed line indicates a line of slope one relating yield stress to yield strain. (c,d) The “stuff” level or height of creme was not found to influence mechanics of failure or creme distribution, and (e) the Oreo flavor did not influence stress levels, although (f) flavors seemed to influence how likely a wafer was to break, with images shown for one cookie each after twisting for the Dark Chocolate and Golden flavors. For the Golden variety, this wafer breakage was substantial enough to influence creme distribution onto some top-wafer segments and some bottom-wafer segments.

**Figure 4.4-4:** Creme distribution for all cookies mapped within a single box of Oreo cookies shows directional biases within the box, shown as a color map for a box with label text running to the right. Creme overall tends to be on right-facing cookies, but also more likely tends to fall to the left wafer for cookies on the rightmost side of the box. Left and right are oriented such that the package text is upright. The Plotted proportions shown in the lower right figure are calculated for cookie positions averaged over the entire row and neighboring two column positions for the single box, with inset images labelling



the most-likely failure type based on position, showing the differences between the left and right halves of the box.

**Figure 4.4-5:** a) While most creme layers failed adhesively in boxes of new cookies, b) cookies exposed to adverse conditions may cause creme to spread from its initial manufactured state, and then cohesive failure was typical for most cookies in the box. These visual signs of changing creme fill levels (indicated by the black arrows in (a) and (b)) are typical but not deterministic predictors of failure mode. c) Failure tests also distinguished between cases in the computed stress-strain curves resulting from the measured torque as a function of imposed rotation angle. There was a single peak stress for adhesive failure, which occurs as a single delamination step, and two or more maxima in stress for cohesively failing creme layers due to the more complex dynamics of cohesive failure propagation along nonplanar surfaces. Cohesive failure was also typically observed to result in a higher failure strain and lower failure stress, as shown here.

**Figure 4.4-6:** Creme was observed to yield slowly under applied stress in the laboratory rheometer. Low, medium, and high stresses were applied (6.7 kPa, 15.5 kPa, and 19.1 kPa, respectively) and the apparent creep compliance (equal to the measured angular strain  $\gamma(t)$  divided by the constant applied stress) was monitored. For high stresses, the creme immediately yielded, showing an apparent compliance increasing quadratically with time (*i.e.*, due to the inertial acceleration of the rotating rheometer fixture and attached wafer, with negligible resistance from the ruptured creme filling). For medium and low stresses, the creme showed a delayed response indicative of material creep, eventually flowing under medium stress. Arrows indicate approximate locations of slope change.

**Figure 4.4-7:** A wafer was mounted on the laboratory rheometer and subjected to milk imbibition at a time  $t = 0$  s. The shear elastic modulus of the wafer dropped to 0.5% of its initial value after 40 s and settled at a new equilibrium static value of 1 kPa. Inset images show the dry wafer on the rheometer at early times and the wafer surrounded by milk at later times.

**Figure 4.4-8:** The time to failure of a suspended wafer (1) or full cookie (2) was measured. The mean value for a single wafer was 30.2 seconds ( $n = 8$ ), and for a full cookie was much more variable but a mean of 63 seconds ( $n = 6$ ). The variability is ascribed to differences in milk takeup rate depending on how exactly the cookie is dunked, due to interference from the creme.

**Figure 4.4-9:** A 3D printed Oreometer is used to perturb cookies with scientific precision by applying a known and controlled torque. a) In this device, (1) the cookie is mounted first into one half and then (2) the second half of the rubber band-powered clamps, which are then (3) placed into the vertical assembly mount. (4) "Penny castles" are mounted on the wings and coins are successively loaded to one side to apply controlled torque until (5) The creme yields. b) Results replicate values measured by the laboratory rheometer. c) Photographs demonstrate the same tool, also including the rubber bands in two different arrangements designed to apply different levels of gripping strength in the clamps.

**Figure 5.4-1:** CNT ink formulation and rheology: (a) Flow curves of shear stress versus shear rate for CNT-based aqueous ink at five concentrations spanning  $0.06 < c < 18$  mg CNT per mL or  $0.02\% < \phi < 2.4\%$  volume fraction, showing shear-thinning behavior and (b) a yield stress increasing sharply with CNT

concentration. (c) As CNT concentration increases, CNTs eventually form nematic domains, which are (d) observed using polarized optical microscopy, shown here for five selected inks, in which the highest three concentrations exhibit birefringence. (e) As CNT inks are deformed under large strain amplitude,  $\gamma < 30\%$ , the elastic modulus collapses. (f) Upon cessation of shearing, the elastic modulus reaches a steady value within seconds and maintains a stable value over hundreds of seconds.

**Figure 5.5-1:** (a) CNT ink is dispensed at an average speed  $v_{ink}$  from a nozzle of inner diameter  $D_0$  moving at a speed  $v_{nozzle}$  over a dry substrate. (b) Photographs of the experimental 3D printer writing cursive text onto a Kapton film. (c,d) As  $v_{ink}/v_{nozzle}$  is increased, the resulting denser deposition of CNTs controllably increases both the dimensionless line width,  $w/D_0$ , and (e) the electrical conductivity of the printed line.

**Figure 5.6-1:** (a) The linear conductivity of printed CNT traces is controlled by the material deposited per area, and varies with a range of 108 due to percolation effects. (b) Printed lines with CNT inks at different loading show enhanced opacity and increasing line edge smoothness with higher concentration of CNTs and higher  $v_{nozzle}/v_{ink}$ .

**Figure 5.7-1:** CNT ink printed onto several flexible substrates. (a) Here, we show traces deposited onto six ink-impermeable substrates with different wettabilities  $\cos(\vartheta^*) = r\cos\vartheta$  and (b) one permeable chromatography paper. (c) The (reduced) line width of prints is consistent between substrates and print conditions, in agreement with an equilibrium wetting model balancing surface tension and gravity. The model cross section is shown schematically inset into the figure. (d) During the printing, liquid was initially large in volume for large  $v$ , later drying into a flat layer. When printing at small  $v$ , prints dried almost immediately, forming flat traces. (e) Topographic scans show the overall surface height variations ranging from dark blue ( $0 \mu m$ ) to red ( $+10 \mu m$ ), which are initially different on porous and impermeable bare substrates, but the surface of CNT traces printed on each results in a similar final texture. (f) The effect of wetting on different substrates is a limiting factor at minimum resolution, where the paper substrate, having lower  $\cos(\vartheta^*)$ , most readily held ink in place. (g) A spiral with narrow inter-line spacing is printed using  $v = 0.07$  on Kapton film.

**Figure 5.8-1:** (a) A CNT trace was printed to spell “mechano synthesis” with (b) a blue surface mount diode (1 mm in length) manually placed between words (c) to illuminate when powered. (d) The conductivity of printed traces is constant within 3% when bent at a radius of  $>1$  mm, which is shown by sustained illumination of the diode when wrapping the printed artifact around containers with radii of (e) 35 mm, (f) 13 mm, (g) 1.5 mm, and (h) 2.7 mm. Scale bars in (e-h) are all 10 mm.

**Figure 5.8-2:** (a) Contact resistance is measured for CNTs printed onto papers as a function of applied pressure at the contact point. Here, contact resistance  $R_c$  is normalized by  $R_m$ , the resistance of the CNT trace for 1 mm of length. (b) The contact resistance normalized by CNT network resistance decreases with printed linear density, indicating improved contact. (c) During printing onto glossy paper, the LED, indicated by the arrow, is placed by the printer at a designed 2 mm break in the printed line, making physical and electrical contact with the still-liquid ink. (d) The overall CNT circuit connected a power source, LED, and button that close the circuit to illuminate the power source. (e) The LED was protected with an adhesive overlayer to prevent detachment and (f) the button is made by a folded paper section

holding a discontinuous line segment. (g) This blue LED is used to illuminate an image of a (SpaceX Dragon) rocket blasting off when the button was pressed through an overlaid illustrated page.

**Figure 5.8-3:** (a-c) A device for sensing fluid wicking speed is fabricated by printing a six-line interdigitated capacitive sensor with a two-sided circuit on a sheet of chromatography paper and (d) directly incorporating circuit elements to amplify the measured signal. (e) The two faces of the circuit are connected by conductive vias. (f) A second version of the circuit uses a two-line capacitive sensor connected by wires to the main circuit. (g) The height of wicking fluid is verified by video analysis, and (h) measured by sensor output. After calibration, (i) the wicking speed is measured within 12% (1 mm of height) for two different fluids (distilled water, isopropyl alcohol).

**Figure 5.9-1:** A comparison of the elastic compliance of conductive materials versus their specific conductivity. Below a compliance equal to the compliance of typical substrates (paper, Kapton), a material will increasingly stiffen the flexible electronic device. Above this level, the device is stiffened predominantly by the substrate, and we consider the printed material to be fully compliant. We targeted and achieved printed traces in the conductive and compliant material regime. We also include data for low-density CNTs (light pink circles) which have directly measured compliance, while the mechanical compliance shown here is projected from mechanical tests of the more dense printed CNTs, while the specific conductivity is directly measured for both.

**Figure 5.11-1:** Evolution of (a) the consistency index,  $k$ , and (b) shear thinning index,  $n$ , for the inks shown in **Figure 5.4-1** as a function of CNT volume fraction,  $\varphi$ .

**Figure 5.11-2:** Following from **Figure 5.4-1**, we show (a) the frequency response of the inks in small amplitude oscillatory shear tests and (b) the onset of nonlinearity at large strain amplitude and subsequent recovery. Storage moduli,  $G'$ , are shown by filled symbols while loss moduli,  $G''$ , are hollow symbols with the same color and shading.

**Figure 5.11-3:** The edge of a printed CNT line was imaged under transmission polarized microscopy, showing in brightfield and polarized light. No long-range order is apparent.

**Figure 5.11-4:** (a) For CNT lines printed onto a range of substrates, the conductivity increased linearly with deposition rate. (b) Using equation S5, the conductivity of the constituent CNTs, reduced by the contact resistance of the network and residual surfactant, was estimated to be 1,900 S/m.

**Figure 5.11-5:** The concentration of CNT ink affected the width of printed lines. For a range of deposition rates, the low concentration ink systematically spread wider than the high-concentration inks, which is attributed to the yield stress rheology of the high concentration inks.

**Figure 5.11-6:** Three commercial CNT inks show similar behavior as CNT inks formulated in-house, denoted as grey symbols. Greater noise in the data for the commercial system is ascribed to use of lower concentrations. Error bars show standard deviation of 5 repeated tests.

**Figure 5.11-7:** (a) CNTs were printed, dried, and removed from the low-adhesion substrate to directly test their mechanical properties. (b) The typical failure surface was a simple fracture, with no apparent CNT pull-out. (c) Tensile data is presented for lines with linear density from 0.2 to 27 mg/m, and (d-f)

repeated tests are shown for three selected linear densities, showing similar elastic moduli among all tests, while the failure strain and strength were more variable, particularly for the largest sample.

**Figure 5.11-8:** A diagram of (a) the puddle model and (b) the droplet model shows the assumed geometry where the puddle contacts the edge of the drop at a given contact angle and reaches an equilibrium shape with a maximum possible height  $h_c$  set by a balance of gravity and surface tension/wetting effects.

**Figure 5.11-9:** a) Measured data of printed line widths is compared to model predictions. (b) The vertical axis has been rescaled by the nozzle inner diameter, showing some collapse of the data. (c) The vertical axis has been rescaled by the nozzle inner diameter and the relevant substrate roughness parameter ( $\tan\theta$ ) for each print, showing better collapse of data onto the model line for a range of process parameters and substrates.

**Figure 5.11-10:** The resistance of printed lines was monitored after printing to determine the drying time.

**Figure 5.11-11:** Printed straight lines are shown as a function of deposition rate,  $v$ , for (a) nonwetting (viscose filter) and (b) wetting (glossy paper) substrates. (c,d) Lines printed closely together are shown on Kapton film.

**Figure 5.11-12:** The roughness of printed lines is shown as a function of (a) the substrate roughness and (b) the substrate. Colors are the same as in **Figure 5.7-1**.

**Figure 5.11-13:** (a) The mean conductivity of our printed traces are constant within 2% for at least 1,000 bending cycles with a full inward crease. For significantly less dense CNT traces with  $v_{ink}/v_{nozzle} = 0.05$ , the conductivity degrades linearly with bend cycles up to a mean 28% increase over 1,000 bending cycles, with an initial resistance  $RO \approx 300\text{--}2100\Omega$ . (b) The folding cycles are performed manually, creating a full crease in lines between two electrical probes.

**Figure 5.11-14:** For impermeable substrates, adhesion of CNT traces is much lower and so lines may partially delaminate, mechanically affecting a wider (darker) spatial area of CNTs. When the substrate is porous, much less material is incorporated, which causes more acute destruction of the CNT network in the narrower (lighter) region, and this effect is amplified when less overall CNT material is deposited, denoted by low  $v$  values. The lines shown for  $v = 9$  are approximately  $3000 \mu\text{m}$  in width, and for  $v = 0.3$  are approximately  $800 \mu\text{m}$  in width.

**Figure 5.11-16:** CNT material resistance was measured using contact of two probes with varied length between probes on the same substrate. By varying the length between probes, the probe-CNT contact was measured separately from the base material resistance. In a second test, a CNT-CNT contact was introduced, and the contact resistance was measured the same way by varying the total length of measurement for the same CNT line as measured in the first case. Example data sets are shown for CNT lines with high and low linear density.

**Figure 5.11-17:** The contact point between two CNT traces printed onto paper was loaded to apply cyclic compressive forces. (a) The cycles were controlled by displacement, which (b) generated an applied

pressure. (c,e) The conductance (defined as the inverse of resistance) was monitored over the same cycles and (d,f) the contact resistance was compared to pressure over several cycles. The data with black circles in (d,f) here is reproduced for the same substrate and conditions as shown in **Figure 5.8-2a,b**.

**Figure 5.11-18:** (a) Voltage signal recorded upon measuring the impact of a small droplet of distilled water on a two-line printed CNT capacitive sensor. (b) The sensor is sensitive to the volume of the droplet through the initial spike in response and the area under the full curve. (c,d) The sensor can register addition of multiple droplets in quick succession (red arrows) and is still sensitive to the total volume, where the response after 60 seconds is equal for equal volumes deposited as separate drops or all at once. Here, each drop is a constant volume of  $0.5 \mu\text{L}$ . (e) The experimental setup is shown, where droplets are deposited by a calibrated micropipette.

**Figure 6.4-1:** Printing paradigm. (a, b) A vertically-mounted syringe moves in x, y, z around a printbed within a liquid reservoir with a free upper surface. (c) Extrusion of ink through a nozzle submerged in an antisolvent or coagulant causes the ink solvent to diffuse outward, precipitating the ink into a solid coil that settles down to the substrate. (d) Photograph of the nozzle moving on the printer, extruding coiled CNT structures into ethanol. The nozzle is shallowly submerged, with liquid only 1 mm above the bottom end of the nozzle.

**Figure 6.5-1:** Ink rheology. (a) Shear stress as a function of shear-rate; dashed black line indicates Herschel-Bulkley model fit as shear stress  $\sigma = \sigma_y + k\dot{\gamma}^n$  with labeled parameters. (b) Viscosity as a function of shear rate. (c) Transmission polarized imaging of CNT ink showing 10-200 micron wide liquid crystalline domains.

**Figure 6.6-1:** Printing regime map. For high mechanical draw ratios  $v^*$  fibers were fragmented rather than continuous due to the drawing force, though this transition happened later when antisolvent strength was greater. At lower  $v^*$ , continuous, straight fibers were observed. Only for the case of antisolvent strength  $c^* = 1$ , a regime of coiling instability was observed. Righthand images: printed fragments in the liquid bath for  $c^* = 0$  increasing in  $v^*$  from top to bottom, resulting in decreasing fragment size. Inset images show printed fibers with morphology of each regime.

**Figure 6.6-2:** Effect of ink-bath interaction. (a) Micrographs of carbon nanotube lines as-printed in liquid with antisolvent strength of  $c^* = 0$ . With increasing applied draw ratio  $v^*$ , the diameter decreases due to mechanical drawing. (b) Observed shrinkage ratio compared to applied draw ratio. This follows the power law trend of -0.5 only for antisolvent strength  $c^* = 0$ , showing a shallower slope for the other cases due to influences of solvent exchange and the coiling instability.

**Figure 6.6-3:** Effect of ink-bath interaction. Ranging from none (0) to antisolvent (1) has minor effect on (a) the swell ratio, which is nearly constant, and (b) diameter which is mostly affected by the applied draw ratio  $v^*$ , with a large effect on (c, d) conductivity and (e, f) specific conductivity. Error bars indicate range of measured values over  $v^*$ . Data are only reported for process values forming continuous linear or coiled fibers, resulting in different ranges spanned by the three conditions.

**Figure 6.6-4:** Coordinated impact of antisolvent. Increasing antisolvent strength induces a decrease in diameter and increase in specific conductivity.

**Figure 6.7-1:** Printing within the coiling regime. A printed bed containing a continuous thread made by a series of linear paths with progressively increasing  $v^*$ , resulting in less dense coiling from bottom left to upper right.

**Figure 6.7-2:** Exploring the coiling regime. Printed CNT filaments immediately after extrusion into pure ethanol ( $c^* = 1$ ) for (a) a 0.21 mm diameter nozzle and (b) a 0.6 mm diameter nozzle for the same linear motion speeds and approximate range of  $v^*$ . (a) Coiling patterns include translated coils, double meanders, and linear lines with increasing draw ratio  $v^*$ . (b) Stretched coiling and broken lines are also observed at high  $v^*$ . In these images dark spots between lines were removed for better visibility. Images of the lines themselves were untouched.

**Figure 6.7-3:** Scanning electron micrographs of printed coils. (a) Coils were printed at  $v^* = 0.16$ , dried, and inverted onto a metal stub for imaging. (b) After drying, the coil shown was pulled apart, remaining unbroken. The smooth righthand region (red arrow, c) shows the original region of overlap between coils. An otherwise wrinkled surface morphology is indicative of shrinkage from the solidification process.

**Figure 6.7-4:** Design and layout of testing apparatus. (a) Mounted coils were attached to a loading frame in a rheometer with lightweight cables connected to an LCR meter. (b) Fiber grips used a textured mount to hold the cardstock mount on the rheometer. The schematic shows the upper fixture.

**Figure 6.7-5:** Fibers and coils were subjected to mechanical strain while monitoring the electrical resistance. (a) Mounted coils were attached to a loading frame. (b) A linear fiber printed with  $v^*=1.31$ , a meandering coil printed with  $v^*=0.43$ , and (d) a coil printed with  $v^* = 0.16$ .

**Figure 7.2-1:** Schematic of field emitter between two charged plates, with tip radius  $r$ , overall height  $l$ , and interelectrode spacing  $d$ .

**Figure 7.3-1:** (a,b) Schematics and (c,d) photographs of the emitter fabrication process. (e,f) Transmission polarized micrographs of the surfactant assisted aqueous carbon nanotube (CNT)-based ink shows birefringent micro-domains that grow from (e) small,  $10\mu\text{m}$  structures to (f) extended domains  $> 1\text{ mm}$  with the addition of 0.05wt % high molecular weight poly (ethylene oxide) to 0.72 wt% CNT, enabling the fabrication process.

**Figure 7.3-2:** (a) Photograph and (b-e) micrographs of a representative emitter with aspect ratio of 10, showing a widened base and a blunt tip, approximately  $120\mu\text{m}$  diameter. (d) A close view shows densely-packed, long, and aligned CNTs/bundles on the emitter tip. (e) An overhead view better shows the far-reaching, rooted contact with the flat base substrate, which provides mechanical support and enhanced thermal/electrical contact.

**Figure 7.3-3:** X-ray microscale computed tomographs ( $\mu\text{CTs}$ ) of an emitter. (a) Side view of 3D reconstruction with (b) a vertical cross section and (c) representative horizontal cross section. (d) A cross section in the same location as (c) is shown after annealing to remove polymer, showing size reduction and no void generation.

**Figure 7.4-1:** I-V and Fowler-Nordheim curve showing measured field emission properties of one representative deposition-fabricated CNT emitter. The performance shows no change following the first half cycle (labeled, orange line).

**Figure 7.6-1:** The performance of our printed CNT emitters compares favorably with benchmark literature values for previously-made CNT fiber-based emitters from [20], [240], [275], showing (a) field enhancement, (b) turn-on voltage (determined by the peak in the second derivative of the FN curve), and (c) current density at 58 kV/m externally applied electric field, versus emitter aspect ratio (height/tip diameter) or tip diameter. Current density is compared to results from CNT emitters of varying geometries, fabrication processes, and analysis modes (continuous, pulsed), with unlabeled points reviewed in [285].

**Figure 7.6-2:** Post-testing scanning electron micrographs of a printed CNT emitter show no degradation or fraying of the tip. (Note that this emitter began without a flattened top.)

**Figure 8.3-1:** First printing method and fabrication results. A) CNT ink is extruded onto a substrate before quickly drying and shrinking. B) 4x4 emitter array as being printed. C) Zoomed-in optical image of an array fabricated on indium tin oxide coated glass. D) Top-view SEM of one emitter after test showing hairlike fuzz from CNTs emerging on the top surface. The width of the image in (D) is 10  $\mu\text{m}$ .

**Figure 8.4-1:** CNT inks viewed by transmission polarized microscopy, with stretched and deposited ink viewed through a 50  $\mu\text{m}$  thick capillary. A red arrow in (B) indicates an applied pressure to cause shear from left to right, which was removed before imaging. Inks are composed of (A) a 0.75% CNT ink stabilized by DOC, (B) the same ink with added PEO, and (C) a 5% wt CNT ink stabilized by SDBS.

**Figure 8.4-2:** A measurement of extensional viscosity using a capillary breakup extensional rheometer for a CNT solution in water, a PEO solution in water, and a mixture of CNTs and PEO.

**Figure 8.4-3:** Material behavior and process for the second printing method including (1) depositing, (2) adhering to a plate and stretching vertically, while drying time is allowed, and (3) removal of the top plate, leaving a freestanding array of emitters.

**Figure 8.4-4:** Second printing method fabrication results (SEM colors are inverted for clarity). A) Emitter array with spike and ribbon morphologies (size variations are from material inhomogeneity and oblique contact with the ink droplets). B) Spike emitter. C) Closeup of spike emitter tip. D) Closeup of a spike emitter tip after field emission. E) Closeup of CNTs protruding from emitter tip. F) Tip failure following emission at high current. G) Photograph of emitter stretch-printed onto the conductive pad of a printed circuit board. H) Closeup of the emitter in (G).

**Figure 8.5-1:** Emission results for emitter arrays made by both printing methods, with 3 tests per 2x2 array. A) Direct emission, where the arrows indicate turn-on voltage. In comparison, a flat coated sheet of CNTs emitted no current over the same voltage range. B) Fowler-Nordheim plot showing comparative field enhancement factor  $\beta$  for emitters from both printing methods.

**Figure 9.3-1:** Printing of arrays of individually addressable field emitters. A) PCB wiring schematic. B) Rendering of point-by-point printing process from cylindrical printing nozzle; each emitter is extruded on top of a different PCB vias, yielding an array of individually addressable field emitters.

**Figure 9.3-2:** Effects of ink modulation. A) Schematic showing individual emitter geometry as affected by ink yield stress. B-C) Optical photographs of FEAs as affected by ink yield stress variation (top row 250 Pa, bottom row 610 Pa).

**Figure 9.3-3:** Scanning electron micrograph (SEM) views of a 3D-printed emitter. A) Overhead view, showing an as-printed tip diameter of  $\sim 65 \mu\text{m}$ , with far finer features derived from the CNT ink. B-C) CNT bundles protruding from emitter. The effective emission length scale from Fowler-Nordheim analysis is 4-7 nm per emitter, visually corresponding to protrusions on the multi-walled CNTs viewed in C.

**Figure 9.4-1:** Emission data from an individually addressable FEA (“Addressable”) activated in bulk and a variant printed on a bulk copper substrate for heat dissipation (“Thermal base”). A) Direct emission current (left axis) and array current density (right axis) vs. nominal electric field strength (bottom axis) and applied bias voltage (top axis) for both bulk activation tests and for representative activations of two individual emitters, whose locations in the array are marked by colored shapes (inset). Data are shown for three voltage sweeping cycles per sample. B) Fowler-Nordheim plot for both bulk activation tests, from which field enhancement factors and activation areas were computed. Dotted lines show linear fits of  $\ln(I/E^2)$  vs  $1/E$ ; a linear fit implies Fowler-Nordheim model conformity.

**Figure 9.6-1:** Emission data from CNT emitter arrays printed with peaked shape onto PCBs and a bulk copper substrate, and arrays with a mound shape printed onto PCBs. A) Direct emission current (left axis) and array current density (right axis) vs. nominal electric field strength (bottom axis) and applied bias voltage (top axis) for bulk activation tests. Data are shown for three voltage sweeping cycles per sample. B) Fowler-Nordheim plot for each test, from which field enhancement factors and activation areas were computed. Dotted lines show linear fits of  $\ln(I/E^2)$  vs  $1/E$ ; a linear fit implies Fowler-Nordheim model conformity.

**Figure 10.4-1:** The base carbon nanotube substrate used for experiments is buckypaper which is a micro/nanoporous CNT mesh. This image shows a macro-scale photograph and a scanning electron micrograph of the buckypaper.

**Figure 10.4-2:** The system used for controlled electrodeposition coating onto CNTs uses small vessel to hold a glass slide with a CNT mesh parallel to a copper electrode while a controlled current is applied. The device measures 1 inch x 1 inch x 3 inches to match standard glass slide dimensions.

**Figure 10.4-3:** A conductivity map shows the influence of applied current density and time of application on the achieved conductivity of our Cu-CNT composite structures for buckypaper and for CNT tape.

**Figure 10.4-4:** Process control in the system covers (a) copper mass deposition, (b) mass deposition rate, and (c) conductivity are explained using reduced variables to understand what may be tuned for the process control. Black dotted lines show predicted behavior with no fitting parameters using equations described in the text.



**Figure 10.5-1:** Overview of the process development allowing controlled composite generation, combination with printed CNT spiral structures, and anticipated combination with fully-embedded printed structures.

**Figure 10.5-2:** Uniform nucleation of Cu is possible onto these CNT sheets, shown by optical microscopy, scanning electron microscopy, and electron-dispersion spectroscopy to mark the elemental composition of materials studied, denoting copper (Cu) and carbon (C).

**Figure 10.6-1:** Electrolyte solutions on buckypaper meshes show hydrophobic behavior.

**Figure 10.6-2:** High contact angles caused copper to only deposit on the surface of structures, whereas a modified electrolyte allowed deposition homogeneously inside pores of the CNT mat. Various treatments to the deposited electrolyte control the apparent contact angle on the textured substrate, leading to marginal wetting behavior. As a direct result, electrodeposition forms Cu nuclei either only on the outer surfaces or throughout the CNT mat, as shown by scanning electron micrographs (SEM) and electron dispersion spectrographs (EDS) for each case.

**Figure 10.6-3:** At higher concentrations, bulk conductivity measurements begin to discriminate between core-shell and homogeneous composites prepared via different deposition strategies. These are compared with models for conductivity including Hashin-Shtrikman bounds which delineate thresholds for isotropic composite conductors, a fitted percolation model (with critical density 10% and scaling exponent 1.5), and the standard model for the conductivity of three-dimensional Cu foam, which scales as density ratio cubed and has no fitting parameters.

**Figure 10.7-1:** Time-series showing the coating of Cu onto a printed CNT planar Archimedes spiral inductor progressing from the outside to the center. A bright, continuous coating is formed.

**Figure 11.1-1:** Thesis road map. Developing an understanding of CNT-based ink rheology, to inform and coordinate with printing processes to create functional items. Additional functional items not covered in this thesis are published elsewhere, most notably in [33].

**Figure 11.2-1:** Scaling of yield stress and rheology design maps from **Chapter 2**.

**Figure 11.2-2:** Printed CNT artifacts from **Chapter 5** keeping resolution during printing and then drying into thin films, and from **Chapter 8**, showing a large difference in morphology based on ink yield stress for drops deposited onto a PCB.

## List of Tables with Captions (Clickable Links)

**Table 2.3-1:** Data sources and details for CNT ink rheometry

**Table 5.11-1:** Substrate wetting parameters: contact angle  $\vartheta$ , roughness  $r$ , Wenzel wetting parameter  $\cos(\vartheta)$ . References are listed for contact angle values in the rightmost column.

---

## Chapter 1. Project Introduction

---

### *1.1. Manufacturing of electronics across length scales*

The additive manufacturing of flexible and conductive parts is a developing field. Commonly, metal nanoparticles and carbon nanomaterials are printed using a range of methods to form desired 2D and 3D objects. Metal nanoparticles require sintering and remain inflexible, although they reach high conductivity ( $>10^7$  S/m), while carbon nanomaterials suffer from low conductivity ( $<4 \times 10^3$  S/m) but due to high aspect ratios and small diameters are more flexible. This thesis seeks to address the conductivity of the carbon nanomaterials to make flexible and conductive printed parts.

Carbon nanotubes (CNTs) are well known for their outstanding mechanical, electrical, and thermal properties. In particular, a single CNT has been shown to be a little less conductive than metals and stronger than steel with one tenth of the density, due to their pristine molecular structure and potential for ballistic electron transport, making a single CNT one of the strongest and most conductive materials known and giving them the capacity to form ultra-lightweight circuitry. In addition, CNTs do not exhibit the “skin effect” which limits conduction in bulk metals below a certain physical size and at high AC frequencies, and exhibit extremely high current carrying densities ( $>10^9$  A/cm<sup>2</sup>, vs  $10^6$  A/cm<sup>2</sup> for copper, the highest metal), as well as resistance that does not decrease even at high ( $>400^\circ\text{C}$ ) temperatures, due to the mix of metallic and semiconducting nanotubes in unsorted CNT batches. More significantly, the properties of macroscopic fibers and films

made from pure CNTs have failed to achieve the same properties as individual nanotubes due to the low alignment of the fibers and the low CNT-CNT adhesion causing slipping and gaps between fibers, such that demonstrated mechanical and electrical properties of these CNT-based fibers typically are 1/10 or less than what a single CNT will exhibit, indicating room for drastic improvement.[1]–[4] As individual CNTs have a diameter of 0.5-50nm and length of 0.5-10  $\mu\text{m}$ , this limits the application of their most powerful properties to small scales. However, while the properties of a bulk CNT object always fall far short of the properties of an individual CNT, the quality of CNT-CNT contact in macrostructures can make up some of the difference. Indeed, in macroscale fibers and films, the alignment of the CNTs has been found to influence the electrical and thermal conductivity, elastic modulus, fracture toughness, and ultimate tensile strength, with each property increasing substantially with greater CNT alignment, also showing increased strength with decreased porosity [5]–[7]. Mechanical properties of polymer composites with small amounts of CNT (<0.3%) increase similarly with alignment.

## *1.2. New performance needs*

As a motivating example, it takes considerable energy to launch a spacecraft into space, and a rocket is typically 85% fuel by weight.[8] Thus, any methods to reduce the total weight of the launch vehicle can lead to considerable savings in fuel and overall cost. According to NASA's 2015 Technology Roadmap,[9] a significant area for potential weight reduction is in electronics and circuitry, which are commonly made of copper.

Carbon-reinforced materials are already a crucial part of NASA's catalog of materials as part of carbon fiber mats, and as a filler embedded in other composite material because of the strength they give to the material. By packing CNTs densely within polymer matrices, they can also create ultra-strong composites. However, the fabrication necessary to achieve this material replacement has been limited first by the ability to mass-produce very pure starting CNT material, though private companies like Meijo Nano Carbon Co. and OCSiAl are emerging with methods to make larger quantities of high-quality nanotubes.[10] Secondly, and more significantly, the properties of macroscopic fibers woven from CNTs have failed to achieve the same properties as individual nanotubes due to the low alignment of the fibers and the low adhesion causing slipping and gaps between fibers, such that demonstrated mechanical, thermal, and electrical properties of these CNT-based fibers are typically 1/10 or less of what a single fiber will exhibit, indicating room for drastic

improvement.[1]–[4] As a result, materials made of CNTs have been tested but are not widely used by NASA.[11]

Along another vein, resources in space are limited, while the versatility of 3D printing is extensive, as the fabrication process allows the creation of customized, net-shape and complex structures from a uniform stock of material. From its use in making intricate fuel injection nozzles for aviation,[12] to 3D-printing needed tools on board the International Space Station,[13] to dreams of 3D printing structures from locally available regolith on the moon or on Mars,[14] 3D printing will dependably provide enormous value to space exploration.

### *1.3. Aims of this thesis*

In this thesis, I describe a roadmap supported by examples to enable the intelligent process design for the construction of macroscopic 3D structures out of carbon nanotubes by the extrusion of liquid-based CNT inks carefully tailored for the desired applications. Uniquely, this incorporates an understanding of complex fluid mechanics as it pertains to rheological behavior.

In **Part I**, a discussion of ink development is presented using solutions of carbon nanotubes, with a particular focus on the rheology, or deformation of flow of these materials. As CNTs form liquid crystalline materials, yield stress fluids. The foundational experiments for this project developed a working understanding of the rheology of suspensions of CNTs with multiple concentrations and lengths and how properties in shear flow are influenced by nanotube alignment, solidification steps, electrical, and various mechanical properties of resulting printed structures. Although much progress may be made by iterative formulation and experimentation to assess printability, a more fundamental approach incorporates measurement of the fundamental material flow behavior as a characteristic tool to assess printability. As such, Part I also further develops an understanding of the rheology of yield stress fluids and the interaction of flowing materials with measurement tools to introduce a vane tool for making measurements that has a fractal cross-section.

In **Part II**, applying insight from rheological measurements and ink design, carbon nanotube solutions are used in three demonstration areas of manufacturing, capitalizing on the mechanical advantages of native flexibility of CNTs to print two-dimensional sensors in **Chapter 5** and coiled high-strain sensors in **Chapter 6**, the paired conductivity and

nanostructure to create field emitters and a field emission device in **Chapter 7**, **Chapter 8**, and **Chapter 9**.

In **Part III**, a method is developed to further increase conductivity of fabricated items by intercalating copper into nanostructured CNT assemblies. in **Chapter 10**.

Finally, a thesis summary and forward-looking perspective are presented in **Chapter 11**.

#### *1.4. Contribution and funding statements*

In order to clearly acknowledge all collaborators and funding sources for work presented in this thesis, chapter-wise contributions are listed here.

**Chapter 2, 3, and Chapter 6** were created by C. Owens alone with input from John Hart and Gareth McKinley. A version of **Chapter 3** is published as Owens, et al 2020 [15].

**Chapter 4** was created by C. Owens with help in construction of the Oreometer by Max R. Fan with input from John Hart and Gareth McKinley. Thanks to Cody Moose for the pun that inspired the entire paper. A version of **Chapter 4** is published as Owens, et al 2023 [16].

In **Chapter 5**, Crystal E. Owens performed the rheological characterization and imaging, printing tests, device designs. Amanda Fike assisted in the construction of the printer used in experiments. Robert Headrick and Steven Williams at Rice University designed, produced, and provided the CNT ink. Matteo Pasquali supervised the work at Rice University and A. John Hart and Gareth McKinley supervised the work at MIT. A version of this text is published as Owens, et al 2021 [17].

In **Chapter 7**, Crystal E. Owens developed the ink with extensional modifier. Joy Ma at MIT provided help on initial experiments with ink development and Megan Creighton helped with ideation and some field emission testing. Robert Headrick and Steven M. Williams at Rice University produced the base inks that were used in tests, advised by Matteo Pasquali. At the AFRL, Jon Ludwick performed field emission testing and scanning electron micrography of emitters, along with extensive help with data analysis and measuring emission orthodoxy, as advised by Tyson C. Back and Benji Maruyama. At MIT, Gareth McKinley and John Hart advised.

In **Chapter 8**, Crystal E. Owens performed the ink design and rheometry, Alex Kachkine designed the printing process and substrate, printed the ink over several iterations, tested field emission properties and reported their analysis. This section was co-written by Crystal and Alex, with advice from John Hart, Gareth McKinley, and Luis Fernando Velázquez-García.

In **Chapter 9**, Crystal E. Owens performed the project conception, ink design (with advice from Megan Creighton) and rheometry, Alex Kachkine designed the PCBs, printed the ink over several iterations, and tested field emission properties. This section was co-written by Crystal and Alex, with advice from John Hart, Gareth McKinley, and Luis Fernando Velázquez-García.

In **Chapter 10**, partial support was received by Lincoln Laboratory - MIT Mechanical Engineering Seed Fund. Reported results are based upon work supported by the Under Secretary of Defense for Research and Engineering under Air Force Contract No. FA8702-15-D-0001. Any opinions, findings, conclusions or recommendations expressed in this material are those of the author(s) and do not necessarily reflect the views of the Under Secretary of Defense for Research and Engineering. All designs, data collection, and experimentation was performed by C.E.O. with assistance in printing FDM parts by Andrew Doan, who was supported by the MIT UROP office over the summer of 2022. Input from Prof. Martin Z. Bazant is also gratefully acknowledged.

Crystal E. Owens was supported by funding from an NDSEG fellowship and MIT MathWorks fellowships.

All text of this thesis was drafted in full by Crystal E. Owens unless otherwise noted. However, the use of “we” and “our” is used throughout the text as a stylistic choice to maintain uniformity between sections.

### *1.5. How to read this thesis*

Each chapter is written as a standalone piece of writing. While notation and acronyms are usually consistent between chapters, where they may be changed the new definition is described at the first new point of use in each chapter.

---

***Part I:***

***Carbon Nanotubes in Solution and Their  
Rheology***

---



---

## Chapter 2. Rheology of Carbon Nanotube Solutions and Implications for Printing Functional Items

---

### 2.1. Abstract

Rheological properties describe the flow and deformation of fluids and soft solids. For extrusion-based properties and complex fluids, such as CNT-based inks, rheological parameters can be used to describe fluid structure and tailoring rheological properties can enhance extrudability and printability of printed parts. Here, using established scaling laws for the phases of rigid rods in solutions, and data from literature and our lab, an understanding is developed of scaling laws and influence of aspect ratio and volume fraction of CNTs in solution on yield stress, consistency index, shear-thinning index, and shear elastic modulus, and emergence of liquid crystalline behavior. Inks having a yield stress are found to fall into concentrated or liquid crystalline regime based on their aspect ratio. Inks in the liquid crystalline regime develop similar levels of yield stress or modulus at 1/10 the concentration of inks in the concentrated regime. The power law dependence of the yield stress on concentration is consistently 2.7 for the datasets observed here. The modulus has a stronger power law varying widely between 2.5 and 5.5 for different inks, which is attributed to the details of CNT-level network mechanics in solution. Shear thinning index metric of solution quality, where stable rigid rods should have a value never more than 0.5, and decreasing from there with increasing concentration, confirmed by experimental rheology of liquid crystalline formations. The consistency index is related to

the yield stress by a power law dependence. Power law trends are given for the rheological values as a function of concentration, enabling calculation of fluid behavior at different concentrations. However, the power laws themselves depend on the solvent and CNT size. This is finally connected to considerations of printability to create self-supporting structures.

## 2.2. Background

Carbon nanotubes (CNTs) exhibit outstanding electrical and thermal conductivity, and mechanical strength, flexibility, and stiffness, among other properties, leading to wide-ranging interest in their development and use [1]. The use of carbon CNTs as fillers is most common, and can imbue manufactured parts with increased electrical conductivity and mechanical strength compared to pure plastics; however, the achieved properties remain limited compared non-plastics [18]. Instead, to achieve maximal properties, and even exceed those made by traditional manufacturing, parts must include majority CNTs, where greater CNT-on-CNT contact increases part strength as a function of contact surface, particularly overlap length [19], density [6], and alignment for the case of uniaxial structures (i.e., fibers) [6], [19], [20] and aligned thin films [21].

As one major obstacle, a wide spectrum of manufacturing methods including molding, casting, 3D printing, inkjet printing, liquid-based coating, and fiber spinning require handling of fluids in solution form. Typically, the conductivity of 3D printed CNT-based inks is very low due to the use of fillers [22]–[26]. For example, very manufacturable doughs have been produced that have very poor conductivity due to poor suspension quality in solvents like *m*-cresol [27] or in polyvinylpyrrolidone (PVP) mixtures [22], resulting in great ability to coat and print geometries, but exhibiting final part conductivities under 4,000 S/m, compared to the maximum theoretical conductivity of a single CNT, which is on the order of 100,000,000 S/m (double that of typical metals) [28].

In contrast, methods using raw, as-produced CNTs, particularly via dry spinning, in which a CNT yarn is made by spinning directly from the production source of the chemical vapor deposition (CVD) reactor, and achieve electrical conductivity commonly above 1,000,000 S/m [29] due to increased length and ease of CNT-CNT alignment [19], and absence of impurities introduced for processability within a liquid. The conductivity especially increases if spun fibers are also doped with additives like iodine (I<sub>2</sub>), chlorosulfonic acid (HSO<sub>3</sub>Cl), or sulfuric acid (H<sub>2</sub>SO<sub>4</sub>) [29] This is only paralleled by wet

spinning from solutions of highly pristine, long CNTs suspended in superacids, the only known true thermodynamic solvent for CNTs at high concentrations [30], which stabilize dispersed CNTs by an electrostatic double layer of protons and negative counterions, and enables spun fibers with conductivities up to 10.9 MS/m and tensile strength up to 4.2 GPa [31]. The nature of the most typical superacid solvent, chlorosulfonic acid, presents severe handling and environmental challenges, although safer acid formulations with excellent CNT-suspending qualities have recently been introduced, notably using methanesulfonic acid [32], [33]. With careful attention to creating a suspension of well-dispersed CNTs, a much safer fiber spinning process has recently been demonstrated using CNTs suspended in concentrated form in aqueous solvents, and can achieve conductivities of 0.58 MS/m and tensile strengths of 1 GPa [34]. This work suggests that the methods of manufacture of CNT inks require both suitable CNT handling and suspensions in which CNT-CNT contact is readily achieved, and that much progress is yet to be made within solution handling and in applying understandings from fiber spinning to other common manufacturing processes.

In this chapter, an overview is provided of the rheology of CNTs as a function of concentration and tube aspect ratio, with reference to a guiding phase chart, and present and compare data from multiple sources for CNTs of different dimensions and in different solvents to understand the influence of properties on measured rheological properties. Finally, a conclusion presents a perspective on implications of these findings for printability of CNT-based and similar yield-stress inks.

### 2.3. Data sources and methods

#### *List of sources of CNT rheology data:*

Rheology data is displayed for multiple sources and multiple solvents using either CNT/solvent or CNT/surfactant/water mixtures (**Table 2.3-1**). Two in-house inks were used. What is denoted aqueous ink with long CNTs uses CNTs with length of approximately 9.4  $\mu\text{m}$  and mean diameter 1.5 nm, and is featured in **Chapter 5** and **Chapter 6** and [35]. What is denoted aqueous ink with short CNTs uses CNTs with 0.5-2.0  $\mu\text{m}$  length and 10-20 nm diameter, which is also featured in **Chapter 9**. Inks from Rahatekar use CNTs with mean length of 58.4  $\mu\text{m}$  (“long”) or 3.8  $\mu\text{m}$  (“short”) and about 50 nm diameter, sourced from [36]. General superacid ink rheology uses long CNTs in methanesulfonic acid, with data from [33], which was refit including only the highest shear rate range, using data at 10  $\text{s}^{-1}$  and above, to find the shear-thinning index  $n$ , and refit using the entire range to extract a

yield stress. Other data is from Davis, et al [37] using chlorosulfonic acid as a solvent, data from Hobbie et al [38] for CNTs in epoxy used directly for yield stress  $\sigma_y$ , and refit to extract the shear thinning index  $n$ , and data from Mirri, et al, 2012 [39] and Mirri, et al, 2016 [40] using CNTs in chlorosulfonic acid refit in the highest shear rate regime of  $10 \text{ s}^{-1}$  and above to extract the shear thinning index  $n$ .

**Table 2.3-1:** Data sources and details for CNT ink rheometry

CNT name and source	Solvent	Length	Diameter	Aspect ratio	Notes
Aqueous ink (long CNTs) (also in <b>Chapter 5</b> , <b>Chapter 6</b> , and [35])	Water / sodium deoxycholate (DOC)	<9.4 $\mu\text{m}$	1.5 nm (mean)	<6300	Rheology measured here
Aqueous ink (short CNTs)	Water / sodium deoxycholate	0.5-2.0 $\mu\text{m}$	10-20 nm	$\approx 80$	Rheology measured here
Rahatekar (short) [36]	Epoxy	3.8 $\mu\text{m}$	$\approx 50 \text{ nm}$	$\approx 76$	
Rahatekar (long) [36]	Epoxy	58.4 $\mu\text{m}$	$\approx 50 \text{ nm}$	$\approx 1170$	
Superacid ink [33]	Methanesulfonic acid	9.65 $\mu\text{m}$	1.5 nm	6430	Refit for $\sigma_y, n$
Davis, et al [37]	Chlorosulfonic acid				
Hobbie et al [38]	Epoxy				Refit for $\sigma_y$
Mirri, et al, 2012 [39]	Chlorosulfonic acid				Refit for $n$
Mirri, et al, 2016 [40]	Chlorosulfonic acid				Refit for $n$
Dan, et al [46]	Water / sodium dodecylbenzene-sulfonate (SDBS)				

- Refit for  $n$ : Data from the superacid ink, Mirri, et al, 2012 and Mirri, et al, 2016 were refit to a Herschel-Bulkley model (Equation 3), including only the highest shear rate range, using data at  $10 \text{ s}^{-1}$  and above, to find the shear-thinning index  $n$ , Data from Hobbie, et al was refit in whole to extract  $n$ .
- Refit for  $\sigma_y$ : Data from Hobbie, et al was used directly for yield stress  $\sigma_y$ . Data from the superacid ink was refit in whole to a Herschel-Bulkley model (Equation 3) **Error! Reference source not found.**, to extract a yield stress.

#### 2.4. Carbon nanotube ink rheology

While CNTs have many unique material properties, and unique challenges suspending them in solution, once adequately suspended in solution they theoretically will behave as

rigid rods. Rod-like particles are found in many new high-strength and high-composite manufacturing applications, due to their ability to align in flow to form semi-crystalline and therefore strong material regions. Common examples besides carbon nanotubes in solution [41] are nanomaterials like cellulose nanocrystals [42], as well as the rod-like tobacco mosaic virus [43], and the stiff backbones of typical rigid polymers, especially high-strength aramids such as Kevlar [44], [45], all of which are observed to transition through similar phases in solution due to their rod-like nature.

In particular, the particle shape allows these materials to form liquid crystals, which are aligned structures of particles in solution in which the long axis, the director, has nearly the same orientation for all particles within a given region although the particle centers are isotropically distributed, forming nematic liquid crystals. In the case of cellulose nanocrystals, which are chiral, the director has a constant pitch.

#### 2.4.1. Concentration thresholds

Several important regimes can be denoted. Based on the Graessley diagram for polymers [47], our Stick plot (**Figure 2.4-1**) delineates regimes of CNT solutions based on volume concentration,  $\varphi$ , and aspect ratio  $AR$ , the ratio of the length  $L$  to diameter  $d$  of the CNTs. With increase in either  $\varphi$  or  $AR$ , suspensions travel from dilute, to semidilute, to concentrated, to two-phasic including liquid crystalline (LC) and isotropic, and finally to the fully liquid crystalline (nematic) regime.

In a dilute suspension of rigid rods [48], each particle has more than enough room to rotate freely within a sphere with radius equal to the particle length, or the concentration  $\varphi$  is

$$\varphi \leq \frac{\pi d^2 L}{4\pi L^3} = \left(\frac{d}{L}\right)^2 = AR^{-2} \quad (1)$$

When concentration exceeds this value, it becomes semidilute. In a semidilute suspension, each particle has more than enough room to rotate freely within a disk of radius  $L$  and thickness  $d$ , yielding [48]

$$\varphi \leq AR^{-1} \quad (2)$$

for randomly oriented rods, or  $\varphi \ll 1$  for aligned rods [48]. The Flory Lattice and Onsager theories describe the predicted transitions to liquid crystalline behavior [48]. The Onsager

relationship has been observed to fit better to carbon nanotube solutions in superacid solvents [10].

Such regimes are denoted based on concepts of rheological percolation, or how much each CNT interacts with its neighbors. In the dilute regime, CNTs act as individuals. In the semidilute regime, they interact during flow but not at rest [48], contributing non-Newtonian flow behaviors including shear-thinning and a zero-shear viscosity [37]. In the concentrated and liquid crystalline regimes, they interact at all times, contributing yield stress, which is often observed [38]. In contrast, electrical percolation for conductive rigid rods happens when a spanning network is formed at rest [49], equal to the concentrated regime here and above. Therefore, an ink that is conductive in liquid form must have non-Newtonian behavior. And an object printed from a liquid ink that is non-conductive must undergo considerable concentration by solvent loss or other methods [50], adding complexity. Therefore, when considering CNT-based inks for manufacturing, one must handle non-Newtonian flow behavior, typically yield stress or liquid crystalline behavior.

Following the Stick plot (**Figure 2.4-1**), for example, to formulate an ink CNTs having an aspect ratio of 100, fairly “short” CNTs, it becomes concentrated with a volume fraction of 0.01, or 1%. For “long” CNTs, with aspect ratio 1,000 or above, it becomes concentrated with a volume fraction of 0.001, or 0.1%. This leads to a natural observation that higher-concentration inks can be formed with proportionally shorter CNTs [36] but at the loss of conductivity and tensile strength. For example, spun fibers from CNTs exhibit scalings of tensile strength $\sim$ AR<sup>1</sup> [7], [19], [51] and conductivity $\sim$ AR<sup>0.8</sup> [51], which have considerable impact when AR can easily span 2 decades. And in specialty applications like cold cathode field electron emission, higher processing decreases important metrics like emission current from printed CNT pastes [52]. However, for the improvement in manufacturability, using short CNTs is often praised [36], [53], as a suitable dispersion is essential to coating continuous films and fibers [53].

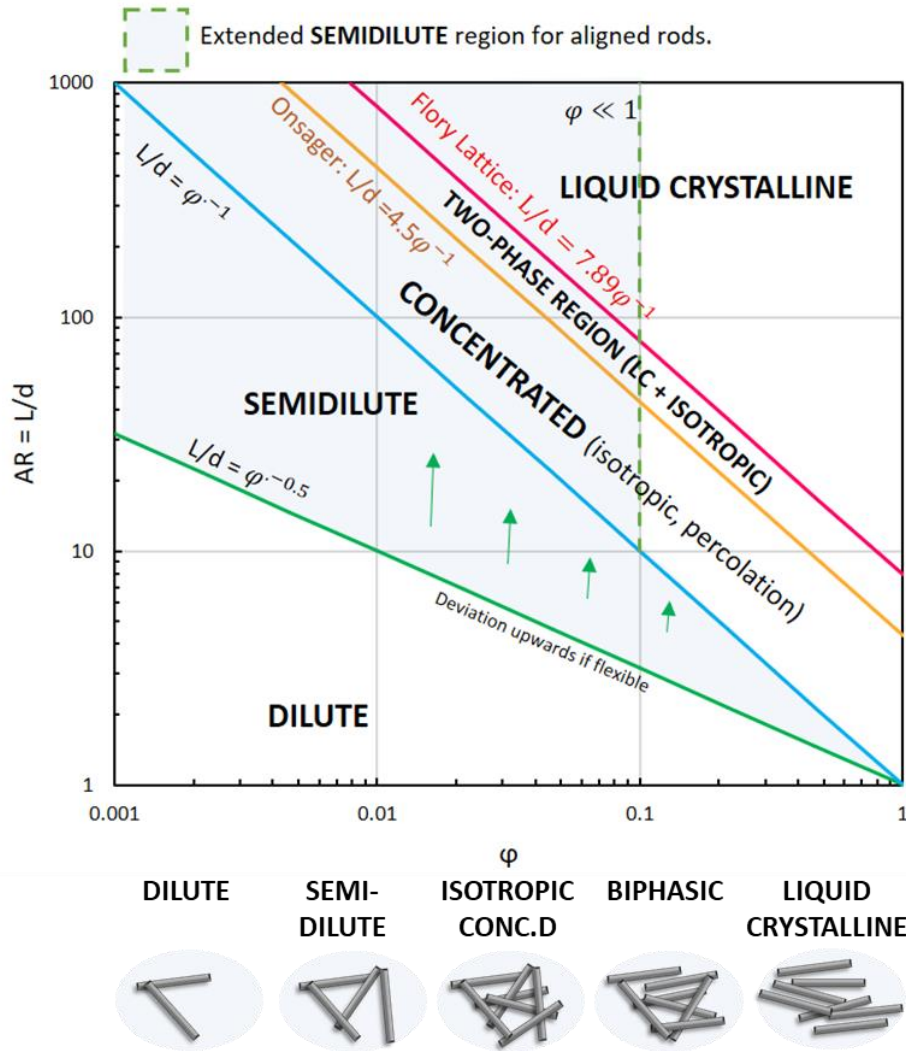


**Figure 2.4-1:** Stick plot. Based on the well-known Graessley diagram for polymers [47] and using insight from polymer dynamics literature of rigid rods [48], this chart delineates regimes of CNT solutions based on volume concentration,  $\phi$ , from 0.001 to 1 (0.1% to 100%) and aspect ratio AR, the ratio of the length L to diameter d, from 1 to 1,000. With increase in either property, isotropic suspensions travel from dilute, to semidilute, to concentrated, two-phasic including liquid crystalline (LC) and isotropic, and finally fully liquid crystalline regimes. A vertical line at  $\phi = 0.1$  marks the boundary of the semidilute regime if rods are aligned. The boundary for the semidilute regime is increased for flexible materials.

Historically, efforts to generate concentrated liquid CNT solutions have relied on shear mixing or tip sonication, which disperses CNTs well into solution [54] but also cleaves the CNTs, shortening them to below a critical length based on the input power [55]. Better dispersion methods are always under investigation. Graphene is dispersible at high quality with a kitchen blender [56], [57], and coffee grinders have now been shown to assist in CNT

dispersion [58], though not replacing sonication entirely. Still, no method besides use of superacids as the solvent is known to disperse solutions with high concentration (above  $\approx 1\%$  by volume) without some loss of length [30]. In addition, the higher the CNT concentration, the higher the tendency for the suspension to aggregate [59], especially in solvents like epoxy that stabilize solutions by high viscosity delaying aggregation rather than favorable chemical interactions with CNTs. Organic solvents such as chloroform [60], dimethylsulfoxide (DMSO) and N, N-Dimethylformamide (DMF) may disperse CNTs readily, but none form stable solutions above 0.1%. There is also no known method to evaluate *a priori* whether CNTs will be dispersible in a new solvent, although methods using Hansen solubility parameters highlight some trends [61], but in general solvents and stabilizers like surfactants must be tried experimentally or through molecular dynamics simulations [62], limiting the choice of solvents for CNTs, and solvents and surfactants may disperse CNTs differently based on their diameter, chirality, or quality. In fact, this effect has been used to sort CNTs by type using a variety of solvents, surfactants, bio-macromolecules, and conjugated polymers [63].

#### 2.4.2. Experimental rheology of CNTs

While ideal rheology is useful guide, in experiments rigid rods often misbehave, showing periodic collective oscillations like wagging and kayaking [64], also exhibited by CNTs. These can readily influence manufactured goods as well, for example by creating films in which some CNTs lay orthogonal to the alignment direction of most others [40]. CNT solutions can also show formation of helical bands [65], aggregation and shear-induced aggregation [59], and thixotropy [52].

One might expect yield stress to emerge when the concentration of material within an ink becomes concentrated, due to percolation forming a fully connected elastic network in the liquid ink from suspended fibers, which can sustain elastic stress at rest. In theory this yield stress can be tuned by altering concentration and aspect ratio, and shear thinning index from concentration and solvent. To explore the effect of concentration on CNT rheology, a range inks were tested comprising CNT solutions in water stabilized by DOC ranging from 0.02% to 6.4%, having an aspect ratio of 6200 or less (unknown exactly due to possible shortening during processing). As the concentration increases, the shear stress  $\sigma$  smoothly increases, and the power law of  $\sigma$  as a function of the shear rate  $\dot{\gamma}$  becomes



shallower. These are most readily described by a Herschel-Bulkley model, where the shear yield stress is [66]

$$\sigma = \sigma_y + k\dot{\gamma}^n \quad (3)$$

with yield stress  $\sigma_y$  at low  $\dot{\gamma}$  (*i.e.*, at and near rest) and varying proportional to the consistency index  $k$  and  $\dot{\gamma}$  with a power law of  $n$ , the shear-thinning index. Looking back to **Figure 2.4-2**, this indicates that as the concentration increases,  $\sigma_y$  and  $k$  increase while  $n$  decreases. However, the Herschel-Bulkley model is a simplification, and liquid crystalline behavior can be observed in data at higher concentrations. In **Figure 2.4-2** it is seen as an inflection in curves in the range  $\dot{\gamma} = 10^0 - 10^1 \text{ s}^{-1}$ , observed for 0.7%, 0.8%, and 6.4%. Most literature presents rheometric data in terms of viscosity,  $\eta = \sigma/\dot{\gamma}$ , a representation in which this characteristic inflection is invisible.

One generalized flow curve for CNT solutions with Herschel-Bulkley behavior was asserted by Rahaketar, et al [36] for solutions of long or short CNTs in epoxy. The proposed nondimensionalization scaled the shear stress by yield stress,  $\sigma/\sigma_y$ , and the shear rate by solvent viscosity over yield stress,  $\dot{\gamma}\eta_s/\sigma_y$ , which is used here to generalize the data presented in **Figure 2.4-3** for comparison. At low shear rate, all plots converge to the yield stress. At high shear rates, they converge to the solvent viscosity. In the middle, Rahaketar, et al [36] observed two branches of behavior: an upper one ascribed to the motion of agglomerated short CNT structures, and a lower one ascribed to the motion of long CNTs within a network. Data covers slightly different ranges due to instrument limits in measuring torque and their use of viscous epoxy as the CNT solvent, which allows them to access more of the higher rate curve region. Our data follows the same general trend, and lies within a factor of 5 in stress over 10 decades of shear rate, and within a factor of 2 for the more concentrated solutions. While the superposition is not entirely satisfying at high shear rates for each curve, at low shear rates it works well. This phenomena is likely due to the influence of liquid crystalline behavior, as data diverges from overlapping above the inflection points previously noted in **Figure 2.4-2**.

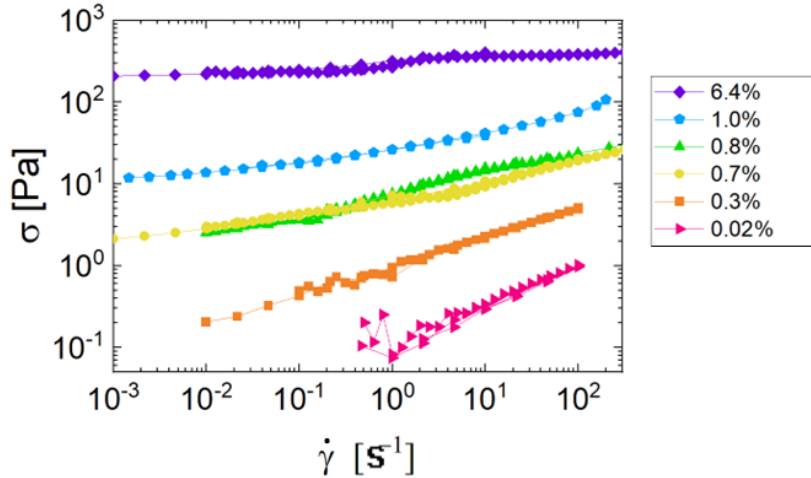


**Figure 2.4-2:** CNT ink rheology for long CNTs in aqueous suspension. Shear stress  $\sigma$  as a function of shear rate  $\dot{\gamma}$  for an array of CNT concentrations spanning the maximum measured extent in our lab in concentration and shear rate.

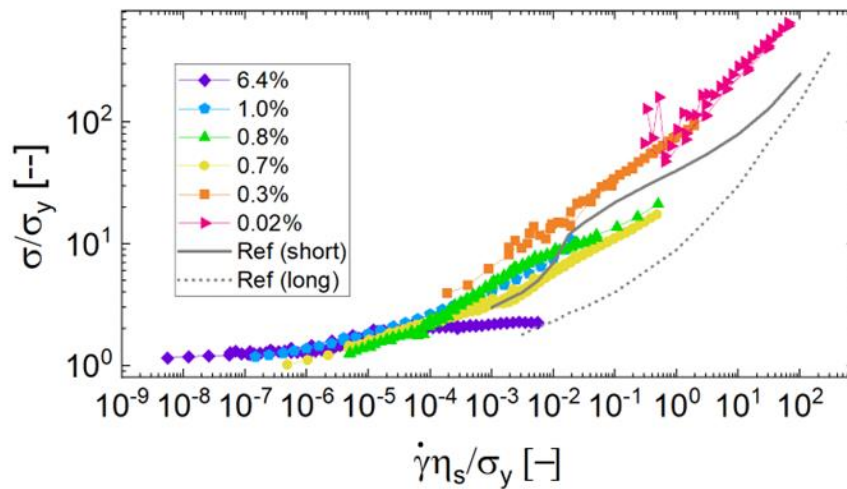


**Figure 2.4-3:** Nondimensionalized CNT flow curves for long CNTs in aqueous suspension. Nondimensionalized shear stress per yield stress  $\sigma_y$  as a function of shear rate nondimensionalized by solvent viscosity  $\eta_s$  per yield stress  $\sigma_y$ . Two grey lines indicate reference curves from [36] for short CNTs (—) and long CNTs (- -) in epoxy.

### 2.4.3. Shear yield stress and shear modulus

Compiling multiple data sources from literature for CNTs in different solvents, an observation is made of the influence of CNT length, concentration, and solvent on the development of yield stress. Yield stress may be difficult to distinguish from slip behavior so is not often reported for CNT rheology in published research articles; meanwhile, slip is particularly a challenge for concentrated solutions. Instead, solutions may be treated as

purely viscoelastic, or only report an extracted shear-thinning index. As a function of concentration, CNT inks increase yield stress with strong power law behavior, here with the power law exponent ranging between 2.1 and 5.1 (**Figure 2.4-4**). Between populations, inks with long CNTs in three kinds of solvent exhibit high yield stress for concentration of 0.1% to 1% volume. Short CNTs require an order of magnitude more CNTs, 1% to 10%, to achieve similar yield stress levels.

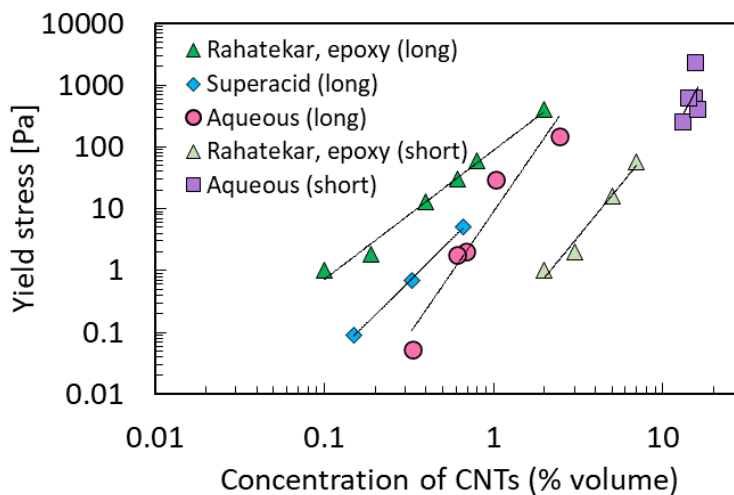


**Figure 2.4-4:** CNT ink rheology for a series of inks as a function of concentration. Aspect ratios are approximately <6200, 6400, 76, 1168, and 80 following the legend order (or data order from left to right). Power laws are 2.1, 2.7, 3.9, 3.3, and 5.1 in the same order.

To continue this analysis, an assumption is made that data presented in literature represents the approximate range of producible inks with the given composition. This means that concentrations below those presented in literature had very low yield stresses. Considering that presented data from outside our lab tends to have a lowest value of  $\sigma_y \approx 1$  Pa, a low value, this seems reasonable. And this means that concentrations above those presented in literature were not easily produced. Considering maximum values around  $\sigma_y \approx 100$  Pa, a relatively high value, this also seems reasonable, and inks far above this range experienced measurement failure in our own lab (*e.g.*, **Figure 2.4-5**). The aqueous ink with long CNTs and superacid ink datasets are known to behave in this way (personal correspondence). However, the aqueous ink with short CNTs was made purely at the upper limit of concentration and serve as an exception to this assumption.

Data was next plotted onto the Stick Plot (**Figure 2.4-6**) to observe the presence of yield stress within phase domains. Data all falls above the concentrated region and can extend

into the liquid crystalline region. Indeed, the two inks entirely within the liquid crystalline region have demonstrated liquid crystalline behavior as imaged by crossed polarizing microscopy (**Chapter 5** and [33], [35]). It is intriguing to note that within LC, stops before the boundary for semidilute with aligned rods. It remains an open question whether the limit to higher, stable concentrations is practical (*e.g.*, requires excessive mixing times) or based on thermodynamic properties of the dissolution phase reaching a limit.

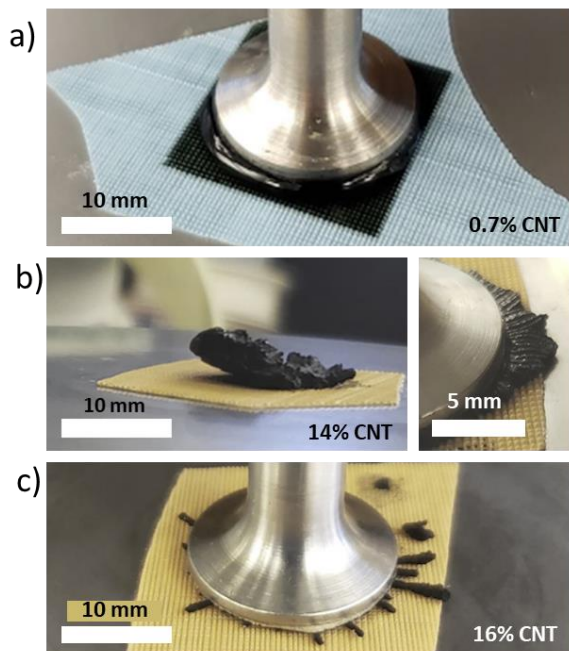


**Figure 2.4-5:** Rheometry in action. a) A 0.7% CNT ink appears as a liquid, flowing into channels confined on a square gridded sandpaper, and having apparent curvature due to surface tension around the rheometer upper disk for fluid measurement. b) A high-concentration ink shows self-supporting behavior at a distance from the blot, appearing more as a solid. When confined between rheometer plates before testing, the structure retains a fine grooved texture inscribed by the sandpaper. c) Rheology measurement failure of very high concentration CNT ink showing excursion of CNT paste as arm-like protrusions out of the measurement geometry.

Using the Stick plot as a guide, the yield stress is plotted again for all data, now as a function of aspect ratio times volume fraction,  $\phi AR$  (**Figure 2.4-7**). Immediately, the emergence of two distinct populations is apparent, one within the concentrated regime ( $\phi AR > 1$ ) and one within the liquid crystalline regime ( $\phi AR > 7.8$ ). Both populations fit independently to a power law of 2.7 with some noise. No insight is drawn from this power law, besides a previously-observed relationship to the fractal dimension of the CNT network

in the ink for short CNTs (which fails for long CNTs) [36], and the consistency between the two populations is considered coincidence.

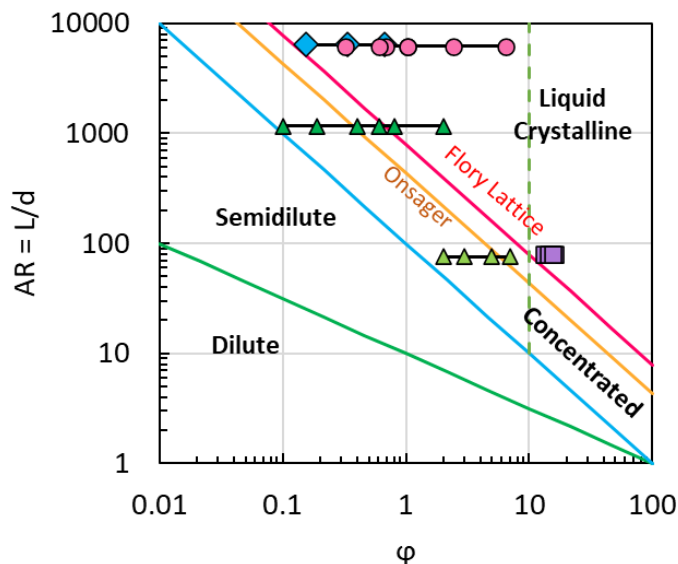


**Figure 2.4-6:** CNT data on rheology map for data shown in **Figure 2.4-4**. Data all falls above the concentrated region and can extend into the liquid crystalline region.

All datasets with short CNTs fall into the concentrated regime, with one set with long, while all sets in the liquid crystalline regime are long. This also separates out multi-walled CNTs (MWCNTs) on the left from single- and double-walled CNTs on the right.

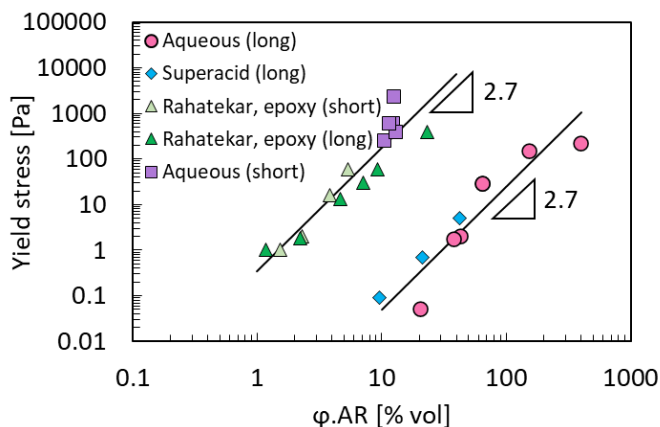


**Figure 2.4-7:** CNT ink yield stress vs aspect ratio times volume fraction for data shown in **Figure 2.4-4**. Data collapse into two distinct populations, one within the concentrated regime ( $\phi AR > 1$ ) and one within the liquid crystalline regime ( $\phi AR > 7.8$ ). Both populations fit independently to a power law of  $\approx 2.7$ .

While the bending stiffness of CNTs is not infinite [67], especially for small diameters, one might propose to base the aspect ratio, instead of on the entire length, on the persistence length, which is the effective length within a single CNT that it does not bend. If such a length is considered as  $\approx 500$  nm for a diameter of  $\approx 1.5$  nm, the two tested populations converge (**Figure 2.4-8**) and follow a master equation of  $\sigma_y = 0.34(\phi AR)^{2.7}$ , such that a yield stress of 1 Pa is typically reached for a size-adjusted concentration of  $\phi AR = 1.5$  %. However, for CNTs with a diameter of 1.5 nm, the smallest considered here, the persistence length is more likely above  $200 \mu\text{m}$  [67], much longer than all CNTs considered in this comparison, and so the CNTs may all be considered rigid rods. In addition, the observation of birefringence in the two longest populations in accordance with their location on the Stick Plot within the liquid crystalline regime (**Figure 2.4-6**) suggests that they behave as liquid crystals and not as concentrated solutions.

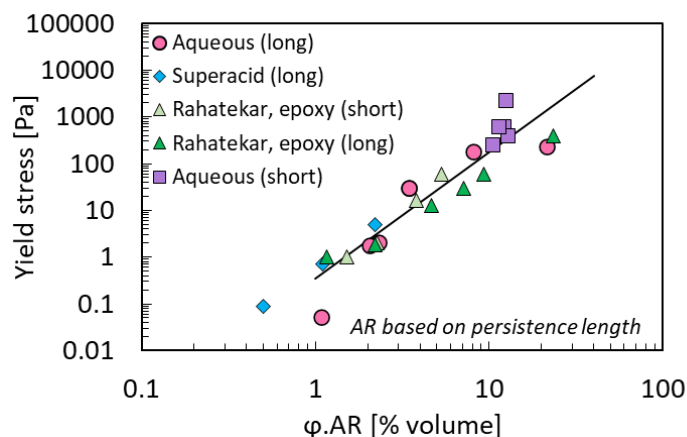


**Figure 2.4-8:** CNT ink yield stress vs aspect ratio times volume fraction for data shown in **Figure 2.4-4**. Data collapse into two one population when aspect ratio is based on the persistence length of  $\approx 500$  nm for a diameter of  $\approx 1.5$  nm. Both populations seen in **Figure 2.4-7** now fall within the concentrated regime and fit again to a master power law of 2.7.

This comparison could be improved in future work with additional datasets of ink rheology for formulations with known concentration and CNT size. The convergence of data presented here already suggests a high degree of predictability of yield stress development for a wide range of CNT types (multiwall, single wall), diameters, and lengths in a range of solvents with or without surfactants, and so to support manufacturing efforts it certainly deserves further study to elucidate the range of applicability of the scaling.

#### 2.4.4. Structure at rest: shear modulus and yield strain

While yield stress indicates material strength under flow, shear modulus indicate strength at rest. These values are related by the yield strain, most simply as  $\sigma_y = \gamma_y G$ . For a set of CNT rheology data, as for yield stress trends, again diverging power laws are observed (**Figure 2.4-9a**). The power law for short CNTs in epoxy, 5.5, has been justified as a scaling describing the network of aggregates of CNTs, indicating a fractal dimension of  $\approx 2.27$ , which is matched by the fractal dimension of the yield stress of 2.7, indicating a fractal dimension of  $\approx 2.26$  [36]. The yield strain ranges between 0.01 and 0.3% for all but the most concentrated solution, but behaves with no obvious overall trend among populations (**Figure 2.4-9b**).

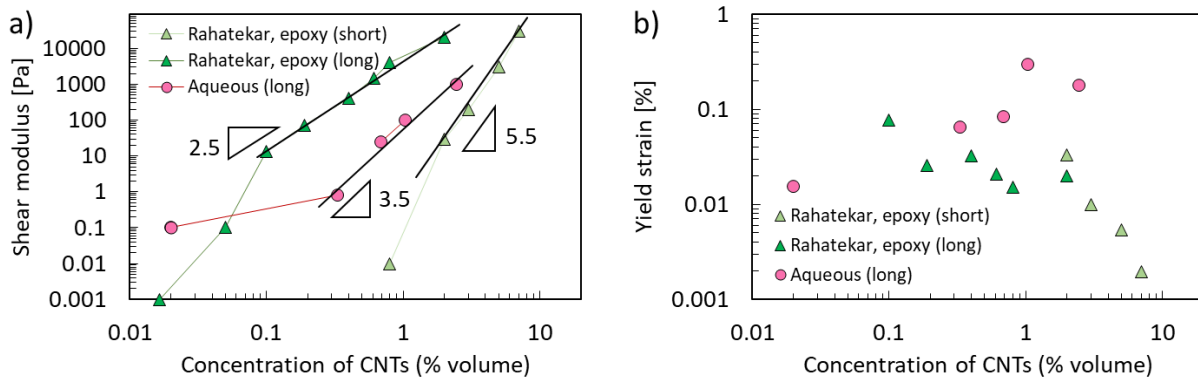


**Figure 2.4-9:** Linear elasticity of CNT solutions showing (a) elastic shear modulus and (b) yield strain as a function of CNT concentration.

When plotting with reference to our Stick plot (**Figure 2.4-10**), there is no clear convergence. This is due to the more pronounced difference in linear elasticity at short strains due to the difference in network deformations between short, long, and long/liquid crystalline inks [36]. Rather, the network mechanics dictate long CNTs should scale differently than short CNTs.

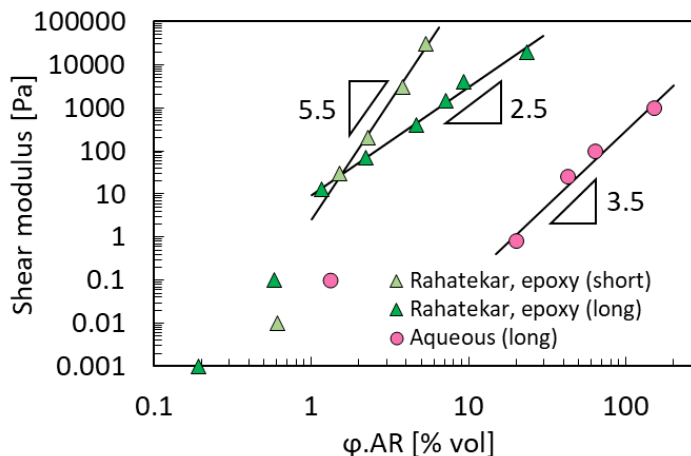


**Figure 2.4-10:** Modulus variation of CNT solutions as a function of volume fraction times aspect ratio, showing multiple behaviors.

#### 2.4.5. Shear-thinning index

Due to its direct application in the thickness of coatings [39], [40], and ease of measurement from plots of viscosity, the shear-thinning index  $n$  is the most widely reported rheometric value in literature about CNTs. This is especially relevant as dip-coating of CNTs has been shown to form remarkably dense, well-ordered aligned films [21]. A fully Newtonian fluid will have  $n = 1$ . However, a solution of semidilute CNTs is theoretically expected to have an exponent of 0.5 in the low-concentration limit of an isotropic solution of rigid rods in the absence of aggregation [37]. CNT suspensions with aggregates tend to demonstrate stronger shear-thinning behavior (lower  $n$ ) [68], and flow-aligning behavior also gives rise to stronger shear thinning. A value of  $n = 0$  indicates fully plastic flow where shear stress  $\sigma$  is no longer a function of shear rate  $\dot{\gamma}$ . As the solids content of a suspension increases, it may be expected to approach this limit. Due to the presence of viscous dissipation in CNT-based inks, a value of  $n = 0$  is physically impossible.

Data for the shear-thinning index is shown for a range of CNT solutions (**Figure 2.4-11**) from literature, with several of the literature datasets refit as indicated in **Section 2.3** to exclude errant effects from liquid crystalline behavior in the computation of  $n$ . Four of the datasets coordinate on the same trend, with an approximate intercept at 0.5 for low concentration followed by  $n$  decreasing linearly or exponentially. Two datasets present low-concentration values above 0.5: one aqueous solution presents a value of 0.85 for 0.1% SWCNT in SDBS surfactant [46] and one mixture in epoxy has a value of 0.6 for 0.1% [38]. These are likely due to clumps, where CNT aggregates behave as isotropic bodies rather



than individualized anisotropic rods. The higher-than-expected values in [40] are likely aggregation due to high concentration.

Although much of this analysis is based off of supposition from divergence from expected trends, the shear-thinning index may prove a good metric for testing CNT suspension quality. When plotted as a function of volume concentration (**Figure 2.4-13**), the shear-thinning index no longer converges but the overall decreasing trend is observed in all sets.

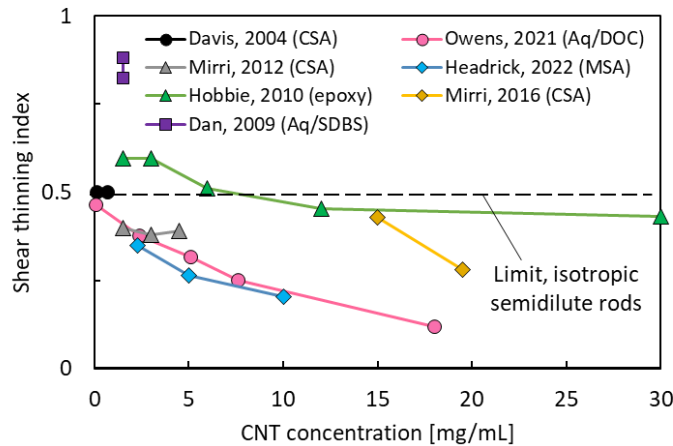


**Figure 2.4-11:** CNT ink shear thinning index as a function of CNT mass concentration.

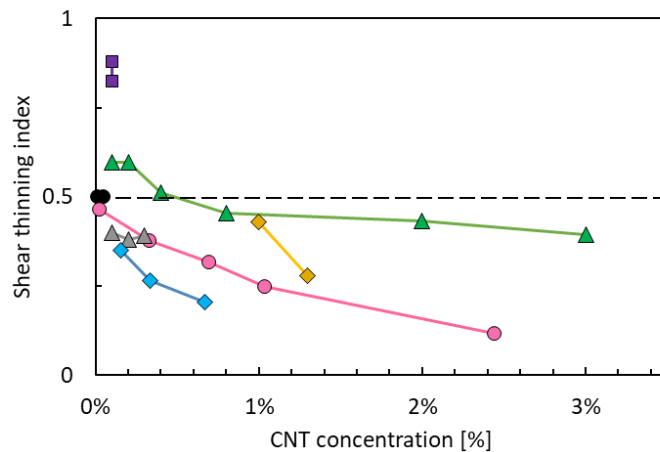
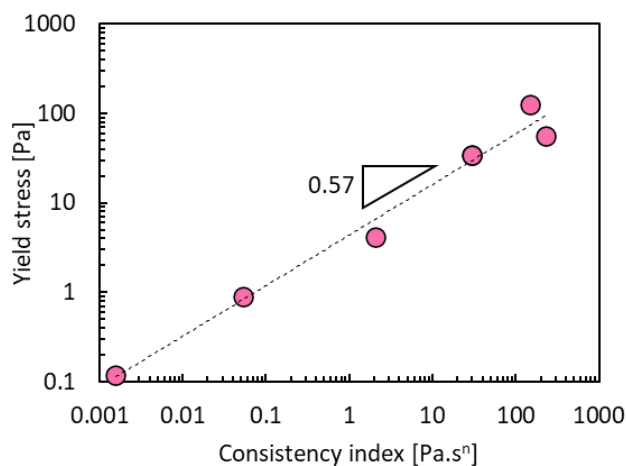


**Figure 2.4-12:** CNT ink shear thinning index, same as in **Figure 2.4-11** but plotted by concentration in percent volume fraction to show separation of data due to different solvent densities.

#### 2.4.6. Consistency index

Finally, the consistency index as a function of yield stress is examined (**Figure 2.4-13**). This parameter shows a coordinated increase with concentration (increasing to the right).

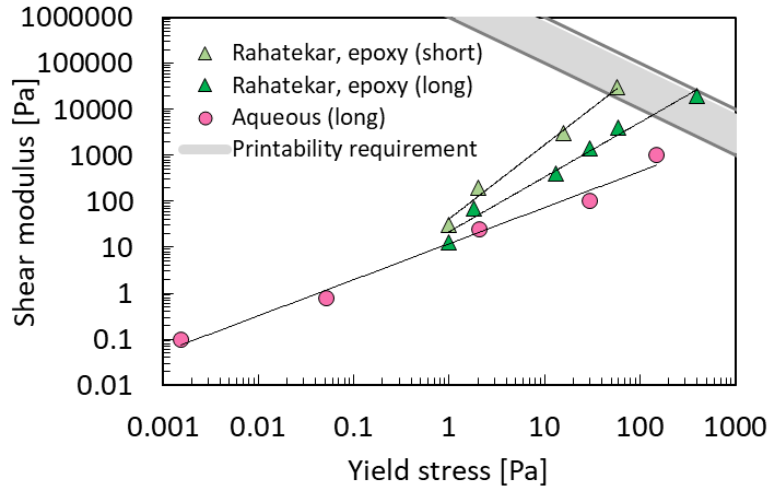
For this dataset, the consistency index is generally predictable from the yield stress for the range of inks tested.



**Figure 2.4-13:** CNT ink yield stress vs consistency index for aqueous ink with long CNTs.

### 2.5. Implications for 3D printability

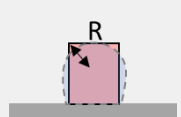
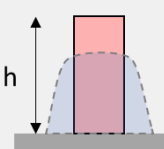
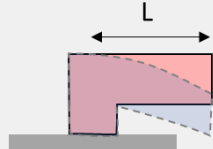
The printing of materials into three dimensions requires that printed material becomes self-supporting. The shear modulus is plotted vs the yield stress, and a benchmark empirical threshold of 3D printability for ceramics [69], [70] (**Figure 2.5-1**), above which inks resist slumping. Two of the CNT inks considered here have the potential to form stable 3D structures. It would be hard to formulate an ink with CNTs alone that would allow for 3D printing, which is exactly the impetus for the use of fillers [22]–[26] to imbue printability, even when it then impedes electrical connection. In other printability assessments, the yield stress alone is the most critical feature, and especially for fine features the required value can be calculated based on desired part height and minimum radius of features [71].



**Figure 2.5-1:** CNT ink printability. The shear modulus is plotted vs the yield stress, and a benchmark empirical threshold of 3D printability for ceramics [69], [70].

In a more granular comparison of printable feature morphology to yield stress and strain, there are several key features (**Figure 2.5-2**). Laplace pressure  $\gamma/R$  driven by surface tension  $\gamma$  and a critical minimum radius  $R$  balances with yield stress to set a minimum possible feature size of a printed liquid ink, below which surface tension will round out features. Force due to gravity  $\rho gh$  as acceleration due to gravity times mass density  $\rho g$  acting upon a characteristic height  $h$  induces slumping of parts and sets a maximum self-supporting height. When yield stress is low, surface tension and gravity together balance to set a minimum resolution as the capillary length, wherein a small amount of printed liquid ink will form a rounded droplet with radius as the capillary length, or a larger amount will form a puddle with edge curvature as the capillary length (See horizontal lines in **Figure 2.5-3**). For typical values of surface tension, smaller resolution features can only be reached for yield stresses above 10 Pa. Finally, overhanging structures found in lattices and wireframes will sag also under gravity leveraged by the length of the beam (**Figure 2.5-2**).

As yield stress increases, potential smallest feature resolution increases (**Figure 2.5-3**). For typical values of surface tension, sub-mm feature sizes will require yield stresses  $\sigma_y \gg 10$  Pa, and features below 0.1 mm will require  $\sigma_y \gg 100$  Pa, setting high threshold requirements. When printing onto a substrate, ink-substrate wetting interactions must also be considered, as the contact angle and wetting compared to nonwetting characteristics of the ink on the substrate will further influence printing resolution.

Feature	Resolution	Height	Lattice beam
Morphology			
Condition	$\sigma_y > \gamma/R$	$\sigma_y > \rho gh$	$\gamma_y < \frac{\rho g L^3}{GR}$
Opposing force	Surface tension	Gravity	Gravity, leveraged

**Figure 2.5-2:** Interactions between mechanics and yield stress  $\sigma_y$  or yield strain  $\gamma_y$  and modulus  $G$ .

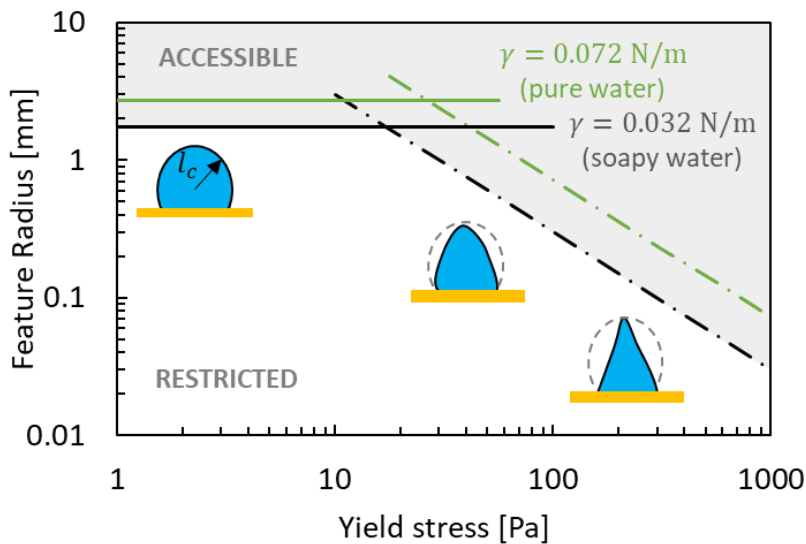


**Figure 2.5-3:** Interactions between feature radius and yield stress  $\sigma_y$ . Thresholds based on gravity (horizontal lines) and yield stress (descending lines) are shown. Inset schematics show representative morphologies compared to a dashed outline showing a droplet with size set by the capillary length. The accessible region is above the threshold lines, shaded here in grey.

## 2.6. Conclusions and Perspective

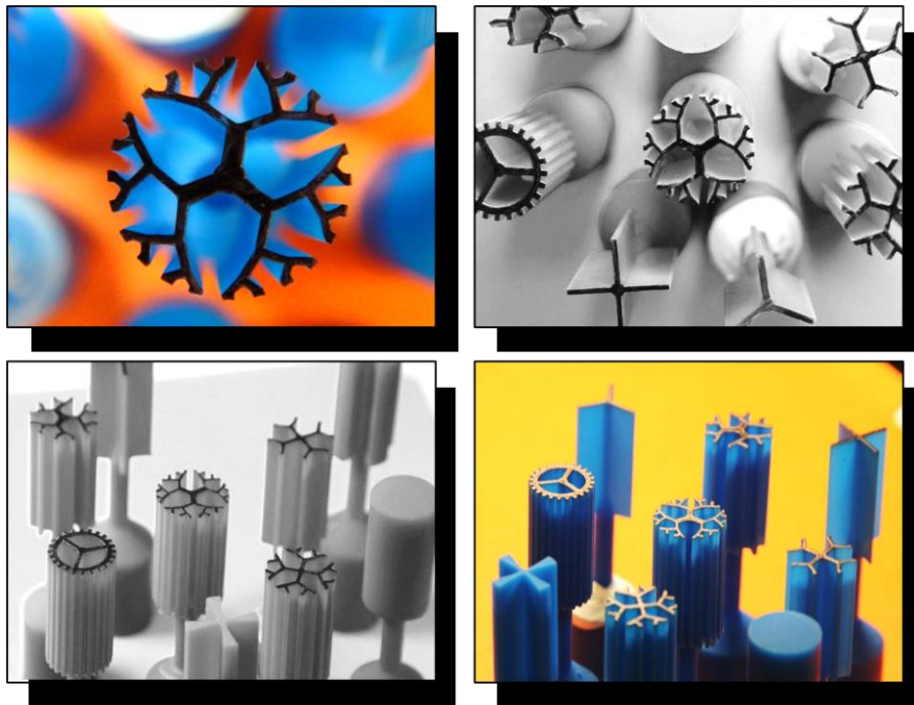
Rheological behavior of the flow curves for steady shear of CNT inks was discussed, comparing CNTs of multiple lengths and diameters in superacids, water, and epoxy. Inks having a yield stress fall into concentrated or liquid crystalline regime based on their aspect ratio. Inks in the liquid crystalline regime develop similar levels of yield stress or modulus at 1/10 the concentration of inks in the concentrated regime. The power law dependence of the yield stress on concentration is consistently 2.7 for the datasets observed here. The

modulus has a stronger power law varying widely between 2.5 and 5.5 for different inks, which is attributed to the details of CNT-level network mechanics in solution. Shear thinning index metric of solution quality, where stable rigid rods should have a value never more than 0.5, and decreasing from there with increasing concentration, confirmed by experimental rheology of liquid crystalline formations. The consistency index is related to the yield stress by a power law dependence. Power law trends are given for the rheological values as a function of concentration, enabling calculation of fluid behavior at different concentrations. However, the power laws themselves depend on the solvent and CNT size.

---

## Chapter 3. Improved Rheometry of Yield Stress Fluids Using Bespoke Fractal 3D Printed Vanes

---



Chapter Introduction Image: Printed Fractal Vanes

### 3.1. Abstract

To enable robust rheological measurements of the properties of yield stress fluids such as concentrated solutions of carbon nanotubes, we introduce a class of modified vane fixtures

with fractal-like cross-sectional structures. A greater number of outer contact edges leads to increased kinematic homogeneity at the point of yielding and beyond. The vanes are 3D printed using a desktop stereolithography machine, making them inexpensive (disposable), chemically-compatible with a wide range of solvents, and readily adaptable as a base for further design innovations. To complete the tooling set, we introduce a textured 3D printed cup, which attaches to a standard rheometer base. We discuss general design criteria for 3D printed rheometer vanes, including consideration of sample volume displaced by the vanes, stress homogeneity, and secondary flows that constrain the parameter space of potential designs. We also develop a conversion from machine torque to material shear stress for vanes with an arbitrary number of arms. We compare a family of vane designs by measuring the viscosity of Newtonian calibration oils with error  $<5\%$  relative to reference measurements made with a cone-and-plate geometry. We measure the flow curve of a simple Carbopol yield stress fluid, and show that a 24-arm 3D printed fractal vane agrees within 1% of reference measurements made with a roughened cone-and-plate geometry. Last, we demonstrate use of the 24-arm fractal vane to probe the thixo-elasto-visco-plastic (TEVP) response of a Carbopol-based hair gel, a jammed emulsion (mayonnaise), and a strongly alkaline carbon black-based battery slurry.

### *3.2. Introduction to yield stress fluids and measurement challenges*

A yield stress fluid is a material that has a critical stress above which it flows like a viscoplastic liquid, and below which it deforms as a viscoelastic solid. Common yield stress fluids include emulsions, foams, particulate suspensions, and granular materials, in which particles, bubbles, emulsions, or other microparticle constituents interact via weak physico-chemical forces and geometric packing/jamming constraints [72]–[75]. As the imposed stress acting on these soft solids increases, complex time-dependent rheological signatures arise from underlying microstructural processes such as shear-induced break-down and restructuring [74], [76]. In addition, other effects can arise such as time-dependent aging and onset of non-homogeneous flow, resulting in common rheological signatures, including a strong influence of the history of deformation, hysteresis, thixotropy, shear-banding, and of slip of the material on the surface of the tool used for rheological measurements [77], [78]. As a result, sensitivity to loading conditions, ensuring kinematic homogeneity, and unambiguous control of history of deformation each pose particular challenges for rheological measurements of yield stress fluids [76], [79].

Despite this complexity, yield stress materials find enormous application in a wide variety of commercial products, consumer goods, and construction materials due to the desirable mechanical properties imbued by the presence of a critical yield stress. Yield stresses in industrial processes influence the strength of concrete, the most utilized artificial material in the world [80], and the processing, quality, and final texture of a vast range of foodstuffs, skincare and haircare products [81]–[86]. Further, thixotropic materials with high values of the yield stress are particularly suited to high-resolution direct-write printing. Examples include printing of structures using foams, elastomers, concrete, cell-laden gels, and conductive inks [87]–[92]. To assist in understanding and optimizing yield stress materials for applications, rapid, reliable, and accurate measurements of the material behavior are required. Simultaneously, a key research aim of the field over the past 20 years has been to develop better descriptive and predictive constitutive models that capture the complex rheological behavior of these fluids including description of the full thixo-elastoviscoplastic (TEVP) response (see, for example, [93]–[95]).

As a result of the complexities encountered in measuring the rheology of TEVP yield stress fluids, the vane has become the rheometric tool geometry of choice, as it prevents the slip of material and minimizes sample damage/alteration during the sample loading process [77]. The vane geometry initially was developed in the 1980s by civil engineers as a tool to quantify the yield stress of soils and thick clays. Seminal work by Nguyen and Boger adapted the vane for muds and slurries and derived a simple quantitative relationship between the torque imposed on the rotating vane and the resulting shear stress acting on the sample [81], [96]. The vane subsequently has become a standard tool for measuring the yield stress of delicate materials and structured fluids [77].

The vane geometry most typically consists of four to six straight blades of equal length fanning out from a center point in a cruciform or hexagonal arrangement [77]. We will call the blades more generally “arms” here. The vane is submerged inside a cup of the sample material and then rotated about its central axis; the rheometer records the torque and rotation angle. This rotation deforms an approximately cylindrical plug of material, generating an ideally axisymmetric stress field, while also restricting sample slip, which is a key issue for cylindrical Couette rotors [77]. The vane, despite its more complex geometry, has been used to impose a range of standard rheometric test protocols, including measurement of steady state flow curves, start-up of steady shear, creep/recoil, small amplitude oscillatory shear (SAOS), and large amplitude oscillatory shear (LAOS) [83], [92],



[97]. Systematic comparisons of rheological measurements made using vanes to those using other standard rheometric tools generally have found good numerical agreement between values measured with vanes and with other geometries. Meanwhile, any differences in measured values typically occur due to wall slip and differing sample history, affecting primarily large strain measurements and general level of repeatability in data measured with vanes compared to other geometries. In particular, we note the following specific examples: for bentonite, direct comparisons have revealed that cone-and-plate tests systematically underestimate yield stress as compared with vanes, due to thixotropy associated with sample loading [98]; for foams, SAOS measurements with vanes agree well with measurements made with parallel plate fixtures, while vanes induce less bubble coalescence [99]; for soft cheeses, SAOS measurements with a parallel plate geometry agree well with vanes, though only vanes were capable of imposing reproducible larger-amplitude strain deformations due to sample slip occurring against the parallel plates [100]. In direct comparisons of inter- and intra-laboratory tests, yield stress measurements made with vanes in start-up of steady shear tests have been found to be more reproducible than measurements made by other tools including slump tests on inclined planes, or creep experiments or stress ramp tests with cones and textured concentric cylinders [101].

The shearing profile around the vane is axisymmetric only for certain materials and under specific flow conditions. Secondary flows arise when the viscosity is too low, resulting in recirculation between neighboring pairs of arms [102], [103]; these are exacerbated when the power-law index of a shear thinning fluid is  $>0.5$  (more Newtonian) [104]; and when the vane has too few arms to hold a given material securely (typically needing greater than three arms) [105], and flow kinematics are measurably influenced even with six arms [106]. For viscoelastic materials, this recirculation has been shown to cause a significant artificial increase in the apparent viscosity reported by the instrument at high Reynolds numbers [107]. Detailed theoretical and computational analysis of the region near a single knife-edge of a vane reveal that the stress field is singular at the tip, and consequently the stress field around a multi-arm vane tool shows spatially periodic variations for any material with Newtonian, yield stress, or linear elastic behavior [102], [108], [109]. Consequently, even when the streamlines in a sheared fluid sample are circular, instantaneous structural parameters characterizing the local properties of thixotropic fluids can be strongly influenced by the location of the blades, becoming non-axisymmetric with the vane rotation [109].

Despite these difficulties, vanes are particularly useful for ensuring repeatability of measurements and for characterizing structurally-sensitive materials. This is because vanes displace far less material and impose a much weaker deformation history during initial sample loading, which is particularly important for thixotropic samples [110]. With a cone-and-plate, parallel-plate, or concentric-cylinder tool configuration, the sample must be compressed and sheared to fill the thin gap between the two fixture surfaces. Compared to a bob, a vane can more easily be inserted into a cup that has been previously filled with a structured material, and the vane typically displaces less than 20% of the sample volume compared to a bob of equivalent radius. This results in more repeatable measurements and control of the material's initial shear history [111]. Furthermore, use of vanes allows samples to be prepared and aged in containers for long waiting times before testing on the rheometer [98].

Alternatives to the vane geometry that have been proposed for yield stress fluids include paired helical blades for preventing sedimentation while measuring dense samples such as concrete with large aggregates, torsional mixers, and planetary rotating systems [112], along with other styles of test including penetration and slump tests [76], [113]. Due to their easy insertion into fluids, four-armed vanes also find wide-spread use in field tests for industrial measurements, with designs for “bucket rheometers” for concrete and industrial slurries powered by a hand drill [114] and a similar extended rod for *in situ* or “*syn-eruptive*” measurements of lava flows oozing from active vents, where the magnitude of the yield stress is a strong indicator of probability of eruption [115], [116].

In the interest of allowing easier design and fabrication of rheometric tooling, Bikos and Mason recently introduced 3D-printed (3DP) cones and annular rings for rheometers as a cost-effective approach to create bespoke parts [117]. Other researchers have used 3DP to make custom drag-reducing surfaces for viscous skin friction tests utilizing the rheometer motor and torque sensor [118]. In other fields, 3D printing, a subset of a class of processes broadly known as additive manufacturing, has become widespread for production of complex geometries from a vast library of possible base materials [119]. In the present case, 3DP is well-suited to create functional vane-like geometries, compared to other manufacturing methods, due to the need to produce fine (<1mm) features with very high aspect ratios that retain dimensional accuracy over O(cm) length scales [120].

In this chapter, we present the design, fabrication, and use of a 3D printed fractal-like vane geometry. The branching, tree-like fractal structure was optimized to give a large

surface area and large number of perimeter contact points with the test fluid, while the internal structure remains sparse in terms of displaced volume relative to a bob, in order to limit pre-shearing of a structurally-sensitive material during sample loading. In **Section 3.4**, we discuss the relevant stress and strain fields for a generic vane geometry, combining and adjusting published expressions to propose a composite formula for converting torque to stress, incorporating variations in the number of arms, the vane geometry, and the influence of end effects from a vane with finite length. We also discuss the impact of design variations on the projected area displaced by the vane geometry, and on the stress profile around the vane geometry. In **Section 3.5**, we discuss the design and manufacturing of vanes by stereolithographic 3D printing, using a methacrylate-based photopolymer to create vanes with fine (200  $\mu\text{m}$ ) feature resolution and with chemical compatibility with a broad range of solvents and sample materials. We also discuss a printable coupling to a common rheometer interface, and propose a design for textured 3D printed cups that assists in preventing sample slip at the outer walls, while also being detachable from the rheometer base for easy cleaning. In **Section 3.6**, we quantify the accuracy of the new designs by comparing vane measurements of Newtonian calibration oils and a simple (*i.e.*, non-thixotropic) yield stress material (a Carbopol microgel) with reference measurements obtained in a roughened cone-and-plate fixture, and compare these results to our proposed torque scaling factors. In **Section 3.6.4**, we use these vanes to perform start-up of steady shear flow measurements of the TEVP response of a Carbopol-based hair gel, a jammed emulsion (mayonnaise), and an alkaline carbon black-based battery slurry with pH 12. Following our conclusions in **Section 3.7**, we provide four appendices discussing in more detail (**Section 3.8.1**) the stress field around the new vane geometries; (**Section 3.8.2**) the definitions and selection of particular fractal structures; (**Section 3.8.3**) the displaced area filled by vanes of different designs; and (**Section 3.8.4**) how to ensure a vane meets acceptable standards for accurate and reproducible rheological measurements, with the goal of facilitating adoption of our design and fabrication method in other laboratories.

### 3.3. Theory of yield stress flow behavior

#### 3.3.1. Rheology of yield stress fluids

The generic term “yield stress fluid” typically applies to a fluid that exhibits a characteristic stress below which it may deform viscoelastically (*i.e.*, as it creeps) but does not flow, and above which it flows steadily like a (typically shear-thinning) liquid. For

further details, see the extensive reviews provided by [74], [77], [121], [122]. In addition to the key role of a critical material stress, time-dependent degradation and rebuilding of the underlying material structure may occur, leading to complex rheological responses that depend both on time and on sample history.

The simplest constitutive model appropriate for describing the steady flow curve of yield stress fluids is the Herschel-Bulkley model, [66]

$$\begin{aligned} \sigma(\dot{\gamma}) &= \sigma_y + k\dot{\gamma}^n & \sigma &\geq \sigma_y \\ \dot{\gamma} &= 0 & \sigma &< \sigma_y \end{aligned} \quad (1)$$

where  $\sigma$  is the shear stress,  $\sigma_y$  is the yield stress for a fluid in pure shear flow,  $k$  is the consistency index,  $\dot{\gamma}$  is the shear rate, and  $n$  is the power law index.

This may also be written in terms of the flow rule

$$\dot{\gamma} = (\sigma - \sigma_y/k)^{1/n} \text{ for } \sigma \geq \sigma_y \quad (2)$$

When  $n = 1$ , this corresponds to a Bingham fluid, with  $k \rightarrow \mu$  being the plastic viscosity. While many more complex models exist which can account for viscoelastic responses below yield as well as time and rate-dependent thixotropic responses (*ex.*, the soft glassy rheology model [95], the isotropic kinematic hardening model [94], [97], and models by Saramito [123], [124] and Coussot [125]), the simple Herschel-Bulkley viscoplastic model is sufficient for comparison with the results of steady state measurements presented here.

### 3.3.2. Torque-shear stress and rotation rate-shear rate relations for the vane geometry

The typical vane (**Figure 3.3-1a**) has four arms connected in a cruciform design; it is inserted centrally into a cup of material and rotated about its axis while the torque is measured as a function of rotation angle and rate. Due to the presence of a yield stress in the material being measured, the sample in the cup deforms as a sheared cylinder guided by the vanes, preventing slip and generating kinematics that closely approximate those of a concentric cylinder system. The essential question that arises is how to relate the global values measured by the rheometer (*i.e.*, the torque  $M$ , yield torque  $M_y$ , and rotation rate of the vane  $\Omega$ ), to constitutive variables  $\sigma$  and  $\dot{\gamma}$  introduced in equation (1) so that the three model parameters  $\sigma_y$ ,  $k$ , and  $n$ , can be calculated.

In a vane measurement, an  $N$ -arm vane with radius  $R_v$  rotates inside a cup of radius  $R_c$  at a rotation rate  $\Omega$ . There are two regimes of material response for yield stress fluids. When the applied torque is below the yield torque,  $M < M_y$ , or correspondingly  $\sigma < \sigma_y$ , the sample is entirely plastically unyielded, although a transient viscoelastic creep may occur throughout the entire sample when the torque is first applied. Due to the radial dependence of the true strain in the material, it is useful to define an “apparent strain” which can be calculated as the observable angle rotated by the vane through a time  $t$

$$\theta_{app} \approx \int_0^t \frac{R_v \Omega(t') dt'}{R_v} \approx \theta(t) \quad (\text{for } \sigma_w < \sigma_y) \quad (3)$$

and a rotation rate  $\Omega(t)$ , where the wall shear stress  $\sigma_w = \sigma(R_v)$ . Full computation of the radially-varying elastic strain field in the gap would require choice of an appropriate linear or nonlinear elastic constitutive equation.

The conversion of torque to stress depends purely on the test geometry. In their original analysis, Nguyen and Boger used a cylindrical model for the yield surface and calculated the stress on the cylindrical yield surface enclosing the vane including the cylindrical wall and both end caps to the total torque:

$$M = 2\pi R_v^2 \sigma_w \int_0^L dz + 4\pi \int_0^{R_v} \sigma(r) r^2 dr, \quad (4)$$

where  $L$  is the finite length of the vane. The additional contribution from the thin rod holding the vane is neglected here, as our vane has  $(R_{rod}/R_v)^2 \approx 0.1$  and  $(L_{rod}/L_v) \approx 0.17$ . In the common “Couette analogy” for measuring Newtonian fluids with a vane rotor, usually one uses the same equations as for a cylindrical rotor, with a  $R_{effective} < R_v$  calibrated from experiments. For our more general analysis, including flow of yield stress fluids for which an equivalent  $R_{effective}$  would be a function of shear rate and fluid properties [126], complicating discussion, we use the true radius  $R_v$  and do not assume an axisymmetric flow. Usually, one assumes  $\sigma(r) = \sigma_y$  everywhere on the two end cap surfaces to integrate equation (3), as in [81], to obtain

$$M = \pi R_v^3 \left( \frac{L}{R_v} + \frac{2}{3} \right) \sigma_w \quad (5)$$

This relationship enables an interconversion between the observable (torque) and the desired rheometric variable, *i.e.*, the wall shear stress along the outer perimeter of the vane.

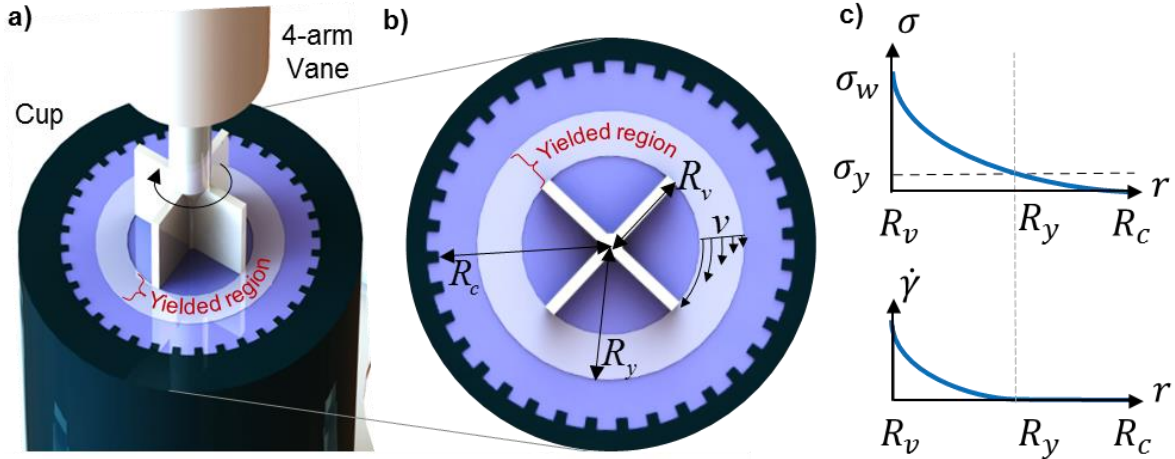


**Figure 3.3-1.** (a) Schematic of a 4-arm vane ( $N = 4$ ) inserted halfway (for illustrative purposes only) into a cup of yield stress material (blue) for measurement. As the vane rotates, the shearing of material exerts a torque on the vane that is measured by the rheometer. (b) The local stress decays radially from the cylinder of material cut by the vane, out to a radius  $R_v$  where  $\sigma(r) = \sigma_y$ . Inside the vane boundary  $r < R_v$ , material ideally moves as a solid plug guided by the vane arms, and the radial velocity  $v(r)$  decays from  $v = \Omega R_v$  at the edge of the vane to  $v = 0$  at  $r = R_y$ , although the velocity profile is expected to deviate from an axisymmetric path, especially if the vane has few arms. (c) The shear stress field in the sheared region of fluid decays from a wall shear stress  $\sigma_w$  at  $r = R_v$  to the yield stress  $\sigma_y$  at a critical radius  $R_y$ , beyond which material is unyielded. The shear rate  $\dot{\gamma}(r)$  of material elements also decays to zero at  $R_y$ .

When  $M > M_y$ , or  $\sigma_w > \sigma_y$ , the sample begins to yield and eventually rotates at a constant rotation rate  $\Omega$ . If the flow is assumed to be purely axisymmetric (due to conservation of angular momentum), the solution of the Cauchy momentum equation shows that the shear stress field in the sample decays radially as  $\sigma \sim 1/r^2$  until the shear stress  $\sigma(r) = \sigma_y$  at a critical radius  $R_y = R_v \sqrt{\sigma_w / \sigma_y}$ , beyond which  $\dot{\gamma} = 0$  by definition (**Figure 3.3-1b-c**). The surface at  $r = R_y$  is called the yield surface. In the *partially yielded case*, the outer edge of the plastically flowing material does not reach the outer wall of the cup ( $R_y < R_c$ ). In the *fully yielded case*, the fluid is plastically yielded throughout the cup, and  $R_y \geq R_c$  and this necessitates the use of a different analysis [96]. In the present study, the chosen gap is large enough (or, equivalently, the applied torque is maintained at values close enough to the yield stress) that the fluid is only partially yielded for all measurements, which means that  $\sigma_y c_v^2 \leq \sigma_{w,max}$ . We note that the yield surface reaches the outer wall in our system when the shear stress computed from equation (4) reaches a threshold value

$$\sigma \gamma \left( \frac{R_c}{R_v} \right)^2_{w,max} \quad (6)$$

and we demarcate this upper bound as a dashed line on the relevant figures in this chapter. For all results presented here,  $(R_c/R_v)^2 \geq 4$  so that we can often measure the entire flow curve accessible with the rheometer using only the equations presented above.

A wide gap system is defined as one in which the gap between the vane and the cup,  $(R_c - R_v)$  is on the same scale as the vane radius,  $(R_c - R_v)/R_v \sim O(1)$ . The shear rate  $\dot{\gamma}(r)$  in the material is related to the rotation rate of the vane by the identity  $\dot{\gamma}(r) = \frac{1}{r} \frac{d}{dr} (rv_\theta)$ . As described by [96], this expression can be rearranged and integrated to obtain:

$$\Omega = \int_{R_v}^{\infty} \dot{\gamma} \frac{dr}{r} = -\frac{1}{2} \int_{R_v}^{R_y} \dot{\gamma}(R_v) \frac{d\sigma}{\sigma}. \quad (7)$$

The relationship between rotation rate and stress depends on the specific (*a priori* unknown) constitutive response of the fluid sample in the gap, and not on geometry alone. However, when  $R_v < R_y < R_c$ , this implicit equation can be solved without presuming any specific fluid model (besides the presence of a critical yield stress) by realizing that  $\dot{\gamma}(R_y) \rightarrow 0$ . Differentiating equation (6) by  $\sigma$ , evaluating it at  $r = R_v$  where  $\sigma = \sigma_{wall}$ , and substituting the relationship between wall shear stress and torque derived in equation (4) then gives the shear rate at the vane surface to be

$$\dot{\gamma}(R_v) = 2\sigma \left( \frac{d\Omega}{d\sigma} \right) \Big|_{\sigma=\sigma_w} = \frac{2\Omega}{(d \log M / d \log \Omega)} \quad (8)$$

This expression depends on the actual stress-shear rate (or torque-rotation speed) relationship of the material being tested, and so only a prescribed rotation rate and not a prescribed shear rate may be imposed *a priori* for experiments on an uncharacterized material. Other expressions for calculating  $\dot{\gamma}(r)$  from the imposed rotation rate  $\Omega$  when the entire sample is yielded (*i.e.*, when  $R_y \geq R_c$ ), or for materials without a yield stress are compared in [96], [103], [127]. For the specific case of measuring a viscous Newtonian fluid, the wall shear rate,  $\dot{\gamma}_w$ , at the perimeter of the vane can be evaluated as [96]

$$\dot{\gamma}_w = \frac{1}{r} \frac{d}{dr} (rv_\theta) \Big|_{r=R_v} = \frac{2\Omega}{1-(R_v/R_c)^2} \quad (9)$$

### 3.4. Generalized torque-to-stress conversion relations for vane geometries

While the vane geometry is well suited for measuring the instantaneous torque  $M_y$  (and the corresponding yield stress  $\sigma_y$  at the instant of yielding), the streamlines become noncircular when measuring strongly shear-thinning materials at higher shear rates, or for measuring viscous Newtonian fluids, due to secondary flows (*i.e.*, slow recirculation of fluid eddies) between the vane arms [104]. Essentially, the fluid-filled space between each pair of vane arms functions as a lid-driven cavity [128] with a slow steady recirculating flow that contributes additional dissipation to the total measured torque. A design that occludes more internal space may be more suitable for these measurements, as was recognized even in early work by Keentok et al: “*A more theoretically acceptable vane would be designed in such a way as to eliminate the possibility of secondary flows between the blades.*” [105]. Yet, this requires an intricate vane geometry (*e.g.*, containing many thin blades), which is expensive to mold or machine, making their manufacture cost-prohibitive at that time.

In addition, the stress field in the sheared sample is non-uniform and localized around the perimeter at the edges of each arm of the vane. In fact, analysis by Atkinson and Sherwood for the stress field (in a Newtonian fluid or a linear elastic solid) near a knife-edge singularity in torsional deformation shows that at each arm tip, there is a stress singularity that scales inversely proportionally to the number of vane arms [102]. By increasing the number of tips in contact with outer fluid, the stress field becomes progressively more homogeneous along circles of constant radius from the vane center. To illustrate this, we evaluate the azimuthal shear stress  $\sigma_{r\theta}$  field for a Newtonian fluid along the line at  $r = 1.05R_v$  as shown in **Figure 3.4-1a, b**. The azimuthal shear stress profile ( $\sigma_{r\theta}$ ) is plotted in **Figure 3.4-1b** along the angular spacing between two adjacent vane arms, and in **Figure 3.4-1c** the same stress is plotted for each vane. All stress fields are  $N$ -fold azimuthally periodic, approaching an axisymmetric Couette flow in the limit  $N \rightarrow \infty$ . Additional details of this solution structure are provided in Appendix A.



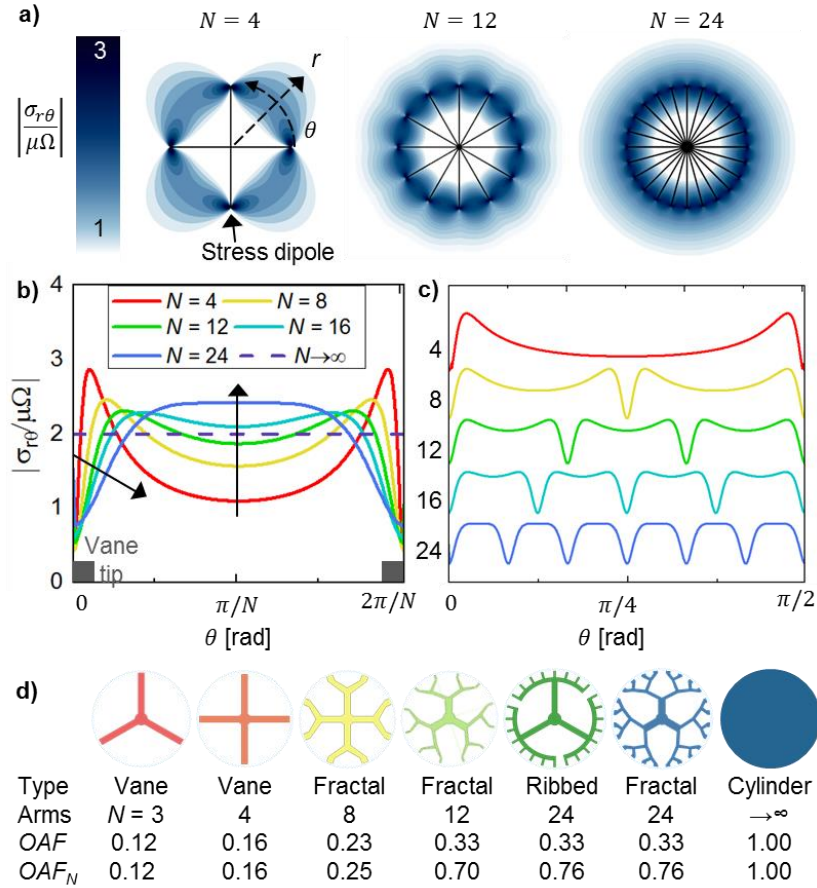


**Figure 3.4-1.** (a) Analytical contour plot of the shear stress field for a Newtonian fluid calculated using equations (A1-A3) around a 4-armed vane in an unbounded domain, normalized by  $\mu\Omega$  as a representative scale for the viscous stress. Strong dipolar stress concentrations are present at each vane tip. Progressively smoother profiles form around 12 and 24-armed vanes. Profiles are all  $N$ -fold azimuthally periodic, approaching an axisymmetric Couette flow in the limit  $N \rightarrow \infty$  (b) The azimuthal shear stress profile  $\sigma_{r\theta}(\theta)$  as a function of angle  $\theta/N$  between two neighboring vane tips for a family of vanes with increasing number of arms, calculated at a constant radius of  $r = 1.05R_v$ . The first vane arm is located at  $\theta = 0$ . The stress initially increases sharply due to the stress dipole, and then decreases between arms. (c) Profiles for  $0 < \theta < \pi/2$  for the same vanes in (b), shifted vertically for clarity. The y-axis labels indicate the number of arms. (d) A series of vane designs considered in the present chapter, along with the number of vane arms  $N$ , the occluded area fraction (OAF) displaced by the solid vane compared to an equivalent circle, and a comparison of the area occluded by the vane compared to the corresponding area of a vane with  $N$  straight arms (denoted  $OAF_N$ ).

As the vane rotates, it creates a dipolar stress field emanating from each vane tip. As a result, the minimum values of shear stress are attained on lines emanating radially outward from the vane tip ( $r \approx R_v, \theta = 0$  in the coordinate system shown in **Figure 3.4-1** (a)).

Moving away from the arm tip along the direction of increasing angle  $\theta$ , the stress initially increases sharply, and then decreases to a local minimum in the gap between arms. As the design is changed to incorporate a greater number of vane arms, the background shear stress between the arms approaches an increasingly homogeneous plateau value. Evaluating equations (A1-A3) in Appendix A for a Newtonian fluid, with  $r = R_v$  and  $0 \leq \theta \leq \pi/2$  we find that the stress drops by 60% for a 4-armed vane, by 18% for a 12-armed vane, and has no drop between arms but increases 2% for a 24-armed vane.

Although the analysis leading to equations (2)-(4) discussed above considers the torsional stress field in the test material to be axisymmetric, in reality the shearing stress varies in  $r$  and  $\theta$  and is spatially localized at the outermost contact edges between the vane and the fluid as indicated in **Figure 3.4-1** (a). In the 1990s, Sherwood and Meeten [108] simulated the influence of the number of arms,  $N$ , on a vane tool as well as end effects arising from 3D flow and showed that the measured torque,  $M$ , and the wall shear stress are related more accurately by the following expression by:

$$M = 2\pi R_v^2 L \sigma_w \left[ \left(1 - \frac{1}{N}\right) + \frac{R_v}{4L} \left(2.75 - \frac{3}{\sqrt{N}}\right) \right]. \quad (10)$$

This expression accounts for both sensitivity to the shape of the vane in the first parenthetical term, and shape-sensitive end effects for a 3D vane of finite length in the second parenthetical term.

It is evident from this relationship that increasing the number of vane arms brings the stress closer to the homogeneous wall shear stress expected for a cylindrical bob ( $N \rightarrow \infty$ ), and increasing the vane aspect ratio ( $L/R_v$ ) reduces the contribution of the end caps of the vane to the total torque. Later, Atkinson et al. [102] derived a similar relationship between the total torque and the wall shear stress for a vane with an arbitrary number of arms by using a 2D theoretical analysis for the stress field in the vicinity of a knife edge (thin plate) undergoing torsional deformation, which is valid when  $L/R_v \rightarrow \infty$ . Detailed enumeration of the integrals resulted in an expression for the torque per length on a 2D representation of an  $N$ -vane cross-section, which for a vane of length  $L$  gives a total torque:

$$M = 2\pi R_v^2 L \sigma_w \left(1 - \frac{1.113}{N}\right). \quad (11)$$

We have combined this 2D analytical solution with the 3D simulation result, guided by experimental data obtained with silicone oils and a simple yield stress fluid to validate its

performance at intermediate  $6 < N \leq 24$  which is outside the range of Sherwood and Meeten's original 3D simulation (which used  $2 \leq N \leq 6, N \rightarrow \infty$ ). We use these to develop two practical stress-torque conversion factors (denoted  $S_\sigma$ ) based on geometric features of the vane geometry that we can then compare with our experimental data. From equation (4), we can see that if we assume a *cylindrical stress profile expression*, then the appropriate torque conversion factor ( $S_\sigma^O$ ) is given by:

$$S_\sigma^O \triangleq \frac{M}{\sigma_w} = 2\pi R_v^2 L \left(1 + \frac{2R_v}{3L}\right). \quad (12)$$

We expect this expression to perform well when the deformation in a sample is nearly ideally cylindrical (for example at stresses below and close to the yield stress, and for vanes with a large number of arms). By combining the precise 2D scaling of equation (10) and the numerical calculations underpinning the end effect correction term in equation (9), we also construct the following *N-dependent expression* for the stress conversion factor:

$$S_\sigma^N \triangleq \frac{M}{\sigma_w} = 2\pi R_v^2 L \left[ \left(1 - \frac{1.113}{N}\right) + \frac{R_v}{4L} \left(2.75 - \frac{3}{\sqrt{N}}\right) \right]. \quad (13)$$

We expect this expression to be more accurate for structurally-sensitive materials with rheology that depends on the local kinematics near each vane. Instead of using the ‘‘Couette analogy,’’ equation (12) calculates the torque from a more realistic flow field that becomes more axisymmetric as the number of arms  $N$  increases. By considering the typical reproducibility of experimental rheometric data with yield stress fluids and enumerating equations (11) and (12) for a range of  $N$  (with  $L \gg R_v$ ), we find  $N = 24$  to be the lowest even-numbered vane geometry in which the difference between the two expressions varies by less than 5%, and this is the largest value of  $N$  used in the present study.

However, simply adding more arms also displaces and disturbs more material when the vane is inserted into a sample, which has been shown to lead to underestimations of the yield stress [111], and may make measurements on thixotropic fluids that exhibit a strong memory of their initial deformation history during loading less repeatable. To quantify this effect and explore it systematically, we define the occluded area fraction (*OAF*) as the cross-sectional area of fluid displaced by an  $N$ -arm vane normalized by the area of a circle with the same outer radius:

$$OAF \triangleq A_{vane} / \pi R_v^2. \quad (14)$$

Computing numerical values of this expression obviously depends on  $N$  as well as the thickness  $t$  of each vane. For example, a 4-arm vane with a thickness of  $0.13R_v$  (typical of commercial vanes) has an  $OAF$  of  $4 \times 0.13/\pi = 0.16 = 16\%$ . In addition to displaced area, more complex material systems (e.g., thixotropic fluids or multiphase systems with large particulate inclusions) may also be influenced by the overall vane structure and by loading procedures such as speed of insertion of the tool.

Our design objective, then, is to reduce recirculation of fluid between the vane arms and increase the shear stress homogeneity in the sample close to the vanes without substantially increasing the occluded area fraction of the vane. For this purpose, we propose a fractal design. Certain classes of fractals have well-defined recursive branching structures that lead to particularly high surface area-to-volume ratio [129]. In particular, we explore finite Bethe lattice-like fractals with  $N = 12$  and  $24$  arms, and compare these new designs to classical designs for vanes with  $N$  radial arms, and a ribbed cylinder textured with 24 ribs. Cross-sectional profiles of each of these designs are shown in **Figure 3.4-1 (d)** along with numerical values of  $OAF$  for each design, and corresponding values for vanes with  $N$  straight radial arms (denoted  $OAF_N$  for clarity). These designs are discussed further in Appendix B.

The area minimization problem was approached through analysis of the area occluded by each profile. The different design families we compare were guided by results from a pre-programmed Steiner tree algorithm [130], which generates the fully optimal, global minimum length path spanning a set of input points. In this case, the input design was a set of  $N$  points spaced evenly around the perimeter of a circle with radius  $R_v$  plus one additional point at the center (corresponding to the spindle location). These computational results revealed the sparsest network connecting the  $N+1$  points along with the lower bound of the achievable  $OAF$  for a given  $N$  (and fixed arm thickness,  $t$ ). Further details of this analysis are included in Appendix C.

### 3.5. Design and 3D printing of vanes and rheometer tools

#### 3.5.1. A. Design of vane for stereolithography

Rheometric tools are typically manufactured via machining of aluminum or of stainless steel. The introduction of a new fractal-based vane geometry requires a manufacturing method that can achieve complex features without excessive cost, and that is capable of creating thin and closely-spaced features such as the profiles shown in **Figure 3.4-1 (d)**. 3D

printing is exceptionally well suited for this task, as its layer-by-layer nature allows complex geometries to be created in three dimensions with, ideally, minimal post-processing or shaping. In particular, designs such as these extruded vanes that are geometrically complex along a single axis and without overhanging features can be printed with high quality using stereolithography [120]. Manufacturing thin, high-aspect ratio cavities by other methods such as machining, injection molding, or casting would be more challenging [131].

We selected the overall dimensions and rheometer coupling of our fractal vanes based on the commercial vane ( $N = 4$ ) available for the TA Instruments DHR series of rheometers with a diameter of  $2R_v = 15\text{mm}$  and a length of  $L = 30\text{mm}$ . The vane body was printed via stereolithography on a Form2 printer (Formlabs, Inc.) using Clear resin (Formlabs, Inc.), a methacrylate-based translucent photopolymer with Young's Modulus  $E = 1.6\text{ GPa}$ , and ultimate tensile strength  $\text{UTS} = 38\text{ MPa}$  (pre-curing) [132]. To facilitate attachment of the vane directly to the draw rod of the rheometer, we included a threaded coupling as shown in **Figure 3.5-1**. The  $45^\circ$  slope indicated in **Figure 3.5-1** (a) on the mating joint between the spindle holding the vane and the coupling to the rheometer allowed the vane to be printed entirely without a supporting structure, increasing printing speed and quality, as well as obviating the need for support removal. To enable this, the vanes were printed vertically, vane-end first (**Figure 3.5-1c**). We determined that this orientation ensured the best concentricity of the vane geometry with the printed rheometer coupling and best surface texture as it avoided consecutive layers giving a "stair stepping" texture on the surface and negating any imprecision in the x-y and z-stage calibrations (**Figure 3.5-1d**). The feature resolution is found to be  $200\ \mu\text{m}$  over several cm (**Figure 3.5-1e, f**), and vanes were printed with the coarsest  $100\ \mu\text{m}$  layer height setting of the Form2 printer. Printing took 3-3.5 hours per single build platform (*i.e.*, per tray shown in **Figure 3.5-1** (c)). The print time scales sublinearly with the number of vanes printed in each tray due to the high speed of lateral in-plane motion that can be achieved in stereolithography, compared to the time required to recoat resin and incrementally move the build platform after each layer. For example, we printed one vane in three hours and 12 vanes in seven hours.

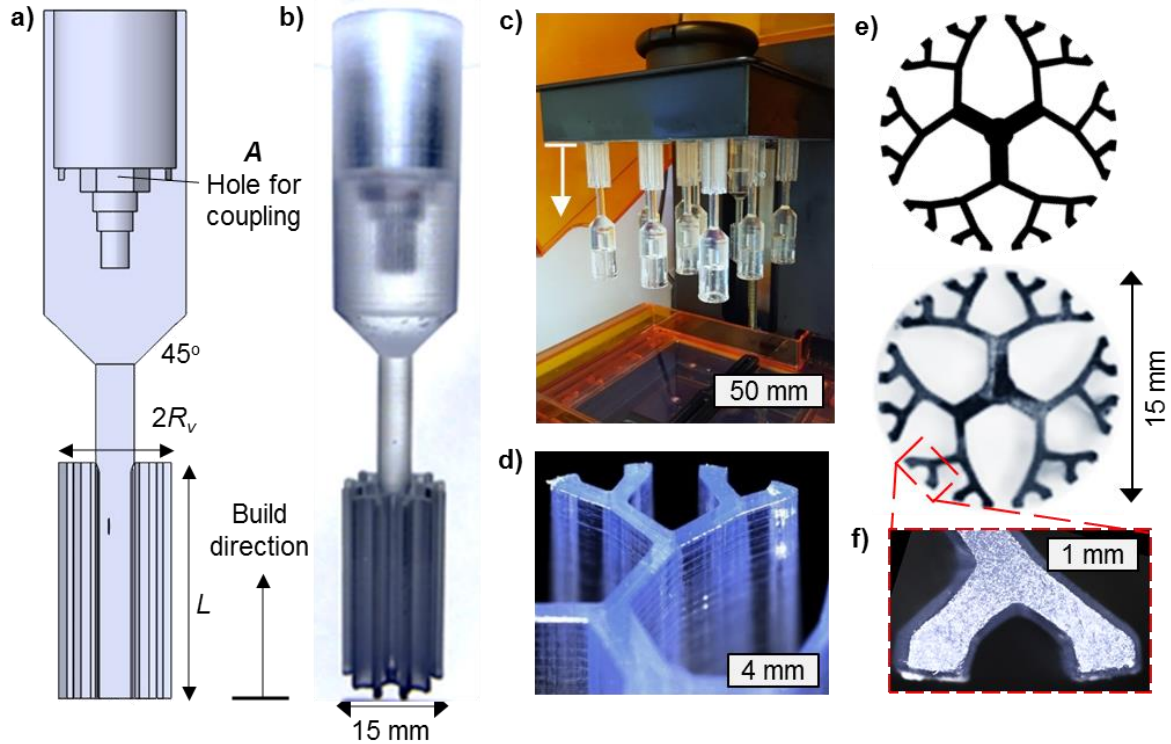


**Figure 3.5-1.** a) A complete vane design for the case of a finite 3-generation Bethe lattice with  $N = 24$  contact points at  $r = R_v$  and (b) the printed vane mounted on a DHR-3 rheometer spindle. The mounting design (A) allows us to directly connect the spindle coupling to the chosen vane geometry. A  $45^\circ$  transition angle and otherwise straight cylindrical features allows the vane to be printed via stereolithography without supports, building vertically from the vane end first, which is the upper surface in the 3D printer tray shown in (c). An oblique view shows smooth sidewalls despite the presence of visible stacked layers (d). This is because of the chosen printing orientation. (e) The input fractal shape design and a photograph of the fabricated part on end. (f) An optical micrograph of one edge of the printed design shows the  $\sim 200\mu\text{m}$  feature resolution achieved with 3D printing.

Stereolithography, which locally cures photopolymer resin via a light-initiated chemical reaction, allows the use of polymers with wide chemical compatibility [133]. The methacrylate blend material we selected is compatible with solvents such as acetone, mild acids, and also strong bases (including at least one carbon black-based battery electrolyte with pH 12 that corrodes aluminum). The printed vanes have a cost of material of  $\sim \$1.90$  (including the metal threaded insert). We previously determined the repeatability of stereolithography under similar printing parameters is  $30\ \mu\text{m}$  standard deviation in dimensions between prints [134]. Thus, even in the case in which the material to be tested

slowly degrades and/or adheres to the vane, 3D printing is still an attractive solution. Relative to the value of an accurate measurement, the low cost of 3DP vanes may justify their single-time use.

### 3.5.2. Design of the coupling for attachment to the rheometer

In order to robustly attach to a commercial rheometer, the printed vane geometry was designed to accommodate a threaded insert, rather than by including printed threads integral to the vane. The coupling (A) shown in **Figure 3.5-1** (a) was designed to be 3D-printed, fitted with an M4 threaded insert, and attached directly to a DHR3 or AR-G2 rheometer spindle (Discovery Hybrid Rheometer 3 or Advanced Rheometer-Generation 2; TA instruments, New Castle, DE). These two generations of controlled-stress rheometers have a drag cup motor, radial air bearings, magnetic thrust bearings, and an optical encoder in the head of the rheometer. The stationary base has a temperature sensor and Peltier plate assembly (**Fig 4a**).<sup>[135]</sup> A standard geometry slides up onto the spindle and is held axially in place by a long threaded rod (**Figure 3.5-2b**).

The printed vane is designed to fit over the rheometer spindle with slight interference (0.05 +/- 0.02 mm diametrical interference), and a hole to position a threaded nut insert to hold the part in place (**Figure 3.5-2c-e**). The diametrical runout  $\Delta R_\theta$ , a measure of the eccentricity of rotation of a spindle, is reported here as the diameter of the path traced out by the central axis at the lowest end of the vane. If the runout is zero, the rotation of the vane is perfectly concentric. The runout was measured using a laser-based line profilometer (LJ-V7080, Keyence) as  $0.35 \leq \Delta R_\theta \leq 0.70$  mm total runout at the lowest end for printed vanes, compared with 0.31 mm for a commercial metal vane (TA Instruments, Part 546027.901). Note that the inner diameter of the printed coupling may change slightly when exposed to solvent during the post-print cleaning step, affecting the amount of interference.

For the vane-rheometer coupling, a variety of designs were compared, including five types of threaded inserts and various combinations of dimensional interference and structural compliance; these are shown in Appendix D. The final design using a press-fit nut as a threaded insert (shown in **Figure 3.5-2e**; McMaster press-fit nut, 99437A145), was selected for consistently giving the lowest runout on repeated attachment/detachment of the tool. In addition, the specific nut chosen had a flat top surface, and this surface was pressed flush against the rheometer spindle, and likely contributes to the lower runout

achieved. Couplings could easily be designed to fit other rheometers available in the marketplace, and in the supporting information we provide the design of a vane coupling to ARES strain-controlled rheometer with this chapter.

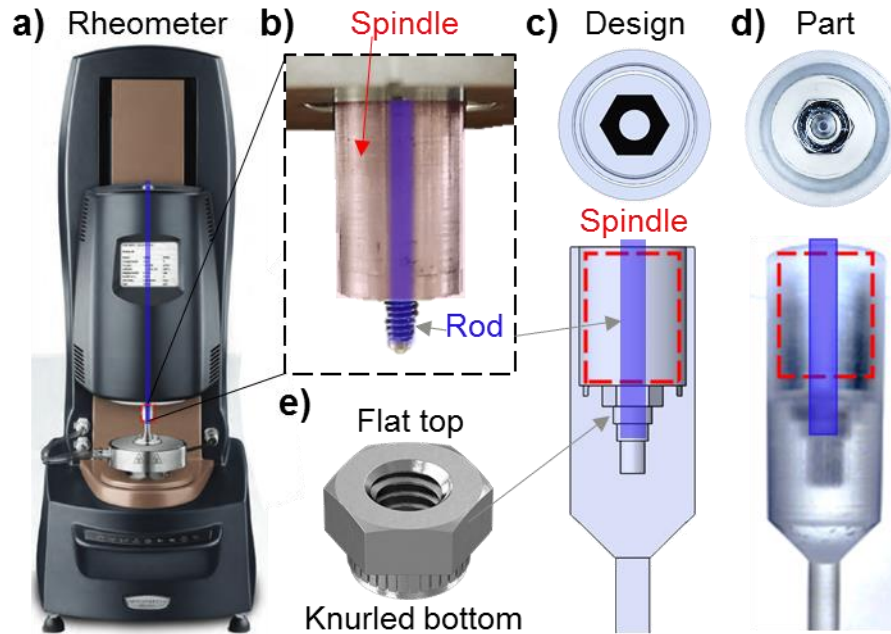


**Figure 3.5-2.** (a) The DHR and AR-G2 family of controlled stress rheometers have a loose threaded “draw rod” extending through the drag cup motor housing and sensing head (outlined in blue), with (b) a spindle (highlighted red) that aligns the geometry to the axis of rotation of the rheometer. (c) An on-end view of the as-designed coupling and (d) a photograph of the 3D-printed part, which has a loose interference fit (50 $\mu$ m overlap) on the spindle for radial positioning, and locks in place axially using the spindle M4 screw with a threaded nut insert. (e) Computer drawing of the press-fit M4 nut that connects the part to the rheometer. The knurled bottom surface holds it in place within a centered hole in the printed vane.

Further, the rotational inertia of a 3D printed acrylic vane ( $I_v \approx 0.8 \mu\text{N.m.s}^2$ ) is much smaller than that of a metal vane ( $I_v \approx 6 \mu\text{N.m.s}^2$ ), although both moments of inertia are much smaller than that of the rheometer head itself ( $I_{inst} \approx 18.5 \mu\text{N.m.s}^2$ ), and the mass of fluid trapped by the vane arms will add to both moments of inertia during measurements, so this has a negligible effect on most measurements.

### 3.5.3. 3D-printed cup with textured wall

We also designed a cup to complement the 3D printed vane, and serve as the sample holder. The inner surface of the cup is textured to help prevent slip of the sheared sample



at the outer wall, with square steps of 1 mm width by 1 mm depth, spaced apart by 2 mm. These dimensions were chosen to give similar spacing as the arms of the 24-armed fractal vanes and to promote infill of the material into the gaps between ribs (**Figure 3.5-3a, b**). In addition, the cup fastens onto the Peltier plate that is a standard lower fixture on the DHR or AR-G2. The Peltier plate holds it either by an interference fit of six protruding arms or by using the arms as guides and using double-sided tape under the base for a more adjustable hold, as a well-calibrated Peltier plate is orthogonal to the axis of the rotating spindle but is not necessarily concentric with it. The yielded area is set entirely by the location of the vane perimeter and extends radially outwards. Provided the yielded area does not reach the outer wall (*i.e.*, provided the imposed stress is  $\sigma_w/\sigma_y < (R_c/R_v)^2$ ), the cup shape and position only influences the spatial homogeneity of the linear viscoelastic deformation that occurs pre-yielding, with an effect proportional to the offset of the rotation axis (Appendix D). Thus, for measurements of yield stress fluids with a wide-gap geometry, precise concentricity of the cup is not critical.

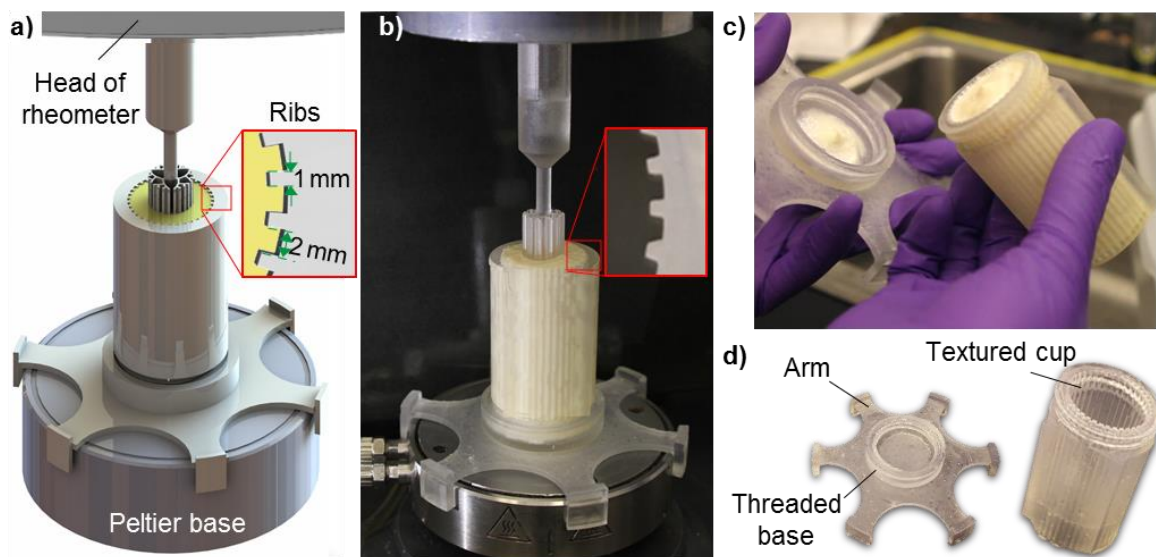


**Figure 3.5-3.** (a) A 3D-printed cup featuring a textured inner wall to prevent slip. Lower arms clip onto the standard Peltier plate base, and the cup walls disassemble from the base via a threaded mating feature for ease of cleaning out thick yield stress materials from within the ribbed surface texture. The inset shows the crenelated ribs around the outer surface, which have 1 mm width and side length, and 2 mm spacing. (b) The assembled cup mounted onto a Peltier plate base, filled with mayonnaise, and (c) the disassembled cup with material still inside, and (d) a cleaned and disassembled cup and base.

The cup was designed for facile use with yield-stress fluids, which often are challenging to fill into the cup without bubbles and to clean out after an experiment, especially given the crenelated walls. As a result, the cup was designed to unscrew from the base, making it straightforward to access material in the cup for filling and cleaning (**Figure 3.5-3c, d**). As an added benefit, this means that a single base can be used interchangeably with several 3D printed cups that differ in height and diameter, or that are pre-filled with different fluid samples, as long as they use the same (custom) 3D-printed mating thread. This enables multiple samples to be pre-filled and conditioned with a controlled waiting time and thermal history, if desired, then mounted directly onto the rheometer just prior to testing.

### *3.6. Experimental validation: rheological measurements vs tool design*

Here, we compare measurements of viscous Newtonian oils and a simple yield stress fluid made using our family of vanes to measurements made with standard roughened cone-and-plane fixtures (which we assume to provide true reference values). Although flow curves and viscosity measurements of yield stress fluids often are reported as single values and single curves, the measurements in fact are inexact and repeated measurements commonly vary by more than a few percent for challenging materials. Our aim is to unambiguously compare the performance of a series of vane tools with repeated measurements made using standard cone-and-plate tools to quantify mean error and variability. We use these results also to compare performance among vane designs. Having determined the optimal designs, we then use a printed fractal vane to measure the transient rheological response of multiple TEVP materials.

#### *3.6.1. A. Measurements of viscous oils*

A strain rate sweep experiment was performed on a high viscosity silicone oil ( $\mu = 1.0$  Pa.s at 25° C; **Figure 3.6-1a-c**) using a series of vane designs, and compared to the reference measurement made with a cone-and-plate geometry (**Figure 3.6-1a-c**). The measured rotation rate at each torque was converted to shear rate using equation (7) and the torque was converted to stress using equation (12), the  $N$ -dependent expression.

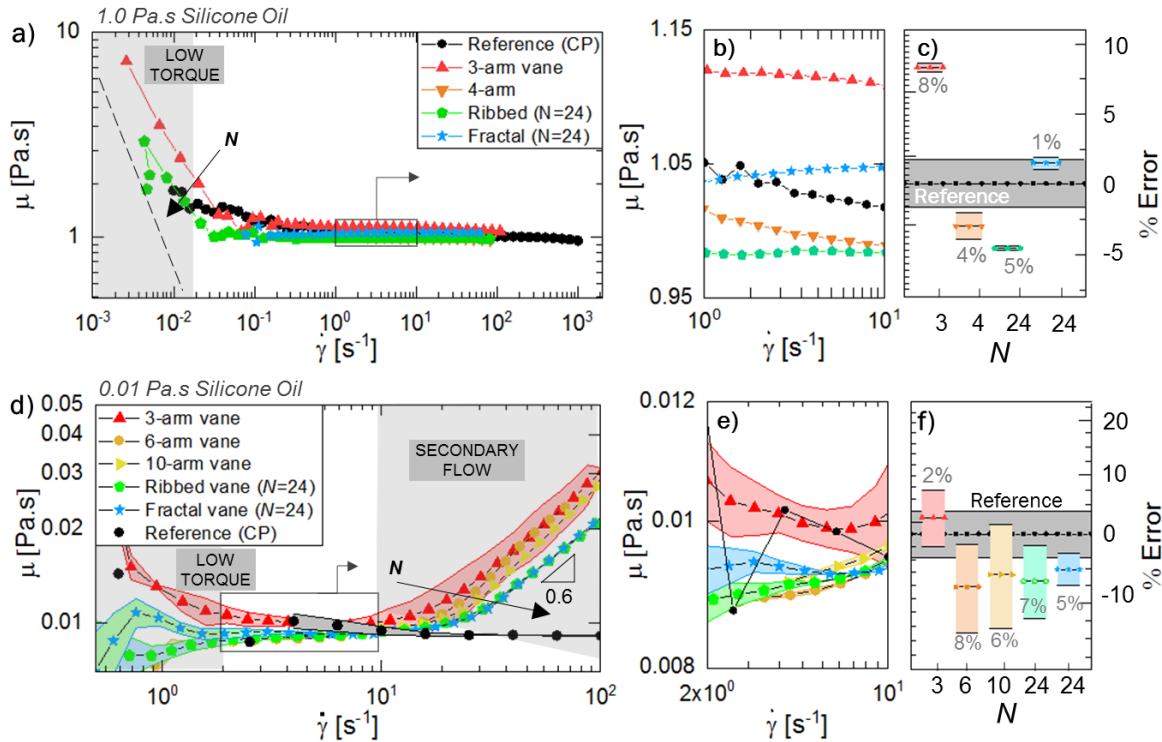


**Figure 3.6-1:** a) Measured viscosity of a viscous Newtonian silicone oil (1.0 Pa.s) measured using several 3D printed vanes (including regular  $N = 3$  and  $N = 4$  arm vanes plus a 24-armed fractal vane and a ribbed cylinder (see Appendix C for details)), and (b) an expanded view of  $1 < \dot{\gamma} < 10 \text{ s}^{-1}$ . (c) Viscosity values measured for each geometry compared to the reference measurement made with a cone-and-plate geometry, with the mean percent difference labeled, averaged for three or more measurements for the shear rates in (b). (d) Measured viscosity of a lower viscosity Newtonian silicone oil ( $\mu = 0.010 \text{ Pa.s}$ ) measured by several 3D printed vanes ( $N = 3, 6, 10, 24$ -arm fractal, and 24-arm ribbed cylinder). Data is shown with lines indicating mean values and clouds of similar color representing the standard deviation from three or more repeated measurements. At low shear rates  $\dot{\gamma} < 2 \text{ s}^{-1}$ , machine limitations of torque sensing caused noise. At high shear rates  $\dot{\gamma} \gtrsim 20 \text{ s}^{-1}$ , secondary flow cause the torque to increase due to inertial effects, with the effect delayed to higher  $\dot{\gamma}$  for vanes with more arms. For shear rates of  $2 < \dot{\gamma} < 10 \text{ s}^{-1}$ , the viscosity was approximately constant for all vanes, and so results are inter-compared in this region. (e) Enlarged view of the region within  $2 < \dot{\gamma} < 10 \text{ s}^{-1}$  together with percentage error. (f) Measurement range shown for each geometry compared to the reference measurement made with a cone-and-plate geometry, with the mean percent difference labeled, averaged for three or more measurements over the range of shear rates shown in (e).

When viewed on rheologically-typical log-log axes (such as **Figure 3.6-1** (a)), the results all appear to overlap well, provided the tests are performed above the minimum torque range of the instrument. To investigate the geometric variations we need to look much more

closely as shown in **Figure 3.6-1** (b). Here we can see that viscosity measurements using vanes were within 8% of the cone-and-plate reference measurement for shear rates  $1 < \dot{\gamma} < 10 \text{ s}^{-1}$ , with the fractal design having the smallest error at 1.4% (**Figure 3.6-1e,f**). Because of the large torque values for this viscous fluid and the small variance in the shear stress data for a well-behaved Newtonian oil, the viscosity values measured with the 3-arm vane, 4-arm vane, and 24-arm ribbed vane were statistically distinct from the cone-and-plate measurement (t-test;  $p < 0.05$ ), while only the results obtained using the fractal vane ( $N=24$ ) were not statistically different from the reference curve.

Below the range of shear rates used for this comparison, systematic errors must be recognized. At low shear rates, data becomes noisy when the torque measured by the rheometer reaches the minimum limit of sensitivity ( $\approx 10 \mu\text{N.m}$ ). Using a vane with more arms increases the window accessible for accurate measurement. The useful range of data was expanded in the low shear rate regime as the number of arms on the vane increased (**Figure 3.6-1a**). A higher number of arms  $N$  increases the wetted area of contact between the fluid and the fixture, increasing the conversion factor  $S_\sigma$  and leading to a larger torque at low shear rates, thus extending the minimum resolvable stress.

The measurements were repeated using a low viscosity silicone oil ( $\mu = 0.010 \text{ Pa.s}$ ; **Figure 3.6-1d-f**). As before, the minimum torque sensitivity of the rheometer ( $10 \mu\text{N.m}$ ) was observed to limit the useful data range at low shear rates. In addition, due to the much lower fluid viscosity raising the Reynolds number characterizing the flow, inertial recirculation between vane arms becomes significant at high shear rates. Within these limiting bounds,  $2 < \dot{\gamma} < 10^4 \text{ s}^{-1}$ , the measured viscosity was nearly constant (within  $\pm 10\%$ ) for all vanes. Using a vane with a larger number of arms expanded the window accessible for accurate measurement in the low shear rate regime as before, as well as in the high shear rate regime as the number of arms on the vane increased (**Figure 3.6-1a**). At high shear rates, the onset of secondary flow is delayed to higher shear rates, most likely due to the smaller internal characteristic lengths,  $l \approx 2\pi R_v/N$ , of the lid-driven cavities that exist between neighboring vane arms. [128]

For the low viscosity oil, the variation in the average viscosity measured by all tested vanes was within 8% of the true value, and was less than 5% for the fractal design (**Figure 3.6-1b,c**). However, the measured viscosity was not statistically different from the value measured with a cone-and-plate fixture for any vane (t-test;  $p > 0.05$ ).

### 3.6.2. B. Measurement of a simple yield stress fluid

Carbopol is a hydrogel composed of crosslinked poly(acrylic acid) microgel particles that swell in neutral or basic pH to form a physically-jammed microstructure and which, providing the preparation is done carefully, convey a remarkably “simple” yield stress behavior that has been well-studied [75], [97], [136]. Furthermore, we use a Carbopol-based hair gel (Clear Ice Ultra Hold, Ampro Pro Style) that we found to show simple yield stress behavior. Also, this type of material does not exhibit shear banding, making it useful for calibration [78]. We measured the steady-state flow curve with four 3D printed vanes ( $N=3, 4, 12$ -fractal,  $24$ -fractal, as well as with a solid cylindrical bob) and compared measurements with the reference flow curve obtained using a roughened cone-and-plate geometry. The cone and plate were both roughened by attaching a micropatterned adhesive sandpaper (Trizact A5; 3M; average surface roughness  $5\ \mu\text{m}$  on top of pyramidal features with  $120\ \mu\text{m}$  side lengths, as measured with a Zeiss SmartZoom 5), which removes the effect of slip for all measurements. For our measurements, the vanes were inserted into the material until a lower gap equal to  $R_v$  was obtained between the bottom of the vane and the lower surface of the cup, and similarly a depth of at least  $R_v$  of sample was ensured between the top of the vane and the sample surface.

When using the vane fixtures, the torque measured at each rotation rate increases with the number of outer contact points with the fluid, as expected (**Figure 3.6-2a**). We converted the measured rotation rate to the shear rate in the material at the edge of the vane using equation (7). As shown in **Figure 3.6-2b**, the resulting conversion is rate-dependent rather than a single constant factor, but the curves behave similarly for all vanes. To convert the shear rate precisely, we fit each data set to a functional form  $M = a + b\Omega^c$  and inserted that formula into equation (7) for conversion. We found other methods, such as pointwise evaluation of derivatives using centered difference formulae, were substantially less accurate - particularly at low shear rates.

Next, torque was converted to stress using either equation (11) (**Figure 3.6-2c**) or equation (12) (**Figure 3.6-2d**). The solid cylindrical bob showed the onset of slip at low shear rates below  $\dot{\gamma} = 0.3\ \text{s}^{-1}$ , as detectable by a systematic deviation to lower measured stresses at a given rate. By contrast, the use of any vane geometry eliminated slip, and each measured curve could be fit to a Herschel-Bulkley model with  $R^2 > 0.97$ . When using equation (11), it is clear that the flow curves presented in **Figure 3.6-2 (c)** fall systematically

below the reference curve, with progressively smaller errors as the number of arms  $N$  increased. When using equation (12), most curves collapse onto the reference curve so as to be indistinguishable, with the exception of the cylindrical bob due to slip at low shear rates, and the 3-arm vane, which has substantially larger deviations. The errors (with respect to the reference cone-and-plate data) are shown for each curve as a function of shear rate in **Figure 3.6-2e, g**, and the mean error averaged over all shear rates are shown in **Figure 3.6-2f, h**, respectively, with labels indicating average percent error.

The total error is much lower when the  $N$ -dependent stress conversion given by equation (12) is employed, which assumes that the fluid stress and velocity fields depend on the vane shape, and are  $N$ -fold azimuthally periodic but are not constrained to be an axisymmetric Couette flow. In this case, standard errors are only 0.8-3% and the data fall well within the most likely experimental window expected from the cone-and-plate values (grey shaded region in **Figure 3.6-2f-h**). In comparison, the total error obtained from using equation (11), which assumes axisymmetric stress and velocity fields, results in standard errors up to 4-23% in the final flow curves. We further observe that this total error decreases systematically as  $N$  increases, to a minimum for the fractal vane with  $N=24$  (**Figure 3.6-2f**), indicating that for the 24-arm vane, the stress field is well-approximated by a cylindrical expression, confirming one of our major design objectives. Our results further support the assertion of Keentok [105] that a 3-armed vane is insufficient for accurate measurement of flow curves in yield stress fluids. We finally note that the error plots of **Figure 3.6-2e, g** show relatively uniform error for the range of shear rates considered, indicating that the conversion equation for rotation rate to shear rate is not introducing errors.

As we would expect, the level of error obtained when measuring yield stress fluids is less than that for the measurements of Newtonian fluids, which flow at every point inside the cup, are more sensitive to the internal structural details of the vane, which can enhance or inhibit local recirculations. By contrast the deformation in yield stress fluids is more sensitive to the number of outer contact edges,  $N$ , while the limited radial extent of the yield surface cloaks the geometric details of the vane's inner structure from the flow field [137].

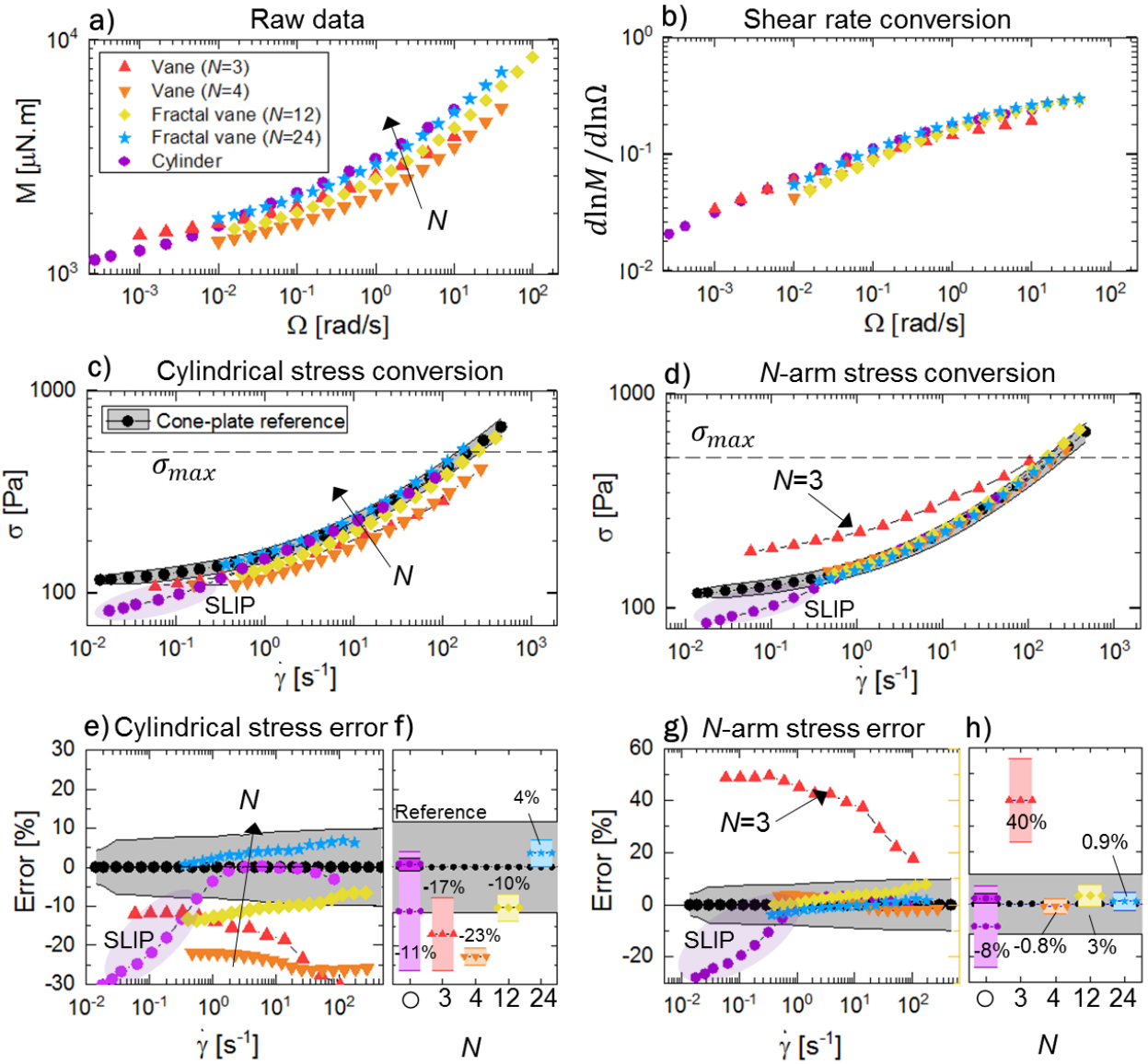


**Figure 3.6-2:** Comparison of vane performance when measuring the flow curve of a Carbopol-based hair gel, a simple (non-thixotropic) yield stress fluid. a) Raw torque vs rotation rate for a range of 3D printed vanes (cylinder, vanes with  $N = 3, 4, 12, 24$  arms), and (b) shear rate conversion factor from equation (7). (c) Final flow curve of shear stress-shear rate after converting stress via equation (11), compared to the cone-plate reference curve (black filled circles). (d) For stress converted via the  $N$ -dependent equation (12), most data falls on top of the true curve. The exceptions are for the sparse 3-armed vane, and the cylinder which experiences slip at low shear rates. (e,g) The error in the vane data compared to cone and plate reference is shown, along with an error cloud (grey shaded region) showing error from three repeated cone-and-plate measurements of the Carbopol microgel. (caption continued on next page)

(f, h) Mean error and the range of error for each vane for three repeated measurements, averaged along the entire curve, where the mean percent error is labeled. The background grey bar shows the range of repeated cone-and-plate reference measurements. The error from the cylinder is represented for both the entire curve including slip (light purple bar) as well as for the partial curve without slip at higher shear rates (dark purple bar). Computing the sample stress using the  $N$ -dependent expression (h) leads to the lowest overall error for all vanes (excluding the 3-armed vane) with  $<1\%$  mean error for the fractal and 4-armed vanes, indicating the universal applicability of this conversion expression (equation (12)).

### 3.6.3. Direct comparison of torque/stress conversion factors with models

In order to determine the best expression to predict the torque/shear stress conversion factors, we calculated the optimal value of  $S_\sigma$  to translate the flow curves for a series of fluids exactly onto the reference curve with zero average error over a range of shear rates  $10^{-1} < \dot{\gamma} < 10^1 \text{ s}^{-1}$ . In **Figure 3.6-3**, we plot these values against the values predicted by equations (11)-(12). Here we combine results for a Newtonian fluid (low viscosity silicone oil shown in **Figure 3.6-1**), a simple yield stress fluid (Carbopol data shown in **Figure 3.6-2**), as well as a more complex thixotropic yield stress fluid (mayonnaise), which is discussed in more detail later. We observe best agreement with equation (12), as well as progressively smaller error bars in the data obtained using vanes with a higher number of arms  $N$ . the convergence of both expressions at high  $N$  allows data taken with a 24-armed vane to compare well with the expected values of  $S_\sigma$  for both expressions.

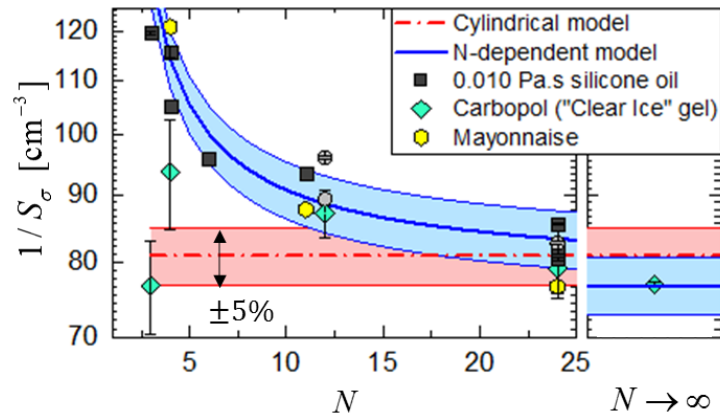


**Figure 3.6-3.** The optimal torque conversion factors calculated from experimental data for three different fluids were compared with the torque conversions factors computed using the two expressions in equations (11) and (12) for a series of  $N$ -armed vanes. Separately, we also show the conversion factor expected for a Couette “bob” (cylinder) with  $N \rightarrow \infty$ .



### 3.6.4. Start-up of steady shear flow

Elasto-visco-plastic yield stress fluids also have a characteristic viscoelastic response to start-up of steady shear. Initially, the shear stress increases monotonically with imposed strain before the onset of irreversible plastic yielding and flow. The initial stress growth may be linear, indicating Hookean linear elasticity, or sublinear, indicating a viscoelastic solid response. At a critical apparent strain, the material will begin to fluidize and flow plastically. Eventually the flow will develop a terminal, constant stress at or above the yield stress. If the yield stress fluid is thixotropic, there is often an overshoot before the stress decreases to a constant terminal value [76]. Depending on the imposed shear rate, it will take a different length of time to reach the yielding point. However, in many systems we expect the curves for different shear rates will superpose when plotted against an apparent strain, consistent with a dominant elastic response. Having determined that the  $N = 24$  fractal arm vane gives optimal results for a range of fluids, we now perform start-up of steady shear tests on three yield stress materials using a 24-armed fractal vane.

### 3.6.5. i. Carbopol

Carbopol was loaded into the textured cup shown in **Figure 3.5-3** and a constant rotation rate was imposed, ranging from  $1.8 \times 10^{-4}$  to  $6 \times 10^{-1}$  rad/s, corresponding to shear rates in the range  $4 \times 10^{-3}$  to  $8 \text{ s}^{-1}$ . The rotation rate was imposed for a set time that varied inversely with the rotation rate and increased sequentially in steps, as shown in **Figure 3.6-4a**, with a 10 s waiting time between steps. In response to a single rotation rate, the stress initially grows linearly in time elastically followed by a plastic flow regime as shown in **Figure 3.6-4b**. When this transient stress response is plotted as a function of apparent strain,  $\theta = \Omega t$ , the curves superpose for all shear rates, as shown in **Figure 3.6-4c**. The initial deformation is nearly linear in applied strain, allowing us to calculate a shear modulus of  $G = 810 \text{ Pa}$  from the average slope of the elastic response,  $\Delta\sigma/\Delta\theta$ , for all curves. At a critical apparent strain,  $\theta_y \approx 0.2$ , the material yields and undergoes plastic deformation, reaching a terminal stress that is nearly independent of shear rate over three decades of deformation rate. This is because the very low shear rates applied correspond to the stress plateau region shown in **Figure 3.6-2b** so  $\sigma_w \approx \sigma_y = 110 \text{ Pa}$  at long times for all of these deformation rates. In response to increasing the imposed rotation rate  $\Omega$ , the terminal stress increases slowly and monotonically with rotation rate as expected, but all

curves reach the plastic flow regime with a terminal stress within the range  $122 \leq \sigma^+(t \rightarrow \infty) \leq 182$  Pa.

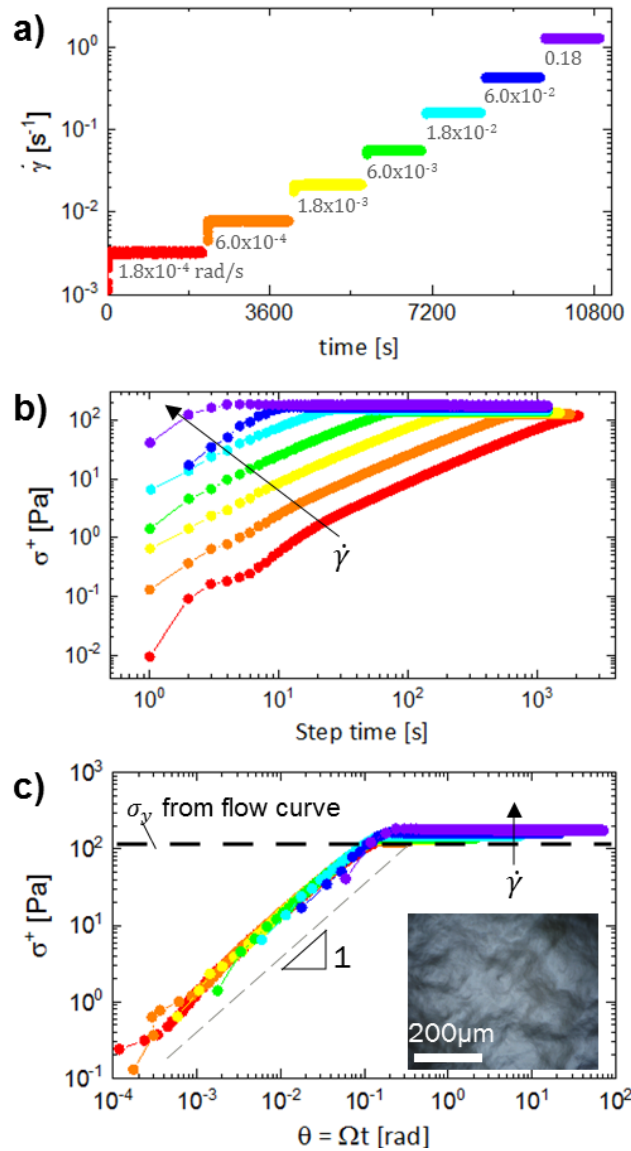


**Figure 3.6-4.** Transient yielding behavior of a Carbopol-based hair gel shows simple yield stress behavior in start-up of steady shear flow tests using a fractal vane ( $N = 24$ ). (a) A series of shear rates were applied, with 1,000-2,000 s per step, to understand the transient response of the Carbopol. (b) For all imposed rates, the Carbopol shows an initial elastic response followed by plastic yielding at a constant terminal flow stress. (c) When the data are plotted using the apparent strain  $\theta = \Omega t$  rather than the experimental step time on the abscissa, they superimpose, revealing a consistent material response. In all cases, the material elastically deforms until it yields at a critical apparent strain  $\theta_y \approx 0.2$  rad and immediately plateaus at an almost constant value of the stress. The inset shows an optical micrograph of the material microstructure.

### 3.6.6. ii. Mayonnaise

Mayonnaise (Hellmann's Squirtable) is a vinegar-and-egg-based emulsion of oil in water (**Figure 3.6-5a** inset). Over time, the fat globules coalesce and particle flocs aggregate, yet imposed stress breaks up structures and/or induces particle migration and mild phase separation [138]–[140], thus resulting in a thixotropic yield stress response. This makes rheometry of such structured materials very difficult as they show sensitivity to their entire history, including the loading step required to place a sample into the rheometer. For this reason, the mayonnaise samples were held in the original off-the-shelf container for experiments. To investigate the thixotropy of the mayonnaise, a conditioning step was performed to reset the material history after the vane was inserted using a pre-shear rate  $\dot{\gamma} = 0.1 \text{ s}^{-1}$  for 10 s, followed by a waiting time,  $t_w$ , varying from 3 s to 10,000 s. Last, we imposed a constant rotation rate of  $1.6 \times 10^{-4} \text{ rad/s}$  for times  $t > t_w$ . The resulting material response to this pre-shear history is shown in **Figure 3.6-5(a)**. For all waiting times, the initial viscoelastic response is a power law with slope less than unity, indicating strain-dependent plastic losses [141]. Subsequently, the material yields, showing a stress overshoot that depends strongly on the waiting time,  $t_w$ , before approaching a steady state terminal shear stress. This thixotropic overshoot is indicative of progressive structural buildup following the cessation of preshearing.

The initial power law characteristics of the transient stress growth are common in many microstructured food gels [142]. One way of compactly modeling this response is by using a Scott Blair fractional element to quantify the rate-dependent material properties. This model has two parameters: a viscoelastic quasi-modulus  $\mathbb{G}$ , and a fractional exponent  $\alpha$  characterizing the order of the fractional derivative [143]. For instance,  $\alpha = 0$  indicates a purely elastic response, and  $\alpha = 1$  indicates a purely viscous response. The stress-strain relationship for a Scott Blair element is defined as

$$\sigma_{yx} = \mathbb{G} \frac{d^\alpha \gamma}{dt^\alpha} \quad (15)$$

with the fractional derivative dependent on the exponent  $\alpha$ . For start-up of steady shear after a waiting time  $t_w$ , where the apparent strain  $\gamma \triangleq \theta = \Omega(t - t_w)$ , integration of equation (14) results in

$$\sigma_{yx} = \frac{\mathbb{G}}{\Gamma(1-\alpha)} (\Omega(t - t_w))^{1-\alpha} \quad (\text{for } \alpha \neq 0,1) \quad (16)$$

where  $\Gamma(\cdot)$  is the gamma function. This time-dependent relationship was fitted to the transient stress growth curves shown in **Figure 3.6-5(a)** for times  $t_w \leq t \leq t_{lin}$  where  $t_{lin}$  is the point at which the stress first reaches a value equal to its terminal stress. For more details on this fractional model and related analysis, refer to [141]–[144]. The value of the quasi-property, or scale factor  $\mathbb{G}$  in equations (14)–(15) increases from  $\mathbb{G} = 600 \text{ Pa}\cdot\text{s}^\alpha$  at  $t_w = 3 \text{ s}$  to  $\mathbb{G} = 1080 \text{ Pa}\cdot\text{s}^\alpha$ , beyond which it plateaus for  $t_w \geq 100 \text{ s}$  (**Figure 3.6-5b**). The fractional exponent similarly decreases from 0.46 to 0.14, beyond which it plateaus after 100 s, consistent with the increasingly solid-like nature of the material that occurs during restructuration.

Similarly, the yield strain (at which  $\sigma = \sigma_{peak}$ ) increases slightly for all measurements with increasing waiting time, from  $\theta_y = 0.05 \text{ rad}$  to  $\theta_y = 0.09 \text{ rad}$ . After the initial viscoelastic buildup of stress, the mayonnaise exhibits a second thixotropic behavior with a stress overshoot, in which the stress increases to a maximum value  $\sigma_{peak}$  before decreasing to a terminal asymptotic flow stress that is independent of sample age. The terminal stress was 65–70 Pa for all waiting times. The peak stress  $\sigma_{peak}$  was constant at 67 Pa for waiting time  $t_{wait} < 100 \text{ s}$  and increased afterwards up to 90 Pa.

The overshoot stress compared to the terminal stress,  $(\sigma_{peak} - \sigma_\infty)/\sigma_\infty$ , is plotted in **Figure 3.6-5c** as a function of waiting time. Comparing the results in **Figure 3.6-5 (b)** and 10(c), it is clear that there are distinct timescales for restructuring of the linear viscoelastic solid response and for the rise in the nonlinear overshoot stress in this material, which may both be called “thixotropic” timescales. Dividing the material response into multiple timescale processes has recently been suggested by Wei et al [145].

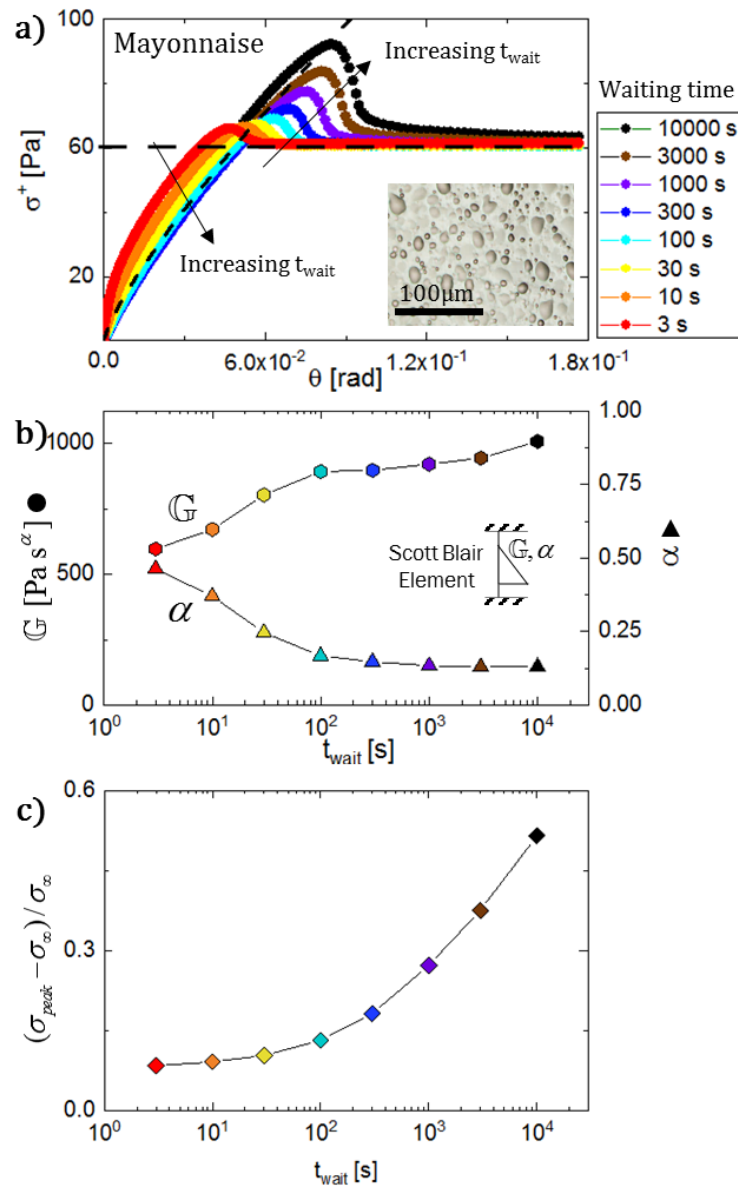


**Figure 3.6-5.** Yielding behavior of mayonnaise (a thixotropic jammed oil-in-water emulsion) measured with a 24-arm fractal vane. A start-up of steady shear test at a constant rotation rate  $\Omega = 1.6 \times 10^{-4}$  rad/s was performed after a sequence of pre-conditioning at a shear rate of  $0.1 \text{ s}^{-1}$  followed by a waiting time  $t_w$ . An inset image in (a) shows an optical micrograph of the material microstructure. (b) A fractional model with a single Scott Blair element was used to describe the viscoelastic material response for times  $t_w < t < t_{peak}$ . Up until 100 s, the quasi-modulus  $G$  increases and the exponent  $\alpha$  decreases rapidly, indicating stronger and more solid-like behavior arising from restructuration. For waiting times  $t_w > 100$  s, changes in the viscoelastic solid properties were more gradual while (c) the magnitude of the stress overshoot began to increase more rapidly, indicating a complex multiscale reformation of the microstructure between tests.

### 3.6.7. iii. Aqueous Battery Slurry

Finally, we measured the yielding characteristics of an aqueous battery slurry composed of Carbopol (Lubrizol, USA; 1 wt%), carbon black (acetylene black, Chevron, USA; 6 wt%), and 7 molar KOH (30 wt%); this mixture results in a paste with  $\text{pH} = 12$ . The strong alkalinity increases electronic conductivity, improving performance as a battery material [146]–[148]. It also causes this slurry material to corrode many metals including commercial steel rheometer vanes. While the dispersed carbon black discolored our 3D printed resin, the vane did not show evidence of physical degradation even after 20 hours of experiments.

As with the other materials, a steady rotation rate was imposed ( $10^{-4}$  rad/s), without modification between trials. There was no conditioning pre-shear, because no combination of speeds and equilibration times were found to “reset” the material to give a repeatable initial stress response (*i.e.*, the material ages irreversibly). The waiting time was therefore held to a constant value of  $t_{wait} = 1000$  s between each test. As shown in **Figure 3.6-6**, the initial stress growth is weakly sublinear in strain but remains almost constant with the number of times the sample is sheared. Fitting the data with equation (15) gives  $\mathbb{G} = 430 \text{ Pa}\cdot\text{s}^\alpha$  and  $\alpha = 0.17$ . The yield strain, taken at the strain at which stress is a maximum, is  $\theta_y \approx 0.1$  rad for the first step, and nearly constant thereafter at  $\theta_y \approx 0.06$  rad.

This battery slurry also shows mildly thixotropic behavior with a weak stress overshoot. The stress overshoot remained constant at 20 Pa, while the terminal yield stress decreased with each successive trial from 40 Pa down to 30 Pa, indicating irreversible material aging with repeated shearing. This effect may be due to shear-induced gravitational settling and flocculation, or shear-induced particle migration [106], [149], which would be important phenomena to understand further within a flow battery. Therefore, this particular slurry recipe would not be stable during use as an electrolyte in a flow battery. Yet, the ability to rapidly and reliably make such measurements using a fractal vane with absence of slip or sample loading artifacts makes the fractal vane useful for assessing development of a functional battery slurry recipe.

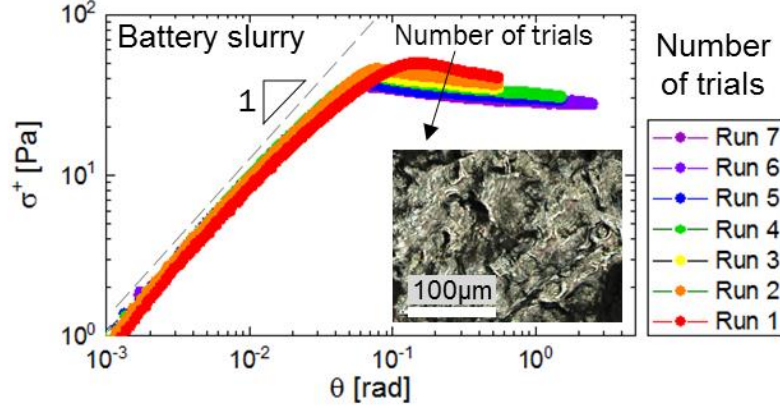


**Figure 3.6-6.** Yielding behavior of a carbon black-based battery slurry measured with a 24-arm fractal vane. The sample permanently degraded with each yielding event, instead of fully recovering, and the stress overshoot decreased with each repeated trial. The inset image shows an optical micrograph of the material microstructure.

### 3.7. Conclusion and Perspective on Rheometric Tool Choice

We have introduced a family of fractal vane geometries, characterized by the number of arms  $N$ , that can readily be manufactured using cost-effective desktop stereolithographic 3D printing. The design of this new class of fixtures gives a larger surface area-to-volume ratio to the tool, leading to improved axisymmetry of the yield surfaces at the point of yielding and a more accurate determination of the yield stress.

Specifically, we have shown that vanes and textured cups made by desktop stereolithography can be used to obtain rheological measurements that are consistent with “reference” measurements made by machined cone-and-plate geometries with carefully roughened surfaces to eliminate slip. We have also presented expressions for interconverting between measured torque and sample shear stress for a general vane with any number of equally spaced arms, as well as for converting between rotation rate and shear rate for a wide-gapped vane-in-cup configuration. Notably, these equations do not require calibration experiments, as all vane-specific terms depend on the invariant, physical geometry of the vane. For completeness we repeat these expressions again below.

The torque-to-shear stress conversion is (from equation (12))

$$\sigma = M / \left( 2\pi R_v^2 L \left[ \left( 1 - \frac{1.113}{N} \right) + \frac{R_v}{4L} \left( 2.75 - \frac{3}{\sqrt{N}} \right) \right] \right), \quad (17)$$

and the shear rate conversion at steady state is (from equation (7))

$$\dot{\gamma} = \frac{2\Omega}{d \ln M / d \ln \Omega} \quad (18)$$

where  $d \ln M / d \ln \Omega$  is computed from the measured torque-speed curve for the sample under study.

Fabrication of the vanes by 3D printing enabled us to explore various vane designs, and to validate these expressions against experiments. We showed these equations to give accurate data within 3% of reference data for sparse, 4-arm vanes through dense, 24-arm fractal vanes. Stress conversion factors derived for an  $N$ -arm straight-armed vane accurately convert measurements even from a fractal structure with  $N$  circumferential points; this is due to the presence of the yield stress, which “cloaks” or hides the internal structure of the vane from the yielded region [137], so that only the number of outer contact edges, and not the internal structure of the vane, affects the yield profile (**Figure 3.4-1a**). The remainder of the fluid plug trapped between the  $N$  arms rotates with the vane as a rigid body.

Moreover, vanes made by 3D printing of photopolymer are inexpensive, disposable, and chemically compatible with a wide range of solvents. The total runout of the vanes was measured to be 0.4-0.7 mm at the lower tip of the vane after fitting the printed vanes with an M4 nut as a threaded insert, and without any other post-processing. The printable rheometer coupling is readily adaptable to future design innovations and other rheometer-mounting systems. Such concepts may include designs to minimize moments of inertia, to fit various rheometer and cup geometries, to sharpen or taper the lower surface of each vane arm for easier insertion into soft solids, and to adjust texture, compliance, or porosity for tailoring of specific measurement needs.

We have shown that vanes with consistent, reliable dimensions can be manufactured using a commercially-available desktop 3D printer, yet when using a new 3D printer or a new print material it is always prudent to re-evaluate the chemical compatibility and dimensional accuracy of each printed vane. This can be done using standard alignment calibration fixtures, or by making measurements using a viscous Newtonian calibration oil and comparing these measurements to reference standards, as we have shown in **Figure 3.6-1**.

The average value of the wall shear stress acting on the sample has to be computed from the measured torque, which depends on the (unknown) constitutive model describing the test sample, and so there is unlikely to be a singular “best” vane design for best



measurement of all materials. As we and previous researchers have found, viscous Newtonian fluids are more sensitive to internal structural details of the vane which can enhance or inhibit recirculation, whereas yield stress fluids are more sensitive to the number of outer contact edges  $N$ . As a result, in this chapter we have considered in detail two key design features; (i) the stress field homogeneity, as shown in **Figure 3.3-1** and Appendix A, and (ii) the total displaced material as described by the occluded area fraction (OAF), discussed in Appendix C. A schematic representation of the general design tradeoffs we have considered in this chapter are summarized in **Figure 3.7-1**, together with a qualitative graphical indication (on a sliding scale) of how effective different designs are at addressing each tradeoff.

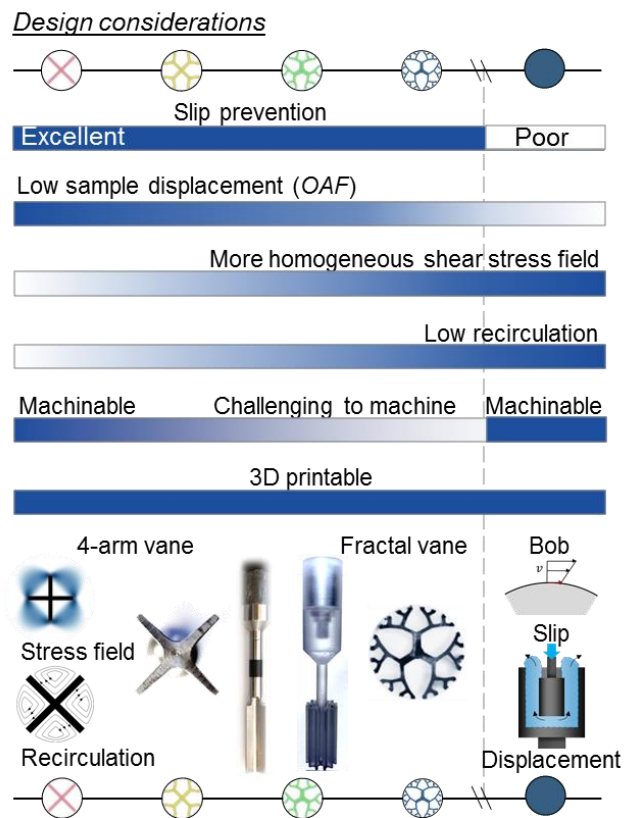


**Figure 3.7-1.** Competing factors affect choice of the rheometric test fixture, *i.e.*, vane, bob, or an intermediate structure. Relative merits are shown with a graded performance scale from excellent (blue) to poor (white). General design criteria include slip mitigation, consideration of sample volume displaced by the vanes, stress homogeneity, recirculation of fluid, and manufacturability. Schematics of these main sources of error for 4-arm vanes and cylindrical bobs are shown above, together with photographs of the 4-arm and 24-arm vanes.

Three-dimensional printing allows us to rapidly explore and screen the performance of a variety of geometric designs. We have found that multipoint fractal designs such as the  $N=12$  and  $N=24$  designs shown in **Figure 3.4-1** and **Figure 3.7-1** provide excellent compromises balancing stress homogeneity, low occluded area fraction, and minimal slip artifacts. In addition, our proposed torque-to-stress conversion equation (equation (12)) performs well for a wide range of geometric designs incorporating the role of end-effects and an arbitrary number of arms. This equation, combined with the considerations summarized in **Figure 3.7-1**, allow researchers to identify a bespoke design that addresses specific needs, and tune their own 3D-printed geometries to the specific rheology of the material of interest.

### 3.8. Appendix

#### 3.8.1. Full field stress distribution around $N$ -bladed vane

In 1992, C. Atkinson and colleagues analytically calculated the complete two-dimensional stress field around an infinitely long vane with  $N$  infinitely thin straight arms drawn from the center to the perimeter of a circle of radius  $R = 1$  using the Wiener-Hopf method of solid mechanics [102]. We apply their results here. In particular, for the case of plane strain, the shear stress is

$$\sigma_{r\theta} = \frac{a_{ns}}{\sqrt{\xi}} \left[ \frac{1}{4} \sin\left(\frac{\varphi}{2}\right) \sin(\varphi) \right] \quad (\text{A1})$$

Here, the coordinate system is a local polar coordinate system with origin at the vane tip and  $\varphi = 0$  aligned outwards along the thin straight arm with radius  $\xi$  as shown in **Figure 3.8-1**. The prefactor is

$$a_{ns} = \frac{\mu\Omega\sqrt{\alpha/\pi}}{\exp(I/\pi)} \quad (\text{A2})$$

Here,  $\alpha = 2\pi/N$  is the angle between each vane arm, and the integral  $I$  is given by

$$I = \int_0^\infty \left( \frac{\log[1+x \sin(\alpha) \operatorname{cosech}(ax)]}{1+x^2} \right) dx \quad (\text{A3})$$

Equation (A2) gives an appropriate viscous scaling for the stress and in **Figure 3.8-1** we plot contours of  $|\sigma_{r\theta}/\mu\Omega|$  computed from equations (A1-A3).

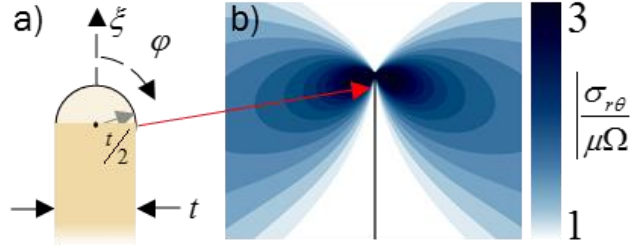


**Figure 3.8-1.** Coordinate system of  $(\xi, \varphi)$  used here for a vane of thickness  $t \ll R_v$ . (b) An example of the local dipolar stress field evaluated around a vane tip for a vane with  $N = 4$  arms.

In our calculations, we truncated the expression near the vane tip at  $\xi = t/2$  where  $t$  is the (finite) thickness of an actual vane arm to remove the singularity at  $\xi = 0$ . In addition, as the stress decays slowly in the far field ( $\sigma \propto \xi^{-1/2}$ ), we truncated the effect of one vane tip at a distance  $\xi = 2\pi R_v/Nt$  to include the effect of each blade to the stress around the first neighboring arm but no further. These truncations generate an integrated shear stress that agrees well with the overall torque equation presented in [102].

### 3.8.2. Fractal design

The fractal designs considered here are based on finite Bethe lattices. They can be parametrized by the number of initial branches from the center ( $Z$ ) the number of layers or generations ( $G$ ) and the number of new branches emerging from a single branch with each successive generation (which is always two here).

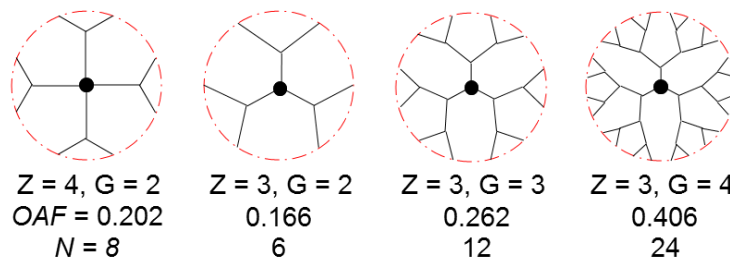


**Figure 3.8-2.** Designs of the fractal vane geometries analyzed here and subsequently 3D printed. (Left) A finite Bethe lattice with  $Z = 4$  central branches and  $G = 2$  generations. (Right) Lattices with 3 center branches and 2, 3, and 4 generations. The occluded area fraction (OAF) defined in equation (13) are labeled for each design. The values of occluded area fraction are calculated assuming a constant vane thickness of  $t = 0.13R_v$ .

In addition, the radius ratio of the generations of each subsequent layer can be optimized to minimize the total length of the vane arms. Here,  $\beta = r_{i+1}/r_i$  where  $r$  as the radius of

layer  $i$  and  $\beta \geq 1$ . If  $\beta = 1$ , we can recover a version of the ribbed cylinder. If  $\beta \rightarrow \infty$ , we can recover the straight-armed vane.

### 3.8.3. Occluded Area Fraction (OAF) of a vane

For a vane with  $N$  straight arms of constant thickness  $t$  radiating from the center point, the total occluded area is approximately

$$A = NRt. \quad (C1)$$

Even for thin vane arms with  $t \ll R_v$ , if  $Nt$  is large, a circular core of the structure is solid to a radius  $R_1 = Nt/2\pi$ , and the occluded area is

$$A = \pi R_1^2 + N(R - R_1)t. \quad (C2)$$

Another possible shape is a ribbed cylinder as sketched in **Figure 3.4-1(d)**. For this structure,  $Z$  branches extend from the central point to  $N$  equally spaced points along the outer perimeter connected by chords. The filled area is minimized by drawing a regular polyhedron with  $N$  sides between outer points, connected by one line to the base. The area of that structure is

$$A = Rt[2(N - Z) \sin(\pi/N) + Z]. \quad (C3)$$

For a more general geometry, we employ a Steiner tree algorithm implemented in freely distributed software called GeoSteiner 5.1 [130]. This calculates the global minimum path connecting a series of inputted points by allowing the insertion of additional ‘‘Steiner points’’ along with the input points, which can generate a shorter fully-connected graph than similar problems such as variations on the Traveling Salesman Problem. In this case, the input points are  $N$  points evenly spaced around a circle of radius  $R = 1$  and one point in the center. The resulting designs are shown in **Figure 3.8-3**.

We can compare and contrast the different designs presented in **Figure 3.8-2** and **Figure 3.8-3** by calculating the occluded area fraction (OAF) and plotting this against the number of arms as shown in **Figure 3.8-4**.

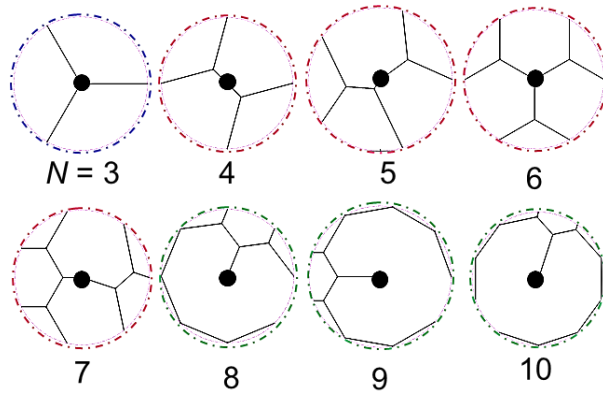


**Figure 3.8-3.** Optimal shapes connecting a center point to  $N$  equidistant points on the outside of a circle (solved for using a Steiner Tree algorithm [130]).

For low values of  $N < \pi + 1$ , the OAF of the optimal Steiner tree is most similar to values obtained for vanes with straight radial arms (eg  $N = 3$ , shown in **Figure 3.8-3**). For  $\pi + 1 < N < 2\pi + 1$ , the Steiner tree structure is more fractal-like and has additional branching in the inner spaces of the circle (**Figure 3.8-3** for  $4 \leq N \leq 7$ ). For  $N > 2\pi + 1$ , the Steiner tree structure is most consistent with the ribbed cylinder structure ( $Z = 1$ ), with a single connecting support arm extending from the center. Most of the occluded area is located at the perimeter of this design.

It is also clear from **Figure 3.8-4(b)** that regular stereosymmetric finite Bethe lattice designs can closely approximate the results of Steiner optimization. To further illustrate these choices, we show in **Figure 3.8-5** four potential designs of an 8-armed vane with corresponding values of  $OAF$  listed. While the Steiner tree is optimal, a basic fractal and ribbed structure are only 4% more space-filling, and would be considered “good” designs compared to the straight-armed design, which fills 30% more space. In general, if ease of insertion of the vane is a high priority for material tests, all three styles of design are suitable for  $N < 2\pi + 1$ , while one would be limited to ribbed cylinder designs and a subset of fractal designs at higher  $N$ .

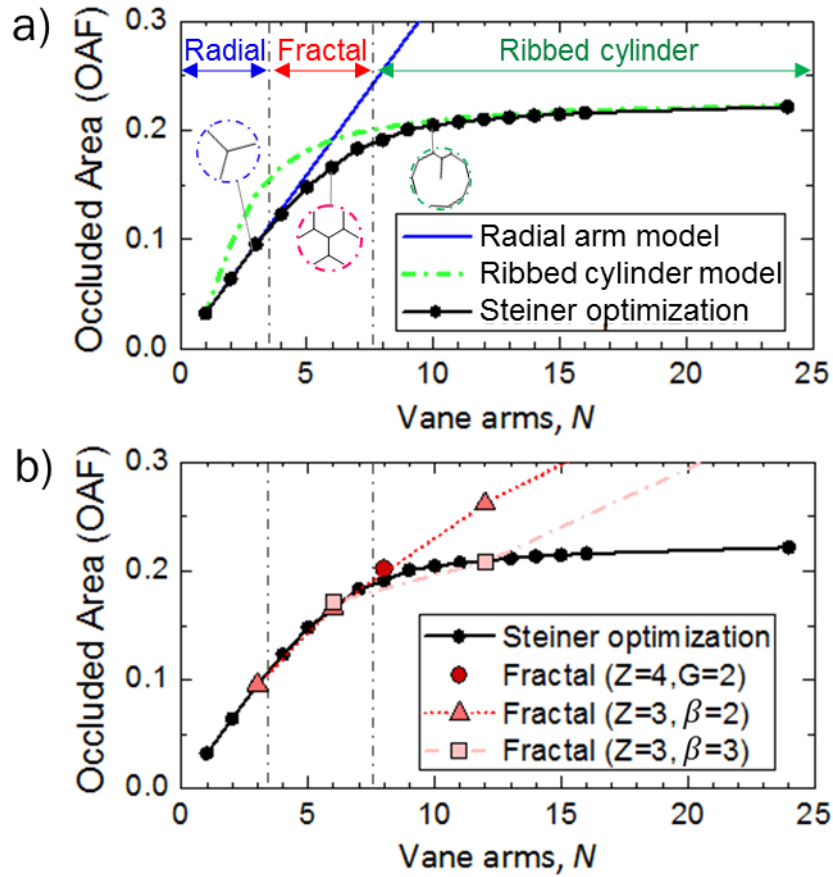


**Figure 3.8-4.** (a) Comparison of the Occluded Area Fraction (OAF) for a series of designs of vanes (see equations C2, C3, and (13) in the main text), versus the number of arms,  $N$ . (b) Comparison of the occluded area for the local optimum shape (as determined by Steiner optimization) as compared to a set of fractal designs such as those shown in **Figure 3.8-2**.

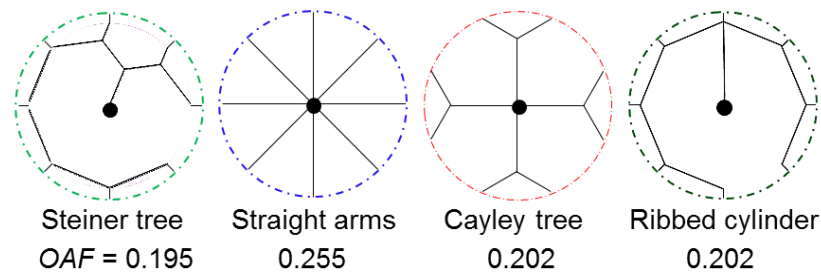


**Figure 3.8-5.** Comparison of four designs of an 8-armed vane using the optimum Steiner tree, straight arms, a fractal structure with  $120^\circ$  angled branches, and a ribbed cylinder. The occluded area fraction (OAF) is calculated for a vane thickness of  $t/R_v = 0.13$ .

However, the occluded area fraction is not the only essential design criterion. The more structured, space-filling fractals are more suitable than the hollow ribbed structures both


for limiting recirculation (by minimizing the distance between any two nearest walls) and for increasing mechanical strength against torsional deformation of the vane features during imposed shearing in stiff materials.

#### 3.8.4. Printing and qualifying a new geometry

Vanes were printed on the Form2 3D printer using Clear v04, Grey v04, White v03 and Black v03 resins from Formlabs, Inc., in an orientation with the vane printing first and the coupling adapter section printing last, without supports (see **Figure 3.5-1c** in the main text). The vanes will have an oblong shape or fail entirely if they are printed at an angle or on their side, due to the nature of stereolithographic printing. The files for the printed vanes are available freely online ([github.com/crystalowens/Printable Vane Tools for Rheometry](https://github.com/crystalowens/Printable_Vane_Tools_for_Rheometry)).

Runout, the eccentricity of rotation of a spindle, is reported here as the diameter of the path traced out by a central axis at the lowest end of the vane. If the runout is zero, the rotation of the vane is perfectly concentric. Runout was measured for a series of threaded inserts or other tapping methods to couple the printed geometry to the rheometer, and results of average runout are summarized in **Figure 3.8-6**. The effect of eccentric rotation is an increase in torque measured by the rheometer, which has been calculated previously [150]. For our vanes with a diameter of  $2R_v = 15$  mm and thickness  $t = 1$  mm, this corresponds to an expected variation in the measured torque that is shown in **Figure 3.8-7**. This is smaller than the typical measurement errors we observed when testing yield stress materials, even for a runout as large as  $\sim 0.5$  mm that is visible by eye.

Coupling type	Runout
Commercial TA vane	0.3 mm
<b>Press-fit nut</b>	<b>0.4-0.7</b>
Tapped plastic	0.9
Press-fit outer hole	1.0
Helicoil	1.3
Brass tapping insert	1.4



**Figure 3.8-6.** Measured runout for six coupling methods or inserts.

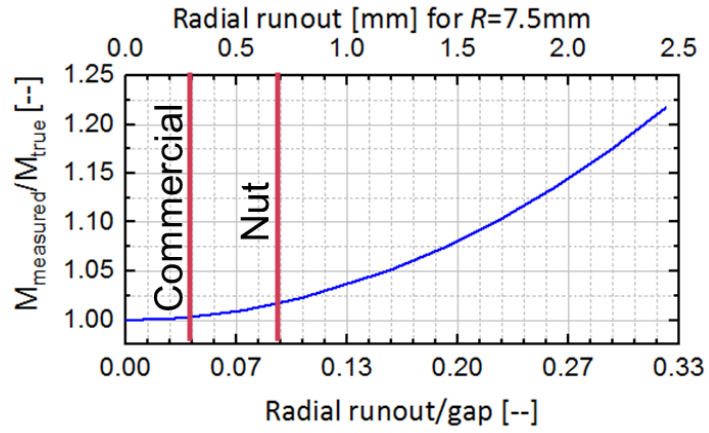


**Figure 3.8-7.** Effect of runout, or eccentricity of rotation of the spindle, on torque measurement, calculated as equation 1C4 in [150]. Lines mark the measured runout for the commercial TA vane and press-fit nut, which give  $\lesssim 2\%$  error in torque.



---

## Chapter 4. On Oreology, the fracture and flow of “milk’s favorite cookie®”

---

### 4.1. Abstract

The mechanical experience of consumption (*i.e.*, feel, softness, texture) of many foods is intrinsic to their enjoyable consumption, one example being the habit of twisting a sandwich cookie to reveal the cream. Scientifically, sandwich cookies present a paradigmatic model of parallel plate rheometry in which a fluid sample, the cream, is held between two parallel plates, the wafers. When the wafers are counter-rotated, the cream deforms, flows, and ultimately fractures, leading to separation of the cookie into two pieces. We introduce *Oreology* (*/ɔːriːˈɒlədʒi/*), from the Nabisco *Oreo* for “cookie” and the Greek *rheologia* for “flow study,” as the study of the flow and fracture of sandwich cookies. Using a laboratory rheometer, we measure failure mechanics of the eponymous Oreo’s ‘creme’ and probe the influence of rotation rate, amount of creme, and flavor on the stress-strain curve and post-mortem creme distribution. Results typically show adhesive failure in which nearly all (95%) creme remains on one wafer after failure, and we ascribe this to the production process, as we confirm that the creme-heavy side is uniformly oriented within most boxes of Oreos. However, cookies in boxes stored under potentially adverse conditions (higher temperature, humidity) show cohesive failure resulting in the creme dividing between wafer halves after failure. Failure mechanics further classify the creme texture as “mushy.” Finally, we introduce and validate the design of an open-source, three-

dimensionally (3D) printed Rheometer powered by rubber bands and coins for encouraging higher-precision home studies to contribute new discoveries to this incipient field of study.

## 4.2. Introduction

Rheology is broadly defined as the study of the flow of materials with complex or non-Newtonian viscosity. Within kitchen-relevant flows, rheology has been used to address diverse challenges in food science[151] in order to rigorously understand and engineer the deformation and flow of these materials at kitchen, lab, and industrial scales. For an accessible introduction to practical rheometry, the reader is referred to A. Ghanbari, et al[152]. Rheology applied to food science (i.e., “food mechanics”) has found applications ranging from understanding the structure of cheese using fractional calculus models[153] and improving the processing of chocolate to more evenly distribute cocoa butter and thereby enhance quality[154] to understanding how flow properties[155] and microstructure[156] influence the perceived texture of a wide range of foods. This area of study more recently has expedited the industrial development of new specialty foods, giving a framework to study the composition and flow of gluten-free batter and breads,[157] modeling the texture of starch thickeners for sauces,[158] and informing the choice of sweeteners used in low-calorie chocolate to create optimal yield stress and “sensory acceptance” of the sweets,[159] as the sensory perception of chocolate is heavily influenced by flow and composition[160].

For materials with multiple ingredients and time-dependent properties, rheological study may be particularly insightful for understanding and tuning the properties. For example, the flow of Swiss cheese fondue may be reliably tuned by adding starch (corn flour) or ethanol (wine)[161], while emulsions like mayonnaise restructure significantly over time after shearing,[15] requiring careful care of their composition and preparation using bulk and interfacial rheology.[162]

While rheology cannot address questions like whether beans belong in chili, or whether a spoon or fork is the more appropriate utensil for mac ‘n cheese, it can describe why larger grains of cereal or larger nuts rise to the top of mixtures when shaken (by granular convection[163]), and quantify useful food descriptors like “creamy,” “mushy,” “slippery,” “rubbery,” and “astringent,” [155], [164] and pinpoint ingredients and length scales that imbue these textures. Fluid mechanics beyond rheology has also been applied to understand and improve food science,[151] including revealing better methods to dip

biscuits into morning tea (horizontally, not vertically) by understanding liquid flow through porous carbohydrate media,[165] showing why microwaving tea is less effective than heating a teapot from below (due to fluid convection)[166], clarifying what causes cold milk droplets to bounce across the surface of hot tea or coffee,[167] and solving how you can carry your nearly-full coffee cup without spilling (i.e., by walking backward)[168], [169]. At the kitchen sink, interfacial fluid mechanics can describe the changing appearance of bubbles as they drain.[170]

Understanding the flow behavior of food ingredients and products has widespread impact on economies of production, public health, and individual diets. Likewise, the experience of consumption (i.e., feel, softness, texture) of many foods is intrinsic to their enjoyable consumption, with one example being the habit of twisting a sandwich cookie apart before eating. In this study, we seek to address this challenge for our everyday trilayer laminate composite, the Oreo cookie. Though unstudied compared to starches, doughs, and condiments, sandwich cookies present a canonical example of parallel plate rheometry, in which a fluid sample (the ‘creme’) is initially fixed between two parallel plates (the wafers). When the wafers are counter-rotated, creme torsionally deforms in shear, flows, and ultimately fractures, leading to separation of two cookie parts (**Figure 4.2-1a-b**). In a cohesive or bulk failure event, the creme itself will flow until it ruptures and will be distributed between the two cookie wafers. In adhesive or interfacial failure, the creme instead delaminates nearly entirely from the wafer-creme interface at one wafer and remains adhered only to the second wafer. In our tests, adhesive failure is most common when manipulating cookies by hand (**Figure 4.2-1c-e**) or laboratory equipment, with some exceptions when some creme appeared to cling to stochastic asperities on the second wafer.

Importantly, the post-mortem creme distribution of sandwich cookies are found to be consistently oriented within a box (**Figure 4.2-1c-e**) for all boxes we tested, as has been suggested before[171]. During the manufacturing process Oreos are constructed by dispensing creme onto a first wafer (which we call Wafer 1), followed by a second wafer (Wafer 2) being placed on top.[172] This difference in initial wafer-creme contact supposedly influences the relative creme-wafer adhesion[171]. Due to the high regularity of manufacturing, this results in the first wafer having a slightly higher level of creme adhesion, and this orientation is preserved when Oreos are placed into the final product box. For instance, in a regular sized box of regular Oreos obtained in Cambridge, MA, Wafer 1 predominantly faces towards the left side when the package text is upright, whereas in a

“family size” box of regular Oreos, Wafer 1 faces to the right side when the package text is upright, both showing 80% of Oreos retaining creme on the wafer facing that preferred side, rather than 50% as would be expected from random chance. We have observed that this in-box preferred orientation varies between flavors and creme “stuff” or creme filling levels, although it is consistent among multiple boxes of a single variety. This challenge prompts the core of our study: to understand the influences of cookie breakage kinematics and inherent cookie properties to control failure stress, failure type, and creme distribution, and ultimately to robustly identify whether Oreos are -- or can be made to be -- “fair,” so that they split creme equally between wafers without bias. To what extent is the result predetermined by manufacturing?

While Oreos are not commonly considered to be a fluid, Oreo creme is a member of the class of flowable soft solids known as “yield stress fluids,” which are fluids that act as soft solids when unperturbed and only flow under a sufficiently large applied stress[122]. Yield stress fluids include a diverse range of important food materials in addition to Oreo creme such as cookie dough, frosting, ice cream, peanut butter, guacamole, and ketchup as well as foams, cosmetics, biological gels, screen-printing and robocasting inks[17], snow and lava[115], drilling muds (e.g., Bentonite dispersions), and concrete and mortar. They also include dry but flowing powder ingredients and granular materials[173], [174], from flour and corn starch to collections of sprinkles, marshmallows, fried rice[175], and fire ants[176]. (We would be curious as well about how the bite-size, edible protein models developed by Baumer, et al[177] would roll down an incline.)

Moreover, the measurement of fluid failure behavior into which sandwich cookie separation can be categorized is a broader topic within rheology. In particular, the study of failure of such amorphous (“glassy”) colloidal soft matter, and particularly stress overshoots and related shear-banding that occur during strain-controlled failure, are an active area of experimentation and simulation within soft glassy rheology to understand the underlying physics[178], [179]. Further, edge fracture is a persistent challenge in parallel plate rheometry wherein normal stress differences build up by application of torsional shearing strain, causing the a fluid meniscus to deform and propagate a radial crack near the outer edge[180], [181], as may happen to initiate the failure of Oreo cookies. While this effect is usually fatal to experimental testing of material properties, it has been productively exploited to rapidly pinch off threads of viscoelastic inks in three-dimensional (3D) printing processes[182], which otherwise leads to stringing defects during printing. In addition,

complex failure mechanisms can occur with torsional failure of thin disks, especially after such edge fracture surfaces have formed[183]. And so, while cookies may be nutritionally lacking, they present an enriching abundance of topics for scientific study.

We introduce Oreology (*/ɔːriːˈɒlədʒi/*), from the Nabisco® Oreo® for “cookie” and the Greek rheo logia for “flow study,” as the study of the flow and fracture of sandwich cookies. We begin this study with a validation (**Figure 4.2-1**) of previously reported[171] suggestions for what causes the creme filling to separate predominantly onto one wafer or the other based on initial orientation within the product packaging. In **Section 4.3**, we present equations to understand creme material deformation, torsional shear strain, and the resulting shear stress in counter-rotated parallel-plate mechanical tests. In **Section 4.4.1** we test Oreos using a laboratory rheometer in a protocol also known as torsional gelometry when applied to cheeses[164]. We monitor the shear stress-shear strain response to observe the characteristic failure response and report key mechanical properties of the creme filling. In **Section 4.4.2**, we investigate how the stress and creme distribution are affected by deformation rate (which mildly influences the resulting stress, indicating viscoelastic behavior), the amount of creme (which is not influential), and the flavor (which is not influential). In **Section 4.4.3**, we map out the spatial dependence of cookie failure orientation in relation to its position within a box. In **Section 4.4.4**, we investigate the observation that occasional boxes of cookies will contain cookies that predominantly all exhibit cohesive rather than adhesive failure of the creme. In **Section 4.4.5**, we explore time-dependent creep of the creme which manifests as “delayed yielding,”[184] under which a constant applied stress causes Oreo creme to flow and break, not immediately but only after long times. In **Section 4.4.6** we follow the degradation of chocolate wafer strength over time following milk imbibition, which causes significant structural loss in the first 30 seconds after contact.

When considering how to enable the broader accessibility of kitchen science, and rheometry overall, we must confront the fact that a laboratory rheometer is not widely accessible. For these reasons, “frugal science” and open-source measurement tools have taken off[185], creating cost-effective research equipment such as origami microscopes[186] wound string-powered centrifuges[187] LEGO-based microfluidic systems[134], microscopes[188], and optical setups[189] and 3D printed tools of many varieties including high-accuracy instrumentation for rheometry[15], [117] and microfluidics[190]. In **Section 4.4.7** we present a 3D-printed torsion testing device designed for Oreos and similarly sized

round objects. We conclude in **Section 4.5** with some ideas for future work and areas of study.

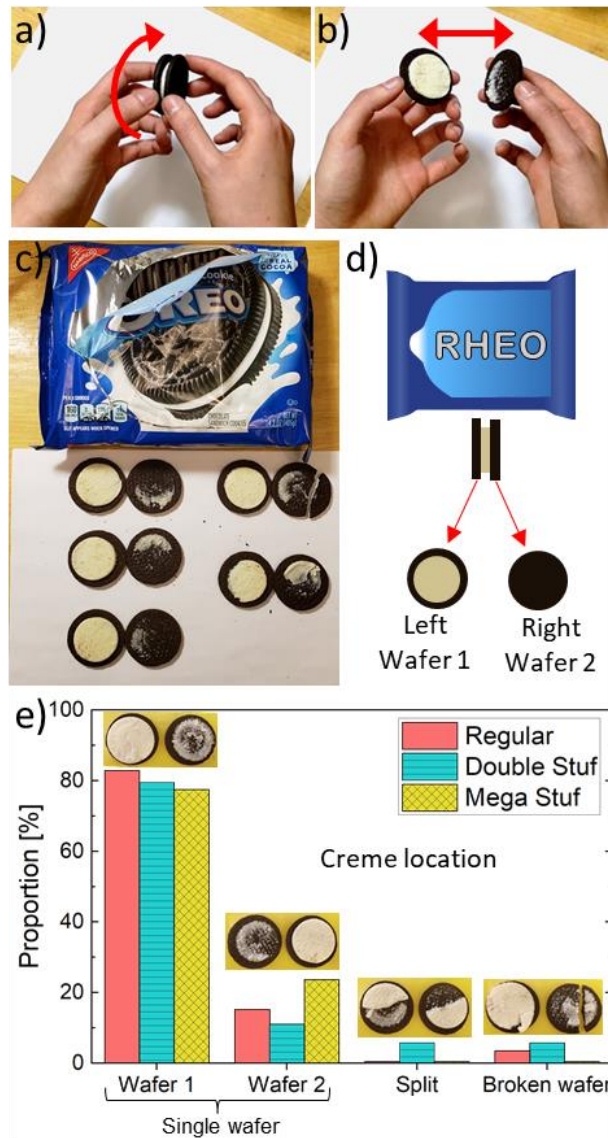


**Figure 4.2-1:** (a) What happens when you twist an Oreo? (b) Eventually it splits into two parts, exposing the creme. (c, d) We observed that in a typical failure profile for Oreos from newly opened boxes, the creme most often tends to remain on one side, “Wafer 1,” with a consistent orientation per box. In this case, Wafer 1 faces to the left side of the upright box for a standard size package of regular Oreos. The creme occasionally splits between sides, often due to defects or small fractures in one or both wafers. (e) This is consistent for cookies with different creme level, with a strong bias towards wafers facing one side of the box rather than the other, facing left for Regular, right for Double, and up for Mega (where rows are oriented vertically rather than horizontally) in standard size packages.

### 4.3. Understanding shear stress and strain in sandwich cookie flow

In laboratory rheometry, a sample fluid is typically placed between two coaxial parallel disks. The lower disk is held fixed while the upper disk is rotated at a constant rotation rate  $\Omega$ . This creates a wall-driven laminar (Couette) flow with internal tangential velocity ranging linearly in height from  $v = 0$  at the fixed lower disk to  $v = r\Omega$  at the upper disk, where  $r$  is the radial position from the center of the disk (**Figure 4.3-1a-c**), and  $z$  is the height above the stationary lower disk. The velocity field in the fluid is thus[127]

$$v_{\theta}(r, z) = \frac{\Omega r z}{H} \quad (1)$$

For sandwich cookies, the analogy is apparent: the wafers are the parallel plates, and the creme is the fluid in between. When one wafer is fixed and the other is rotated, the central cylindrical disk of creme deforms until failure. Through analogy to this parallel plate setup, we calculate the material-level descriptors (shear stress, shear rate, and shear strain) for twisting Oreos, based on measured and applied quantities (torque and angular displacement). The shear rate  $\dot{\gamma}$  arising from the rotation rate  $\Omega$  with creme height  $H$  will be

$$\dot{\gamma}_{rz} = \frac{\partial v_{\theta}}{\partial z} = \frac{\Omega r}{H} \quad (2)$$

which varies from 0 at  $r = 0$  to a maximum value denoted by  $\dot{\gamma}_R$  at  $r = R$ , the creme radius:

$$\dot{\gamma}_R = \frac{\Omega R}{H} \quad (3)$$

The maximum shear strain  $\gamma_R$  arising from the given angular displacement  $\theta$  will be[127]

$$\gamma_R = \frac{\theta R}{H} \quad (4)$$

And the shear stress at the outer perimeter ( $r = R$ ) corresponding to torque  $M$  is

$$\sigma_R = \frac{2M}{\pi R^3} \quad (5)$$

For simplicity of notation, we use  $\gamma$  and  $\sigma$  without subscripts to refer to these quantities, as we only consider the value at  $r = R$  in the following measurements because we focus on failure, which initiates at the location of maximum stress/strain. In fact, due to this non-homogeneous strain, varying as a function of radius, additional corrections have been derived to recover more accurate measurements for large amplitude deformations[191]. For linear elastic materials at low strain (far below yielding), however, we expect the shear stress to be linearly related to the shear strain multiplied by the elastic shear modulus,  $G$ , or

$$\sigma = G\gamma \quad (6)$$

In our analysis, the height  $H$  used in calculations refers to the height of the cream disc alone, even when a rheometer holds wafers as well because the wafers are significantly stiffer than the cream. We found the linear elastic shear modulus,  $G$ , of the wafers to be at least 280 kPa, while the modulus of cream filling is  $\approx 41$  kPa, validating this approximation. Moduli were measured by small amplitude oscillatory shear tests on the rheometer.

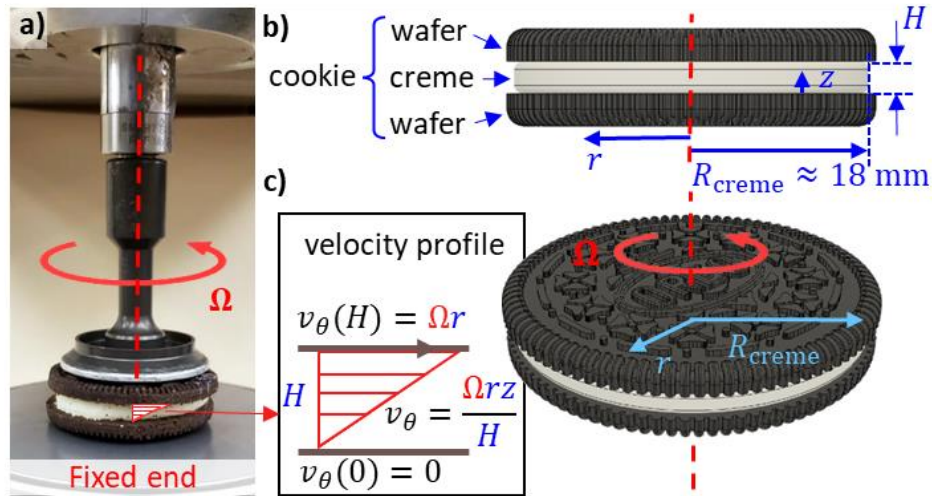


**Figure 4.3-1:** (a) A cookie is mounted for testing on parallel plate fixtures of a laboratory rheometer and adhered to the metal plates by a low-temperature thermoplastic adhesive. (b) The sandwich cookie is a layered composite with two solid wafers enclosing a central cream layer. When one wafer is rotated relative to the other, the creme deforms in torsion. (c) The resulting velocity field within the creme is a function of applied rotation rate, material height, and radius from the center. In this figure, red colors indicate kinematic properties and blue colors indicate geometric properties.



## 4.4. Results

### 4.4.1. Fracture of creme

When the cookie is rotated on the torsional laboratory rheometer (DHR-3; TA Instruments) at a constant speed (here,  $\Omega = 0.1$  rad/s, or about 3.7 rotations per minute), the measured stress shows three mechanical regimes (**Figure 4.4-1**). Initially, **(1)** a linear elastic response occurs, indicating a solid-like response of the creme to the applied strain. The stress-strain curve has an initial slope equal to the elastic shear modulus,  $G$ . Next, **(2)** deviation from linearity indicates material plasticity and onset of irrecoverable yielding, and the stress maximum at the failure stress  $\sigma_f$  and failure strain  $\gamma_f$  mark material failure. Finally, **(3)** structural breakdown of cookie integrity propagates throughout the creme, typically due to creme delamination from Wafer 2, which was affixed to the top rheometer plate for all our studies after identifying the native cookie-preferred orientation in each box by manual tests. Results are shown in **Figure 4.4-1** for several cookies each taken from two separate boxes purchased on separate days (red and black lines, respectively) with the average response ( $n \geq 4$ ) for each shown in bold for clarity. Annotations indicate the failure stress  $\sigma_f$ , failure strain  $\gamma_f$ , and slope corresponding to the linear elastic modulus  $G = \sigma/\gamma$  at low strains, which are also compared in **Figure 4.4-2** showing statistically different failure stress and linear elastic modulus, and statistically similar failure strain between cookies from the two boxes. The corresponding torque required to break open the Oreos in pure rotation is about 0.1 N·m. In comparison, the torque required to open a soda bottle cap is around 2 N·m, and a round doorknob may require 0.6 N·m to turn. Per NASA's human capabilities catalog, humans are able to apply twisting forces up to a range of 1 to 5 N·m using thumb and forefinger grip alone, or up to 15 N·m using full hand grip and forearm rotation[192]. By comparison, sandwich cookies are easy to open.

Within the realm of food science, the range of failure strains exhibited by the Oreo creme is on the brittle end, far below the failure strains of food gum additives and thickeners,[193] and roughly equivalent to the failure strains observed in crumbly Romano or Old Amsterdam variety cheeses[164] or foie gras[156]. The failure stress of the Oreo creme is double that of a typical cream cheese[194] or of peanut butter[195], and of the same magnitude as the failure stress of a soft Havarti or mozzarella cheese, but much less than typical cheeses, and so the creme is relatively soft. The failure stress and strain together

place the Oreo creme within what has been previously identified as the “mushy” texture regime (as opposed to brittle, tough, or rubbery).[164]

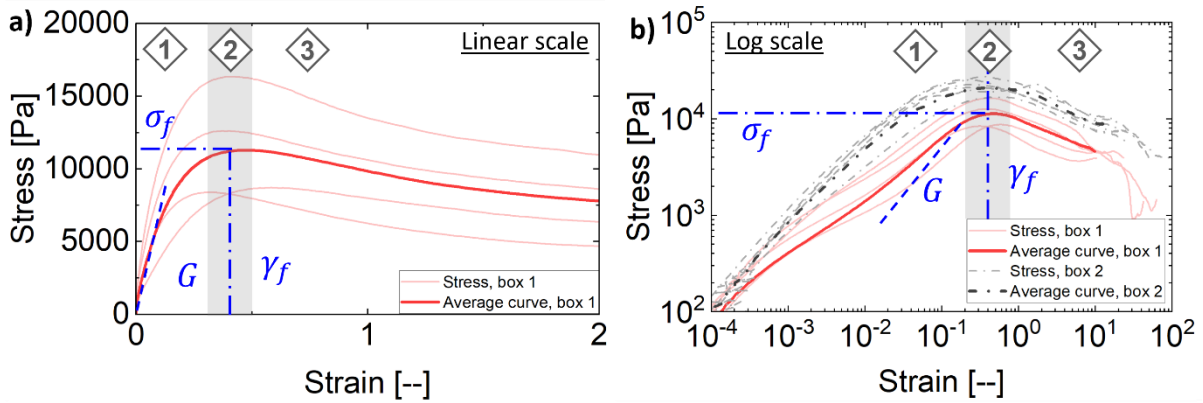


**Figure 4.4-1.** When the cookie is rotated on the rheometer at a constant speed of 0.1 rad/s, the shear stress is measured and plotted (a) on linear axes and (b) on logarithmic axes. The results show three mechanical regimes: (1) a linear elastic response, (2) a stress maximum indicating material plasticity and yielding, and (3) structural breakdown of cookie integrity, typically due to creme delamination from the top wafer (Wafer 2). Results are shown for  $n \geq 4$  repeats of cookies from two separate boxes purchased a week in advance (red solid lines) and the day of the trial (black dash-dotted lines) with the average line for each box shown in bold for clarity. Annotations indicate the failure stress  $\sigma_f$ , failure strain  $\gamma_f$ , and slope corresponding to the linear elastic shear modulus  $G = \sigma/\gamma$  at low strains for the mean red curve.

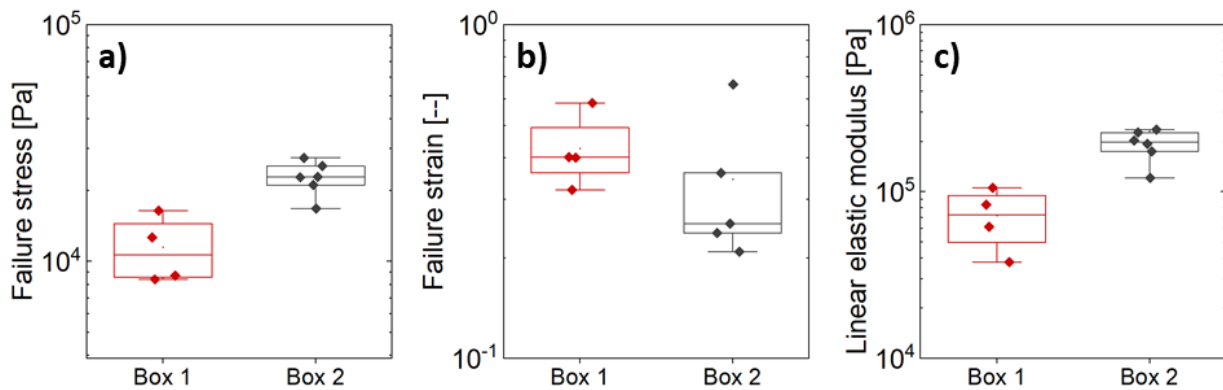


**Figure 4.4-2:** The material mechanics are extracted to compare values between boxes. We use box plots (naturally) to visualize the comparative distributions of (a) failure stress  $\sigma_f$ , (b) failure strain  $\gamma_f$ , and (c) linear elastic shear modulus  $G = \sigma/\gamma$  at low strains. While systematic differences in the measured attributes are visible for all three parameters, only the reported values of failure stress and linear elastic modulus are statistically different ( $p < 0.05$ ) between boxes.

#### 4.4.2. Dependence of fracture on flavor, rotation rate, and creme “stuf” level

Cookie connoisseurs may be prone to slowly or rapidly twisting their sandwich cookies (perhaps based on hunger or anxiety levels). To address the influence of these habits scientifically, in our laboratory rheometer the upper wafers were rotated at a variety of controlled rates ( $\Omega = 0.001$  to  $10$  rad/s, **Figure 4.4-3a,b**). We found that rotation rate influences the failure stress and strain by up to an order of magnitude, so that faster twisting results in higher yield stress and strain. This rate-dependence of the failure stress indicates a viscoelastic response in the creme, because a purely elastic or elasto-plastic failure would have a consistent failure stress at all applied rates. Rotation rate does not, however, influence the creme distribution – except at the highest testable rate which tended to energetically free the creme from both wafers nearly simultaneously, and in some cases to also fracture the wafer (shown in the inset to **Figure 4.4-3b**).

Next, the height of creme filling, or “stuf” level, was found to have only small influences on the failure stress and strain, as shown in **Figure 4.4-3c,d**. It was observed that double stuf cookies were filled to the largest outer radius, and so they required the most torque to separate, with some exceeding the torque limit of the laboratory rheometer ( $M_{max} = 200 \mu N.m$ ) and causing greater uncertainty in these measurements. As has been previously observed, “double” and “more” stuf levels are in fact only about 1.9x and 2.7x more stuf'd with creme by mass than the regular variety[196]. Finally, we analyzed the influence of creme and wafer flavors, comparing Golden, Dark Chocolate, and Team USA triple-stuf Olympic varieties, as shown in **Figure 4.4-3e**. Again, the required stress did not depend on creme/cookie flavor. Meanwhile, the wafer flavor influenced the likelihood of wafers to break. For instance, the Golden variety wafers fragmented during failure tests, causing creme to redistribute based on the wafer failure planes onto segments of both wafers. Two cookies are shown in **Figure 4.4-3f** post-failure (but pre-consumption).

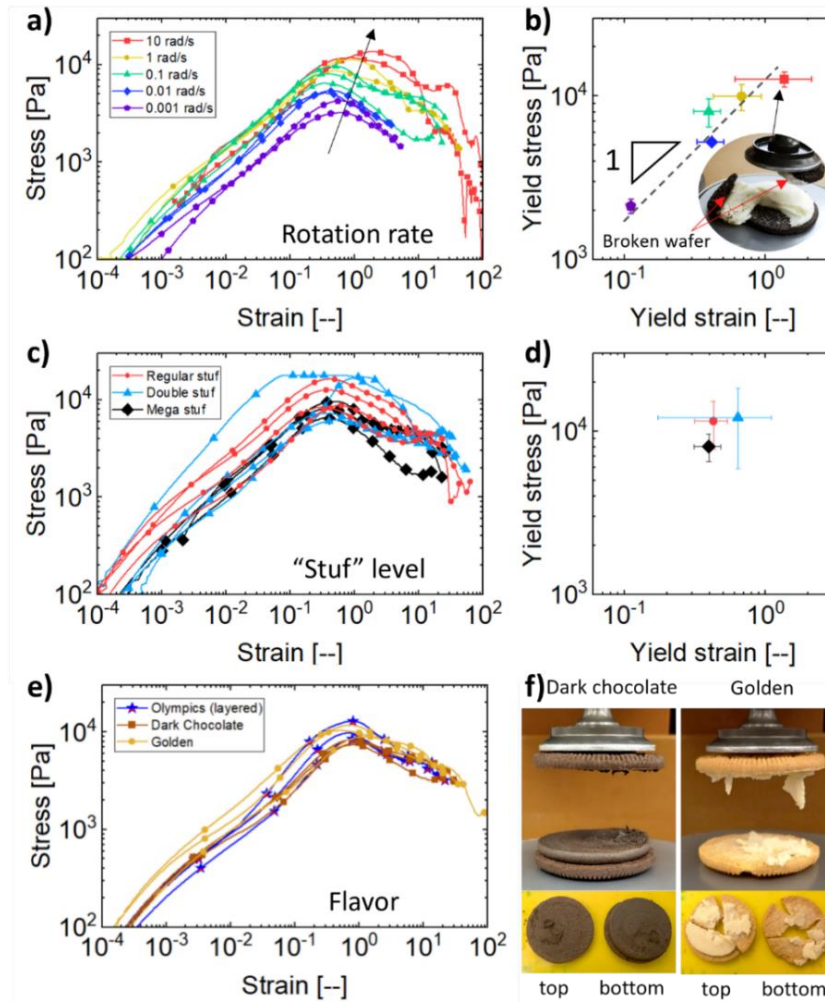


**Figure 4.4-3:** (a, b) Creme failure tests were repeated for different rotation rates, and our tests revealed a rate dependence, with the faster rotation requiring higher stress and strain. At the highest speed only, 10 rad/s (about 370 rotations per minute, as fast as a typical ceiling fan rotates), the wafer tended to break along with the creme, as shown in the inset to b of the cookie post-failure but still mounted on the rheometer. The dashed line indicates a line of slope one relating yield stress to yield strain. (c,d) The “stuf” level or height of creme was not found to influence mechanics of failure or creme distribution, and (e) the Oreo flavor did not influence stress levels, although (f) flavors seemed to influence how likely a wafer was to break, with images shown for one cookie each after twisting for the Dark Chocolate and Golden flavors. For the Golden variety, this wafer breakage was substantial enough to influence creme distribution onto some top-wafer segments and some bottom-wafer segments.

#### 4.4.3. Mapping creme failure in a box

To understand cookie failure types within a full box of Oreos, all cookies were tested while keeping track of original location. In a single, freshly opened box of Family Size

regular Oreos, which contains 3 rows of 16 cookies facing left-right in line with the label text, we found that cookies tend to have broken wafers near the box edges, creme staying on the right-most wafer in cookies on the left side of the box, and creme staying on the left-most wafer in cookies on the righthand side of the box (**Figure 4.4-4**). Here the terms “left” and “right” are oriented such that the package text is upright when the box is viewed from the front. The results show some randomness but average out to show consistent overall trends with several interesting features. The original spatial location of the Oreo in the box contributed a statistically significant impact ( $p < 0.05$ ) on the creme distribution post-failure, with cookies on the left-most edge of the box statistically more likely to be fractured than cookies in other locations, cookies on the left-hand half of the box more likely to fracture with creme entirely on the right-most wafer, and cookies on the right-hand half of the box more likely to fracture with creme entirely on the left-most wafer (**Figure 4.4-4**). Therefore, in addition to the observation that overall creme is most often oriented towards the right for a randomly selected cookie in this type of box, in a competing trend the creme also falls most often on wafers facing inwards into the box and away from the nearest (left or right) edge of the box. This may indicate that environmental impacts (ambient heat or mechanical perturbations) influence the cookies in individual boxes, having greatest influence on cookies near the perimeter. As these influences are uncontrolled by individual consumers, this sensitivity may diminish the predictability of creme failure type and location between different boxes of cookies. No similar trends were observed comparing top-to-bottom distribution among rows rather than columns. How much this distribution changes between different boxes, cookie types, and season or other environmental impacts, and why, may be a topic for future study.

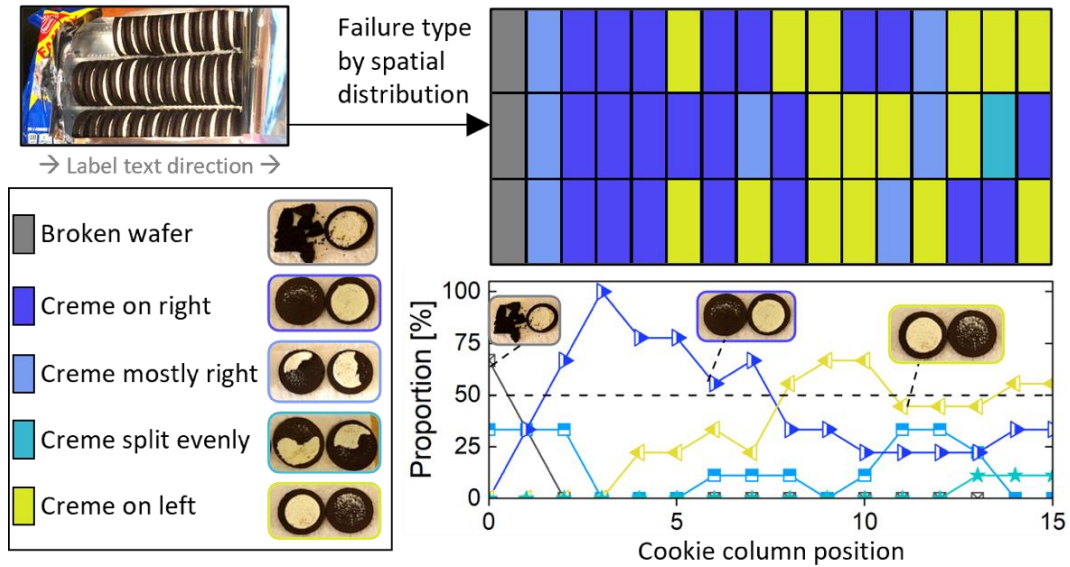


**Figure 4.4-4:** Creme distribution for all cookies mapped within a single box of Oreo cookies shows directional biases within the box, shown as a color map for a box with label text running to the right. Creme overall tends to be on right-facing cookies, but also more likely tends to fall to the left wafer for cookies on the rightmost side of the box. Left and right are oriented such that the package text is upright. The Plotted proportions shown in the lower right figure are calculated for cookie positions averaged over the entire row and neighboring two column positions for the single box, with inset images labelling the most-likely failure type based on position, showing the differences between the left and right halves of the box.

#### 4.4.4. Creme distribution control and predictability

In almost all cases we found cookies in newly obtained boxes to exhibit adhesive failure of the creme. However, after long times of being opened, or for the occasional newly opened box, nearly every cookie in the box split differently, leaving substantial creme on both halves. When this tendency towards cohesive failure was found to occur in a given box, cookies in these boxes tended to have creme filled between wafers to a greater radial extent without having greater total volume, as shown in **Figure 4.4-5a,b**. This suggested that creme had been allowed to flow after initial production, which would alter the creme itself and strengthen the creme-wafer bond enough to allow cohesive creme division. We could not pinpoint the specific reason for this difference, and systematic treatments of heat, humidity, staleness, mechanical agitation, compression, and preshearing only inconsistently recreated this effect. This change may have been due to variations in the

manufacturing process, storage or shipping conditions with hotter temperatures, wafers growing stale, or other effects.

The stress profile measured for different varieties showed a single stress peak denoted  $\sigma_f$  for adhesive failure (**Figure 4.4-5c**). Meanwhile, multiple peaks occur for cohesive failure due to the yield surface dynamically propagating with increasing strain. Because the maximum yield strain occurs at  $r = R$ , inner sections of material at  $r < R$  experience this yield strain at later time points when the top wafer is rotated at a constant angular velocity  $\Omega$ . In the case of cohesive creme separation, the creme failure surface was found to not lie parallel to the wafers but had a distinct “cup and cone” morphology, which would be expected for the failure of a brittle solid material, such as a metal, in torsion. This is because the failure plane for brittle materials is expected to be in the direction of maximum normal stress, which in torsional shear is along a  $45^\circ$  angle from the axis of rotation, thus forming a cone;[197] in contrast, failure would be expected for ductile materials in the direction of maximum shear stress, which in torsion is orthogonal to the axis of rotation. In addition, these cohesively failing Oreos followed the same orientation scheme observed previously; the “cup” side with slightly more creme tended to orient in one particular direction. Creme was distributed by cohesive failure evenly for all rotation rates, yielding 55-73% by mass on the more creme-laden wafer, with the creme division unaffected by the rotation rate, although a few cookies in this type of box would still exhibit adhesive creme failure.

While the fracture surfaces of ductile materials failing in torsion can be modulated by the applied torque, fatigue effects, and simultaneous tensile stresses[197]–[199] (*i.e.*, combined loading, or peeling of an Oreo in addition to simply twisting), this was found to not be tunable for Oreos due to the apparent brittle nature of failure. To confirm this result, using a box of cohesively failing Oreos, we explored the effect of helical twisting profiles for failure. These paired a twist with a vertical push or pull with varying rate combinations of the two steps. No systematic trends were observed on the resulting creme distribution (data not shown). For other brands of cookies with more ductile or “creamier” fillings it is theoretically possible to tune creme distribution by the kinematic profile of cookie twisting alone. It may also be achievable to tune creme distribution yet with Oreo creme at elevated temperatures when creme flows more easily, or through more careful heating and annealing of creme, which has been shown to influence whether colloidal soft matter will

fail via brittle or ductile mechanisms[178]. Though detailed exploration of such tuning is outside the scope of the current study, we performed exploratory experiments with lightly microwaved Oreos to confirm this possibility.

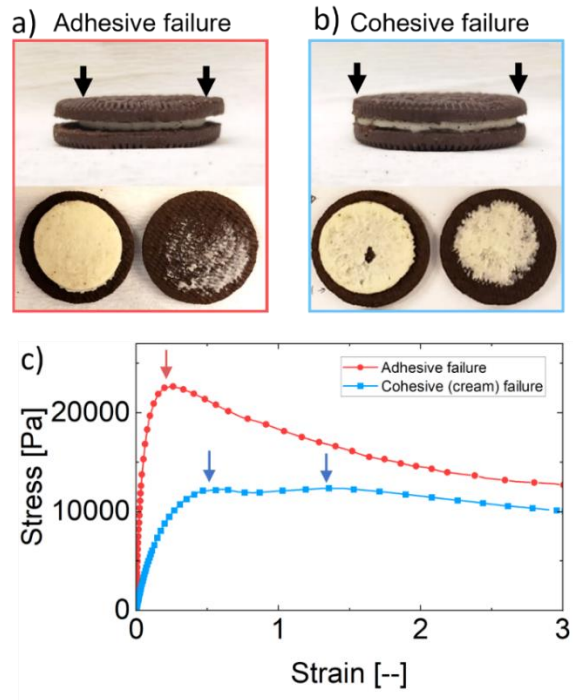


**Figure 4.4-5:** a) While most creme layers failed adhesively in boxes of new cookies, b) cookies exposed to adverse conditions may cause creme to spread from its initial manufactured state, and then cohesive failure was typical for most cookies in the box. These visual signs of changing creme fill levels (indicated by the black arrows in (a) and (b)) are typical but not deterministic predictors of failure mode. c) Failure tests also distinguished between cases in the computed stress-strain curves resulting from the measured torque as a function of imposed rotation angle. There was a single peak stress for adhesive failure, which occurs as a single delamination step, and two or more maxima in stress for cohesively failing creme layers due to the more complex dynamics of cohesive failure propagation along nonplanar surfaces. Cohesive failure was also typically observed to result in a higher failure strain and lower failure stress, as shown here.

#### 4.4.5. Creeping flow causing delayed yielding under constant stress (horeology)

Yield stress fluids typically exhibit time-dependent behavior. This inclusion of time dependence on our Oreos may be considered a venture into a secondary new field, “horeology,” defined as the combination of horology (the study of time) with Oreology, defined previously. To assess how the Oreo creme distribution may change over time, we performed creep experiments with the laboratory rheometer, holding a constant torsional



stress of low, medium, or high values (6.7 kPa, 15.5 kPa, and 19.1 kPa, respectively) relative to the expected yield stress of  $\approx 17$  kPa, with results shown in **Figure 4.4-6**. The creep compliance, or the quotient of the measured angular strain and applied stress, indicates the amount of material flow in response to the applied stress. When a high stress was applied, cookies yielded immediately shown by a sharply increasing compliance, scaling with time squared (and thus is dominated by the acceleration of the upper rheometer fixture, rather than by material behavior). When a low stress was applied, cookies deformed very slightly (*i.e.*, elastically) with some creep behavior emerging at longer times indicated by a change in the power-law slope. At moderate stress, this changing behavior was apparent as a dramatic shift in slope indicating delayed yielding. This phenomenon is also widely seen in creeping solids from mud to mustard[184], [200], and has been implicated as a cause of landslides and avalanches due to sudden catastrophic material flow even under constant applied stress. Further, at elevated temperatures, creep is expected to increase, and this phenomenon may partially explain how creme may spread over time as in **Figure 4.4-5** while wafers remain intact.

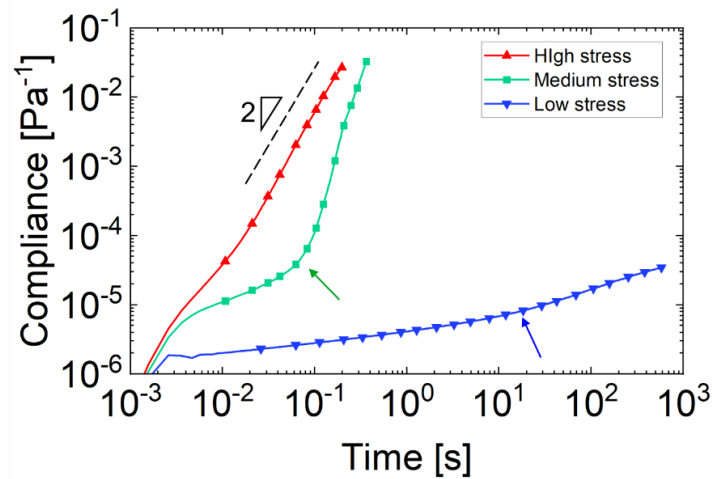


**Figure 4.4-6:** Creme was observed to yield slowly under applied stress in the laboratory rheometer. Low, medium, and high stresses were applied (6.7 kPa, 15.5 kPa, and 19.1 kPa, respectively) and the apparent creep compliance (equal to the measured angular strain  $\gamma(t)$  divided by the constant applied stress) was monitored. For high stresses, the creme immediately yielded, showing an apparent compliance increasing quadratically with time (*i.e.*, due to the inertial acceleration of the rotating rheometer fixture and attached wafer, with negligible resistance from the ruptured creme filling). For medium and low stresses, the creme showed a delayed response indicative of material creep, eventually flowing under medium stress. Arrows indicate approximate locations of slope change.

#### 4.4.6. The influence of milk

Once a cookie has been separated, one is typically left with a wafer with creme and a bare wafer, which may be dipped in milk to enhance final consumption. A wafer in contact with milk will imbibe through wicking of the liquid into its porous structure, which quickly weakens[201]. The laboratory rheometer can sensitively probe the mechanical properties of such material mixtures as they change over time. We affixed a single wafer to our laboratory rheometer using a thin layer of glue to monitor this process. We measured the modulus of the glue to be three times larger than that of the wafer, and the glue layer was under one tenth of the height in total, and so deformation in the glue layer can thus be safely neglected. Low fat (1%) milk was added by pouring around the perimeter of the wafer, and the linear elastic shear modulus was monitored using a small amplitude oscillatory shear test at a small strain ( $\approx 0.1\%$ ). Results show a slight increase in the linear elastic modulus due to swelling, followed by a decrease from an initial value of 560 kPa to a final value of 1 kPa with most change occurring over the first 30 seconds (**Figure 4.4-7**). We connected this mechanical decline with manual experiments in which we dipped a single wafer into 1% milk for five seconds to ensure sufficient takeup of liquid[201] and held it by hand suspended from one point on the rim. In this manual test, the wafer was observed to break under its own weight after an average of 30.2 seconds ( $n = 8$ ) (**Figure 4.4-8**), shown by a dashed vertical line in **Figure 4.4-7**, and corresponding to a loss of mechanics of about 95%. Luckily in a full cookie, sufficient creme remains to hold cookies intact for longer times (an average of 63 seconds,  $n = 6$ , under the same testing protocol), as the (nonporous) creme is not similarly weakened mechanically by the milk. However, the orientation and style of manually dipping a cookie or biscuit into liquid will influence the rate of imbibition and subsequent mechanical collapse, as has been reported before[165]. Though this is beyond the scope of the current study, there is likely a “sweet spot” between immersion time to load the cookie with milk, and consumption time it before loss of integrity. The use of higher-fat milk is expected to lead to a slower uptake of the liquid due to the milk solids clogging pores in the wafer, as has been shown previously for cereal in milk[202], which may make this “sweet spot” easier to find. How the macroscale textured ridges on wafers influence fluid imbibition would also be an interesting area of future study.

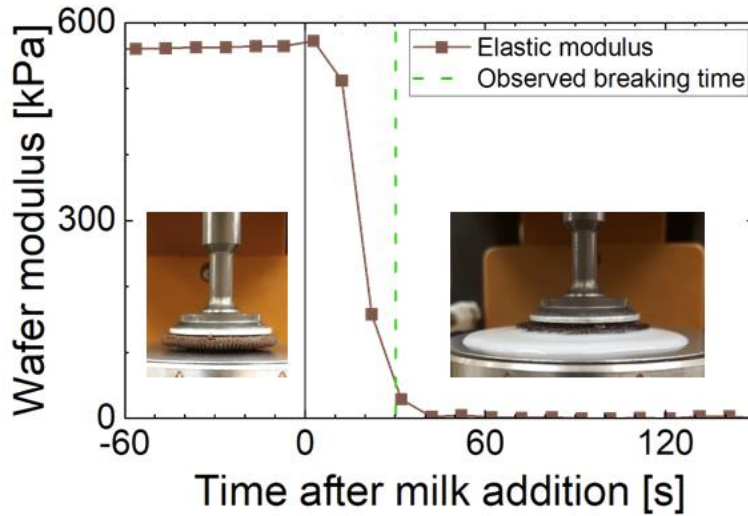


**Figure 4.4-7:** A wafer was mounted on the laboratory rheometer and subjected to milk imbibition at a time  $t = 0$  s. The shear elastic modulus of the wafer dropped to 0.5% of its initial value after 40 s and settled at a new equilibrium static value of 1 kPa. Inset images show the dry wafer on the rheometer at early times and the wafer surrounded by milk at later times.

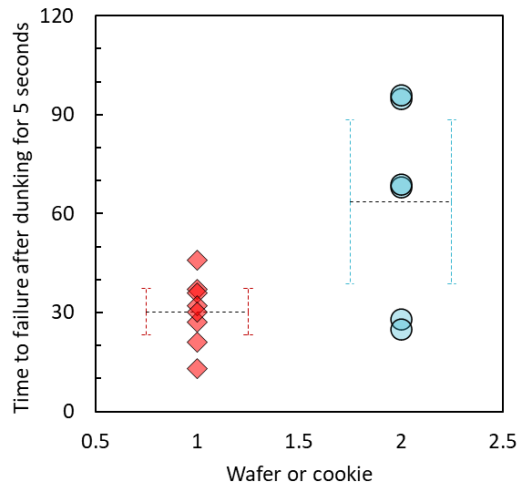


**Figure 4.4-8:** The time to failure of a suspended wafer (1) or full cookie (2) was measured. The mean value for a single wafer was 30.2 seconds ( $n = 8$ ), and for a full cookie was much more variable but a mean of 63 seconds ( $n = 6$ ). The variability is ascribed to differences in milk takeup rate depending on how exactly the cookie is dunked, due to interference from the creme.

#### 4.4.7. Design of the mechanical Oreometer

Explorations of cookie mechanics varying time, rate, and stress using the laboratory rheometer provide a taste of the potential applications of rheology to quantify and thereby

understand flow and fracture of sandwich cookies. To enable further studies beyond the lab, we introduce the Oreometer, which is a 3D-printed torsion testing device designed for Oreos and similarly dimensioned round objects (**Figure 4.4-8**). The device requires no power or electronics and has a material cost of \$6 (including coins and rubber bands), enabling widespread use.

In the Oreometer, cookies are mounted into two rubber-band powered clamps held on a larger fixture. The rubber band pattern adjusts the holding torque on the wafers, as the clamping force tightens when the band is strained by winding around more posts (**Figure 4.4-8c**). For brittle cookies with variable sizes, it was important to find the rubber band configuration that held the wafers securely (*i.e.*, to apply enough torque to complete the measurement) without fracturing wafers due to high clamping forces. Next, pennies (quantity  $N$ ) are loaded into one of two symmetric “penny castles,” applying torque in precise increments (**Figure 4.4-8a4-5, c4-5**). Staggered castle windows, or *balustraria*, in the penny castles have heights equal to five pennies to expedite counting in groups of five. The friction torque in the Oreometer opposing twist of the cookie is overcome by less than one penny’s weight,  $m_{coin}g$ . Torque comes from the applied force  $F$  along the lever arm between the penny castles and center of rotation,  $L = 90$  mm, and the angle  $\theta$  between the lever arm and the force of gravity. The applied torque  $M$  is then

$$M = FL \sin\theta = Nm_{coin}gL \sin\theta \quad (7)$$

Assuming the Oreometer is standing upright without twisting so that  $\theta \approx 90^\circ$  as in **Figure 4.4-8a4**, the applied torsional stress to the cookie inside is then

$$\sigma = \frac{2Nm_{coin}gL}{\pi R^3} \quad (8)$$

The stress calculation does not depend on creme height (which influences only the material strain field, not the stress).

Cookies from both boxes used in **Figure 4.4-1** were tested to failure using the Oreometer, and data were compared to those from the laboratory rheometer. We found that the failure stress measured by the Oreometer is not statistically significantly different ( $p > 0.05$ ) from the set of rheometer data (**Figure 4.4-8b**). Creme distribution results from cookies that were tested to failure on the two devices were also comparable. It was further observed that

cookies left in the Oreometer unyielded but with some torque applied may spontaneously yield after some time without additional coins being added. This is due to the same delayed yielding effect reported in **Figure 4.4-6**.

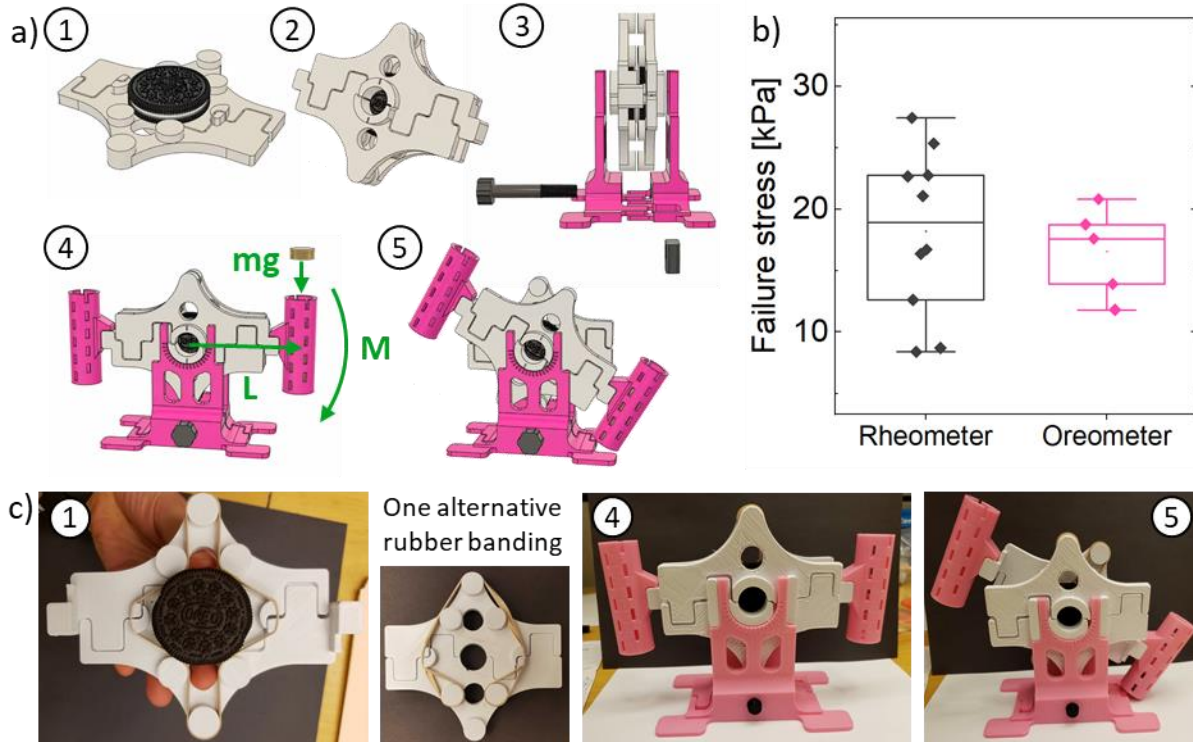


**Figure 4.4-9:** A 3D printed Oreometer is used to perturb cookies with scientific precision by applying a known and controlled torque. a) In this device, (1) the cookie is mounted first into one half and then (2) the second half of the rubber band-powered clamps, which are then (3) placed into the vertical assembly mount. (4) “Penny castles” are mounted on the wings and coins are successively loaded to one side to apply controlled torque until (5) The creme yields. b) Results replicate values measured by the laboratory rheometer. c) Photographs demonstrate the same tool, also including the rubber bands in two different arrangements designed to apply different levels of gripping strength in the clamps.

#### 4.5. Moreology: conclusions and future work

Through a series of experiments with a laboratory rheometer used to hold whole Oreo cookies, we determined that creme distribution upon cookie separation by torsional rotation is not a function of rate of rotation, creme “stuff” (*i.e.*, filling height  $H$ ) level, or flavor, but was mostly determined by the pre-existing level of adhesion between the cookie creme and each wafer. In most cases, creme delaminated from the wafer with a preferential orientation with respect to the package within any one box, allowing prediction of failure

direction around 80%. Despite the consistent failure mode, there was some amount of cookie-to-cookie and box-to-box variation in failure stress and strain. Apparent reflow of creme due to unknown causes had the most significant effect in altering failure type, allowing for improved creme-wafer bond and subsequent cohesive failure of the creme, splitting nearly evenly between the two wafers. Failure mechanics further allowed us to classify the creme texture as “mushy.”

Moreover, questions remain to be explored if we are to fully understand cookie flow phenomena, and for this purpose we have introduced a home-use Oreometer. A topic of particular interest may be what influences the change from adhesive to cohesive failure. If this is due to altering of the creme structure, then one may wish to explore whether it can be affected by compressing cookies before twisting, humidity, temperature, addition of a flow agent, or fracturing wafers before twisting. Other tests could be done with temperature control by using the Oreometer on cookies quickly withdrawn from the fridge, microwaved slightly, or dipped immediately beforehand in milk, where the device can be placed close to the kitchen appliances to minimize transfer time. The mode of failure of cookies may also be investigated manually by peel tests applied at the same time as torsion to study mixed-mode failure. If cookie manufacturers would like to influence creme distribution themselves, providing wafers with through-holes or texture on inner surfaces should promote creme-wafer adhesion onto both halves. Future studies may examine other sandwich-variety cookies, such as other brands of sandwich cookie, custard creams, macarons, and ice cream sandwiches – wherein temperature would be expected to have greater influence – as well as Nutter Butters, peanut butter between crackers, and other savory snacks. Planar shear tests, rather than torsional shear, may probe whether the fruit paste inside Newtons (previously known as Fig Newtons) indeed have the implied Newtonian flow behavior, or whether they are not only sometimes non-fig-containing, but are also rheologically non-Newtonian (and hence may become known as Non-Newton(ian)s). Our results and methods of investigation may also have widespread application in understanding other torsional events in the kitchen, from braided breads and mixing dough to ideal opening kinematics of stubborn jam jar lids. Finally, the development of an Oreology subdivision within the Society of Rheology and the greater Food Mechanics world might be expected as this field of study evolves and expands.

## 4.6. Materials and Methods

### *Rheological measurements*

Rheological behavior was measured using a stress-controlled shear rheometer (DHR-3, TA Instruments) using a parallel plate fixture (40 mm diameter; TA Instruments) at a controlled temperature of 25 °C. The cookies and creme were initialized with a 0.5 N compressive load after loading in the rheometer to ensure a consistent start point, at which point the vertical gap was fixed and the experiment was performed allowing the normal force to vary. Oreos<sup>®</sup> (Nabisco) were obtained from the local grocery store and the wafers were firmly adhered to the plates using thermoplastic adhesive from an “ultra-low temperature” hot glue gun (AdTech, #05690, temperature <100°C). This glue was measured by small amplitude oscillatory shear to have an elastic shear modulus of 1.4 MPa. Cookies with broken wafers were typically not used. Reported modulus, yield stress, and yield strain were extracted from the stress-strain curves, and statistics were performed on these values using an unpaired two-tailed t-test. P-values under 0.05 were considered significant.

### *3D printed Oreometer*

Designs were made in Autodesk Fusion 360 and printed out of PLA using a Creality Ender 3. Parts were sliced with Cura using a 0.3 mm layer height, 20% infill, 210°C extruder temperature, and 55°C bed temperature, and printed with supports for the base halves, Oreo clamps, and penny castles.

---

***Part II:***

***Manufacturing with Carbon Nanotubes***

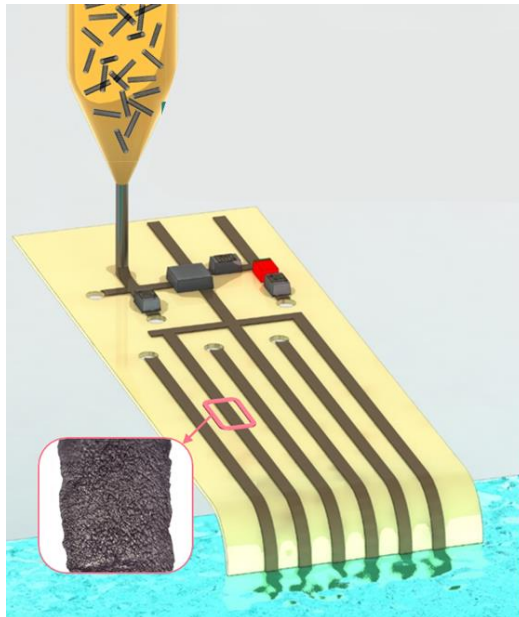
---



---

## Chapter 5. Two-dimensional extrusion additive manufacturing

---



Chapter Introduction Image: Dipping CNT Wicking Sensor into Water

### 5.1. Abstract

Printed electronics rely on the deposition of conductive liquid inks, typically onto polymeric or paper substrates. Among available conductive fillers for use in electronic inks, carbon nanotubes (CNTs) have high conductivity, low density, processability at low temperatures, and intrinsic mechanical flexibility. However, the electrical conductivity of

printed CNT structures has been limited by CNT quality and concentration, and by the need for nonconductive modifiers to make the ink stable and extrudable. This study introduces a polymer-free, printable aqueous CNT ink, and presents the relationships between printing resolution, ink rheology, and ink-substrate interactions. A model is constructed to predict printed feature sizes on impermeable substrates based on Wenzel wetting. Printed lines have conductivity up to 10,000 S/m. The lines are flexible, with < 5% change in DC resistance after 1,000 bending cycles, and <3% change in DC resistance with a bending radius down to 1 mm. Demonstrations focus on (i) conformality, via printing CNTs onto stickers that can be applied to curved surfaces, (ii) interactivity using a CNT-based button printed onto folded paper structure, and (iii) capacitive sensing of liquid wicking into the substrate itself. Facile integration of surface mount components on printed circuits is enabled by the intrinsic adhesion of the wet ink.

## 5.2. Introduction

### 5.2.1. Survey of current applications and inks

Materials that combine mechanical strength, flexibility, and electrical conductivity are key to advances in flexible electronics, robotics, and medical devices. Mainstream approaches to scalable fabrication of electronics in non-wafer formats, such as for flexible displays, smart/RFID labels, and active clothing involve printing of liquid inks with conductive fillers [203]. Typical ink fillers include metal nanoparticles and nanowires, carbon nanotubes (CNTs), graphene (or graphene oxide) sheets, and conductive polymers [204]. The inks are selected for applications based on requirements for conductivity, flexibility, optical transparency, durability, and substrate compatibility.

For these uses, CNTs have advantages including high conductivity, low density, processability at low temperatures, and intrinsic mechanical flexibility. However, high-concentration CNT dispersions are difficult to formulate due to the low dispersibility limit of pure CNTs in almost all liquids, and the need for stabilizers and rheological modifiers, such as polyvinyl alcohol, to create a printable ink. The use of these modifiers inherently limits conductivity and requires post-processing by methods such as rinsing with alcohols [204], acid washing [205], or hot pressing [206].

Cost is also relevant to the production of carbon nanomaterials; however, the base raw material (carbon) is cheap and ubiquitous compared to metals, and CNT synthesis processes increasingly produce greater volume and higher quality carbon nanotubes from

less costly ingredients [207]. In addition, the safety of carbon nanomaterials is a topic with mixed findings that require further study.

CNTs in solution percolate rheologically, or reach a semi-dilute interaction state, at low concentrations, often promoted by depletion-causing surfactants [208]. The formation of this continuous, interacting CNT network influences solution viscosity, processability, and the electrical performance of the final product. High ink concentrations can even generate fluid yield stress behavior [209]. As such, inkjet printing of CNTs has been possible only using dilute CNT dispersions, requiring several layers to generate conductive features [210], [211]. Conversely, a yield stress is beneficial for extrusion-based printing [23], [69], [71], [88], [212]–[215] and screenprinting [216], [217], as well as embedded extrusion printing into a soft matrix [218]. The presence of the yield stress improves feature retention, resolution, and smoothness.

By comparison, printed metal nanoparticles typically have excellent conductivity, yet their low material yield strain (e.g., <0.5% for gold, silver) restricts flexibility of printed metal features. Meanwhile, the use of thinner metal layers to improve flexibility reduces conductivity, mechanical strength, and fatigue resistance. Alternative approaches use more complex manufacturing of wrinkled or pre-folded structures to allow macroscopic flexibility beyond the intrinsic fracture limit of the metal [219]–[221]. Similarly, promising inks made from nanowires, typically silver, show improved flexibility, though the metals remain inherently soft [203]. Metal particles are also prone to oxidation and sedimentation within ink suspensions [204], requiring protective and stabilizing additives, which in turn must be removed after printing, e.g., by sintering at high temperatures. Sintering in turn restricts printing to thermally compatible substrates, and can cause cracking of the metal. For the most stable (i.e., non-oxidizing) metals such as silver and gold, material cost is also of concern.

Moreover, scalable manufacturing of printed electronics demands compatibility with flexible, low-cost substrates [204]. Polymeric films are widely used in roll-to-roll printing of electronics due to their good mechanical properties, and resistance to oxygen and water penetration [204]. Polyimide and polyethylene terephthalate are predominantly used when high temperatures are required during processing such as for sintering of metal inks. Circuitry on paper has also been widely developed [222], such as for microfluidic diagnostics [223] and electrokinetic particle transport [224], disposable RFID tags [225], actuators [226], and sensors for electrochemistry [227]. Paper is readily modified, and clay and

other coatings are commonly used to control ink sorption and fixation, as well as to adjust paper gloss and brightness [228] and to promote adhesion of high-surface tension inks [229].

In this chapter, we describe the production and use of an aqueous CNT-based ink in a direct-write extrusion technique, producing conductive, flexible traces on a variety of impermeable (polymer) and porous (paper) substrates. In **Section 5.4**, we describe a series of aqueous CNT inks having CNT volume fractions up to 2.4% and exhibiting shear thinning, yield stress rheological behavior. In **Section 5.5** we relate process parameters (deposition rate) to feature size and conductivity during extrusion-based printing. In **Section 5.6** we demonstrate the use of process control and percolation behavior to generate CNT traces with conductivity spanning 7 orders of magnitude, including low-concentration traces with a linear density less than  $10^{-3}$  mg CNT/m. In **Section 5.7** we demonstrate CNT printing onto six flexible substrates--glossy paper, hydrophobic paper, vinyl ethylene laminating film, Kapton film, a viscose filter, polyethylene terephthalate, and chromatography paper--and introduce a model to predict the width of features on the impermeable substrates based on the effective Wenzel contact angle. In **Section 5.8** we demonstrate printing of 2D structures with an integrated light-emitting diode, using the ink itself for mechanical adhesion and electrical contact to the circuit. Also, we create an interactive CNT paper button that illuminates an LED, utilizing the low contact resistance of the printed CNTs. Last, we combine a printed CNT capacitive sensor and CNT circuitry on chromatography paper to measure wicking fluid within the substrate itself.

### 5.3. Experimental Methods

#### ***Materials and Preparation of Carbon Nanotube-based Aqueous Ink:***

Carbon nanotube (CNT) inks were prepared to concentrations between 2.4 mg/mL and 7.6 mg/mL of CNTs with sodium deoxycholate (DOC) surfactant to stabilize the suspensions with 2 wt% (20mg DOC / g solvent) for each suspension. The CNTs were tip sonicated for up to 10 hours in water (10 mL) with DOC (0.2 g), adding more CNTs over time (24-76 mg) until the desired concentration was reached. The CNTs used (EC1.5, Meijo, Japan for 2.4 and 5.1 mg/mL) have a mean diameter of 1.5 nm and initial length of 9.4  $\mu$ m [34]. For the lowest concentration ink, 0.06 mg/mL, a low-concentration ink was prepared and then centrifuged for long times, keeping the supernatant. For the highest concentration inks, 7.6 and 18 mg/mL, Tuball (Coat E) (20 mL) was dialyzed in 5-10%wt Dowfax and dialysis tubing was placed in the reservoir and stirred for several days to concentrate the ink, using

the method introduced by Maillaud et al. [33] The final CNT concentration in each ink was determined using the absorbance (550 nm) of serial dilutions of the CNT ink compared to standards of known concentration with the same surfactant concentration, using Beer's Law. Four commercial CNT inks using single-walled CNTs were printed "as-is" alongside our in-house created CNT inks for comparison: CG300 (SWeNT), Coat E (OCSiAl), and Invisicon 3500 and 3400 (Nano-C). For the inks we prepared, CNT concentration,  $c$ , was converted into volume fraction,  $\phi$  by dividing by the CNT mass density,  $\rho_{CNT}$ , using

$$\rho_{CNT} = \frac{4000}{A_s(d + \delta_{vdW})^2} [nd - 2\delta_{vdW} \sum_{i=0}^{n-1} i]$$

where  $A_s = 1315 \text{ m}^2/\text{g}$ ,  $\delta_{vdW} = 0.34 \text{ nm}$ ,  $n$  is the number of walls of the CNT, and  $d$  is the diameter, from [34].

#### *Rheological Measurements:*

Rheological behavior of the inks was measured with a stress-controlled shear rheometer (DHR-3, TA Instruments) using a cone-and-plate fixture (20 mm diameter, 4° cone angle; TA Instruments) with adhesive sandpaper having 10  $\mu\text{m}$  roughness (Trizact A10; 3M) applied to prevent slip of the fluid sample. The shear viscosity was measured by decreasing the shear rate from the maximum to the minimum value to allow the sample to equilibrate. Small amplitude oscillatory shear tests were performed with strain control at  $\hat{\gamma} = 1\%$  strain. Strain amplitude tests were performed at  $\omega = 1 \text{ rad/s}$ , and the subsequent recovery test was performed at  $\omega = 1 \text{ rad/s}$  and  $\hat{\gamma} = 10\%$  strain to obtain a measurable signal while remaining within the regime of small (linear) deformation

#### *2D Printing of CNT Inks*

A 3D printer (MakerGear M2, MakerGear) used a custom syringe displacement system based on a micrometer-resolution single-axis translation stage (PT1, Thorlabs) to print the CNT inks at room temperature. The printer used a 1 mL capacity syringe and sterile blunt-tipped metal needles (Sanants and Nordson). The orifice size of the needles ranged from 0.12 to 0.60 mm inner diameter (30 to 20 gauge). The lateral speed of the printhead ranged from 10 to 3,000 mm/min, and the extrusion flow rate ranged from 0.2  $\mu\text{L/s}$  to 9  $\mu\text{L/s}$ . After printing, samples were left to fully dry in ambient conditions for 20 minutes before further characterization. Substrates used here include regenerated cellulose (10410214, Whatman), chromatography paper (3MM, Whatman), glossy paper (Xerox digital color), hydrophobic

paper (glassine, Cole Palmer), Kapton film (Myjor, 1 mil thickness), polyethylene terephthalate (IVict) and laminating film with heat-sensitive coating (TYH Supplies). Kapton film was roughened with sandpaper (P2000) before printing to promote ink adhesion.

### *Characterization*

Measurements of printed line width were made using an optical microscope (Zeiss SmartZoom 5). Surface roughness was measured using a laser scanning confocal microscope (Keyence VK-X250) and averaged over an area for each substrate. The conductivity of CNT prints was measured using an LCR meter with 4 terminal Kelvin clips (IM3536; Hioki) at room temperature (23-25°C) and ambient humidity (23-52% RH) at least 20 minutes after printing or when lines were visibly dry. Scanning electron micrograph images were taken using a high-resolution SEM (Zeiss Merlin) on printed lines without sputtering or other modification. Linear density was calculated using process parameters, as described in Equation 2.

### *Functional artifacts*

Integrated circuit elements included LEDs that were 20 mA surface-mount units from a reel (Chanzon 0603 SMD LEDs, 1.6 mm x 0.8 mm), a J3Y transistor, and standard 101 and 102 SMD resistors. These were attached manually or using the printer nozzle, using the same wet CNT ink for mechanical adhesion and electrical connection.

## **5.4. Ink and Printing Process Development**

### **5.4.1. Formulation and Rheology of Aqueous CNT Ink**

To begin this study, a variety of CNT inks were produced with volume fractions of  $0.02\% < \varphi < 2.4\%$  CNT stabilized by sodium deoxycholate and Dowfax surfactants, which are known to be highly effective at suspending non-bundled CNTs at relatively high concentrations [31, 32]. Ink preparation involved sonication of CNTs in the water-surfactant mixture, followed by repeated addition of CNTs to increase concentration. Dispersions were centrifuged to remove bundles and impurities. In some cases, CNT concentration was further increased by dialysis as described by Maillaud, et al. [33]. CNTs were used from multiple sources for different inks, but uniformly had high aspect ratios,  $\Lambda = L_{CNT}/d_{CNT} \approx 500-4500$ , as measured previously [34] or reported by the manufacturer. The ink consistency ranges from a liquid to a paste, depending on the concentration. More details can be found in **Section 5.3**. The rheology of the CNT inks is tailored not by using

polymeric fillers, as has been done before to achieve printability [35], but by using higher concentration and higher aspect ratio CNTs to create a fluid with a measurable yield stress. The absence of polymeric fillers or other rheological modifiers enables as-printed features to have high conductivity, without requiring post-processing. In addition, we believe that the yield stress contributes to shelf stability of the inks; we have observed that the inks printed up to two years after initial preparation showed consistent properties after printing, and no phase separation (e.g., no water layer below the solution, or hardened CNT layer on top).

At all concentrations used here, the CNT ink is shear-thinning. Above a threshold CNT concentration of  $\varphi \approx 0.5\%$ , a yield stress develops and increases with concentration, as shown in **Figure 5.4-1a,b**, ranging from 0.05 to 150 Pa with a strong power-law dependence,  $\sigma_y \propto \varphi^{4.0}$ , likely due to the long length of the CNTs [36]. The presence of a yield stress in the CNT suspensions is attributed to the inter-tube interaction of CNTs and the formation of nematic liquid crystalline domains (as shown schematically in **Figure 5.4-1c**), which is a feature of concentrated CNT solutions in various solvents as well as CNT suspensions with dispersing agents. [37–41] This is correlated with higher CNT concentration and length, which are predictors of higher conductivity [37, 38]. To verify this hypothesis, inks were imaged using transmission polarized light microscopy in **Figure 5.4-1d**. The opacity of inks increases with CNT concentration, and at higher concentrations (i.e.,  $\varphi > 0.3\%$ ), the inks become visibly birefringent. An isotropic-to-nematic transition can be expected near  $\varphi = 3.34/\Lambda \approx 0.1\text{--}0.7\%$  using the Onsager transition for rigid rods [34]. By comparison to this percolation threshold, isotropic conductive fillers like carbon black typically percolate electrically at 3 – 15%wt solution, while they do not exhibit liquid crystalline behavior [42, 43].

Upon shearing deformation at large strains,  $\gamma > 40\%$ , mimicking the flow condition of extrusion printing, the CNT inks yield (**Figure 5.4-1e**). All inks restructure quickly and demonstrate no aging, having the storage modulus,  $G^0$ , stable over time (**Figure 5.4-1f**). Videos (available in [17]) taken using transmission polarized light microscopy show similar absence of long-time change, with no visible change in liquid crystalline structure (e.g., coarsening) over time after shearing. Additional rheological measurements showing small amplitude oscillatory shear tests of our CNT inks, and loss modulus data for the large strain amplitude sweep, are included in **Appendix Section 5.11.1**.

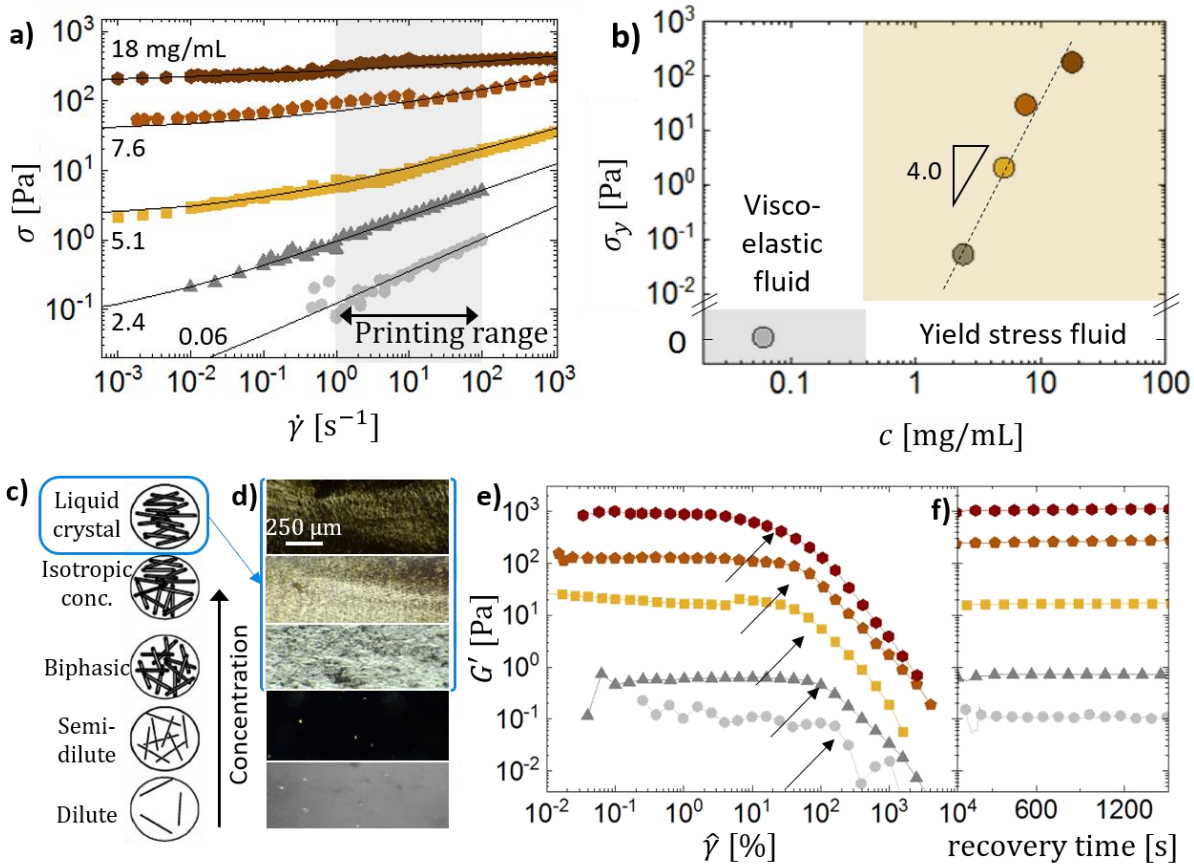


**Figure 5.4-1:** CNT ink formulation and rheology: (a) Flow curves of shear stress versus shear rate for CNT-based aqueous ink at five concentrations spanning  $0.06 < c < 18$  mg CNT per mL or  $0.02\% < \varphi < 2.4\%$  volume fraction, showing shear-thinning behavior and (b) a yield stress increasing sharply with CNT concentration. (c) As CNT concentration increases, CNTs eventually form nematic domains, which are (d) observed using polarized optical microscopy, shown here for five selected inks, in which the highest three concentrations exhibit birefringence. (e) As CNT inks are deformed under large strain amplitude,  $\hat{\gamma} < 30\%$ , the elastic modulus collapses. (f) Upon cessation of shearing, the elastic modulus reaches a steady value within seconds and maintains a stable value over hundreds of seconds.

Ink formulation to achieve the yield stress imparted by liquid crystalline behavior is key to its suitability for direct-write extrusion printing. In extrusion-based printing processes, higher yield stresses enable feature retention at smaller scales and allow greater feature complexity [9–11, 13–15]. The measured attributes of our CNT inks are also beneficial for printing by allowing extrusion through small nozzles at practical, low pressures followed by rapid recovery of full strength of the ink, imparting robustness to the printed structures [15].



### 5.5. Direct-Write Extrusion of CNT Ink

Direct-write extrusion of the CNT inks is performed using a modified 3D printer. Briefly, a custom syringe displacement extruder was constructed using a micrometer linear actuator (Thorlabs) and 3D printed components to hold the syringe. The syringe was affixed to the upper rail of a desktop printer (MakerGear M2). The extruder enabled control of the ink volume dispense rate, ranging here from 0.2  $\mu\text{L/s}$  to 9  $\mu\text{L/s}$ . A stainless steel blunt-tipped needle (diameter = 0.12-0.60 mm) is used as the nozzle, and the ink is extruded with a small (0.1 mm) gap between the nozzle tip and the substrate, which in **Figure 5.5-1** is a roughened polyimide/Kapton film (see Methods for more details). After extrusion, the solvent evaporates over 1-10 minutes, leaving solid CNTs.

During printing, ink is extruded using the 2D motion stage to control the nozzle in a digitally prescribed path, as depicted in **Figure 5.5-1a-b**. The concentration of CNTs in the printed features is independently controlled by adjusting the 2D nozzle motion speed,  $v_{nozzle}$ , and the average dispense speed of the ink,  $v_{ink} = 4Q_{ink}/\pi D_0^2$ . Here,  $Q_{ink}$  is the volumetric flow rate of the ink through the nozzle and  $D_0$  is the inner diameter of the nozzle. The nondimensional ink deposition rate,  $v$ , is therefore defined in Equation 1 as:

$$v = \frac{v_{ink}}{v_{nozzle}} \quad (1)$$

Similar process parameters have been used before to understand dimensional control in hydrogels, [44] while  $v$  is defined here to best parametrize the influences of the printing process on geometry and electrical conductivity. A higher deposition rate increases the amount of ink deposited per linear distance, which also systematically increases the printed trace width,  $w$ , normalized as  $w/D_0$ . This scaling is examined by optical microscopy of printed features, and is plotted in **Figure 5.5-1c,d**. As the deposition rate increases, the resulting conductivity,  $\sigma$ , systematically increases as well. To adopt units commonly reported in the textile literature, we calculate the linear density of deposited CNT material in units of tex (mass per length along the axis of the printing trajectory), as in Equation (2).

$$\rho A_c = \frac{Qc}{v_{nozzle}} = cv\pi D_0^2/4 \quad (2)$$

Here, the mass density of printed CNTs is  $\rho$  and  $A_c$  is the cross-sectional area normal to the direction of printing. While neither property can be reliably measured at these size and mass scales, their product is readily calculated from input process parameters. We further

note that we consider only the density and concentration from CNTs, not from residual surfactant. The initial mass concentration of CNTs in the liquid ink is  $c$ . The DC linear conductance,  $\sigma A_c$ , is defined as

$$\sigma A_c = L/R \quad (3)$$

where  $R$  is the resistance measured by a four-terminal electrical probe, and  $L$  is the length of this line trace that the resistance is measured across. In this case, linear conductivity,  $\sigma A_c$ , increases proportionally to linear density,  $\rho A_c$  (Figure 5.5-1e) as would be expected for fully percolated (dense) conductive rod-like particles [45]. In addition, even at the lowest deposition rates, corresponding to the highest  $v_{nozzle}$  and shear forces applied on the ink between the nozzle and substrate ( $\dot{\gamma} > 100 \text{ s}^{-1}$ ), alignment of CNTs is not observed. Thus, changes in conductivity are attributed to changes in linear density of the printed CNT traces alone (see Chapter Appendix Figure 5.11-3 and Appendix Section 5.11.2 for details on CNT alignment).

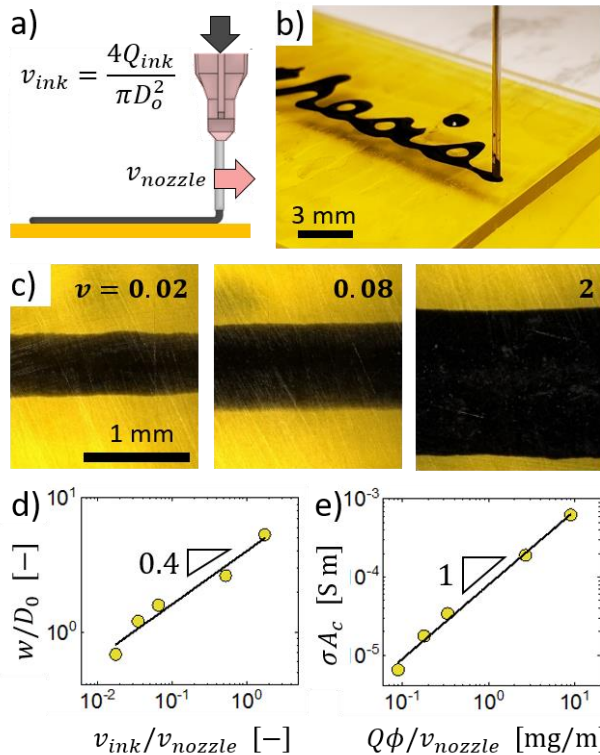


**Figure 5.5-1:** (a) CNT ink is dispensed at an average speed  $v_{ink}$  from a nozzle of inner diameter  $D_0$  moving at a speed  $v_{nozzle}$  over a dry substrate. (b) Photographs of the experimental 3D printer writing cursive text onto a Kapton film. (c,d) As  $v_{ink}/v_{nozzle}$  is increased, the resulting denser deposition of CNTs controllably increases both the dimensionless line width,  $w/D_0$ , and (e) the electrical conductivity of the printed line.

## 5.6. Control of Conductivity During Printing

After printing a CNT feature, the water takes up to 20 minutes to evaporate, depending on the total liquid volume and  $v$ , ultimately removing 95-98% of initial ink volume and leaving a layer of CNTs densified by capillary forces [46]. The conductivity of the printed, dry CNTs may be described by network percolation theory. While the high CNT aspect ratio contributes to a beneficial high yield stress in the liquid ink, it also enables formation of a conductive network at a low CNT loading [42], and thereby enables printed features to span a very wide range ( $\sim 10^7$ -fold) of DC conductivity simply by control of the printing process parameters described above.

To show the percolation scaling, using inks with  $\varphi = 0.02\%$ ,  $0.7\%$ , and  $1\%$ , straight lines were printed onto a porous chromatography paper and the conductivity was measured as shown in **Figure 5.6-1a**. By representing both density and conductivity as products of the cross-sectional area,  $A_c$ , percolation scaling laws can be applied to our data without need to measure  $A_c$  (which is challenging on substrates, e.g., papers, with roughness greater than the thickness of the printed film). Percolation occurs at a linear density of  $(\rho A_c)_{perc} \approx 1.0 \times 10^{-4}$  mg/m. Above this value, the conductivity ( $\sigma A_c$ ) increases quadratically with the linear density ( $\rho A_c$ ), in which the incorporation of additional CNTs increases both the connectivity and the density of the CNT network. At  $\rho A_c \approx 1$  mg/m, the scaling transitioned to a linear relationship  $\sigma A_c \propto (\rho A_c)^1$ , indicating a change in electron transport, after which conductivity increases due to the increase of conductive mass alone. We observe that above this transition, the specific conductivity,  $\sigma/\rho = \sigma A_c/\rho A_c$  is approximately constant. Finally, a lower bound for the conductivity of the CNTs in the network is estimated using the constant of proportionality between  $\sigma A_c \propto \rho A_c$  in **Figure 5.6-1a**, predicting  $\sigma_{CNT} \approx 3,000$  S/m (see **Appendix Section 5.11.3** for full details). This indicates that there remains a large margin of possible improvement in conductivity up to the scale demonstrated for fully-dense and aligned CNT fibers, which is 10.9 MS/m, [47] and the expected conductivity of an individual CNT, which is around 100 MS/m. [48] However, the much lower conductivity of our printed CNT material is expected because of residual surfactant, the higher density of CNT-CNT contacts due to their lower alignment and lower surface area of contact, and the absence of doping, which cumulatively contribute to higher CNT-CNT contact resistance (compared to aligned fibers) as well as lower carrier density within CNTs [49–51] in the sparse isotropically-conductive network.

From these distinctive scaling laws, additional insights into the structure and nature of conductivity in printed CNTs can be made. First, the conductivity of the CNT network is dominated by bulk resistance rather than contact resistance [45], which is an indicator that the stabilizers in the CNT ink are not unduly preventing CNT network formation. Second, the conductivity indicates three-dimensional percolation, showing that the CNT network retains a three-dimensional, foam-like structure [42, 45]. This is likely enabled by the mechanical percolation within the ink resulting in a jammed microstructure and preventing full collapse. Third, as the data for our three inks overlaps, there is again no evidence of large-scale alignment, which would have increased the percolation threshold concentration, and offset the data sets accordingly [42]. These comparisons are also described in more detail in **Appendix Section 5.11.4**.

Microscopic comparison of lines printed with three CNT inks at two deposition rates show key differences in morphology and quality (**Figure 5.6-1b**). Inks with higher CNT concentration and corresponding yield stress result in more narrow lines at equivalent  $v$ , as well as less wavy edges on the printed lines, as also shown in **Figure 5.11-5**. These features may be attributed to the fluid yield stress preventing spreading of printed lines, and to faster drying of more concentrated solutions. In addition, the concentration affects the ability to print continuous lines. At the lowest concentration,  $\varphi = 0.02\%$  only, lines separate into segmented drops at low deposition rates. Higher concentrations of CNTs have been shown to stabilize fluid columns (i.e., via increasing extensional viscosity), slowing such breakup [52]; this allows printing of continuous lines, and may especially aid in high-speed printing of carbon nanotube inks.

We performed identical experiments and analysis using commercial CNT inks. For the same linear density of CNTs, our ink has, on average, 3-fold greater electrical conductivity and percolates at an intermediate concentration. The higher conductivity of our inks is likely due to the long CNT length in our inks, while the use of different surfactants, and CNTs with lower purity (i.e., higher amorphous carbon content) and quality (i.e., crystallinity) likely hinders the conductivity of commercial inks. These results are described more fully in **Appendix Section 5.11.5** and **Figure 5.11-6**.

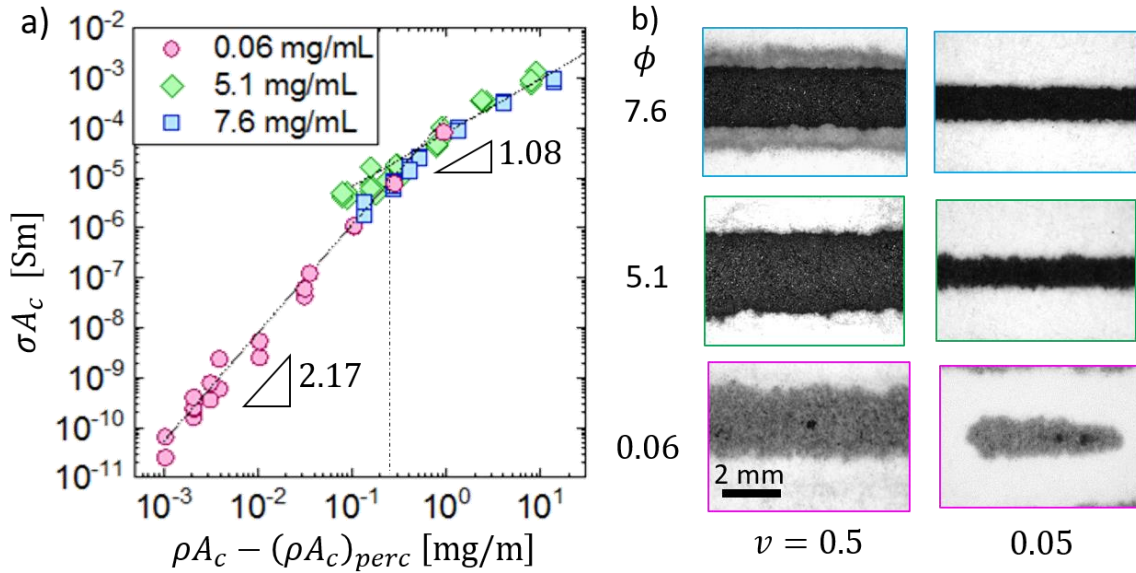


**Figure 5.6-1:** (a) The linear conductivity of printed CNT traces is controlled by the material deposited per area, and varies with a range of  $10^8$  due to percolation effects. (b) Printed lines with CNT inks at different loading show enhanced opacity and increasing line edge smoothness with higher concentration of CNTs and higher  $v_{nozzle}/v_{ink}$ .

### 5.7. Ink-Substrate Interactions for Impermeable Substrates

A wide variety of substrates are useful for printed and flexible electronics, and substrate selection depends on requirements for durability, abrasion resistance, and tolerance to temperature, humidity, and/or chemical exposure [2]. To understand the influence of the substrate on conductivity, feature size, and mechanical flexibility, we print CNTs onto a selection of substrates (**Figure 5.7-1a-b**): glossy paper, hydrophobic paper (glassine), Kapton film, vinyl ethylene-coated film, a viscose filter, polyethylene terephthalate (PET), and chromatography paper. The interaction between the ink and substrate is captured by the contact angle,  $\theta$ , which represents the balance of interfacial energies between liquid ink, solid substrate, and vapor from the ink at the three phase contact line. However, differing surface morphology and texture of the selected substrates has a confounding effect with the contact angle in governing the overall ink-substrate interaction. The texture is captured by the surface roughness,  $r$ , which is defined as the ratio of the true area of the surface solid compared to the normally projected area. In order to condense the menagerie of substrates to a single material parameter, we use Wenzel's law to assemble both terms into an apparent contact angle,  $\theta^*$ , where  $\cos(\theta^*) = r \cos\theta$ . This expression predicts that roughness

amplifies the effect of native surface wetting properties.[53] In **Figure 5.7-1**, we show representative images of lines printed under identical conditions on each substrate including nozzle size (0.6 mm inner diameter), extrusion speed, and printing speed ( $v = 0.5$ ). We also list values of  $\cos(\theta)$  in increasing order from left to right, which transition from  $\cos(\theta) < 1$  for impermeable substrates in **Figure 5.7-1a** to  $\cos(\theta) > 1$  for porous paper in **Figure 5.7-1b**. When  $\cos(\theta) > 1$ , hemi-wicking [54] causes increased lateral flow along the paper, contributing to spreading that is ultimately limited by the deposited fluid volume rather than the contact angle.

Values of  $r$  and  $\theta$  for each substrate are tabulated in Appendix Section 5.11.7.

From this concept of printing, a quasi-static equilibrium model was constructed to predict the width of lines based on the wetting parameter,  $\cos(\theta)$ , and the deposition rate,  $v$ , as depicted in **Figure 5.7-1c** and **Figure 5.11-8**. The Bond number,  $Bo = \rho gh^2/\gamma$ , evaluates the relative influence of gravity and capillary forces on maintaining the droplet shape, where  $g$  is the acceleration due to gravity,  $\rho$  is the mass density of the liquid ink, and  $\gamma$  is the surface tension. When the deposition rate is small, surface tension causes a contraction of the line into a hemicylindrical trace, according to

$$\frac{w}{D_0 \tan \theta^*} = (\pi v)^{1/2}, \quad (4)$$

which we refer to as the “2D droplet model”. This is shown by a schematic inset in **Figure 5.7-1c**. When the deposition rate is large, gravity causes the fluid to spread laterally, as

$$\frac{w}{D_0 \tan \theta^*} = \frac{h}{D_0 \tan(\theta^*)^2} + \frac{\pi v D_0}{4h \tan(\theta^*)}, \quad (5)$$

which we refer to as the “2D puddle model”. Here,  $h$  is set by the balance of gravity and surface tension, as

$$h = \sqrt{\frac{2\gamma(1 - \cos \theta^*)}{\rho g}}. \quad (6)$$

These models are compared to data in **Figure 5.7-1c**. Unreduced data is included in **Figure 5.11-9**. First, we observe that all data within our printable range is within the range of the droplet model due to the small volumes and small dimensions typical for printing. The droplet model adequately predicts the scaling of the printed line widths for all tested substrates and nozzle sizes, with best agreement for intermediate  $0.05 < v < 1$ . In the case

of higher deposition rate, deviations from the model are attributed to more complex effects and solvent evaporation. Further details can be found in **Appendix Section 5.11.8**. We note that the model is generalized to capture the influence of printing our CNT ink onto different non-wicking substrates and to classify or rank these substrates. In addition, the model assumes no specific mechanism of ink application, nor specific details of the CNT ink rheology, but only the deposited volume of ink, the surface tension of the solvent, and the ink contact angle with the substrate. Given this baseline, it should apply more widely to printing of other liquid inks, and maskless printing methods such as inkjet printing that deposit similar relative volumes of ink. This would require further study to understand the influence of wetting across different printing processes.

For a dimensionless deposition rate of  $0.5 < v < 50$  on impermeable substrates, the substrate influences the width of printed lines, but does not influence the conductivity (**Figure 5.11-4**). To understand this more, we compared the morphology of CNT lines on different substrates. In **Figure 5.7-1e**, optical height maps show the surface texture of the hydrophobic paper and chromatography paper before and after printing CNTs. The bare substrates vary in structure and roughness, showing larger voids in the hydrophobic paper and extended cellulose fibers in the chromatography paper. CNT lines printed on both substrates have similar final texture, suggesting that the finer-scale morphology of the printed CNTs is insensitive to the substrate, and hence the conductivity is also insensitive to the substrate. This is similar to results obtained in screen-printing, for which printed layers beyond a critical thickness are no longer influenced by micron-level roughness of the substrate.[55]

As a further exploration, we studied the dynamics of the printing process from extrusion to the fully dried state by monitoring the resistance of the printed trace over time. This is particularly important because even bare CNTs are well-known to have humidity-sensitive resistance.[56–58] Our results showed approximately linear drying rates for each substrate, as is expected for small volumes,[59, 60] and drying times of 1-20 minutes for different substrates and volumes, as shown in **Figure 5.11-10**.

Though not analyzed in detail here, we also observed the influence of the substrate on feature fidelity. In particular, we observed that less rough substrates had better feature fidelity. This was evaluated by low edge tortuosity of printed features, defined as the perimeter length of the line edge normalized by the line length, as shown in **Figure 5.11-12**.

In contrast, rougher substrates increase feature fidelity in inkjet printing when drop impact, contact angle hysteresis, and retraction of the fluid meniscus are also involved. [61]

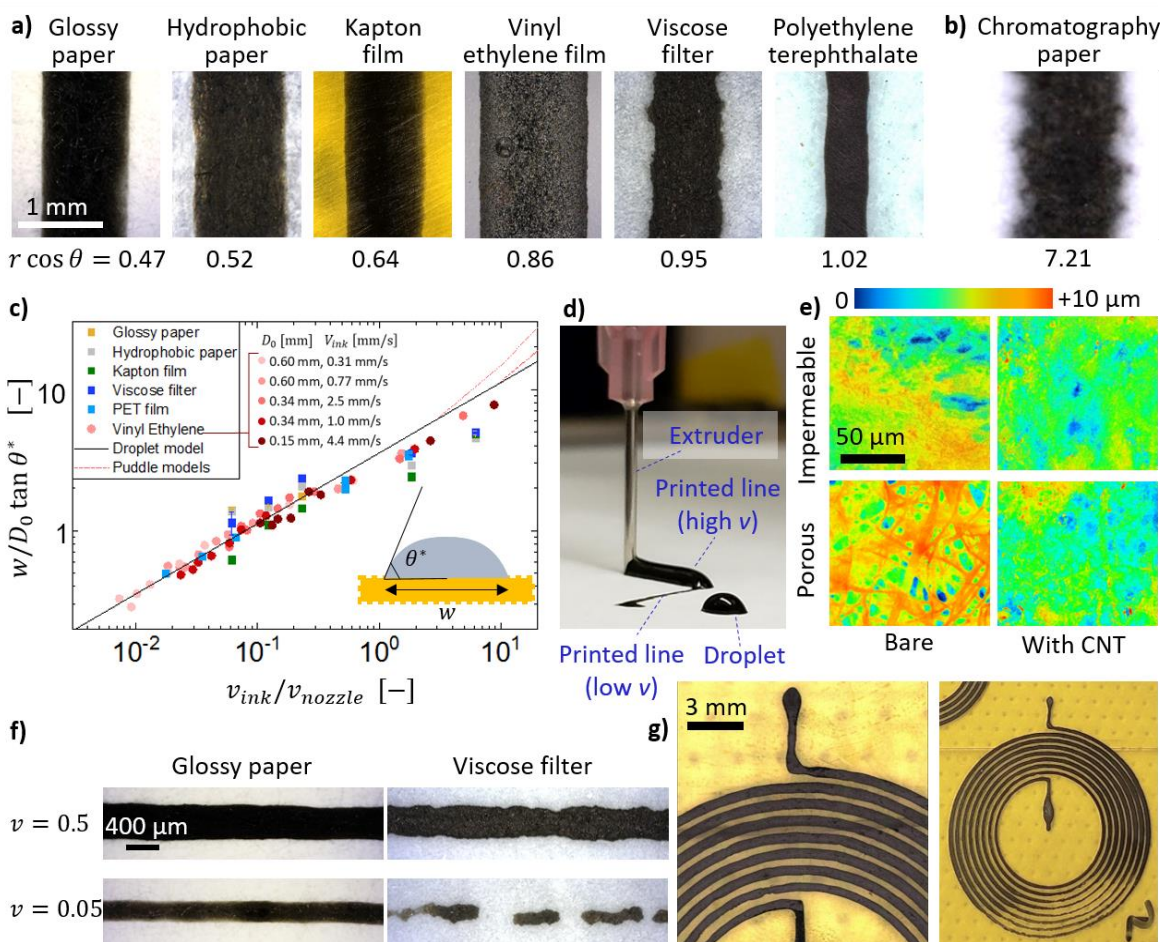


**Figure 5.7-1:** CNT ink printed onto several flexible substrates. (a) Here, we show traces deposited onto six ink-impermeable substrates with different wettabilities  $\cos(\theta) = r \cos \theta$  and (b) one permeable chromatography paper. (c) The (reduced) line width of prints is consistent between substrates and print conditions, in agreement with an equilibrium wetting model balancing surface tension and gravity. The model cross section is shown schematically inset into the figure. (d) During the printing, liquid was initially large in volume for large  $v$ , later drying into a flat layer. When printing at small  $v$ , prints dried almost immediately, forming flat traces. (e) Topographic scans show the overall surface height variations ranging from dark blue (0  $\mu\text{m}$ ) to red (+10  $\mu\text{m}$ ), which are initially different on porous and impermeable bare substrates, but the surface of CNT traces printed on each results in a similar final texture. (f) The effect of wetting on different substrates is a limiting factor at minimum resolution, where the paper substrate, having lower  $\cos(\theta)$ , most readily held ink in place. (g) A spiral with narrow inter-line spacing is printed using  $v = 0.07$  on Kapton film.



In addition, de-wetting of ink from the substrate increases the variation of the width along a line at large scales, impacting feature fidelity, and ultimately limiting minimum feature size. The low wettability of viscose filter paper caused lines to become discontinuous at larger scales on viscose filter compared to the more strongly wetting glossy paper, limiting the minimum width of printed lines (**Figure 5.7-1f**, **Figure 5.11-11a,b**). Similarly, because line edges were smooth when printing onto Kapton film, printed designs could be spaced close together without shorting between them, for instance enabling printing of spiral patterns with a fine gap (see also **Figure 5.11-4g**).

## 5.8. Application of Printed CNTs to Flexible Conductors, Circuits, and Sensors

In the following sections, the fundamental ink formulation and printing process controls introduced above are applied to create functional artifacts on various substrates.

### 5.8.1. Conformal and Extensible Circuit Elements

Conductive traces are useful for delivering power to elements within a circuit, and flexible circuits must do this effectively during bending and twisting deformations. CNTs are known to be piezoresistive when subjected to in-plane strain, [62] and so here we focused on bending deformations, which generate lower material strains and can be applied to a larger variety of substrates. To this end, a CNT trace was printed onto a polyethylene terephthalate film with the name of one of our research laboratories, "mechano synthesis", using  $v = 0.07$ . A gap between words held a blue surface-mount light-emitting diode (LED), which was manually placed onto wet ink immediately after printing so it adhered upon drying, as shown in **Figure 5.8-1a-c**. Using the relationships between material deposition rate and conductivity measured above, the words were designed to have a total resistance of  $450 \pm 15 \Omega$ , allowing the 20 mA LED to be powered by a 9V battery.

We measured the relationship between the bending radius of the substrate and resistance for printed traces with linear density of 0.2-9 mg/m and radii of curvature from 0.02 mm (sharp fold) to 35 mm, corresponding to compressive strains of 1 to 0.002, respectively. Compared to the resistance of traces measured on a flat substrate (of 20 – 1200 $\Omega$ , depending on the linear density), bending the substrate to a radius of  $> 1mm$  show a change in resistance within 3% (**Figure 5.8-1d**). In addition, the conductivity of lines with the highest CNT linear density (9 mg/m) are less sensitive to bend radius even for lower bending radii. To demonstrate this consistent resistance, a sticker with printed CNT text

and a LED was wrapped onto various objects including a glass vial and a fine rod, with radii of curvature of 35 and 1.5 mm, respectively (**Figure 5.8-1eh**). The LED remained illuminated, suggesting compatibility of printed CNTs to conformal electronics that can be printed in a planar configuration and then applied to 3D surfaces.

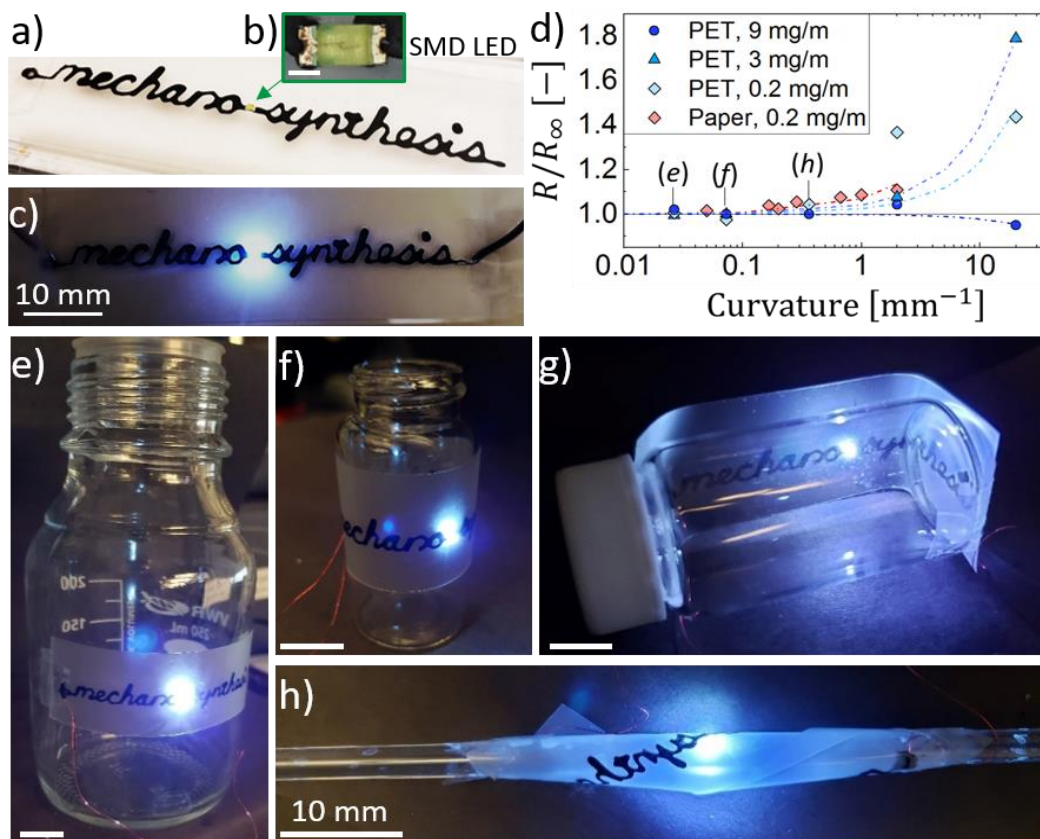


**Figure 5.8-1:** (a) A CNT trace was printed to spell “mechano synthesis” with (b) a blue surface mount diode (1 mm in length) manually placed between words (c) to illuminate when powered. (d) The conductivity of printed traces is constant within 3% when bent at a radius of  $>1$  mm, which is shown by sustained illumination of the diode when wrapping the printed artifact around containers with radii of (e) 35 mm, (f) 13 mm, (g) 1.5 mm, and (h) 2.7 mm. Scale bars in (e-h) are all 10 mm.

### 5.8.2. Interactive Touch Sensor

Based on the percolation results of **Section 5.6**, we judged that printed CNT networks have low contact resistance, which is useful for fabrication of electrical contacts. To understand this further, the contact resistance between printed CNT traces was measured to determine the dependence on CNT linear density and on applied pressure in a single cycle. As shown in **Figure 5.8-2a**, the contact resistance decreases with greater applied

pressure for all paper substrates. For the more compressible chromatography paper, the change is more gradual than for the stiffer glossy paper. In addition, the contact resistance is proportionally larger for lower density CNT prints (**Figure 5.8-2b**). Here, CNT linear density was varied by the CNT volume fraction in the ink,  $\varphi$ , while the dimensionless ink deposition rate,  $v$ , was kept constant so the line width, and contact area, remained constant. Measurements are further described in **Appendix Section 5.11.11**, along with contact behavior over several cycles of applied pressure, which shows no noticeable hysteresis.

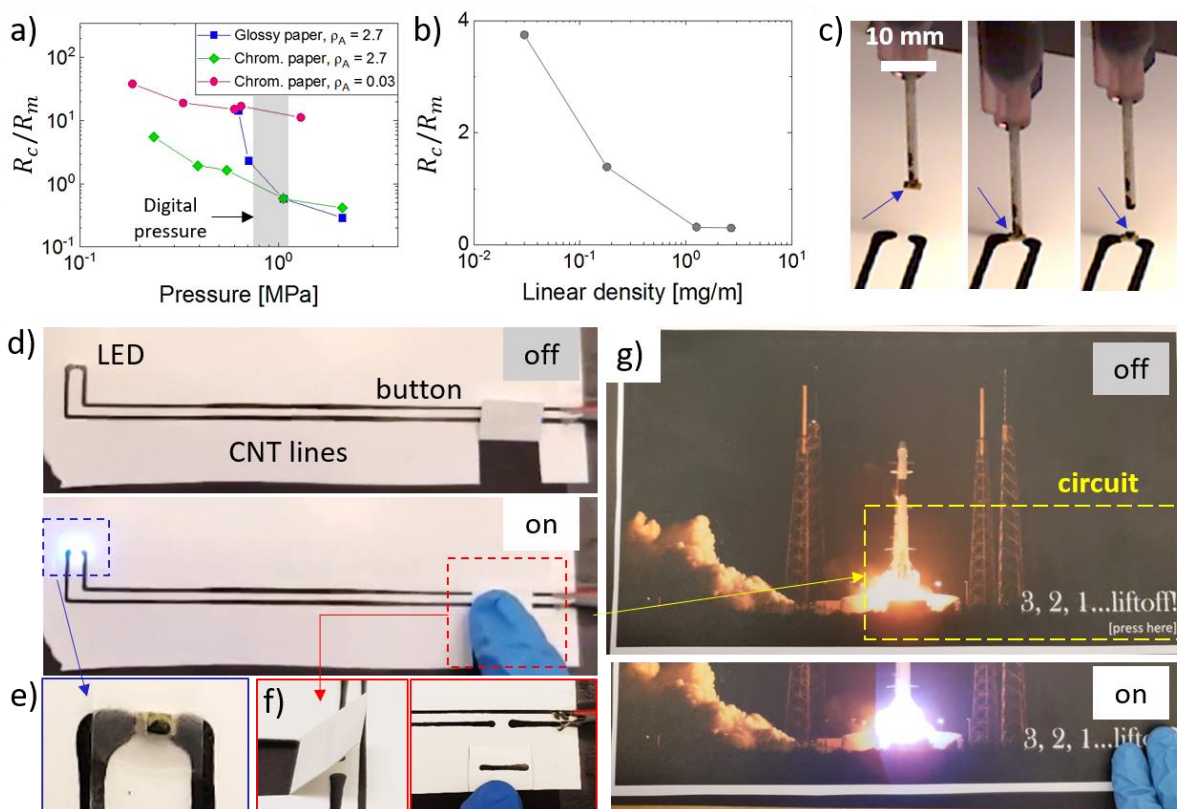


**Figure 5.8-2:** (a) Contact resistance is measured for CNTs printed onto papers as a function of applied pressure at the contact point. Here, contact resistance  $R_c$  is normalized by  $R_m$ , the resistance of the CNT trace for 1 mm of length. (b) The contact resistance normalized by CNT network resistance decreases with printed linear density, indicating improved contact. (c) During printing onto glossy paper, the LED, indicated by the arrow, is placed by the printer at a designed 2 mm break in the printed line, making physical and electrical contact with the still-liquid ink. (d) The overall CNT circuit connected a power source, LED, and button that close the circuit to illuminate the power source. (e) The LED was protected with an adhesive overlayer to prevent detachment and (f) the button is made by a folded paper section holding a discontinuous line segment. (g) This blue LED is used to illuminate an image of a (SpaceX Dragon) rocket blasting off when the button was pressed through an overlaid illustrated page.

Next, we built an interactive CNT-based button activated by contact between two printed CNT traces, inspired by children’s books with interactive elements enabled by embedded electronics. The touch sensor is connected to activate an LED in the circuit, after the user presses the button. During printing, the LED was put in place using the printer nozzle to fill a small, 2 mm break in the printed line, which is shown in **Figure 5.8-2c**. The CNT button uses an additional CNT line printed onto a folded section of paper. When digital (finger) pressure is applied to the button, it closes the circuit to illuminate the LED (**Figure 5.8-2d-f**). When pressure is removed, the folded paper relaxes, breaking the contact and opening the circuit. This button structure is used to create an interactive scene that was illuminated by pressing a location indicated on the page (**Figure 5.8-2g**).

### 5.8.3. A Capacitive Fluid Sensor

Last, we demonstrate the ability to sense fluid motion, leveraging the printing of CNTs onto porous substrates that can imbibe liquid. As such, a device for sensing fluid wicking speed *in situ* or *in papyrus* was fabricated onto chromatography paper by printing a three-part device including (i) a CNT interdigitated capacitive sensor and with circuit elements to (ii) indicate the sensor is receiving power by lighting a red LED, and (iii) amplify the measured signal using a bipolar junction transistor (**Figure 5.8-3a-c**). Printing used  $v = 0.07$  to maintain a high-quality printing range with well-prescribed line thickness. The circuit is designed to change an output voltage signal in response to changing capacitance within the circuit, due to a changing dielectric constant of the spaces between CNT electrodes. The double-sided circuit allows use of a simplified design, and the front and back sides of the circuit are connected by vias constructed by pressing the dispensing needle through the paper. In a second design shown in **Figure 5.8-3f**, the capacitive sensor uses two parallel CNT lines that are on a separate sheet tethered by wire to the base circuit. While performance is similar, this allows for easier reuse of the circuit and ability to place it into smaller confined areas (like an Eppendorf tube).

For both circuits, the height of wicking fluid is measured by recording the sensor output and is verified by video analysis. The wicking followed Washburn’s Law, in which the fluid height  $h \propto \sqrt{t}$  for all tests. [63–65] After calibration, the fluid position and wicking speed are measured by the sensor within 12% (1.0 mm of height) for distilled water and isopropyl alcohol. The printed circuits are reusable once dry.

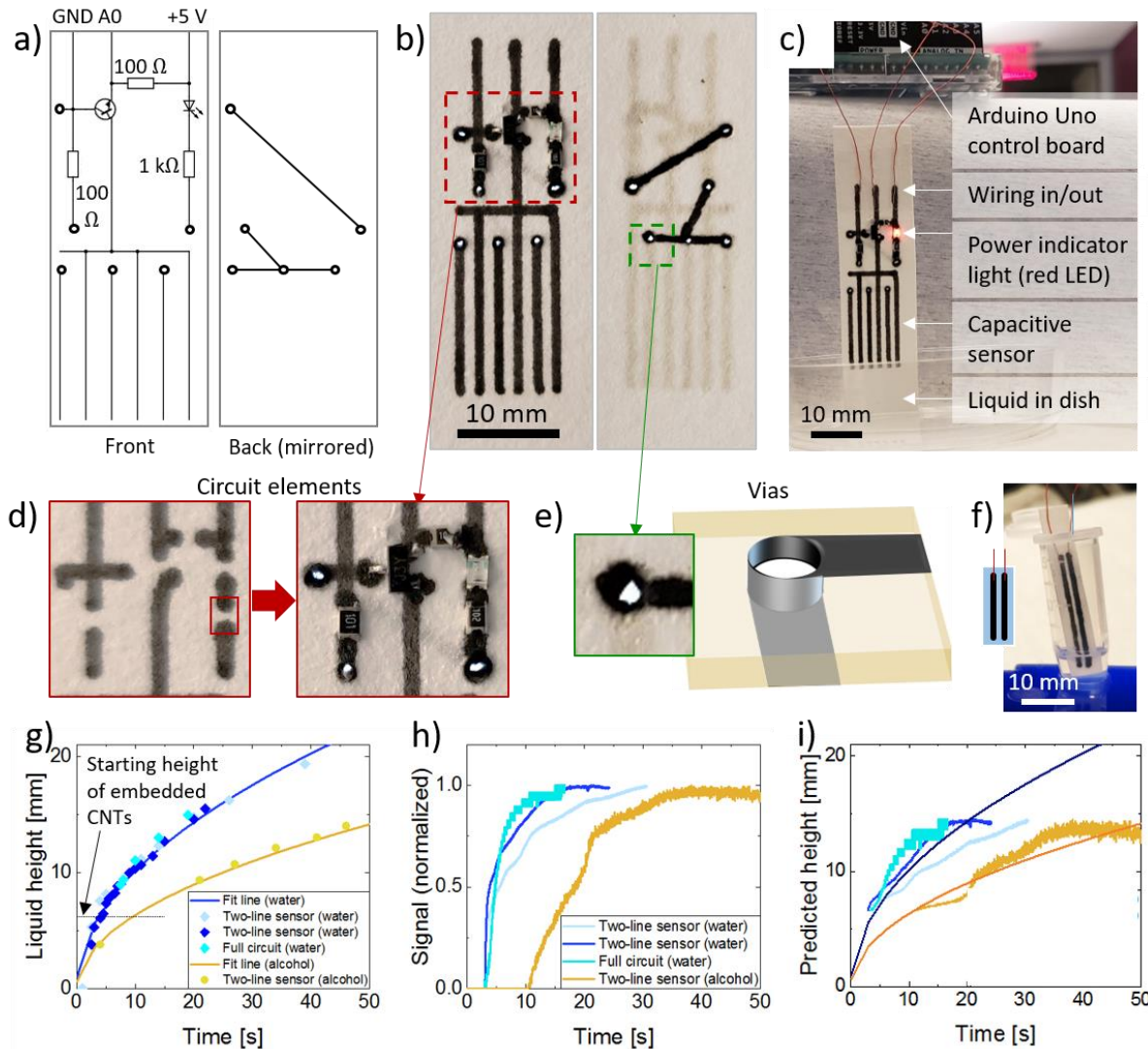


**Figure 5.8-3:** (a-c) A device for sensing fluid wicking speed is fabricated by printing a six-line interdigitated capacitive sensor with a two-sided circuit on a sheet of chromatography paper and (d) directly incorporating circuit elements to amplify the measured signal. (e) The two faces of the circuit are connected by conductive vias. (f) A second version of the circuit uses a two-line capacitive sensor connected by wires to the main circuit. (g) The height of wicking fluid is verified by video analysis, and (h) measured by sensor output. After calibration, (i) the wicking speed is measured within 12% (1 mm of height) for two different fluids (distilled water, isopropyl alcohol).

The capacitive sensor can also be used to interrogate droplet impact. We test this capability by adding droplets of distilled water of different volumes from  $0.2 \mu\text{L}$  to  $2 \mu\text{L}$ , which result in a sharp increase in capacitance within 50 ms of impact, followed by a steady decrease back to the baseline as the droplet spreads and dries (**Figure 5.11-18a**). Both the initial spike and the total area under the response curve vary systematically with the total

volume over the entire tested range (**Figure 5.11-18b**). The sensor can also register addition of sequential droplets, and remains sensitive to the total volume of liquid deposited, whether that volume is added all together or as sequential droplets (**Figure 5.11-18c,d**). Such a sensor could be adapted to measure the influence of droplet impact on various porous substrates, such as face masks or granular beds.

### 5.9. Benchmarking the Conductivity and Flexibility Achieved by Direct-Write CNT Printing

An Ashby-style plot, **Figure 5.9-1**, is used to compare the specific conductivity and the flexibility of the lines printed in this chapter to other materials. Available materials used for producing conductive traces include printable colloidal or nanoparticulate metals [66, 67], metal [68] and carbon nanomaterial [68, 69] foams, bulk carbon nanomaterial-based inks [10, 35, 70–72], and conductive polymers including PEDOT and PEDOT:PSS composites [73–78], filled thermoplastic polyurethanes [79], and zwitterionic polymers [30]. Also compared here are CNT-based fibers made by various spinning processes [80]. Here we only consider homogeneous conducting materials and CNT-based composites.

While the change in resistance with bending angle, and change in resistance after cyclic bending, presented here, are both typical measurements of flexibility and durability, the fine details of the measurements (e.g., bending radius, thickness of substrates and printed features, adhesion) are highly nonstandard and rarely reported in prior literature. In order to compare the flexibility of our printed ink with a spectrum of other printable inks, we compare the elastic compliance, or the inverse of the Young's modulus,  $D = 1/E$ . This compliance, in addition to the thickness of printed wires and substrates, adhesion, and printed geometry, strongly influence the mechanical behavior of flexible printed electronics. A benchmark flexibility is denoted as that of the substrate. When the compliance,  $D$ , of a print is too small/rigid,  $D_{print} < D_{substrate}$ , the printed material will stiffen the entire printed artifact and suffer the brunt of applied mechanical loads, reducing compliance and leading to failures of substrate adhesion.

Here, our printed CNTs exhibit an attractive combination of conductivity and compliance. The specific conductivity and compliance of several printed/printable materials is compared in **Figure 5.9-1**. Vertical bars indicate compliance of two typical substrates for printed electronics: Kapton [81, 82] and paper [83]. Bulk metals and metal features obtained by printing typically have excellent conductivity but low compliance compared to the

substrates, while conductive polymers are generally extremely compliant (and sometimes extensible as well) but have significantly lower conductivity.

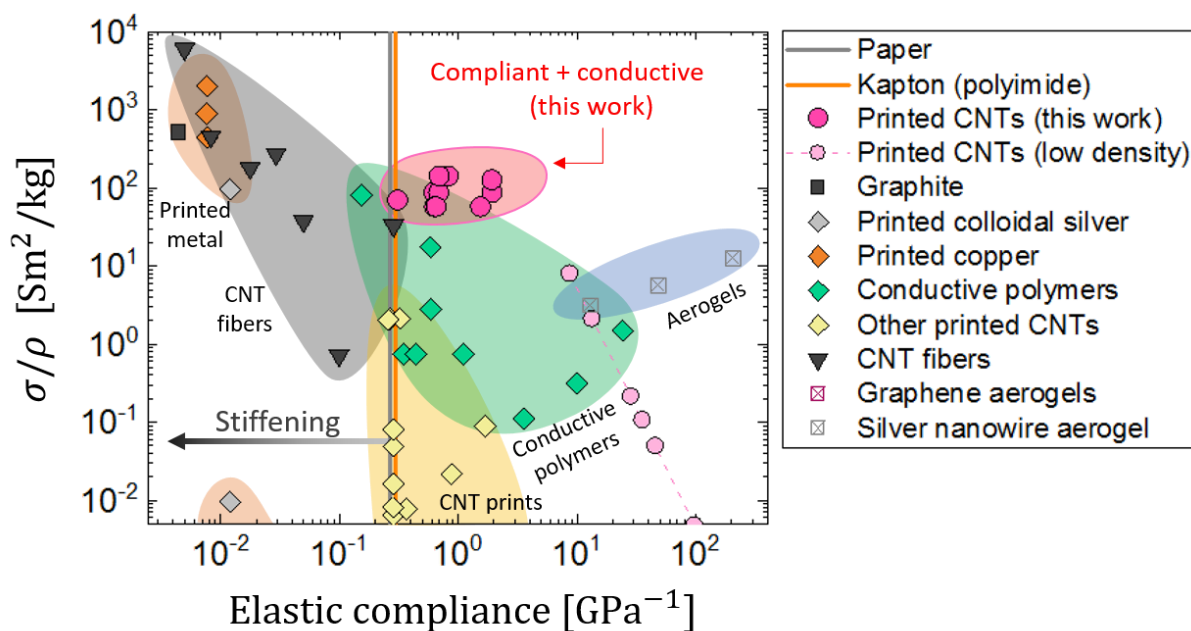


**Figure 5.9-1:** A comparison of the elastic compliance of conductive materials versus their specific conductivity. Below a compliance equal to the compliance of typical substrates (paper, Kapton), a material will increasingly stiffen the flexible electronic device. Above this level, the device is stiffened predominantly by the substrate, and we consider the printed material to be fully compliant. We targeted and achieved printed traces in the conductive and compliant material regime. We also include data for low-density CNTs (light pink circles) which have directly measured compliance, while the mechanical compliance shown here is projected from mechanical tests of the more dense printed CNTs, while the specific conductivity is directly measured for both.

In comparison to other materials, CNT traces have a high maximum specific conductivity of  $\sigma/\rho \approx 1.4 \times 10^2 \text{ Sm}^2/\text{kg}$ , and have a larger elastic compliance than the typical flexible substrates. Our printed CNT lines have a tensile modulus of  $1.4 \pm 0.7 \text{ GPa}$ , an ultimate tensile strength of  $38 \pm 19 \text{ MPa}$ , and a solid yield strain of  $4.2 \pm 2.1\%$ , and exhibit brittle failure. Details of the mechanical characterization are included in **Appendix Section 5.11.6** and **Figure 5.11-7**, but, in brief, we used tensile measurements of printed CNT wires that had been carefully removed from non-porous substrates. Metal foams/aerogels have similar flexibility and slightly lower conductivity, while spun CNT fibers have similar conductivity and much lower compliance. Other printed CNTs are typically more rigid due to the use of polymeric additives such as poly(vinyl alcohol) and thermoplastics to enhance

printability, with significant loss of conductivity. We note that much of the published literature data for many conductive printed inks fell below the lower bound of the plotted data, with printed CNT inks ranging down to  $\sigma/\rho < 10^{-11}$  S m<sup>2</sup>/kg. In addition, data was projected for low-density CNTs, for which mechanical properties were extrapolated from other measurements, increasing the range of possible compliance as CNT mass is reduced.

CNT lines show stable resistance over repeated folding cycles, as shown in **Figure 5.11-13a** and in **Appendix Section 5.11.10**. On both impermeable and permeable substrates, lines made with a linear density of  $\rho A_c = 2.7$  mg/m have a mean percent change in resistance under 2%. This behavior continues for sparser prints with  $\rho A_c = 0.2$  mg/m on impermeable substrates; however, resistance changes by over 30% for lines printed onto porous substrates with the more sparse linear density of  $\rho A_c = 0.2$  mg/m.

While the influence of bending to line conductivity is important for consistent performance of flexible electronics, extension is also relevant. CNTs have much larger strain-to-failure than metals, but are also known to be piezoresistive when large in-plane strain is applied. [62] Optimal stretchability requires not just a stretchable printed feature but also a substrate capable of extension, and often patterned substrate designs are used to most effectively allow macroscopic strain without damaging printed features, e.g. by using cleverly designed, non-affine deformations [20–22, 84].

Because minor flexion does not affect the printed CNT conductivity, we adapt the kirigami design work of Morikawa et al., [84] to design and create an ultra-stretchable PET substrate capable of folding and macroscale extension, with our design and measurements shown in **Figure 5.11-15**. Using the equations presented by Morikawa et al., we tuned the simple kirigami pattern to employ only planar bending of the substrate, minimizing in-plane extension of the CNT network itself while achieving high macroscale strain. CNTs deposited on this substrate show DC conductivity with under 5% change for single cycle up to 830% (maximum) strain of the base substrate, or similarly under 5% change for 100 cycles up to 400% strain each, and under 1% change in resistance for 100 cycles at 200% strain. This extensibility can help one-time integration into devices (e.g. for thermoforming) and for repeated cycles of moderately large (<500%) strain.

## 5.10. Conclusions

We have described the development and application of a series of aqueous, CNT inks for use in direct-write printing of electronically functional features and devices. We showed in



detail how the properties of the ink determine the electrical conductivity of printed features, and the related processing capabilities (feature size, production speed) required for manufacturing success. While the extrusion-based methods presented herein are best suited to localized deposition, the ink could readily be adapted to production-scale methods, such as gravure and screen-printing, that can readily handle and benefit from the rheological properties of yield-stress fluids. Moreover, the ability to process and deposit CNTs from aqueous inks can be beneficial to the development of low-cost and wearable sensors, RFID tags, disposables, and morphable structures.

## 5.11. Appendix

### 5.11.1. Time-Dependent Rheology of CNT inks

Following from **Figure 5.4-1**, we show the remaining Herschel-Bulkley fit parameters,  $k$  and  $n$ , as a function of CNT volume fraction,  $\phi$  in **Figure 5.11-1**. We also include the frequency response of the inks in small amplitude oscillatory shear tests in **Figure 5.11-2a**, and the storage and loss modulus response of two inks to high amplitude deformation, and subsequent recovery in **Figure 5.11-2b,c**.

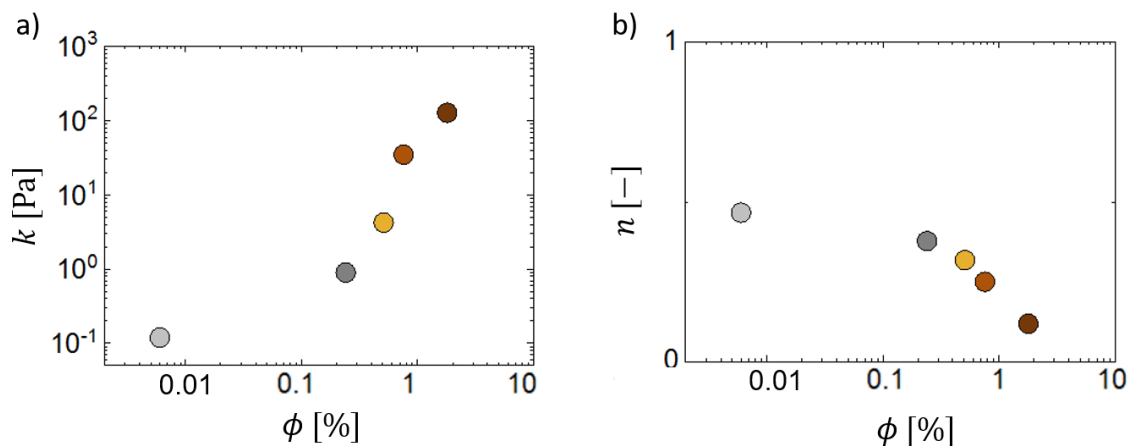


**Figure 5.11-1:** Evolution of (a) the consistency index,  $k$ , and (b) shear thinning index,  $n$ , for the inks shown in **Figure 5.4-1** as a function of CNT volume fraction,  $\phi$ .

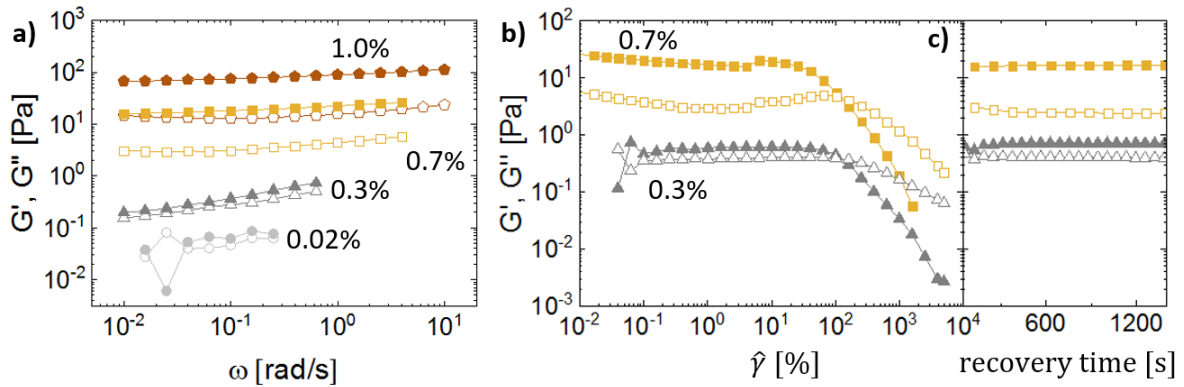


**Figure 5.11-2:** Following from **Figure 5.4-1**, we show (a) the frequency response of the inks in small amplitude oscillatory shear tests and (b) the onset of nonlinearity at large strain amplitude and subsequent recovery. Storage moduli,  $G'$ , are shown by filled symbols while loss moduli,  $G''$ , are hollow symbols with the same color and shading.

### 5.11.2. Evidence of Isotropic CNT Arrangement

High shear forces have been shown to cause alignment of CNTs and other elongated nanostructures [9, 85]. In our printing process, we imaged printed lines on chromatography paper using transmission polarized microscopy and found no evidence of large-scale alignment induced by printing, as shown in **Figure 5.11-3**, which may be due in part to competing elastic instabilities observed in shear flow of CNTs [86, 87]. Additional scanning electron micrographs and polarized Raman scans also showed no orientation, though these null results are not included here.

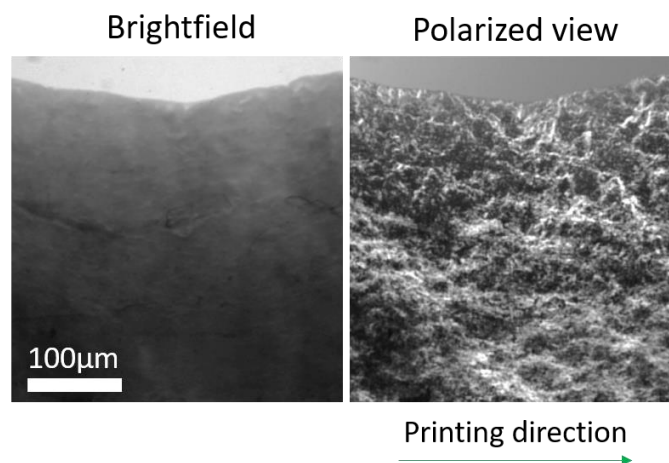


**Figure 5.11-3:** The edge of a printed CNT line was imaged under transmission polarized microscopy, showing in brightfield and polarized light. No long-range order is apparent.

### 5.11.3. Calculating Conductivity of Constituent CNTs

The conductivity of a percolating network of CNTs is described well by the typical percolation law in Equation (S1) [42, 88]

$$\sigma_{system} = \sigma_{CNT} f (\varphi - \varphi_c)^t \quad (S1)$$

where  $\sigma_{CNT}$  is the bulk conductivity of the constituent CNTs,  $t = 1$  is the exponent in the linear regime past percolation, and  $\varphi$  is the volume fraction. For an aspect ratio of  $\Lambda = L_{CNT}/d_{CNT}$ , the percolation volume fraction is  $\varphi_c \approx 2/\Lambda \approx 0.04\%$ , and an empirical dependence on the aspect ratio of CNTs is [88]

$$f = 10^{0.85[\log(\Lambda)-1]} \quad (S2)$$

where  $f \approx 50$  when we use the aspect ratio predicted from the observed transition concentration to liquid crystalline behavior in **Section 5.4.1** ( $\Lambda \approx 1000$ ). Using a theoretical scaling [89], which we rearrange and rewrite here for convenience,

$$f = \Lambda^{0.087 \log(\Lambda)} \quad (S3)$$

giving  $f \approx 6.1$ . We convert our calculated CNT mass density to the volumetric fraction of CNTs in air by

$$\varphi = \rho/\rho_s \quad (S4)$$

where  $\rho_s$  is the bulk density of CNTs ( $1.2 \text{ g/cm}^3$ ), and rewrite equation S1 in terms of known quantities during printing to calculate the bulk conductivity of CNTs comprising our printed lines for  $\phi \gg \phi_{cas}$

$$\sigma_{CNT} = \frac{\sigma A_c \rho_s}{\rho A_c f} \quad (S5)$$

which is found to be constant as in **Figure 5.11-4b** giving  $\sigma_{CNT} \geq 5,000 \text{ S/m}$  using the average of the  $f$  values calculated above. This conductivity is expected to be a minimum bound for the bulk conductivity of the CNTs, and is reduced from the true value of pure CNT conductivity due to contact resistance and effects from network topology [42, 89].

In comparison, the conductivity of the liquid inks before solvent evaporation was  $0.17 \pm 0.15 \text{ S/m}$  and  $1.7 \pm 1.5 \text{ mS m}^2/\text{kg}$ , corresponding to a much lower CNT network conductivity of  $\sigma \approx 27 \pm 35 \text{ S/m}$ , indicating significantly less CNT-CNT contact in solution than after ink has been deposited. This is to be expected from a stabilized suspension.

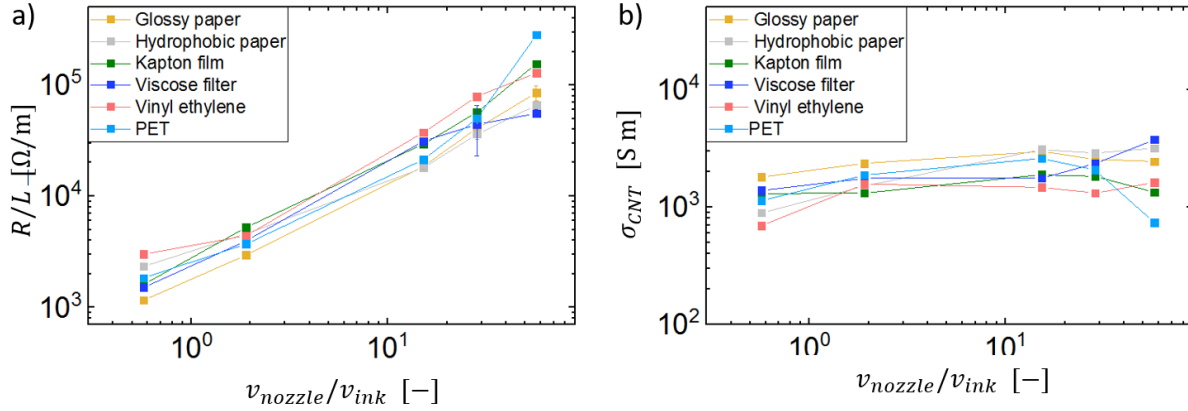


**Figure 5.11-4:** (a) For CNT lines printed onto a range of substrates, the conductivity increased linearly with deposition rate. (b) Using equation S5, the conductivity of the constituent CNTs, reduced by the contact resistance of the network and residual surfactant, was estimated to be 1,900 S/m.

We observe scaling laws of  $t = 2$  directly after percolation and  $t = 1$  after a further transition, as shown in **Figure 5.6-1**. Immediately after percolation, a two-dimensional system would behave as  $t = 1.33$  in equation S1 and a three-dimensional system would be expected to show  $t = 2$  [42], indicating that the CNT networks in the present work form a three-dimensional network.

When conductivity of a 3D network of elongated rods is dominated by contact resistance between individual rods, the scaling exponent should be  $t = 2$  after percolation, without a transition region, due to charge mobility being limited by the number of contacts between individual rods throughout the network. [88] However, when contact resistance is relatively low, the network resistance is dominated instead by bulk resistivity of CNTs. Then, the scaling law of  $t = 2$  is expected, where the overall number of contact points is still limiting, with a transition to  $t = 1$  when the number of contact points has saturated. [88] When the contact resistance and bulk resistance are comparable, this exponent is expected to vary between the lower and upper bounds depending on the precise ratio and the material aspect ratio [90].

A flow-induced or shear-induced alignment of anisotropic materials increases the percolation threshold required for onset of conductivity, which would shift the measured percolation curve laterally [42].

#### 5.11.4. Influence of Concentration on Feature Size

Lines were printed onto paper using CNT-based aqueous inks with three different concentrations of CNTs, and the widths of the lines,  $w$ , were measured after printing and compared to the extruder nozzle inner diameter,  $D_0$ . As shown in **Figure 5.11-5**, as the CNT concentration increased, the line width systematically decreased. This is attributed to a higher yield stress in the higher-concentration inks, as shown in **Figure 5.4-1b**.

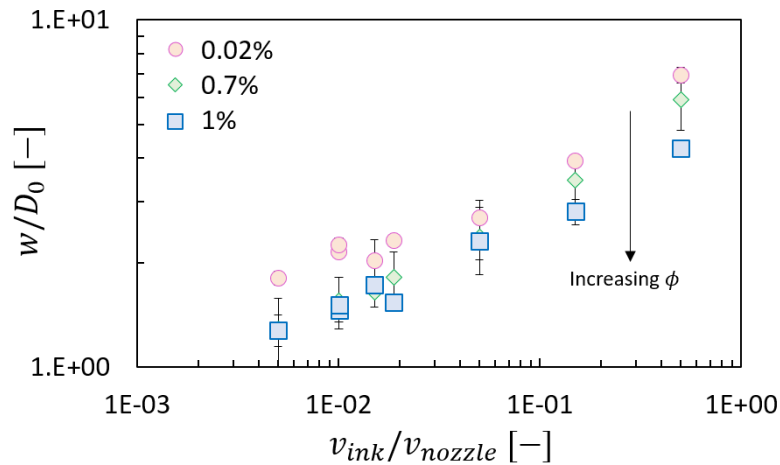


**Figure 5.11-5:** The concentration of CNT ink affected the width of printed lines. For a range of deposition rates, the low concentration ink systematically spread wider than the high-concentration inks, which is attributed to the yield stress rheology of the high concentration inks.

#### 5.11.5. Comparison of Commercial CNT Inks

Four commercial CNT inks using CNTs in aqueous suspensions were printed "as-is" alongside our in-house CNT inks using the same process and control parameters. These included CG300 (SWeNT) with single-walled CNTs in water at 1.00 mg/mL of CNTs, Coat E (OCSiAl) with single-walled CNTs in water with sodium dodecylbenzene sulfonate surfactant around 4 mg/mL of CNTs, and Invisicon (Nano-C) with single-walled CNTs in IPA and water at approximately 5.2 mg/mL for Invisicon 3500 and 3.4 mg/mL for Invisicon 3400. All CNT concentrations are reported by the manufacturers. As shown in **Figure 5.11-6**, the behavior was similar for all inks, roughly following a quadratic relationship between linear density and linear conductivity. The commercial inks exhibited a mean conductivity of approximately 30% of the electrical conductivity of our inks within the testable range, with the highest differences in conductivity of 7% of the value of our inks at

moderate CNT concentration, and a 5-fold greater conductivity at the lowest concentration of the CG300 ink, as both the CG300 and Coat E inks appear to percolate at lower thresholds than our ink, causing greater conductivity at low concentrations. Meanwhile, the average values of conductivity of CNT items reported in published papers is still lower, at most approximately 0.8% of the specific electrical conductivity of our inks (refer to **Figure 5.9-1** for details), which may be attributed to the use of additional polymeric fillers in those papers.

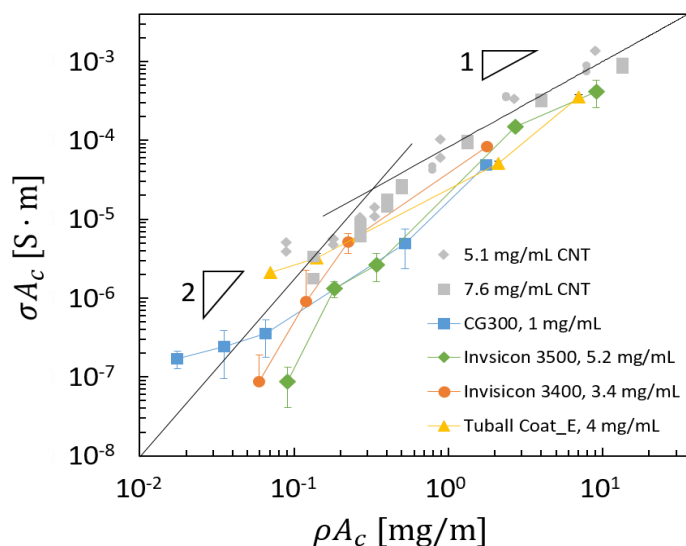


**Figure 5.11-6:** Three commercial CNT inks show similar behavior as CNT inks formulated in-house, denoted as grey symbols. Greater noise in the data for the commercial system is ascribed to use of lower concentrations. Error bars show standard deviation of 5 repeated tests.

#### 5.11.6. Mechanical Testing of CNT Prints

CNT lines were printed onto and carefully removed from impermeable substrate with low adhesion to test the mechanical properties of the printed and dried CNT material (**Figure 5.11-7a**). Examination of the failure surfaces after a tensile test showed simple fractures, with no apparent stretching or CNT pull-out, agreeing with our previous determination of no apparent orientation within the CNT prints. Tensile data is presented in **Figure 5.11-7c-f**.

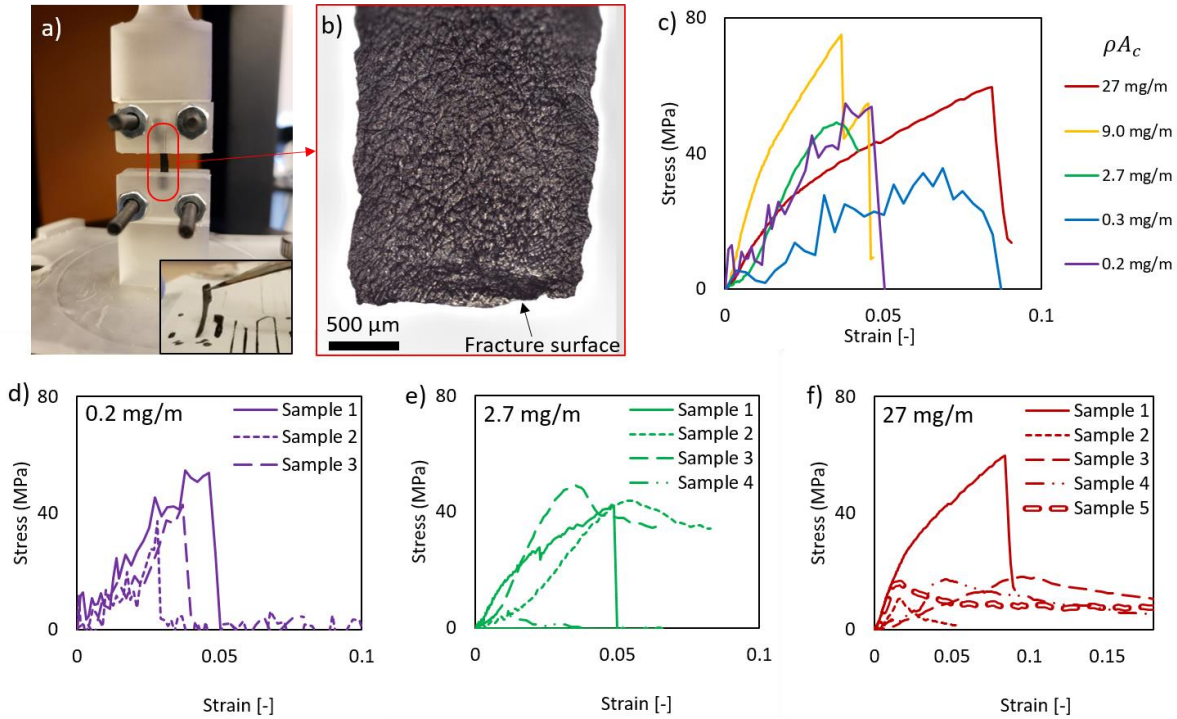


**Figure 5.11-7:** (a) CNTs were printed, dried, and removed from the low-adhesion substrate to directly test their mechanical properties. (b) The typical failure surface was a simple fracture, with no apparent CNT pull-out. (c) Tensile data is presented for lines with linear density from 0.2 to 27 mg/m, and (d-f) repeated tests are shown for three selected linear densities, showing similar elastic moduli among all tests, while the failure strain and strength were more variable, particularly for the largest sample.

### 5.11.7. Predictive Model for Width of Printed Lines

A model was constructed to describe the width of lines as printed onto a range of substrates. These different substrates interact with the CNT ink based on chemistry (wettability/contact angle,  $\theta$ ) and topographic parameters (surface roughness,  $r$ ). The contact angle  $\theta$  is a measure of the balance of interfacial energies between liquid, solid, and vapor. Surface roughness,  $r$ , is defined here as the ratio of the actual area of the surface solid compared to the normally projected area. Both terms are assembled into a single apparent contact angle using Wenzel's law,  $\cos(\theta) = r \cos\theta$ , which predicts that roughness amplifies the effect of native surface wetting properties [53]. This parameter is listed below each image in **Figure 5.7-1a-b**, which are listed in order of increasing  $\cos(\theta)$ , and transition from  $\cos(\theta) < 1$  for impermeable substrates in **Figure 5.7-1a** to  $\cos(\theta) > 1$  for porous paper in **Figure 5.7-1b**.

A summary of the substrate parameters is shown Table 1. Contact angle measurements were taken from literature measurements of water on smooth substrates of the designated material, with references listed in **Table 5.11-1**, while roughness measurements were made using a laser scanning confocal microscope as described in Methods, **Section 5.3**. We note that the use of tabulated values for equilibrium contact angle is an approximation, and subsequent error may affect  $\cos(\theta)$ ; however, this is required here due to the complexity of robustly measuring contact angle on a rough surface with a viscoelastic yield stress fluid.

**Table 5.11-1:** Substrate wetting parameters: contact angle  $\theta$ , roughness  $r$ , Wenzel wetting parameter  $\cos(\theta)$ . References are listed for contact angle values in the rightmost column.

Substrate	$\vartheta^\circ$	$r$	$\cos(\vartheta^*) = r \cos\vartheta$	source for $\vartheta$
Glossy paper	68	1.3	0.47	[91]
Hydrophobic paper	80	3.0	0.52	[92]
Vinyl ethylene film	80	1.1	0.86	[93]
Kapton film	71	2.0	0.64	[94]
Viscose filter	80	5.5	0.95	[92]
Polyethylene terephthalate	70	3.0	1.02	[95]
Chromatography paper	0	7.2	7.21	[91]

A quasi-static equilibrium model was constructed to predict the width of lines printed onto impermeable substrates based on the wetting parameter  $\cos(\theta)$  and the deposition rate through a balance of surface tension and gravity, as shown schematically in **Figure 5.11-8**. The deposition rate determines how much fluid (per unit depth) is extruded in a given area, having a height,  $h$ . The Bond number,  $Bo = \rho gh^2/\gamma$ , evaluates the relative influence of gravity and capillary forces on maintaining the droplet shape, where  $g$  is the acceleration due to gravity,  $\rho$  is the material mass density,  $\gamma$  is the surface tension, and  $h$  is the maximum height of the drop.

The model construction is shown here. The ink deposited (per depth) has an initial cross-sectional area of

$$A_{cross} = Q_{ink}/V_{nozzle} = v\pi D_0^2/4 \quad (S6)$$

When this area is small such that the height of the printed trace is not substantially affected by gravity,  $h < \lambda_c$  or  $\sqrt{Bo} < 1$ , the shape scales as  $v \propto w^2$  or  $w \propto \sqrt{v}$ , with the constant of proportionality depending on the specific geometry. If the cross-section is simplified to be an isosceles triangular shape, then  $A_{cross} = w^2 \tan\theta/4$ , which is combined



with the deposited fluid area to predict  $w/D_0 = \sqrt{\pi v / \tan\theta} = a\sqrt{v}$ . Other literature discusses finer resolution of droplet shape in Newtonian fluids [96], which we neglect here due to complex cross-sectional shapes that will arise from competing effects of yield stress, viscoelasticity, and composition-dependent surface tension of the CNT inks. In addition, we limit our analysis to cases in which the droplet is much larger than surface roughness so the substrate can be considered homogeneously rough. For very small feature sizes, if the roughness of the substrate approaches the size of the drop, gravity-driven spreading would be significantly altered [97]. In addition, this is similar to previous analysis for three-dimensional droplets on rough substrates [98].

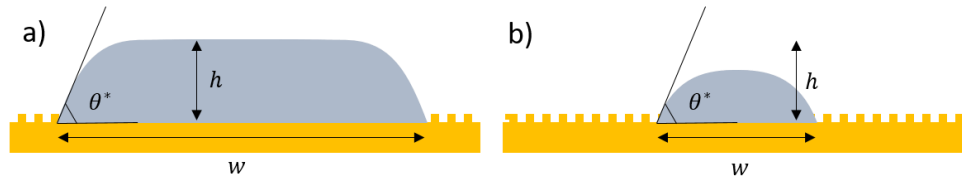


**Figure 5.11-8:** A diagram of (a) the puddle model and (b) the droplet model shows the assumed geometry where the puddle contacts the edge of the drop at a given contact angle and reaches an equilibrium shape with a maximum possible height  $h_c$  set by a balance of gravity and surface tension/wetting effects.

When the cross-sectional area of the printed line is large, the cross-section becomes “puddle-like” and consists of a flattened central plateau with tapered edges, which varies as  $w = b + cv$  through a similar geometric scaling analysis approximating the puddle as a trapezoid with central height  $h$ . The coefficients are  $b = h/\tan\theta$  and  $c = \pi D_0^2/4h$ , where  $h$  is the plateau height of the puddle,  $h_c \approx \sqrt{2\gamma(1 - \cos\theta)/\rho g}$ , marking the transition height between the puddle ( $h < h_c$ ) and droplet ( $h > h_c$ ) models, and ranges 1-2.2 mm here depending on  $\theta$ , and is similar to the capillary lengths for distilled water (2.6 mm) and for water with sodium deoxycholate (1.2 mm, with  $\gamma \approx 44$  mN/m for 0.05 M sodium deoxycholate in water [99]). Results of data compared to the fitted model are shown in **Figure 5.11-9**.

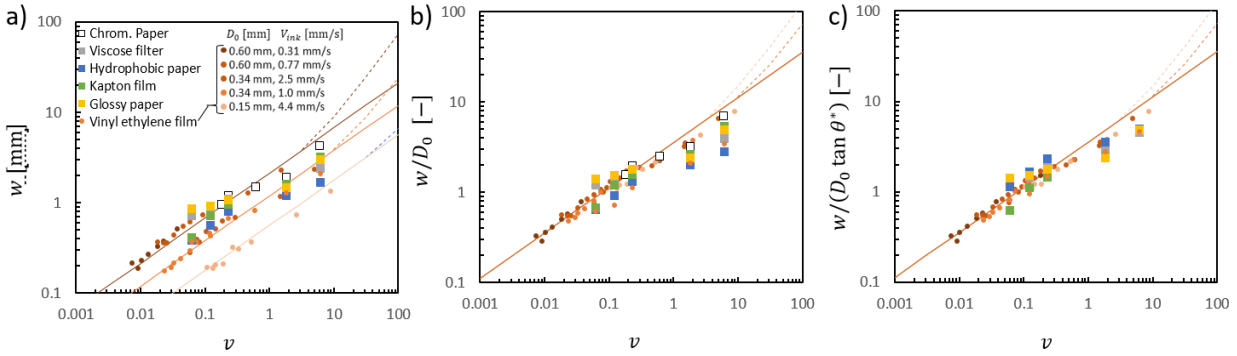


**Figure 5.11-9:** a) Measured data of printed line widths is compared to model predictions. (b) The vertical axis has been rescaled by the nozzle inner diameter, showing some collapse of the data. (c) The vertical axis has been rescaled by the nozzle inner diameter and the relevant substrate roughness parameter ( $\tan\theta^*$ ) for each print, showing better collapse of data onto the model line for a range of process parameters and substrates.

### 5.11.8. Monitoring drying time of printed CNT traces

While it was often apparent by eye when printed lines were mostly dry, we implemented an *in situ* resistance measurement on the printing stage to verify when the resistance had reached a stable level after solvent evaporated. As shown in **Figure 5.11-10** for three cases, the drying time ranged between 1 and 21 minutes. The change in resistance was much sharper at the end for the plastic substrate, vinyl ethylene, than for the porous and absorbent chromatography paper.

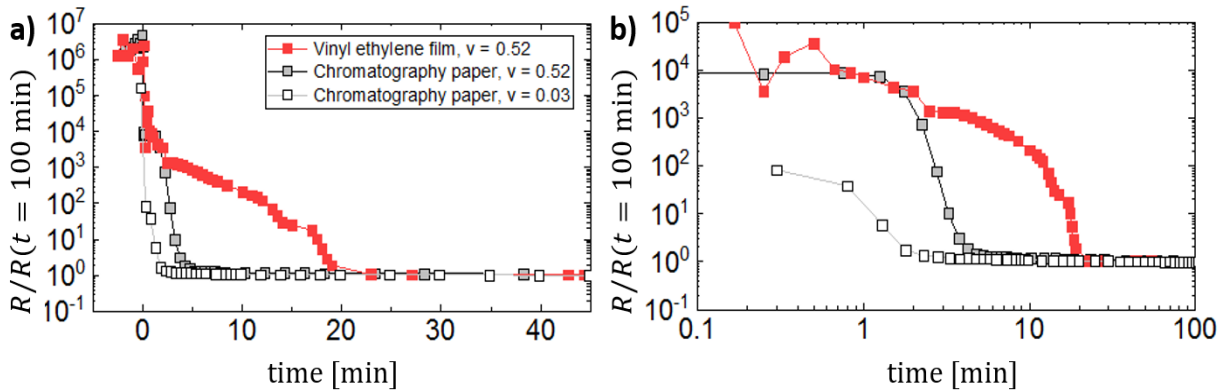


**Figure 5.11-10:** The resistance of printed lines was monitored after printing to determine the drying time.

### 5.11.9. Influence of the Substrate on Minimum Printing Resolution

Line edge roughness and substrate de-wetting influence the minimum achievable feature size and density, respectively. Due to the dewetting process, lines become discontinuous much sooner on nonwetting viscose filter paper compared to coated glossy paper, which is well-wetted by the ink (**Figure 5.11-11a,b**). Similarly, because line edges are smooth when printing onto Kapton film, lines can be printed very close together without shorting between them, increasing the attainable density of coils on a printed spiral (**Figure 5.11-11c,d**).

This was evaluated more precisely by measuring the edge roughness as the excess tortuosity, or

$$\text{roughness} = 1 - L_p/L \quad (S7)$$

where  $L$  is the printed line length and  $L_p$  is the length of its edge perimeter as viewed from microscopy images as shown in **Figure 5.7-1**, which has a minimum value of  $L$ . This roughness correlates strongly with both the roughness and effective contact angle of the substrate, as shown in **Figure 5.11-12**.

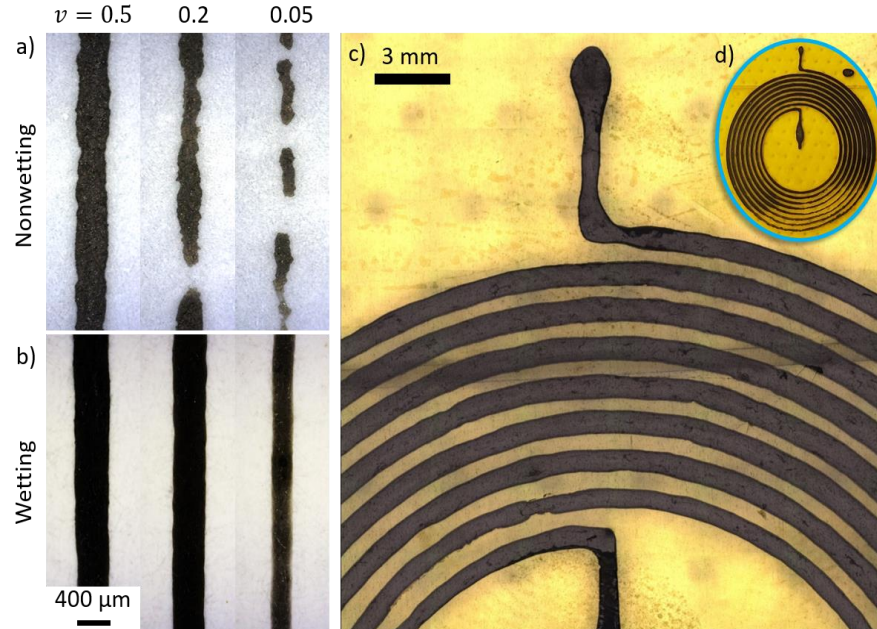


**Figure 5.11-11:** Printed straight lines are shown as a function of deposition rate,  $v$ , for (a) nonwetting (viscose filter) and (b) wetting (glossy paper) substrates. (c,d) Lines printed closely together are shown on Kapton film.

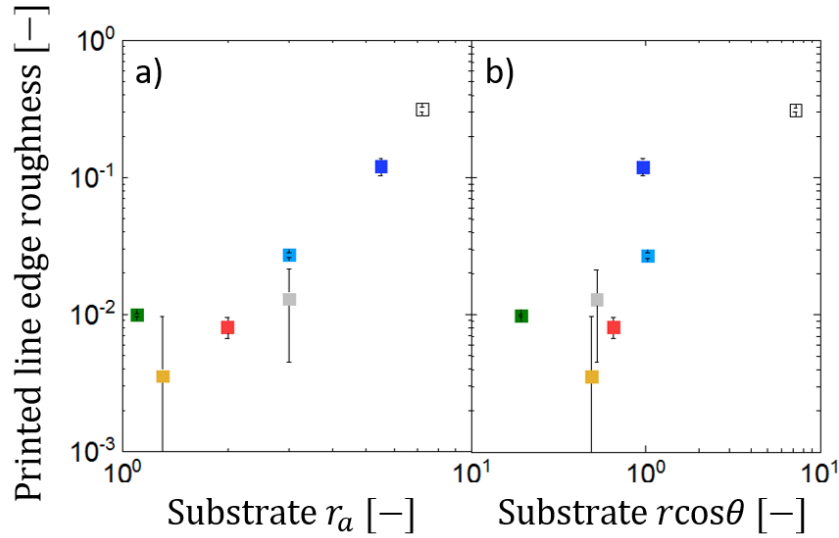


**Figure 5.11-12:** The roughness of printed lines is shown as a function of (a) the substrate roughness and (b) the substrate. Colors are the same as in **Figure 5.7-1**.

#### 5.11.10. Conductivity of CNT Lines for Repeated Bending Cycles

The mean conductivity of our printed traces are constant within 2% for at least 1,000 bending cycles with a full inward crease (bending such that a crease is formed on the paper and the two inner faces on either side of the fold contact each other). However, for significantly less dense CNT traces with  $v_{ink}/v_{nozzle} = 0.05$ , the conductivity degrades linearly with the number of bend cycles up to a mean 28% increase in resistance over 1,000 bending cycles, as shown in **Figure 5.11-13a**. The folding cycles are performed manually, creating a full crease in lines between two electrical probes, as shown in **Figure 5.11-13b**.

These systematic changes are ascribed to adhesion limits between printed CNT lines and the substrate, and how that influences the material involved in the fold. For impermeable substrates, adhesion is much lower and so lines may partially delaminate, as shown in **Figure 5.11-14**, mechanically affecting a wider range of CNTs. When the substrate is porous, much less material is incorporated in the fold because it is more strongly adhered to the paper, which causes more acute destruction of the CNT network in the narrower region, and is more sensitive when less overall CNT material is deposited, denoted by low ink deposition,  $v$ .

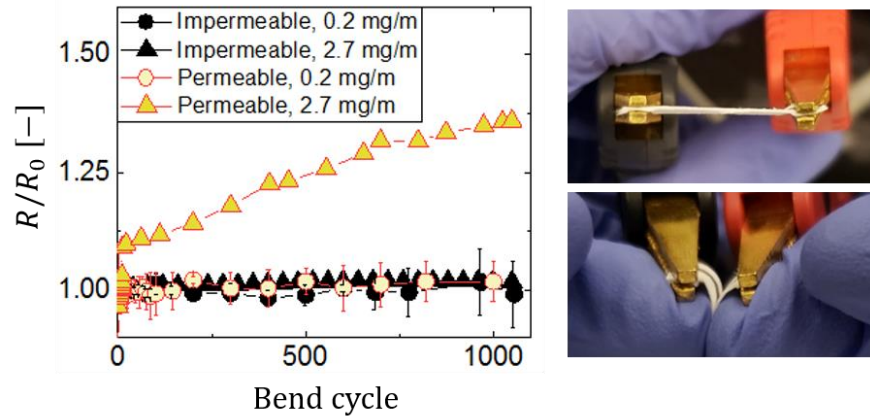


**Figure 5.11-13:** (a) The mean conductivity of our printed traces are constant within 2% for at least 1,000 bending cycles with a full inward crease. For significantly less dense CNT traces with  $v_{ink}/v_{nozzle} = 0.05$ , the conductivity degrades linearly with bend cycles up to a mean 28% increase over 1,000 bending cycles, with an initial resistance  $R_0 \approx 300\text{--}2100\Omega$ . (b) The folding cycles are performed manually, creating a full crease in lines between two electrical probes.

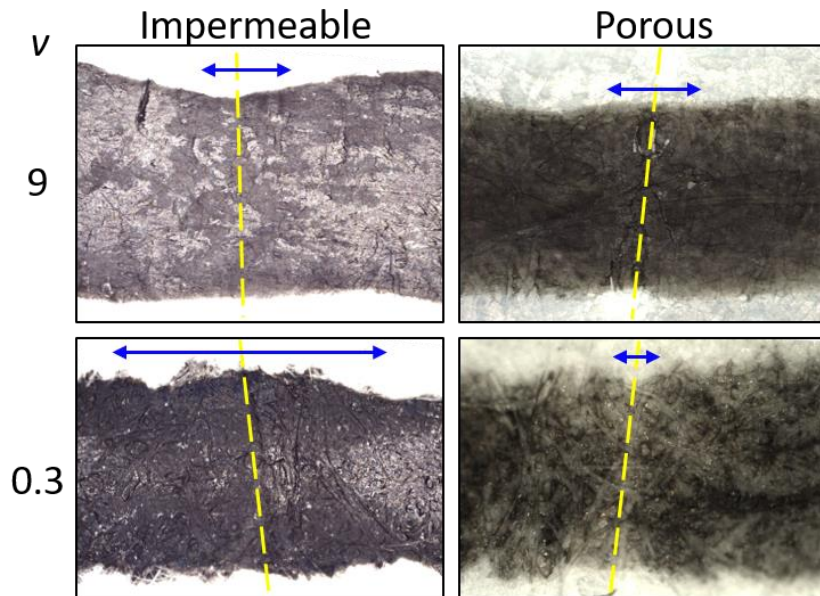


**Figure 5.11-14:** For impermeable substrates, adhesion of CNT traces is much lower and so lines may partially delaminate, mechanically affecting a wider (darker) spatial area of CNTs. When the substrate is porous, much less material is incorporated, which causes more acute destruction of the CNT network in the narrower (lighter) region, and this effect is amplified when less overall CNT material is deposited, denoted by low  $v$  values. The lines shown for  $v = 9$  are approximately  $3000\ \mu\text{m}$  in width, and for  $v = 0.3$  are approximately  $800\ \mu\text{m}$  in width.

CNT lines showed stable resistance over repeated folding cycles, as shown in **Figure 5.11-13a**. On both impermeable and permeable substrates, lines made with a linear density of  $\rho A_c = 2.7$  mg/m had a mean percentage change in resistance under 2%. This behavior continued for more sparse prints with  $\rho A_c = 0.2$  mg/m on impermeable substrates; however resistance increased and showed a greater change in resistance over 30% for lines printed onto porous substrates with the more sparse linear density of  $\rho A_c = 0.2$  mg/m.

Following the kirigami design work of Morikawa, et al.,[84] we created an ultra-stretchable substrate capable of folding and extension, shown in **Figure 5.11-15**. CNTs deposited on this substrate showed DC conductivity with under 5% change for a single mechanical loading/unloading cycle up to 830% (maximum) strain, 100 cycles up to 400% strain, and under 1% change in resistance for 100 cycles at 200% strain. This extensibility can help one-time integration into devices (ex. for thermoforming), even at very high strains, as well as for repeated moderate (<500%) strain cycles. For comparison, human skin can generally stretch 50% [100], so wearable sensors would be well within this range.

In addition, these ultra-stretchable CNT forms were able to deform in planar extension and in an out-of-plane bending deformation, in which they were raised vertically by a central tower composed of LEGO bricks, which are known for having precise dimensions [101].

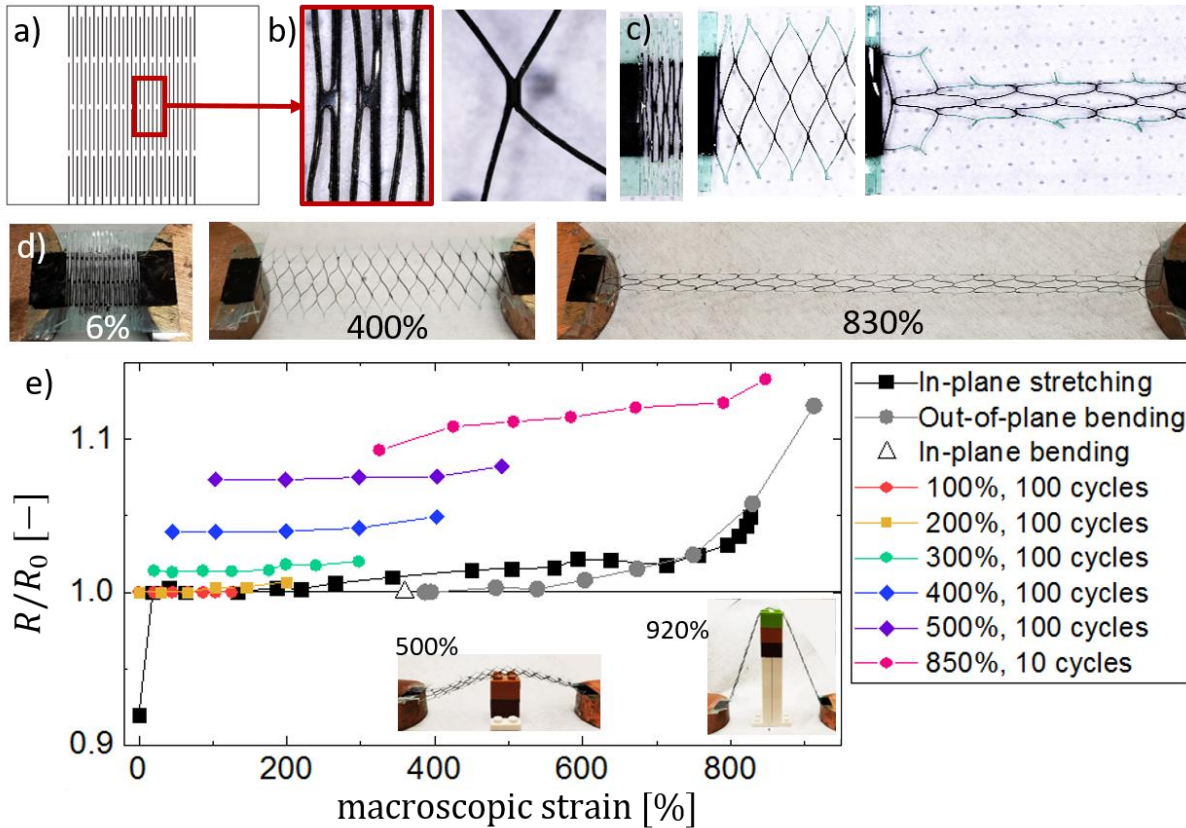


**Figure 5.11-15:** An ultra-stretchable substrate was created with (a) a design of vertical cuts that (b) stretch and extend at a few internal joints to (c,d) extend elastically from unstrained to >900% strain. (e) The strain over time for the flexible substrate, for a single repetition and for sequential repeats of 100 cycles of extension up to the denoted maximum strain. Note that data for repeated cycles were performed in series, so 100 cycles were performed from 0 to 100% strain, and then 100 cycles were performed from 0 to 200% strain, and so on. Data for the in-plane stretching, out-of-plane bending, and in-plane bending only were done separately.

### 5.11.11. Contact Resistance Measurements of CNT Traces

The method of measuring the contact resistance consisted of measuring the conductivity of CNT traces for different printed lengths, using a configuration with a continuous CNT line and two probes, and a second configuration with a break in the CNT line to incorporate a controlled CNT-CNT contact point. From the data collected, which is shown in **Figure 5.11-16**, the slope is  $R_m$ . The intercept of the base measurement is  $2R_{c,probe}$ , and the intercept of the measurement including CNT-CNT contact is  $2R_{c,probe} + R_c$ .

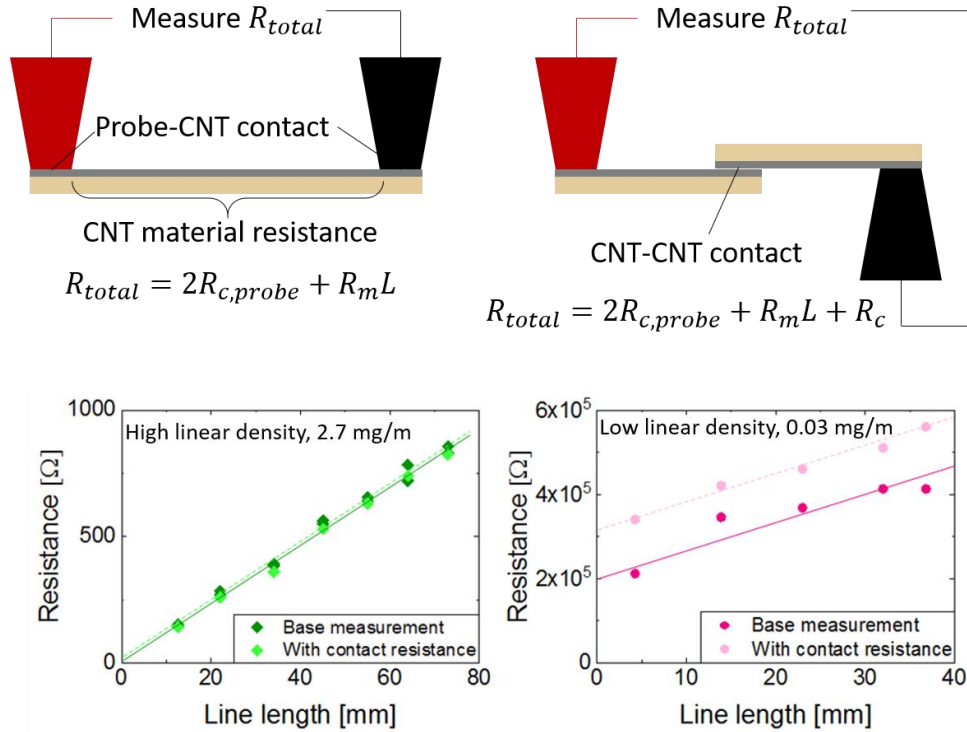


**Figure 5.11-16:** CNT material resistance was measured using contact of two probes with varied length between probes on the same substrate. By varying the length between probes, the probe-CNT contact was measured separately from the base material resistance. In a second test, a CNT-CNT contact was introduced, and the contact resistance was measured the same way by varying the total length of measurement for the same CNT line as measured in the first case. Example data sets are shown for CNT lines with high and low linear density.

The variation of resistance and contact resistance was evaluated over a series of cycles of applied pressure for CNT traces printed onto glossy and chromatography paper, as shown in **Figure 5.11-17**. In displacement-controlled tests, pressure normal to the substrate was applied, resulting in cycles of high pressure alternating with loss of contact with the substrate (**Figure 5.11-17a-b**). The conductance (defined as the inverse of the resistance) was monitored simultaneously (**Figure 5.11-17c,e**) and the ratio of the contact resistance to the trace resistance over 1 mm was calculated to show the cyclic behavior (**Figure 5.11-17d,f**). While the results for the glossy paper were repeatable, the behavior of the chromatography paper drifted over time before reaching a more steady behavior, which we



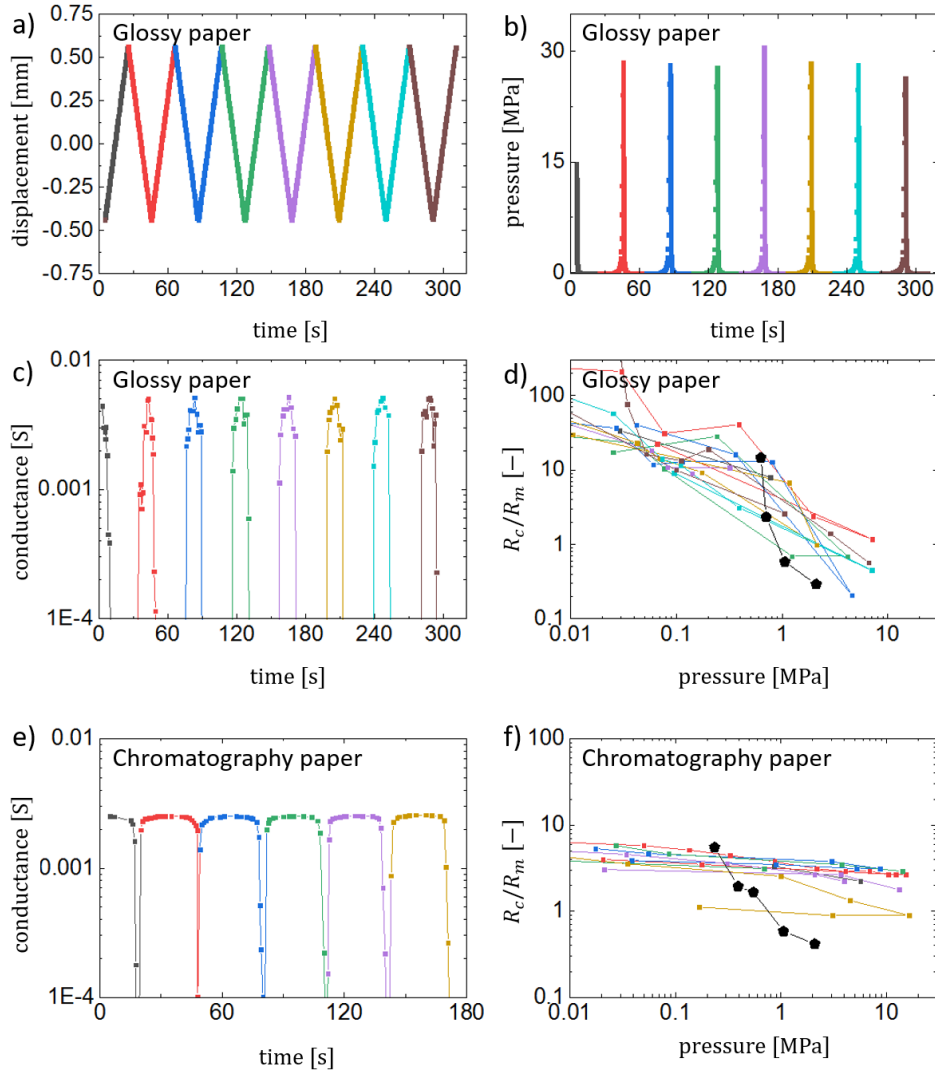


**Figure 5.11-17:** The contact point between two CNT traces printed onto paper was loaded to apply cyclic compressive forces. (a) The cycles were controlled by displacement, which (b) generated an applied pressure. (c,e) The conductance (defined as the inverse of resistance) was monitored over the same cycles and (d,f) the contact resistance was compared to pressure over several cycles. The data with black circles in (d,f) here is reproduced for the same substrate and conditions as shown in **Figure 5.8-2a,b**.

ascribe to plastic deformation of the chromatography paper itself (data not shown). After several cycles, the comparison between substrates continued to show that CNT traces printed onto glossy paper had a much sharper change in contact resistance with applied pressure, while for those printed onto chromatography paper, the response became nearly independent of pressure. This behavior could have strong implications for the design of CNT contact-pressure buttons that are either sensitive or insensitive to applied pressure.

We note that these results are dependent on the behavior of the substrate so that similar papers with different thicknesses or moduli would be expected to behave differently, as well as papers with different mechanisms preventing separation. The glossy paper we used is both thinner (around 120  $\mu\text{m}$ ) and denser than the chromatography paper (around 150  $\mu\text{m}$  in thickness).

### 5.11.12. Fluid Sensor Used For Droplet Impact

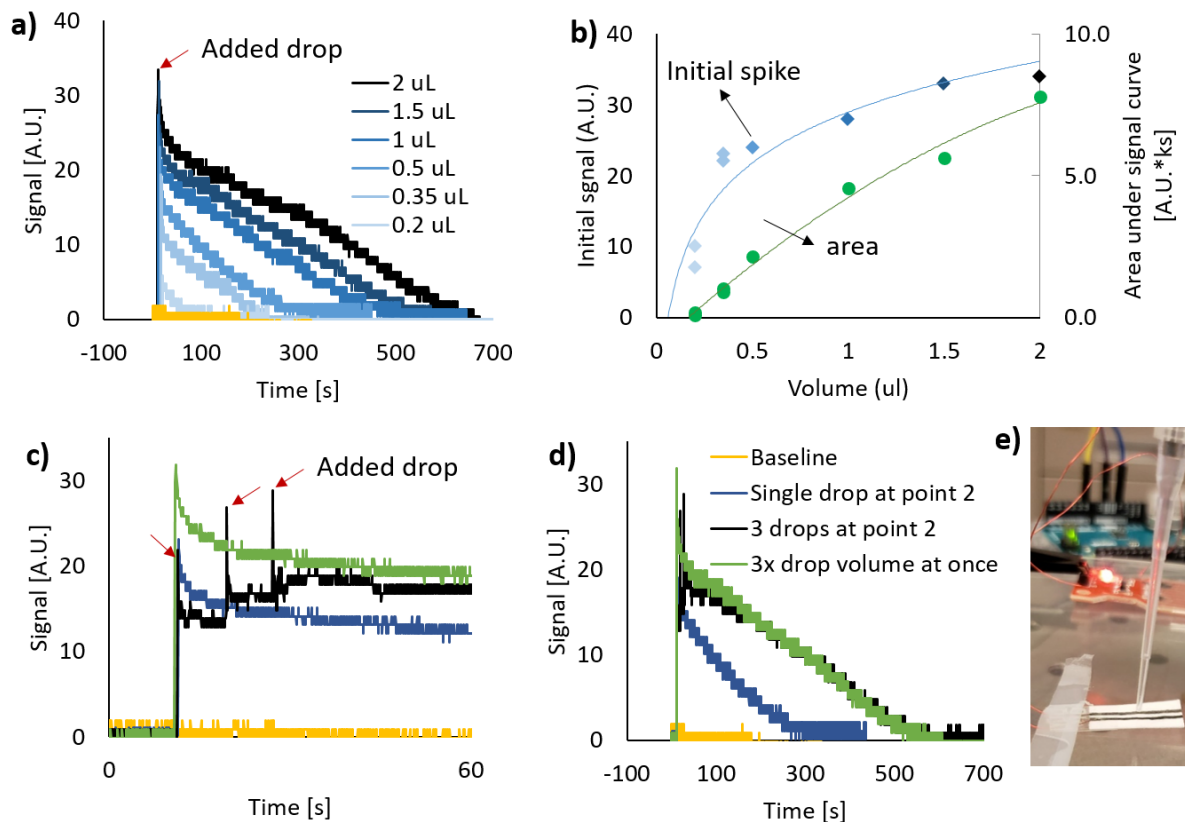


**Figure 5.11-18:** (a) Voltage signal recorded upon measuring the impact of a small droplet of distilled water on a two-line printed CNT capacitive sensor. (b) The sensor is sensitive to the volume of the droplet through the initial spike in response and the area under the full curve. (c,d) The sensor can register addition of multiple droplets in quick succession (red arrows) and is still sensitive to the total volume, where the response after 60 seconds is equal for equal volumes deposited as separate drops or all at once. Here, each drop is a constant volume of 0.5  $\mu\text{L}$ . (e) The experimental setup is shown, where droplets are deposited by a calibrated micropipette.

A two-line CNT-based printed sensor was used to register the impact of a small droplet of distilled water (Figure 5.11-18). The sensor exhibits a sensitivity to the volume of the droplet through the amplitude of the initial spike in response and the area under the full

curve. The capacitive sensor can register addition of multiple droplets in quick succession (red arrows) and is still sensitive to the total volume, where the response after 60 seconds is equal for equal volumes deposited as separate drops or all at once. The experimental approach deposited droplets onto the CNT-based printed sensor using a calibrated micropipette.

---

## **Chapter 6. Immersed extrusion of high-conductivity carbon nanotube threads and extensible coils using an anti-solvent bath**

---

### **6.1. Abstract**

In this chapter, we demonstrate a printing process inspired by methods of wet fiber spinning, creating dense carbon nanotube (CNT) threads and extensible coils with metal-like DC specific conductivity. A printer with an immersed nozzle extrudes an aqueous CNT ink with initially <1% carbon nanotube concentration into a liquid bath of antisolvent, inducing immediate precipitation-driven solidification. This process forms continuous threads of CNTs with conductivity above  $2 \times 10^5$  S/m, exceeding that of dense graphite and approaching that of CNTs spun from similar inks in a continuous fiber spinning process ( $6 \times 10^5$  S/m), and specific conductivity up to  $7 \times 10^3$  S.m<sup>2</sup>/kg, comparable with copper ( $6.6 \times 10^3$  S.m<sup>2</sup>/kg). The accessible printing regimes are analyzed, with consideration of the applied draw ratio during printing. Particular focus is placed on the speed of counter-diffusion of the ink solvent and the bath liquid, which allows for tuning of fiber diameter, conductivity, and specific conductivity respectively over 1, 4, and 5 orders of magnitude. When the speed of solvent counter-diffusion is high, the conductivity of resulting threads is highest. When extrusion speed is also high relative to the nozzle motion speed, we observe a coiling instability which creates threads with regular coil morphology, allowing for intricate designs to be formed along a linear extrusion path. Resulting coils can be easily removed

intact from the liquid bath. Once dried, densely coiled structures can undergo up to 50% strain with <1% change in conductivity or 170% linear extension with 20% change in conductivity as the coils unwind. The realized complex coil structures have salient application to lightweight circuitry and flexible interconnects.

## 6.2. Introduction

Now, over 30 years after the discovery of CNTs [230], industrial CNT production quality and throughput continues to improve [31], [231], and the use of CNTs as additives in plastic parts and as bulk conductors in electronics has been widely demonstrated [29], [50], [232], [233]. Notably, due to their low density, the specific conductivity (*i.e.*, conductivity per weight) of CNTs excels even compared to metals, and inherent flexibility makes CNTs a natural choice for flexible electronics, while the use of carbon-based material appeals to industrial interest in sustainability.

Macroscale CNT objects, such as CNT-based fibers made by solvent spinning achieve conductivity of 10 MS/m using superacid solvents [31]. Similar advancements have been made by CNT thin films [234] and dry-spun CNTs. While outstanding values of conductivity for CNT-based macrostructures continue to fall an order of magnitude short of the theoretical upper limit for individual CNTs, which may reach 100 MS/m [28] (almost double that of silver, the most conductive metal, with 63 MS/m), applications of fabricated CNT fibers, films, and composites are wide-ranging [1], including specialty applications in high-frequency antennas [235], [236], transparent films [33], neural probes for sensing [237] and control [238], field emission sources [239], [240], smart electronics [241], humidity sensing [242], and yarn-based actuators [243]. Meanwhile, the use of CNTs as an additive in 3D printing has enabled general conductivity and strengthening of polymer parts [232], [244], and strain sensing [245], [246], among other uses, alongside demonstrations of conductive bulk structures 3D-printed from CNTs [22], [33].

Meanwhile, the conductivity of printed CNT-based components remains limited, at best 100-fold less than values achieved by fiber spinning (or about 0.005-0.10 MS/m) [35]. This is because an extrudable ink typically requires polymeric fillers to be processed by a printer, hindering conductivity by disrupting CNT-CNT contact. Even with such limitations, due to the diversity of applications, small improvements in achieved conductivity of CNT-based structures provide value.

While fiber spinning has its own complex rheological requirements for the spinning dope [247], spinning is achievable using a single material suspended or surfactant-stabilized in a solvent, and has been demonstrated for CNTs in aqueous solvents to achieve conductivity up to 0.58 MS/m [34]. Also, in 2D and 3D printing methods, the specific conductivity of CNT-based parts has been demonstrated up to 200 Sm<sup>2</sup>/kg [35] despite spun CNT fibers reaching values above 6,000 Sm<sup>2</sup>/kg, fully comparable with metals, marking specific conductivity as a particularly salient measure to improve for printing methods.

Therefore, to develop a route to improve conductivity via printing of CNTs, we combine a 3D printer with the method of wet fiber spinning, in which a viscoelastic ink is extruded through one or more orifices into a liquid bath that solidifies the ink by coagulation or solvent exchange. In our method, we extrude an aqueous solution of CNTs from a single orifice, a printing nozzle, into a liquid bath on a printbed.

Extrusion printing into baths of yield stress fluids has been shown to create three-dimensional items with intricate geometries [248], [249]. However, intrinsic to the fiber-spinning process is a rapid solvent exchange between the printing bath and the extruded ink, which is dramatically slowed in a yield stress bath [250]. In addition, the concentrated microgels or surfactants typically forming the matrices for suspended printing would be expected to interfere with printing of highly conductive materials that depend on CNT-CNT contact without interstitial contaminants. Further, the process of printing into yield stress fluids typically leaves printed parts within the suspending fluid due to difficulties retrieving them, or else requires further curing steps to solidify them for removal, and this challenge becomes even greater when printing finer features such as threads rather than bulk items. As such, for ease of retrieval, elimination of potential contaminants, and speed of precipitation, we elect to print into purely Newtonian fluids.

In **Section 6.4**, we introduce the method of printing and process control parameters including a mechanical draw ratio and antisolvent strength. In **Section 6.5**, we develop an understanding of the rheology of our CNT ink. In **Section 6.6**, we characterize the printing, dividing results into three observed regimes of coiled, linear, and fragmented fibers, and develop an understanding of the influence of draw ratio and antisolvent strength on the fiber diameter, density, conductivity, and specific conductivity. In **Section 6.7**, we explore the coiling regime of printing more thoroughly, and finally demonstrate the extensibility of printed and dried coils.

### 6.3. Materials & Methods

#### *Preparation of Carbon Nanotube-based Aqueous Ink*

Carbon nanotube (CNT) inks were prepared in the same process as in [35]. Dry CNT powder (EC1.5, Meijo, Japan) was wetted with a small amount of sulfuric acid and then mixed in water to a concentration of 0.75 wt% of CNTs with sodium deoxycholate (DOC) surfactant to stabilize the suspensions with 2 wt% (20mg DOC / g water). The CNTs were tip sonicated for up to 10 hours in water (10 mL) with DOC (0.2 g), adding more CNTs over time until the desired concentration was reached. The CNTs have a mean diameter of 1.5 nm and initial length of 9.4  $\mu\text{m}$  [10].

#### *Rheological Measurements*

Rheological behavior of the inks was measured with a stress-controlled shear rheometer (DHR-3, TA Instruments) using a cone-and-plate fixture (40 mm diameter, 2 degree cone angle; TA Instruments) with adhesive sandpaper having 5  $\mu\text{m}$  roughness (Trizact A5, 3M) applied to prevent slip of the fluid sample. The shear viscosity was measured by decreasing the shear rate from the maximum to the minimum value to allow the sample to equilibrate.

#### *Extrusion Printing of CNT Inks*

A 3D printer (MakerGear M2, MakerGear) used a custom syringe displacement system based on a micrometer-resolution single-axis translation stage (PT1, Thorlabs) to print the CNT inks at room temperature. The printer used a 1 mL capacity syringe (Sanants) and sterile blunt-tipped metal needles (27- and 34-gauge, inner diameters respectively 0.21 and 0.06 mm; Nordson). The lateral speed of the printhead ranged from 10 to 3,000 mm/min, and the extrusion flow rate ranged from 90 nL/s to 900 nL/s.

#### *Size and conductivity characterizations*

Optical microscope images of wet and dried fibers were taken using a Zeiss SmartZoom. Polarized transmission microscopy observed CNTs in a glass capillary of 50  $\mu\text{m}$  thickness between two crossed-polarizing lenses with a transmission Zeiss microscope. Scanning electron microscopy (SEM) was performed on dried fibers without modification using a Zeiss Merlin High-resolution SEM. Electrical resistance was measured using an LCR meter with 4 terminal Kelvin clips (IM3536, Hioki) at room temperature (23-25 degrees C) and ambient humidity (23-52% RH). Density was estimated by calculating the volume of printed lines based on the measured radius compared to the extruded volume per unit length, as in

$$\rho_{fiber} = \frac{\rho_{CNT}(\pi R_{fiber}^2)}{Q/v_{machine}} \quad (1)$$

### Mechanical tests

Fibers were mounted onto laser-cut frames of 65 lb weight cardstock (envelopes.com). Conductive carbon black paste connected printed fibers to enameled copper wire (34-gauge, BNTECHGO), and this connection was covered with 2-part structural epoxy (Gorilla). Before measurement, the sides of the cardstock were cut, so that the CNT wire was the only load-bearing member in the axial direction. Strain was applied using a DHR-3 rheometer (TA Instruments) using custom clamping fixtures to hold the cardstock. Axial strain was applied cyclically at a rate of 2% strain per second. An LCR meter (IM3536, Hioki) measured the electrical resistance during axial measurements.

### 6.4. Submerged Nozzle Printing Process

A printer was constructed to hold a an extruder nozzle such that its tip was below the free surface of a liquid reservoir (**Figure 6.4-1a, b**). The printer extruded ink with a flow rate  $Q$  through a nozzle with inner diameter  $2R_0$  moving through the liquid bath with lateral speed  $v_{nozzle}$  (**Figure 6.4-1c**). The reservoir was shallow, typically no more than 2-3 mm deep of antisolvent, allowing agile motion of the nozzle without sloshing (**Figure 6.4-1d**). As the ink encountered the antisolvent, the CNTs precipitated into a solid fiber, settling down under gravity to a substrate placed on the base of the reservoir.

To establish quantitative process control, a nondimensional velocity was constructed, as in [35], [251], as

$$v^* = \frac{v_{nozzle}}{Q/\pi R_0^2} = \frac{v_{nozzle}}{v_{extrude}} \quad (2)$$

leading to stretching of printed filaments for  $v^* > 1$  or compression for  $v^* < 1$ . Borrowing terminology from fiber spinning,  $v^*$  would be an applied draw ratio from mechanical forces of printing. Its counterpart, the observed draw ratio, is the ratio of the final fiber radius to the inner radius of the nozzle orifice. We use the reciprocal of the observed draw ratio as a shrinkage ratio,

$$r^* = \frac{r_{fiber}}{R_0} \quad (3)$$

where  $r^* > 1$  indicates swelling of the fiber due to printing while  $r^* < 1$  indicates contraction, while a value of  $r^{*2} = 1$  indicates a fiber with the same diameter as the extrusion nozzle. By mass continuity,  $\rho v R^2$  should be constant, for density  $\rho$ , speed  $v$ , and



radius  $R$  of a CNT fluid filament. By matching continuity between the extruded ink in the nozzle orifice and the final solidified fiber,

$$\rho_{ink} v_{extrude} R_0^2 = \rho_{fiber} v_{nozzle} r_{fiber}^2 \quad (4)$$

the observed draw ratio would be expected to behave as

$$r^* = \sqrt{\left(\frac{\rho_{ink}}{\rho_{fiber}}\right) v^{*-1}} \propto v^{*-0.5} \quad (5)$$

forming a power-law prediction of -0.5 for the final radius of fibers without substantial solvent exchange between ink and bath. The shrinkage ratio  $\rho^* = \rho_{fiber}/\rho_{ink}$  is evaluated to be

$$\rho^* = v^* r^{*2} \quad (6)$$

so that a value  $\rho^* > 1$  indicates swelling relative to the expected effect of mechanical drawing, and a value of  $\rho^* < 1$  indicates shrinkage relative to the expected effect of mechanical drawing, due to loss of initial solvent. A limiting value of  $\rho^* \approx 0.0075$  would indicate a fully dense CNT fiber with no interstitial voids for our starting CNT concentration in the ink of 0.75 wt%.

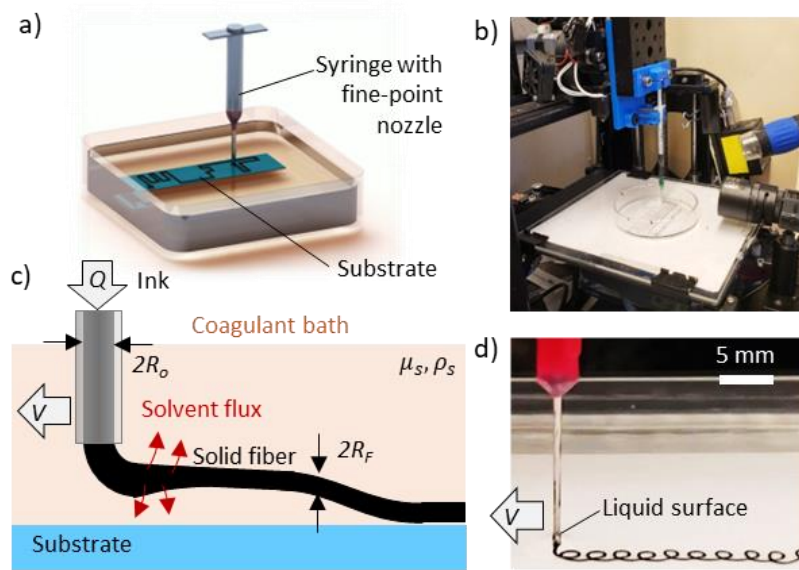


**Figure 6.4-1:** Printing paradigm. (a, b) A vertically-mounted syringe moves in  $x$ ,  $y$ ,  $z$  around a printbed within a liquid reservoir with a free upper surface. (c) Extrusion of ink through a nozzle submerged in an antisolvent or coagulant causes the ink solvent to diffuse outward, precipitating the ink into a solid coil that settles down to the substrate. (d) Photograph of the nozzle moving on the printer, extruding coiled CNT structures into ethanol. The nozzle is shallowly submerged, with liquid only 1 mm above the bottom end of the nozzle.

Finally, a parameter is defined to quantify the relative importance of the chemistry of the solvent bath and its propensity to induce counter-diffusion of the initial solvent (water) and bath solvent, thereby inducing ink precipitation. Antisolvent strength was tuned by printing into pure glycerol ( $c^* = 0$ ) with slow counter-diffusion expected with water, pure ethanol with rapid counter-diffusion ( $c^* = 1$ ), or a mixture of glycerol and ethanol identified by the density of the mixture,

$$c^* = \frac{\rho_{mixture} - \rho_{glycerol}}{\rho_{ethanol} - \rho_{glycerol}}. \quad (7)$$

The diffusion coefficient of water into pure ethanol is  $D = 1.2 \times 10^{-9} \text{ m}^2/\text{s}$ , slowing marginally as the ethanol becomes partially diluted with water ( $D = 0.75 \times 10^{-9} \text{ m}^2/\text{s}$  for 0.63 mol fraction ethanol) [252], and of water into pure glycerol is  $D = 0.014 \times 10^{-9} \text{ m}^2/\text{s}$ , increasing marginally as glycerol becomes partially diluted with water ( $D = 0.078 \times 10^{-9} \text{ m}^2/\text{s}$  for 0.63 mol fraction glycerol) [253]. In addition, the surfactant, sodium deoxycholate, is soluble in ethanol [254]. Thus, an antisolvent strength of  $c^* = 1$  here indicates rapid precipitation and diffusion of ink solvent into the surrounding bath, while an antisolvent strength of  $c^* = 0$  indicates no initial precipitation and substantially slower diffusion.

Other antisolvents known to precipitate aqueous CNT solutions were tested, such as acetone and hydrochloric acid [34], but these were found to precipitate too fast for printing, leading to clogging of the printer nozzle. In addition, the viscosity of the bath needed to be sufficiently high to draw fibers out by shear stress in the absence of coagulation, resulting in glycerol with its high viscosity (1200 Pa.s, >1000x that of water) a better choice than a low-viscosity non-antisolvent like water, into which CNT fibers simply dispersed, or oil, which caused CNT fibers to pinch off into droplets rather than threads (although this could have other beneficial uses [255], [256]).

Other CNT inks were also tested, including Coat\_E (OCSiAl), CG300 (SWeNT), and Invisicon 3500 and 3400 (Nano-C), as well as mixtures made in lab using shorter CNTs (Cheaptubes). However, none of these formed continuous threads when extruded in the available antisolvents, suggesting the need for high concentrations of long CNTs for sufficient entanglement during precipitation, as is well known in the fiber spinning literature that polymers with high molecular weight enable spinnability [257].

## 6.5. CNT Ink Rheometry

The rheology of the chosen ink, 0.75 wt% CNTs in water and stabilized by deoxycholic acid, approximates Herschel-Bulkley behavior where shear stress  $\sigma = \sigma_y + k\dot{\gamma}^n$  for yield stress  $\sigma_y$ , consistency index  $k$ , and shear-thinning index  $n$ . This indicates a shear-thinning behavior with  $n = 0.35$ , which is consistent with a biphasic system with an isotropic CNT solution in equilibrium with an interspersed liquid crystalline phase [40] and which facilitates extrusion by lowering viscosity at high rates. It also presents a moderate yield

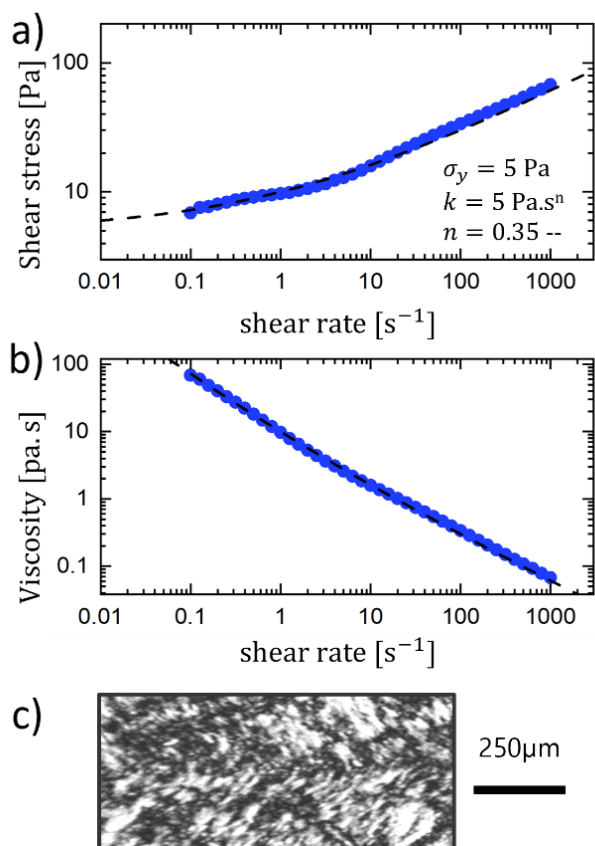


**Figure 6.5-1:** Ink rheology. (a) Shear stress as a function of shear-rate; dashed black line indicates Herschel-Bulkley model fit as shear stress  $\sigma = \sigma_y + k\dot{\gamma}^n$  with labeled parameters. (b) Viscosity as a function of shear rate. (c) Transmission polarized imaging of CNT ink showing 10-200 micron wide liquid crystalline domains.

stress of  $\sigma_y = 5 \text{ Pa}$  (Figure 6.5-1a-b). The rheology further shows a downward inflection in stress at shear rates of 0.1-1 and 10-100 s<sup>-1</sup>, indicating liquid crystalline behavior previously observed in solutions of CNTs [33]. The presence of liquid crystalline behavior was

confirmed by polarized imaging of the static ink (**Figure 6.5-1c**). The rheology was not observed to change with time, showing neither aging nor thixotropy (data not shown).

For the extrusion rates used during printing of 90 nL/s to 900 nL/s (2.5 to 25 mm/s linear extrusion velocity), and for a nozzle of internal diameter 0.21 mm (27 gauge), the approximate shear rate of the ink  $\dot{\gamma}_{print} \approx v_{extrude}/R_0$  ranges from 25 to 250 s<sup>-1</sup>, which is well within the shear-thinning region.

## 6.6. Classification and Measurement of Printed Threads

### 6.6.1. Printing regimes

Three regimes were identified based on the mechanical draw ratio  $v^*$  and the antisolvent strength  $c^*$  (**Figure 6.6-1**). For low and moderate  $c^* = 0-0.33$ , fibers formed continuous strands for  $v^* < 0.3-0.5$ . With increasing  $v^*$  above 0.5, fibers broke into fragments of decreasing size due to higher shear applied by the printing bath fluid [258]. For the highest antisolvent strength  $c^* = 1$ , the transition from linear to fragmented occurred at  $v^* = 1$  and a coiling regime was observed for low and moderate  $v^* < 0.4$ .

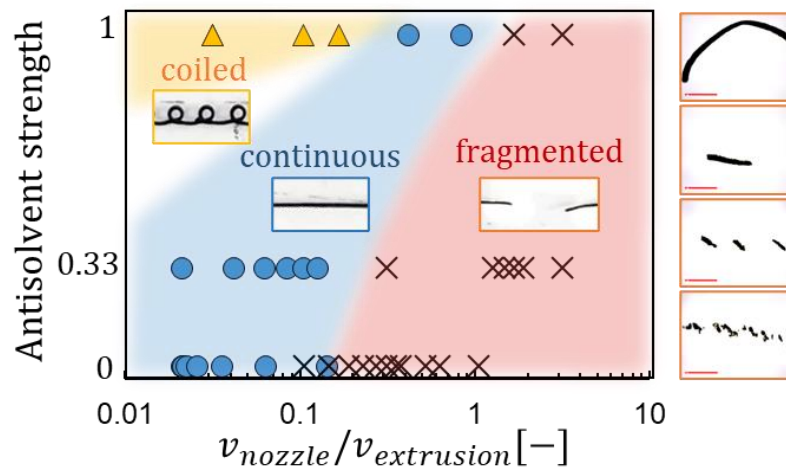


**Figure 6.6-1:** Printing regime map. For high mechanical draw ratios  $v^*$  fibers were fragmented rather than continuous due to the drawing force, though this transition happened later when antisolvent strength was greater. At lower  $v^*$ , continuous, straight fibers were observed. Only for the case of antisolvent strength  $c^* = 1$ , a regime of coiling instability was observed. Righthand images: printed fragments in the liquid bath for  $c^* = 0$  increasing in  $v^*$  from top to bottom, resulting in decreasing fragment size. Inset images show printed fibers with morphology of each regime.

### 6.6.2. Diameter and conductivity of continuous threads

Fibers of diameter 50-500  $\mu\text{m}$  were typically formed under the conditions of this study, using an extrusion nozzle of inner diameter 210  $\mu\text{m}$ . As mechanical draw ratio  $v^*$  was increased for a constant antisolvent strength  $c^*$ , the radius of printed fibers was observed to decrease (Figure 6.6-2a). The diameter was observed followed the predicted power law (Equation 5) for the case of  $c^* = 0$ , otherwise showing less sensitivity to the applied draw ratio, indicating an increased impact from solvent exchange and shrinkage. For  $c^* = 1$ , additional effects come from the coiling instability for  $v^* < 0.4$ , leading to irregular diameter control from the changing compressive axial force in coiling instabilities with different patterns [259].

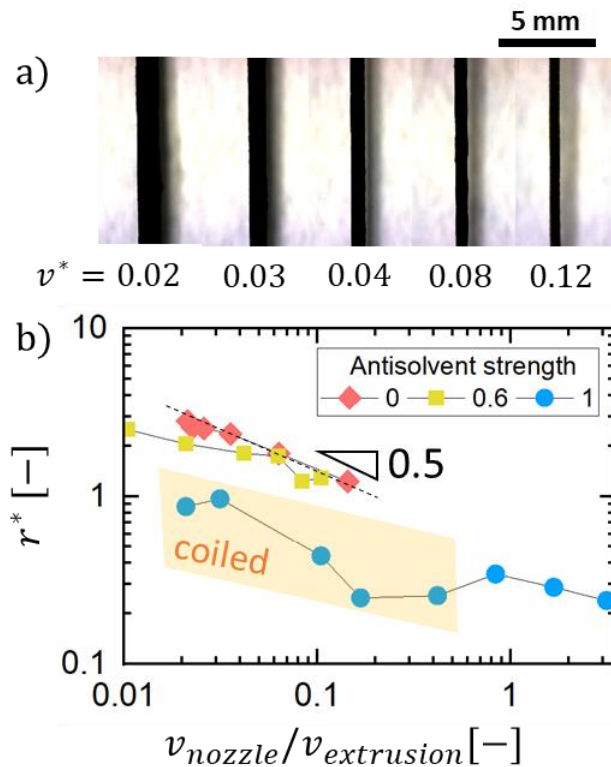


**Figure 6.6-2:** Effect of ink-bath interaction. (a) Micrographs of carbon nanotube lines as-printed in liquid with antisolvent strength of  $c^* = 0$ . With increasing applied draw ratio  $v^*$ , the diameter decreases due to mechanical drawing. (b) Observed shrinkage ratio compared to applied draw ratio. This follows the power law trend of -0.5 only for antisolvent strength  $c^* = 0$ , showing a shallower slope for the other cases due to influences of solvent exchange and the coiling instability.

The shrinkage ratio  $\rho^* = v^* r^{*2}$  was observed decrease with increasing antisolvent strength  $c^*$  (**Figure 6.6-3a-b**), indicating increased solvent loss from the initial printed ink, and in each case thinner fibers than would be expected from mechanical drawing alone. The measured electrical conductivity  $\sigma$  was found to be a strong function of  $c^*$  and not of  $v^*$  (**Figure 6.6-3c-d**), changing from an average value of  $\sigma \approx 7$  S/m (0.000007 MS/m, similar to seawater) for  $c^* = 0$  to  $\sigma \approx 0.1$  MS/m for  $c^* = 1$ , with a highest observed value of  $\sigma \approx 0.2$  MS/m for  $v^* = 0.2$ , above which threads would become more irregular in cross-section and then fragment.

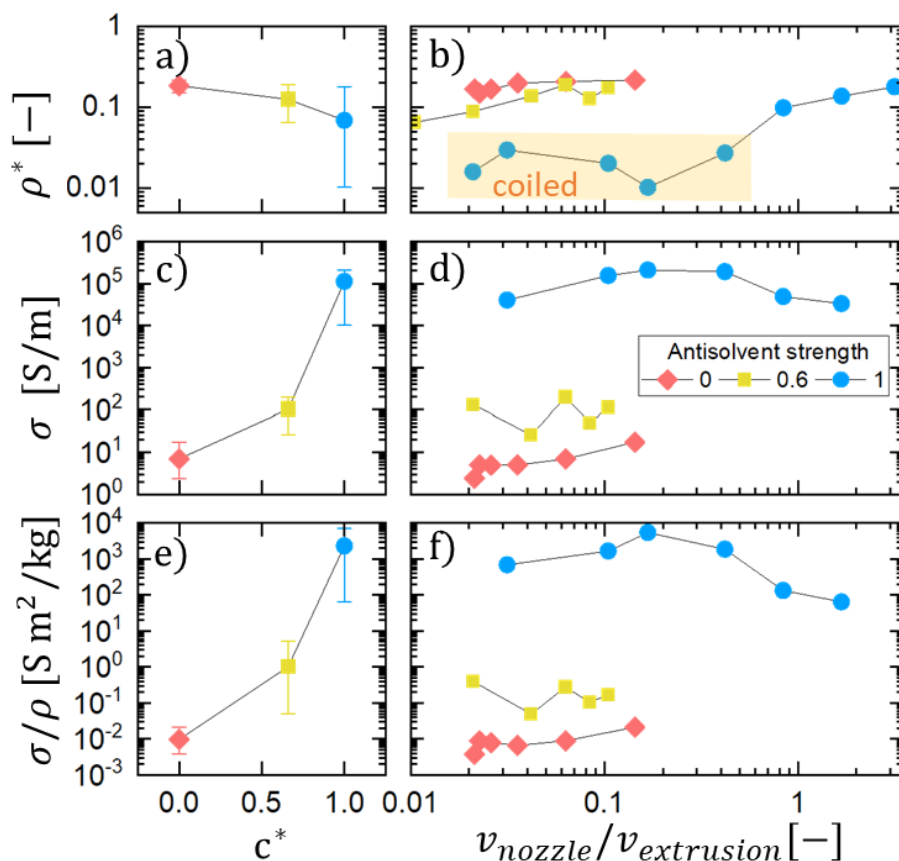


**Figure 6.6-3:** Effect of ink-bath interaction. Ranging from none (0) to antisolvent (1) has minor effect on (a) the swell ratio, which is nearly constant, and (b) diameter which is mostly affected by the applied draw ratio  $v^*$ , with a large effect on (c, d) conductivity and (e, f) specific conductivity. Error bars indicate range of measured values over  $v^*$ . Data are only reported for process values forming continuous linear or coiled fibers, resulting in different ranges spanned by the three conditions.

These conductivity ranges fall short of the high conductivity shown for highly aligned CNT fibers made by wet spinning from superacid-based inks (10.9 MS/m, [31]), as well as

bulk metals (1-60 MS/m). The conductivity was similar to that shown for fibers spun from aqueous CNT-based inks (0.58 MS/m, [34]) and was much greater than that achieved by dry printing of aqueous CNT-based inks (0.01 MS/m, [35]).

As the density of the present fibers did not depend on the extrusion rate and only mildly on the anti-solvent strength (**Figure 6.6-3a-b**), the same trends as for conductivity were shown for the specific or per-weight conductivity,  $\sigma/\rho$  (**Figure 6.6-3e-f**), with average values of  $\sigma/\rho \approx 0.01 \text{ S m}^2/\text{kg}$  for  $c^* = 0$  to  $\sigma/\rho \approx 2,000 \text{ S m}^2/\text{kg}$  for  $c^* = 1$ , and a highest observed value of  $\sigma/\rho \approx 7,000 \text{ S m}^2/\text{kg}$  for  $v^* = 0.2$ . In comparison, the same CNT ink printed onto a dry substrate that solidifies by evaporation of the initial solvent attained a specific conductivity only up to  $200 \text{ S m}^2/\text{kg}$  [35]. The specific conductivity of metals is in the same range as the continuous CNT threads (gold:  $2350 \text{ m}^2/\text{kg}$ ; silver:  $6150$ ; copper:  $6590$ ; aluminum:  $12300$  [20]), as metals have higher conductivity but also higher density than CNTs. While regimes are described by both the mechanical draw ratio  $v^*$  and antisolvent strength  $c^*$ , the geometric and electrical properties are dominantly controlled by  $c^*$ , while  $v^*$  influences the printing regime (coiled, linear, fragmented) and fine-tunes properties within that range. An increase in CNT fiber density is expected to facilitate better electrical conduction due to increased CNT-CNT contact [20], [260], [261]. That was found to be the case here, where a stronger antisolvent resulted in both smaller observed shrinkage ratio  $r^*$  and higher specific conductivity (**Figure 6.6-4**).

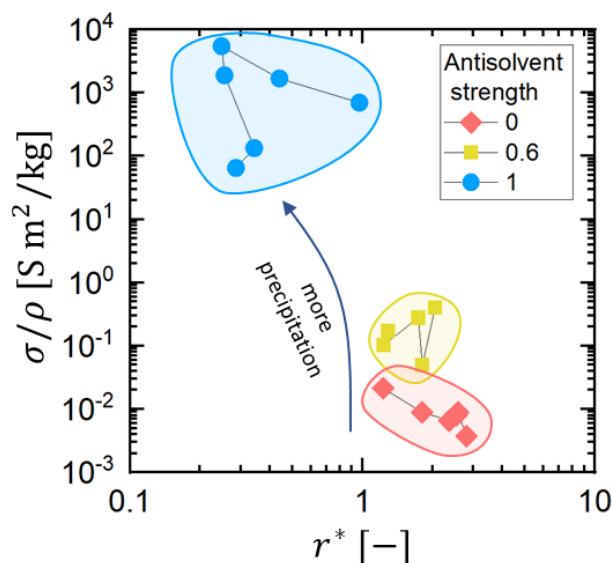


**Figure 6.6-4:** Coordinated impact of antisolvent. Increasing antisolvent strength induces a decrease in diameter and increase in specific conductivity.

### 6.7. Regime 3: Coil printing

The coiling regime observed is due to a phenomenon known as the “fluid mechanical sewing machine” [259], [262] in which falling viscous threads with Newtonian [263] and non-Newtonian [264], [265] behavior, and even elastic solid [266] ropes coil for  $v^* < 1$  and a sufficiently large printing height. This method has been described before in printing processes [251], [267] and effectively controlled using known physics to print challenging materials like glass [268] and nanoscale coiled structures [269].

One result of printing coils is shown in **Figure 6.7-1**. A set of 5 horizontal linear nozzle paths printed with different  $v^*$  for each path; between each path the nozzle took the corner and vertical path. The pitch and regularity of the coil depend on  $v^*$ . As such, upon changes in speed at the corners, the coiling structure immediately changed, forming a continuous path of CNTs transitioning between coiling patterns at transitions in the nozzle path speed. In addition, printed traces were observed started and stopped smoothly with extraction of the printer nozzle into and out of the solvent bath.

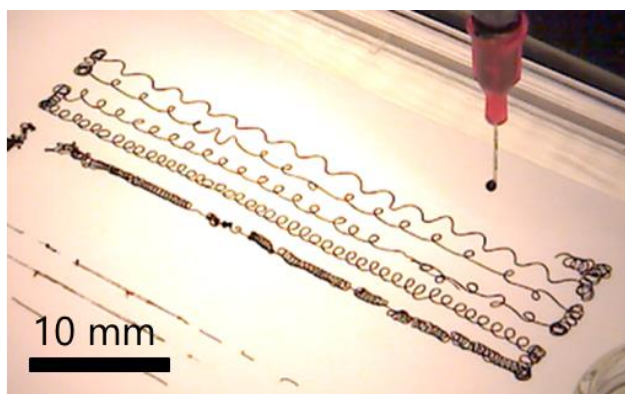


**Figure 6.7-1:** Printing within the coiling regime. A printbed containing a continuous thread made by a series of linear paths with progressively increasing  $v^*$ , resulting in less dense coiling from bottom left to upper right.

#### 6.7.1. Printing control of coiling structures

Coiling patterns observed by printing CNT ink here include translated coils, slanted loops, meanders, sidekicks, and linear lines (**Figure 6.7-2**). The coil regime is also sensitive to the nozzle height, and transitions between coiling structures were observed here due to small changes in printing height (**Fig 2a**,  $v^* = 0.43, 0.21$ ). The coiling of CNTs during ink extrusion and coagulation is more complex than prior studies of fluid coiling due to the changes here in both phase and density of the thread during coiling. For example, an



estimate can be made considering the thread falling as a viscous fluid: given that the nozzle height is constant throughout (2 mm), and assuming the effective ink viscosity is constant with  $v^*$  for a set nozzle size and that the density remains unchanged so the force of gravity (buoyancy) remains the same, based on the transition of coil regimes [259] that **Figure 6.7-2a** shows printing for a dimensionless fall height  $\hat{H} \approx 1.4$ , indicating effective viscosity of 84 mPa.s, and **Figure 6.7-2b** shows printing for a dimensionless fall height  $\hat{H} \approx 1.3$ , indicating effective viscosity of 94 mPa.s. However, these values are much lower than expected for extrusion at shear rates of  $3\text{-}25 \text{ s}^{-1}$  (**Figure 6.5-1b**). Therefore, the coils must physically be behaving more like elastic solids than like viscous threads, due to the rapidity of solidification. The ability to form coils of such density indicates that substantial solidification occurs fast enough to extrude coils at speeds of at least 11 mm/s of coils (for the case of  $v^* = 0.11$  and nozzle diameter  $r_{nozzle} = 0.10 \text{ mm}$ ).

The coiling instability phenomenon has further philosophical implications for the complexity enabled from additive manufacturing. Fiber size is reduced from shrinkage of printing into antisolvent resulting in features down to nine times smaller than the printing orifice, and the speed limitation is established by extrusion rather than mechanical motion speed, allowing coils that are nine times smaller in diameter and nine times longer in overall length (for  $v^* = 0.11$ ) than the motion path, not only is a complex feature formed by intelligent process control, but standard machine constraints for manufacturing are exceeded by nearly an order of magnitude, in both production rate of total extruded length compared to path length and in total size; once the coil may be fully extended into a linear format, it would exceed the dimensions of the printbed.

Although yield stress fluids themselves have been shown to coil, each layer of coils merges with the prior layer upon settling [264], [265]. Here, the contact points between coils are only weakly self-adhered and thus, after printing and drying, CNT coils could be mechanically pulled, dis-adhering the intersection points (**Figure 6.7-3b,c**). This indicates substantial solidification before the second segment of coil had been placed. The remaining smooth surface during detachment indicates the CNT network within the fiber conformed to the smooth printbed surface. In addition, a wrinkled surface morphology is evident due to the shrinkage induced by coagulation, and suggests that the outer layer of CNTs densified first before contracting radially inwards as solvent exchange progressed.

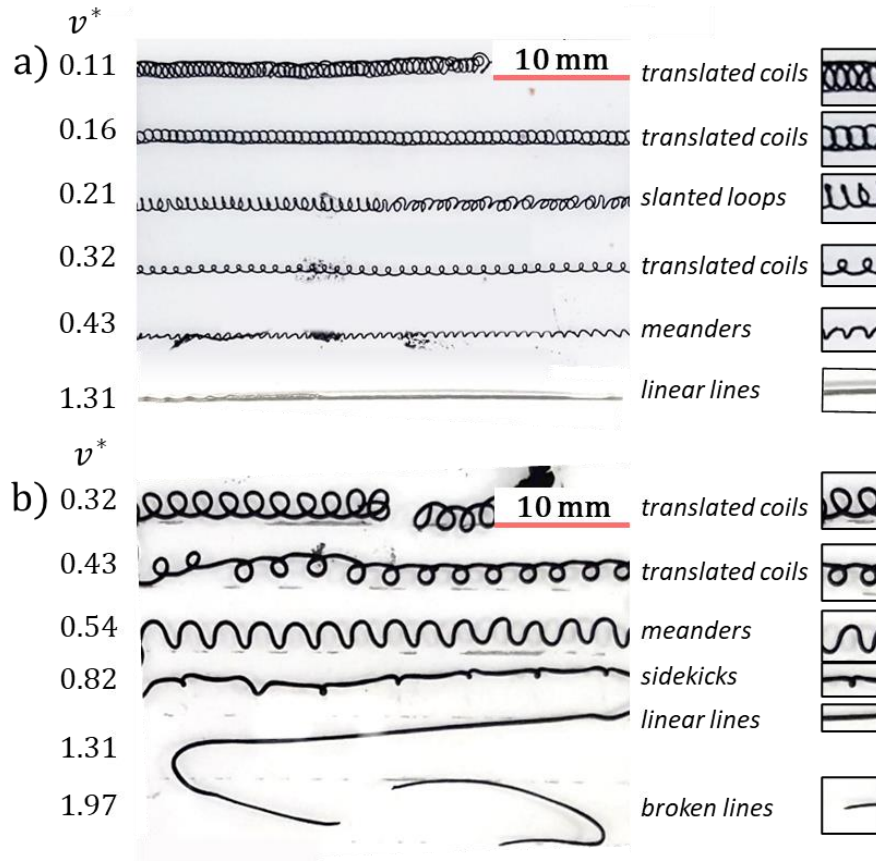


**Figure 6.7-2:** Exploring the coiling regime. Printed CNT filaments immediately after extrusion into pure ethanol ( $c^* = 1$ ) for (a) a 0.21 mm diameter nozzle and (b) a 0.6 mm diameter nozzle for the same linear motion speeds and approximate range of  $v^*$ . (a) Coiling patterns include translated coils, double meanders, and linear lines with increasing draw ratio  $v^*$ . (b) Stretched coiling and broken lines are also observed at high  $v^*$ . In these images dark spots between lines were removed for better visibility. Images of the lines themselves were untouched.

In printing regimes that coiled faster due to smaller coil size or had larger fiber cross-sections (such as in **Figure 6.7-2b**), overlapping coil segments were found to be adhered too strongly together to disengage.

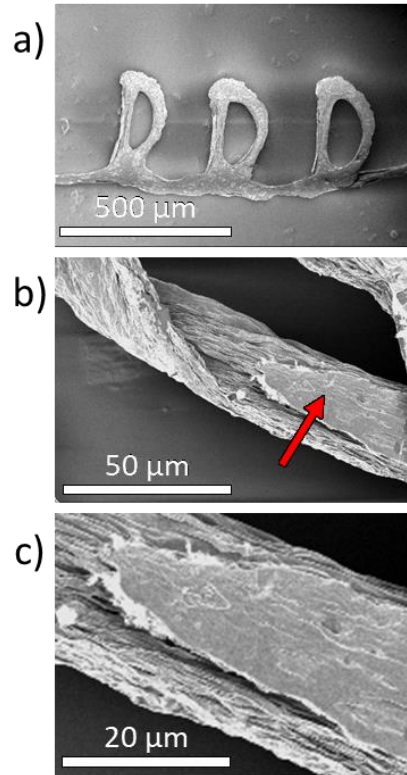


**Figure 6.7-3:** Scanning electron micrographs of printed coils. (a) Coils were printed at  $v^* = 0.16$ , dried, and inverted onto a metal stub for imaging. (b) After drying, the coil shown was pulled apart, remaining unbroken. The smooth righthand region (red arrow, c) shows the original region of overlap between coils. An otherwise wrinkled surface morphology is indicative of shrinkage from the solidification process.

### 6.7.2. Extensibility and Piezoresistivity of Printed Coils

Due to their extensibility from non-adhering contact points, the printed CNT coils can function as extensible conductive materials, with potential applications in flexible electronics. This contrasts metallic coils made by plastic deformation of metal wires [219], [270]. In our case, wires with sub-millimetric features were created without lithographic processes or complex printing paths. These were tested using a custom fixture mounted in a rheometer which was used to apply programmed displacement while measuring electrical properties (**Figure 6.7-4**).

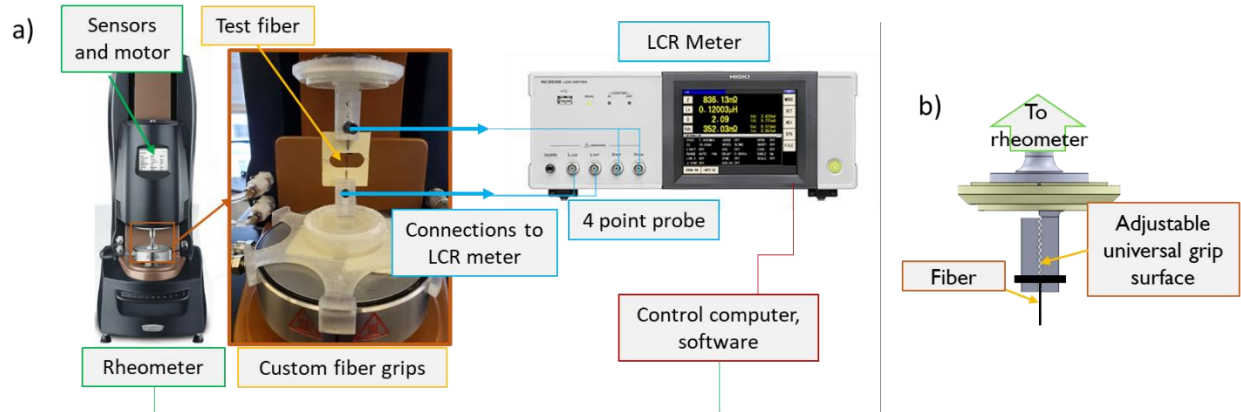


**Figure 6.7-4:** Design and layout of testing apparatus. (a) Mounted coils were attached to a loading frame in a rheometer with lightweight cables connected to an LCR meter. (b) Fiber grips used a textured mount to hold the cardstock mount on the rheometer. The schematic shows the upper fixture.

The extensibility of the printed CNT fibers is shown in detail for 3 representative samples: a linear fiber, a meandering coil, and a dense coil (**Figure 6.7-5**). During mechanical extension, an electrical connection probed the changing resistance of each fiber. The linear fiber reached an extensional strain of 8% before failure, while the meandering line extended to 71% and the dense coil to 216% before failure. The dense coil structure maintained a conductivity within 1% of the original value up to 50% strain, and within 5% up to 216% strain, at which point its initial resistance had increased 20%.

Starting resistances were 361  $\Omega$ , 1140  $\Omega$ , and 592  $\Omega$  for the three cases. The low conductivity of the coiled structure is consistent with the portions of overlapping coil forming electrical connections across the overlap. As such, the coiled structure further showed characteristic jumps as coils systematically unwound in pairs, leading to stepwise increase in resistance at higher strain levels. The doubling phenomenon is likely due to formation of the coils in a “double coiling” regime rather than a “single coiling” regime during printing, which would result in slightly larger spacing between each set of two coils [259]. The final rupture of the fiber occurred at a point where a coil overlap had separated, leading to a sharp section with high curvature in the fiber, which has been shown to lead to failure in coiled fibers [267]. Due to the defects caused by the coiling, the linear fiber showed the greatest strength of 18 MPa. Greater overall fiber strength would be expected with greater mechanical draw ratio.

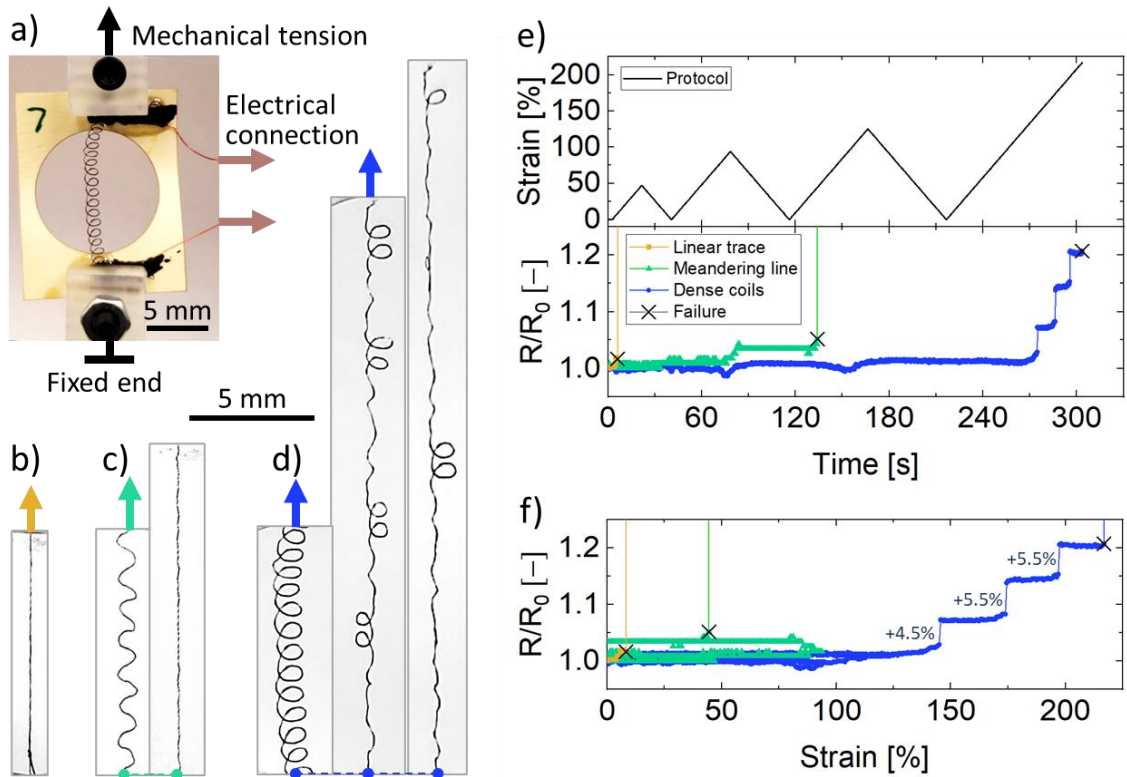


**Figure 6.7-5:** Fibers and coils were subjected to mechanical strain while monitoring the electrical resistance. (a) Mounted coils were attached to a loading frame. (b) A linear fiber printed with  $v^* = 1.31$ , a meandering coil printed with  $v^* = 0.43$ , and (d) a coil printed with  $v^* = 0.16$ .

### 6.8. Perspective

A regime of potentially improved properties could not be accessed because they required stronger and/or faster acting antisolvents which in our process instead clogged the printer nozzle. During fiber spinning, a mechanical draw wheel continuously provides a tensile force on the spun fiber [34], which is much stronger than shear forces attainable within a bulk fluid of standard viscosity. Future steps would include methods to adhere the fiber strongly to the build plate or some projection from it during printing. In exchange, the observed coiling regime would not be possible during fiber spinning because the draw wheel provides a constant tensile force, effectively analogous to  $v^* > 1$ .

### 6.9. Conclusions

We introduce a method of printing into a Newtonian viscous bath that precipitates carbon nanotubes from the extruded ink into linear fibers showing tailorable and high

conductivity and coils showing high extensibility. Printed CNT threads in a strong antisolvent show average conductivity of  $10^5$  S/m and average specific conductivity (conductivity per weight) of  $2 \times 10^3$  S m<sup>2</sup>/kg, comparable with gold. The accessible printing regimes are analyzed, with particular focus on the speed of counter-diffusion of the ink solvent and the bath liquid, which allows for tuning of fiber diameter, conductivity, and specific conductivity respectively over 1, 4, and 5 orders of magnitude. When the speed of solvent counter-diffusion is high, the conductivity of resulting threads is highest. When extrusion speed is also high, we observe a coiling instability which creates threads with regular coil morphology, allowing for intricate designs despite a linear extrusion path. Resulting coils, once dried, can be fully removed from the bath and undergo up to 50% strain with <1% change in conductivity or 170% linear extension with 20% change in conductivity. This methodology allows simple printing of complex coil structures with potential application to circuitry and flexible interconnects.

---

## Chapter 7. Fabrication of columnar field emitters by pointwise deposition and fluidic shaping of carbon nanotubes

---

### 7.1. Abstract

We introduce a new method for fabricating fiber-like field emitters using pointwise deposition of aqueous suspensions of carbon nanotubes (CNTs). Liquid ink is held between a flat base and an upper locating pin as the ink solvent dries and CNTs densify via capillary forces. The resulting field emitters have high aspect ratios, dense packing of CNTs and, importantly, a large base providing mechanical stability and enhanced thermal/electrical contact compared to emitters fabricated from wet-spun CNT fibers and CNT forests. These attributes enable excellent field emission properties—namely, a high field enhancement factor and low turn-on voltage—for a range of tested emitter sizes. The noteworthy improvements in emission from these CNT structures alongside the versatile fabrication process motivates future work on emitter array manufacturing and device integration.

### 7.2. Introduction

#### 7.2.1. Background

Cold cathode field electron emission occurs when a high electric field (typically  $>1\text{V/nm}$ ) is applied in vacuum to a material having a low work function ( $< 5\text{ eV}$ ), causing the sample to eject electrons into the vacuum via quantum tunneling. A sharp apex at the emitter tip

can amplify the resulting local electric field (**Figure 7.2-1**), reducing the applied voltage required to generate emission current. Single emitters and arrays have a wide range of potential applications in consumer, space, and military technologies. They can serve as electron guns in high-powered microwave generators, provide radio frequency amplification in traveling wave tubes for GHz-THz wave generation, and comprise components of flat panel displays, and vacuum micro- and nano-electronics [271]–[273]. Towards these applications, carbon-based and particularly CNT field emitters show particularly high emission current densities and moderate work functions ( $\sim 5.0$  eV), along with an intrinsic high aspect ratio ( $>1,000$  length/radius is typical), resulting in low turn-on fields (demonstrated  $< 1$  V/ $\mu\text{m}$ ).

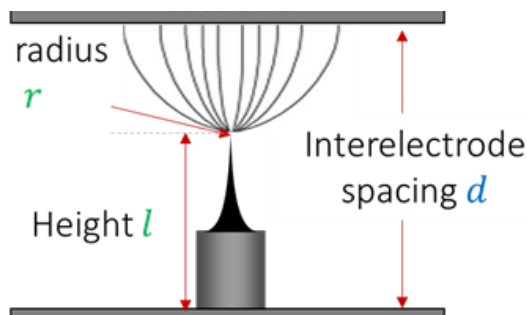


**Figure 7.2-1:** Schematic of field emitter between two charged plates, with tip radius  $r$ , overall height  $l$ , and interelectrode spacing  $d$ .

Various approaches have been used to design field emitters from CNTs. However, CNT-based emitters suffer from short lifespans due in part to low decomposition temperature ( $\sim 1000^\circ\text{C}$  in vacuum) compared to metals [274]. CNT field emitters typically are grown by chemical vapor deposition (CVD) into patterned forests, or assembled by placement of wet-spun CNT fibers. Fiber-based emitters show improved lifespans compared to CNT forests likely due to improved alignment and thermal transport between CNTs, and emission improves further with the quality of the CNT alignment within the fiber [275]. However, due to the methods of production it has been challenging to place CNT fiber emitters vertically onto structures and into arrays, which for uniform emission require a high degree of regularity in height, spacing, and structure, and benefit from good thermal/electrical contact with the base [240]. Recently, Perales-Martinez, et al., demonstrated 2D printing of CNT structures for field emission, allowing facile device integration and particularly low-cost devices [276], and similar approaches to woven fiber emitters appear promising [239],



although this and other work with 2D/3D printed emitters have been limited in performance by material properties and accuracy/resolution limits [277].

In this chapter, we introduce our work on a new, point-wise fluid deposition process to fabricate small, high aspect ratio, aligned CNT structures directly onto a surface, and further show that these emitters exhibit excellent field emission properties. This work builds upon existing methods to produce high-concentration aqueous-based CNT inks [34] and printing in-plane structures with tailored alignment of CNTs [278], and adapts the materials and concepts to out-of-plane, 3D structures to create field emitters that show enhanced performance over current state-of-the-art materials.

### *7.3. Fabrication by static stretch-printing*

We directly fabricate vertically standing CNT field emitters by straining a drop of an extensible (i.e., having extensional rate-thickening viscosity) CNT ink. A 50  $\mu\text{L}$  fluid drop is first deposited by syringe extrusion onto a copper post of 3-6 mm diameter serving as a large base, with a narrow (1 mm diameter) upper locating pin. The suspended CNTs align into a fiber-like structure as the ink dries and densifies via capillary forces (**Figure 7.3-1a-d**), forming self-supporting structures with slender tips in a desired location with a large rooted base.

To maintain extensibility under sustained extensional straining during static evaporation of water, which normally leads to fluid breakup [279], we begin with a surfactant-assisted aqueous dispersion of CNTs and add 0.05 wt% of a high molecular weight rheological modifier (4 Mg/mol poly(ethylene oxide)). This facilitates alignment of CNT microdomains over long distances (**Figure 7.3-1e,f**) and is burned off prior to tests without leaving residue by heating for 30 min at 350°C under inert argon gas flow. We have created emitters with aspect ratio (height/tip diameter) ranging from  $\sim 1$  to 1,000 and tip diameters of 10-500  $\mu\text{m}$ . Evaporation of the initial solvent typically takes 30-60 min, and could be accelerated via convective air drying. Through this process, many emitters can be made in parallel.

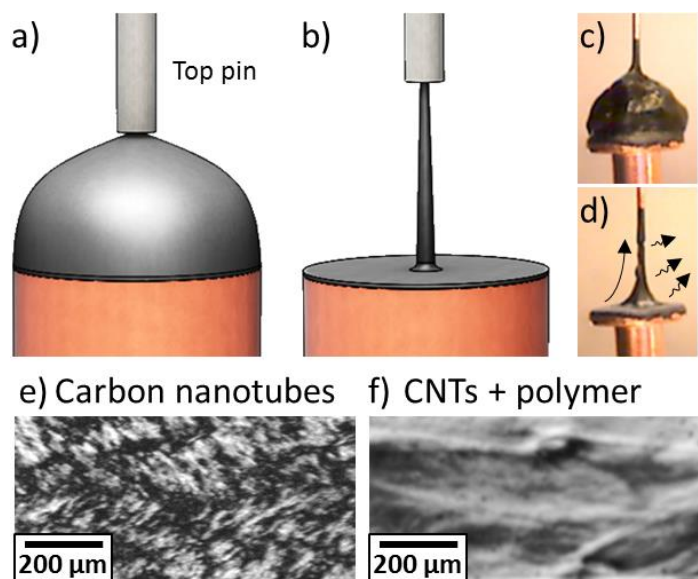


**Figure 7.3-1:** (a,b) Schematics and (c,d) photographs of the emitter fabrication process. (e,f) Transmission polarized micrographs of the surfactant assisted aqueous carbon nanotube (CNT)-based ink shows birefringent micro-domains that grow from (e) small, 10µm structures to (f) extended domains > 1 mm with the addition of 0.05wt % high molecular weight poly (ethylene oxide) to 0.72 wt% CNT, enabling the fabrication process.

The resulting field emitters have high aspect ratios, dense packing of CNTs and, importantly, a large rooted base providing mechanical stability and thermal/electrical contact compared to spun CNT fiber emitters (**Figure 7.3-2**). In addition, x-ray micro-computed tomographs ( $\mu$ CTs, ZEISS Versa 520, taken at 60 kV) show that there is some residual metal catalyst (visible as bright spots) and there are no internal voids within the resolution of the scanner (1  $\mu$ m) before or after polymer removal (**Figure 7.3-3**). In addition, as shown in Figs. 2-3, the top of the emitter structure can have a blunt or flattened surface, which can contribute to more precise height control and distributed charge during field emission when compared to an emitter with a pointed tip.

The CNT-Cu contact resistance was measured to be negligible compared to the resistance of the CNT structure itself using an LCR meter with four-point probe setup (Hioki IM3536), validating the choice of contact structure.

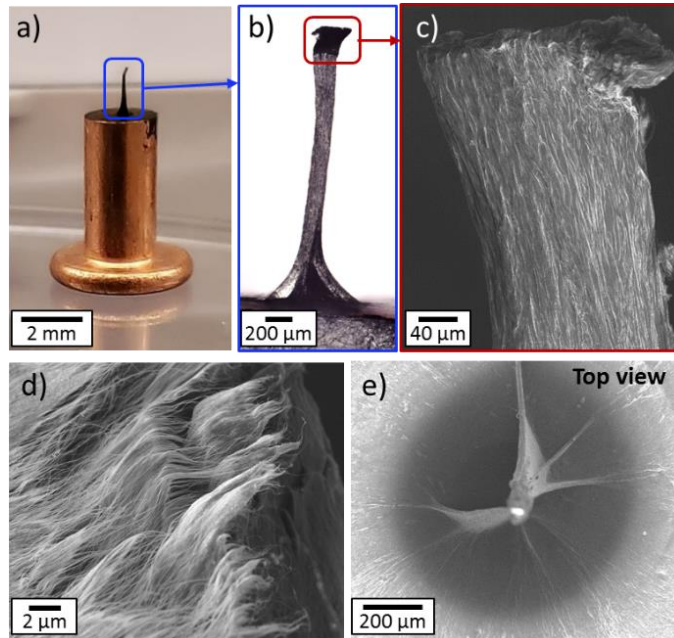


**Figure 7.3-2:** (a) Photograph and (b-e) micrographs of a representative emitter with aspect ratio of 10, showing a widened base and a blunt tip, approximately 120 $\mu\text{m}$  diameter. (d) A close view shows densely-packed, long, and aligned CNTs/bundles on the emitter tip. (e) An overhead view better shows the far-reaching, rooted contact with the flat base substrate, which provides mechanical support and enhanced thermal/electrical contact.

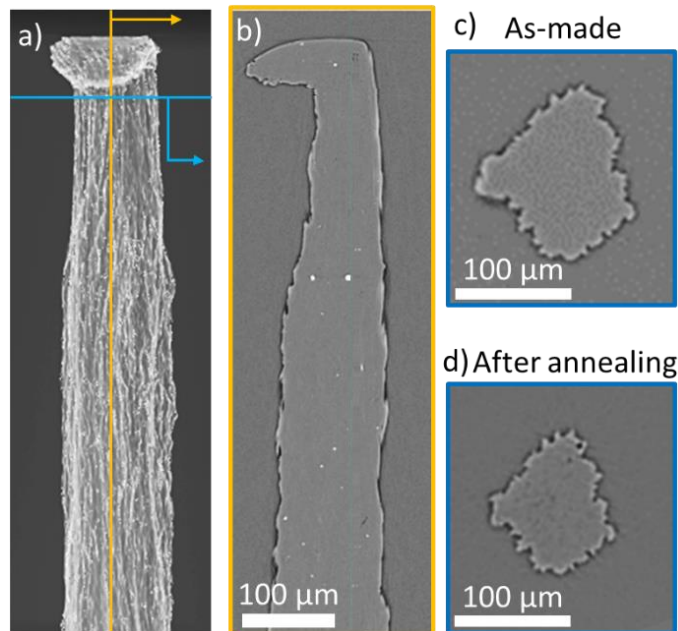


**Figure 7.3-3:** X-ray microscale computed tomographs ( $\mu\text{CTs}$ ) of an emitter. (a) Side view of 3D reconstruction with (b) a vertical cross section and (c) representative horizontal cross section. (d) A cross section in the same location as (c) is shown after annealing to remove polymer, showing size reduction and no void generation.

### 7.4. Field emission theory

The Fowler-Nordheim (FN) theory [280] is most commonly used to describe cold cathode field electron emission, including from CNTs [281] although the nanostructure adds some uncertainties compared to measurements of bulk materials [274], [282], [283]. In addition, the theory assumes that there are no temperature effects (*i.e.*, joule heating from high currents/resistances). The FN equation describes the emitter current,  $I$ , in response to applied electric field,  $E$ , as

$$I(E) = S_{\text{eff}}A(\beta E/\phi)^2 \exp[-B\phi^{1.5}/\beta E] \quad (1)$$

where  $A = 1.54 \times 10^{-6}/W$  and  $B = 6.83 \times 10^9 W^{3/2}$  are constants,  $S_{\text{eff}}$  is the effective emission area,  $\beta$  is the field enhancement factor,  $\phi$  is the work function (taken to be 5.0 here), and  $E = V/D$  is the gap electric field created by applying a voltage  $V$  across a distance  $D$  between the top of the emitter and the charged anode. The field enhancement factor may then be directly measured by plotting  $1/V$  vs  $\ln(I/V^2)$  as in **Figure 7.4-1**, and calculating the resulting slope in the linear region. Our FN data was confirmed to be orthodox for all three samples, with  $f_{\text{low}} = 0.14 < f^{\text{extr}} = [0.34, 0.36, 0.33] < f_{\text{up}} = 0.42$  [284].

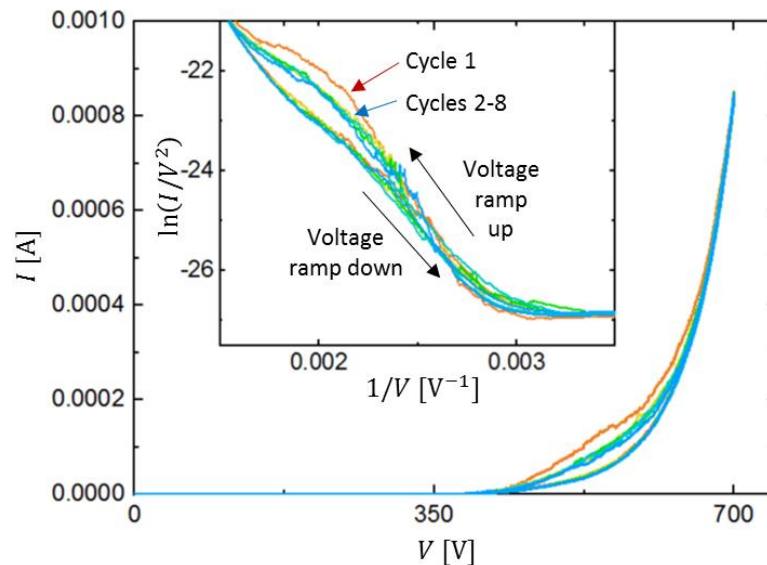


**Figure 7.4-1:** I-V and Fowler-Nordheim curve showing measured field emission properties of one representative deposition-fabricated CNT emitter. The performance shows no change following the first half cycle (labeled, orange line).

### 7.5. Field emission properties

Field emission was tested using a Keithley 2675A source-meter and vacuum chamber at  $5 \times 10^{-8}$  Torr. Our field emitters show repeatable cyclic behavior when tested over 8 cycles from 0 to 700 V and back to 0 (**Figure 7.4-1**), with a constant 500  $\mu\text{m}$  gap between the anode plate and the tip of the emitter cathode. Results showed change only on the initial cycle, likely due to desorption of surface adsorbates and initial outgassing. The same testing protocol was carried out for a series of three emitters with varying aspect ratios and diameters. These showed field enhancement factors of  $2 \times 10^5$ , turn-on voltages below 0.3 V/ $\mu\text{m}$ , and current densities of 32 A/ $\text{cm}^2$  at 58 kV/m externally applied electric field (**Figure 7.6-1**), outperforming similar emitters made by individual, dense CNT fibers in all three metrics. In comparison, typical field enhancement factors for nanowires from many different materials are typically  $2 \times 10^3$ - $2 \times 10^4$ , [274] roughly one to two orders of magnitude lower. The current density measured here was not a limiting/maximum value as these emitters were not tested to failure, but still compares favorably to a range of CNT-based emitters (**Figure 7.6-1c**). Intriguingly, post-run micrographs show no evidence of decomposition (**Figure 7.6-2**) despite exposure to current density levels that have previously been shown to degrade CNT fibers [275], supporting the design choice to increase contact with the base for improved dissipation.

### 7.6. Discussion

Initial results demonstrate fabrication of functioning, CNT field emitters with a range of sizes. Looking forward, this process can be refined further to improve shape consistency of emitters. The fiber aspect ratio is believed to contribute to the field enhancement factor and could be further increased. In this process, the aspect ratio is ultimately limited by the stability of the fluid thread while the solvent evaporates. Use of a more volatile solvent and more polymer can enhance this stability, if such inks can be made without phase separation. The use of liquid ink in the fabrication process further allows complementary techniques to be employed, such as by mixing high conductivity and stable materials such as gold, titanium, and molybdenum powder directly into the precursor ink or by coating the fabricated emitters with similar materials afterwards by sputtering or metal evaporation.

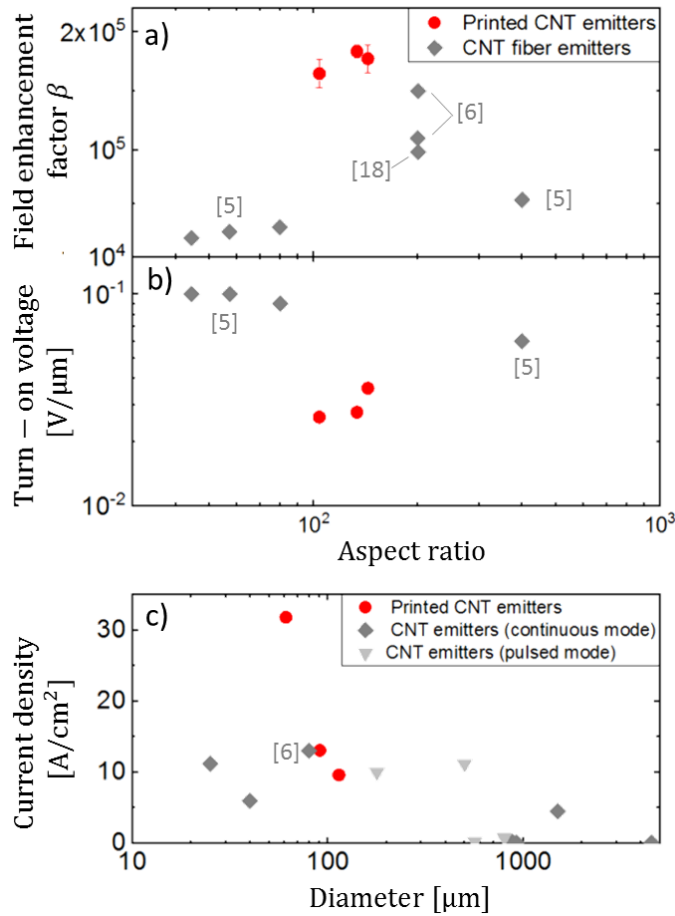


**Figure 7.6-1:** The performance of our printed CNT emitters compares favorably with benchmark literature values for previously-made CNT fiber-based emitters from [20], [240], [275], showing (a) field enhancement, (b) turn-on voltage (determined by the peak in the second derivative of the FN curve), and (c) current density at 58 kV/m externally applied electric field, versus emitter aspect ratio (height/tip diameter) or tip diameter. Current density is compared to results from CNT emitters of varying geometries, fabrication processes, and analysis modes (continuous, pulsed), with unlabeled points reviewed in [285].

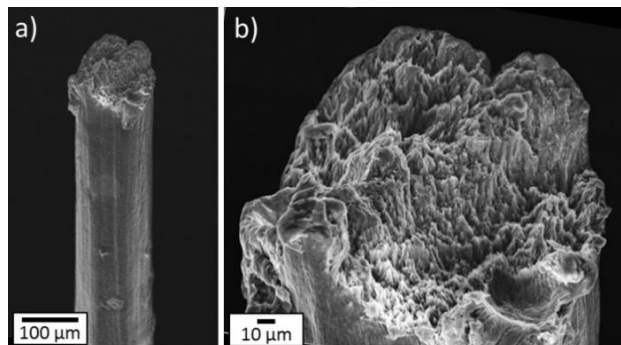


**Figure 7.6-2:** Post-testing scanning electron micrographs of a printed CNT emitter show no degradation or fraying of the tip. (Note that this emitter began without a flattened top.)

The process itself may readily be used to make an array of emitters of unbounded size by using an array of locating pins above a larger surface to tailor the array to be uniform or non-uniform (such as conforming to a nonplanar base; or accommodating screening effects). Indeed, tailorability and positioning accuracy are both critical to large-scale display technology, where uniformity of emitter lateral spacing drives field concentration and ultimate device current density. Notably, this direct deposition process may be used to print emitters onto integrated devices without damage, as the liquid within the ink is confined to the drop and printing is handled at room temperature.

### *7.7. Conclusions*

We have introduced a method of additive deposition of individual, dense, and vertically-aligned CNT emitters. Field emission measurements validated state-of-the-art performance compared to CNT-based field emitters. This method further enables sequential or parallel deposition of emitters onto specified locations on a large base or preformed electronic circuit, enabling production and integration of arrays of high-performance field emitters with controlled shape for a variety of applications.

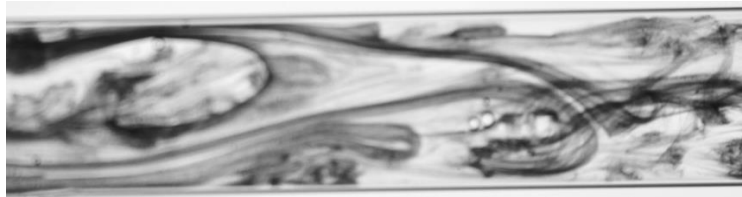
### *7.8. Materials and Methods*

Carbon nanotube inks used for pointwise stretching were prepared by mixing carbon nanotube powder as in **Chapter 5** or [35] and then adding an additional 0.05 wt% of a high molecular weight rheological modifier (4 Mg/mol poly(ethylene oxide)) mixed using a vortexer, as in [286]. Drops were deposited manually and stretching was performed using a modified MakerGear M2 with custom gcode.

---

## Chapter 8. Automating the 3D-printing of carbon nanotube field emitter arrays for high-current performance

---



*Chapter Introduction Image: Polarized transmission micrograph of CNTs with PEO polymer*

### 8.1. Abstract

Advancing the previous work, we have continued to develop the printable CNT ink to automate the process. We report the first 3D-printed arrays of freestanding field emitters, made on diverse substrates with substantially less waste compared to conventional etching techniques. Total fabrication time is <10 minutes, the fastest of any published field emitter array (FEA) production method to our knowledge, with material costs of <\$0.01 per emitter and no cleanroom requirements. Enabled by rheologically tailored carbon nanotube (CNT) inks and two custom direct ink writing methods, our FEAs exhibit aggregate current output over  $100 \text{ mA/cm}^2$  and field enhancement factors over  $10^5$ , surpassing the performance of existing freestanding CNT FEAs [281]. Emission data indicates that our arrays have effective emitting length scales under 100 nm (corresponding to CNT bundles protruding from micron-scale emitter tips), with local emission current over  $10^6 \text{ A/cm}^2$ . These results



have wide applicability to radar, displays, electron projection lithography, mass spectrometry, electric space propulsion, and medical imaging [276], [287].

Field emitters are sharp geometries that quantum tunnel electrons under an applied voltage, requiring less power and having less oxidative degradation than thermionic electron sources. Arraying field emitters across a plane increases emission currents. Conductive nanomaterials enhance the sharpness of such emitters, and planar field emission sources made from CNT inks show good low-vacuum emission current without significant degradation [276], while arrays of high aspect ratio CNT field emitters made through manual positioning of chopped spun fiber show high field enhancement and low turn-on voltage [281]. Alas, 3D printing has only been applied to field emission using conductive plastic composites, which fail to perform at state-of-the-art levels due to intrinsic material properties [277].

## 8.2. Materials and Methods

### *Rheology and ink development*

Carbon nanotube inks used for extrusion while printing were prepared by mixing carbon nanotube solutions to 0.75% in water stabilized by sodium deoxycholate (DOC) surfactant and then adding 1M poly-ethylene oxide (PEO; Sigma Aldrich).

### *Array fabrication*

Arrays were fabricated using an experimental, pressure-controlled extrusion 3D printer (NOVA, Voltera, Kitchener, ON, Canada) with optical alignment and surface mapping, extruded using a 500  $\mu\text{m}$  diameter nozzle tip.

## 8.3. Design of First Printing Method: direct deposition

We print FEAs by pressure-controlled extrusion (Voltera NOVA) of a CNT ink composed of 5% wt CNTs in water, stabilized by 1.5% sodium dodecylbenzenesulfonate (SDBS) surfactant. We characterize their performance as diodes, negatively biasing a FEA relative to a grounded planar steel counter-electrode, in vacuum at  $5 \times 10^{-7}$  torr. In this first printing method, a 200  $\mu\text{m}$  nozzle contacts liquid ink to a substrate, extruding while moving vertically, and various substrates were usable (e.g., copper, paper, indium tin oxide). The high yield stress of the concentrated ink allows for direct printing of 3D morphologies, with the process and resulting emitters shown in **Figure 8.3-1**.

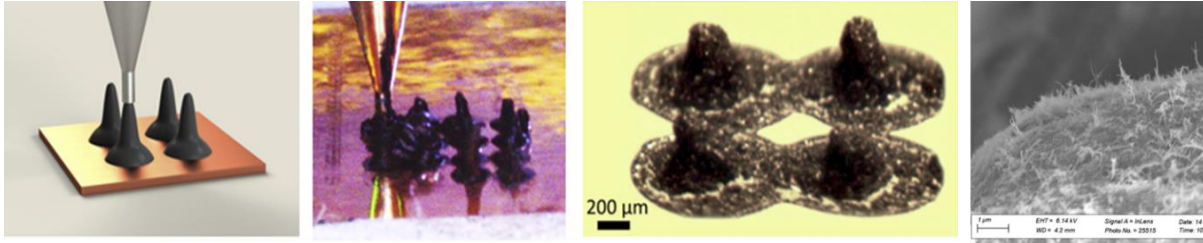


**Figure 8.3-1:** First printing method and fabrication results. A) CNT ink is extruded onto a substrate before quickly drying and shrinking. B) 4×4 emitter array as being printed. C) Zoomed-in optical image of an array fabricated on indium tin oxide coated glass. D) Top-view SEM of one emitter after test showing hairlike fuzz from CNTs emerging on the top surface. The width of the image in (D) is 10  $\mu\text{m}$ .

## 8.4. Design of Second Printing Method

### 8.4.1. Ink design for extensibility

To improve emission performance, we leverage extensional rheology [288] to stretch printed droplets, further reducing tip diameter and inducing CNT alignment. Well-dispersed liquid solutions of CNTs align in extensional flow, though such fluids are also extensionally-thinning, leading to rapid breakup of fluid structure. In this second printing method, addition of polymer (0.5 wt% of poly-(ethylene oxide) with 4 MDa molecular weight) to the base ink allows printed emitters to stretch without breaking, solidifying into freestanding filaments. A comparison of the liquid crystalline structure of three inks after cessation of shear flow in a microcapillary shows revealing that a 0.75% CNT ink stabilized by DOC has micron-scale liquid crystalline microdomains (**Figure 8.4-1a**), while a mixture of the same CNT ink with added PEO exhibits a continuous an extended spanning the frame of the micrograph,  $>400 \mu\text{m}$  (**Figure 8.4-1b**). In contrast, the 5% CNT ink used in the first printing method absorbs too much light to observe (**Figure 8.4-1c**); however, based on the concentration and CNT aspect ratio (5%, 78), it is expected to fall within the concentrated phase and not the liquid crystalline phase (see **Section 2.4** for details).

A second comparison of the rheology of these inks under a stretching step (**Figure 8.4-2**) shows the 0.75% CNT ink breaks into fluid droplets when plates are separated, while a PEO/water solution will form a sustained liquid bridge for long times. A mixture of the two will form a long, sustained bridge.

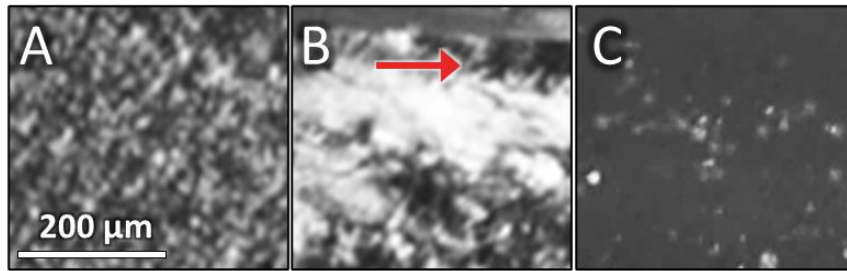


**Figure 8.4-1:** CNT inks viewed by transmission polarized microscopy, with stretched and deposited ink viewed through a 50  $\mu\text{m}$  thick capillary. A red arrow in (B) indicates an applied pressure to cause shear from left to right, which was removed before imaging. Inks are composed of (A) a 0.75% CNT ink stabilized by DOC, (B) the same ink with added PEO, and (C) a 5% wt CNT ink stabilized by SDBS.

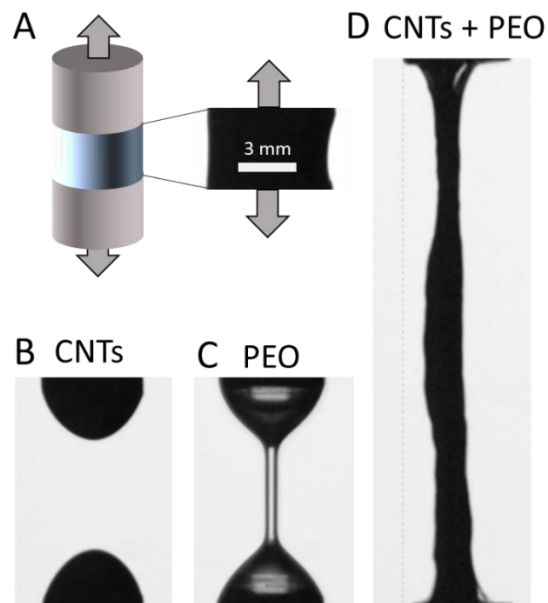


**Figure 8.4-2:** A measurement of extensional viscosity using a capillary breakup extensional rheometer for a CNT solution in water, a PEO solution in water, and a mixture of CNTs and PEO.

Leveraging the cohesive strength of the entangled ink, we create a textured conductive substrate by coating chromatography paper with colloidal silver ink and a diluted dispersion of CNTs. Similar to the direct-print method, we first print ink in droplets onto this substrate, and a glass slide mounted parallel to the substrate contacts the droplets to

stretch vertically, as shown schematically in **Figure 8.4-3**. Following drying for  $\approx 8$  minutes, we cleave the array from the glass slide; fabrication results are shown in **Figure 8.4-4**.

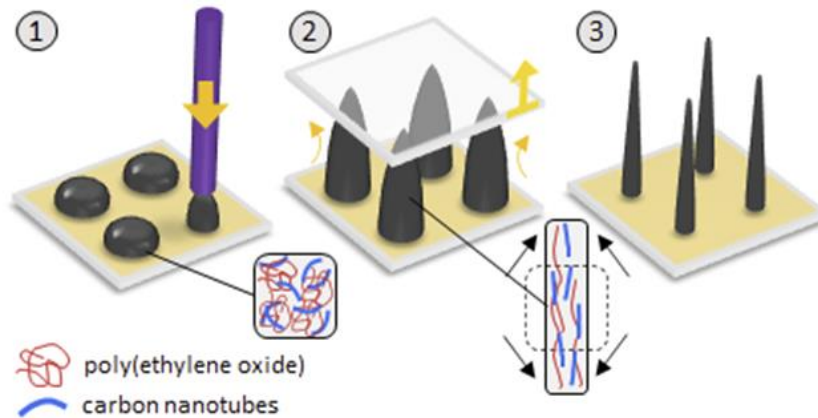


**Figure 8.4-3:** Material behavior and process for the second printing method including (1) depositing, (2) adhering to a plate and stretching vertically, while drying time is allowed, and (3) removal of the top plate, leaving a freestanding array of emitters.

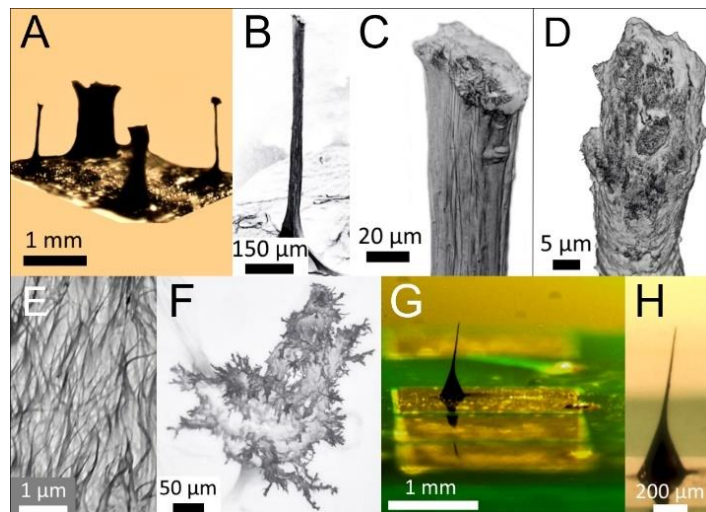


**Figure 8.4-4:** Second printing method fabrication results (SEM colors are inverted for clarity). A) Emitter array with spike and ribbon morphologies (size variations are from material inhomogeneity and oblique contact with the ink droplets). B) Spike emitter. C) Closeup of spike emitter tip. D) Closeup of a spike emitter tip after field emission. E) Closeup of CNTs protruding from emitter tip. F) Tip failure following emission at high current. G) Photograph of emitter stretch-printed onto the conductive pad of a printed circuit board. H) Closeup of the emitter in (G).

### 8.5. Field emission results

FEAs made by the first method have a turn-on field strength of  $1.5 \text{ V}/\mu\text{m}$  and field enhancement factor of  $\beta \approx 2 \times 10^4$  (Figure 8.5-1). Despite imperfect geometric uniformity among emitters, FEAs made by the second method have a turn-on field strength of  $0.6 \text{ V}/\mu\text{m}$  and an outstanding field enhancement factor of  $\beta \approx 2 \times 10^5$ , 10,000 times larger than expected for a metal emitter of the same spiked geometry, owing to the CNT nanostructure.

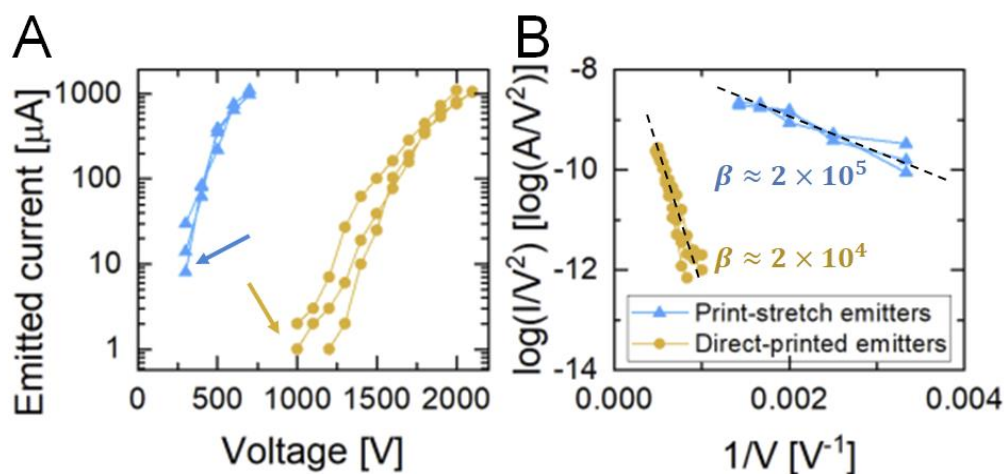


**Figure 8.5-1:** Emission results for emitter arrays made by both printing methods, with 3 tests per  $2 \times 2$  array. A) Direct emission, where the arrows indicate turn-on voltage. In comparison, a flat coated sheet of CNTs emitted no current over the same voltage range. B) Fowler-Nordheim plot showing comparative field enhancement factor  $\beta$  for emitters from both printing methods.

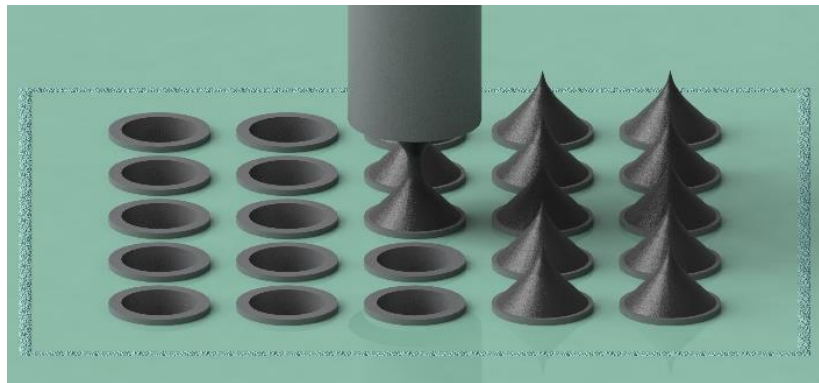
### 8.6. Conclusions

Two methods for the automated printing of arrays of CNT-based field emitters were compared. In the first, a high concentration of short CNTs enabled the direct extrusion of “mound”-like emitters. In the second, an ink designed to have a very stable fluid thread under extension was printed and then stretched to make arrays. Both succeeded in forming arrays, and the print-stretch method showed approximately an order of magnitude improved performance due to the finer resolution and CNT quality. However, the difficulty of the process may impede application compared to other direct-printing methods, especially in areas for which additive manufacturing excels, such as over large or non-flat substrates.

---

## Chapter 9. Individually addressable, 3d-printed carbon nanotube field emitter arrays for large-area vacuum electronics

---



Chapter Introduction Image: Schematic of Printing a Field Emitter Array

### 9.1. Abstract

We report the design, fabrication, and characterization of the first known 3D-printed, individually addressable field emitter arrays (FEAs), created via direct deposition of a made-for-purpose carbon nanotube (CNT) ink. The array fabrication is maskless yet automated, rapid (<2 minutes), inexpensive ( $\ll \$0.01$  per emitter material cost), and produces substantially less waste than traditional subtractive manufacturing methods. Resulting CNT FEAs have tip current density above  $10^6$  A/cm<sup>2</sup>, array current density over

100 mA/cm<sup>2</sup>, and field enhancement factors over 10<sup>5</sup> cm<sup>-1</sup>, matching state-of-the-art CNT-based counterparts. Our approach unlocks the potential for large area (meter scale), individually addressable FEAs, with great relevance to electron projection lithography (EPL), radars, displays, medical imaging, and other vacuum microelectronics applications.

## 9.2. Introduction

Compared to mainstream thermionic cathodes, CNT-based field emission electron sources consume less power and tolerate poorer (>10<sup>-7</sup> Torr), reactive vacuum [289], [290]. Although cleanroom-microfabricated FEAs attain high performance, their manufacturing is costly, time consuming, and environmentally detrimental due to etchants typically used and their waste products; moreover, the area of a monolithic FEA is limited by the size of the wafers employed [240], [286]. CNTs are favored for field emission over many other materials due to characteristic low power needs and outstanding electron transport properties of the nanotubes. However, CNT-based FEAs have required manual assembly of individually-produced emitters [240], dramatically limiting scalability, or otherwise rely on methods of manufacture that prevent individual addressability, such as weaving long fibers [291] or spincoating CNT inks over an area. These factors hinder use of FEAs in large-area applications, especially when externally programmed electric field compensation is required for uniform array operation, *e.g.*, electron projection lithography (EPL)[287].

Additive manufacturing (AM) can address these limitations by enabling customized material deposition on arbitrary substrates in ambient conditions. Existing literature has reported AM of individual, free-standing CNT emitters [286] and planar, 2D CNT traces [276], [292]; expansion to individually addressable, multi-emitter arrays is required for many applications yet has not been achieved due in part to process challenges of material handling and alignment of emitters into regular arrays. The need for this development and resulting devices is apparent in industry. For instance, low-cost FEAs hold great utility for healthcare, potentially enabling phase contrast X-ray imaging of soft tissue without contrast media [293].

## 9.3. Methods

### 9.3.1. Device Design

The proof-of-concept FEAs comprise 5 by 5 arrays of 1 mm-spaced CNT ink aliquots extruded on copper vias of a bespoke PCB (JLCPCB) individually addressed with 127 μm

copper traces (**Figure 9.3-1**). The CNT deposition was performed using an experimental, pressure-controlled extrusion 3D printer (NOVA, Voltera, Kitchener, ON, Canada) with optical alignment and surface mapping. With a 500  $\mu\text{m}$  diameter nozzle tip, we created arrays of free-standing conical emitters ( $384 \mu\text{m} \pm 69 \mu\text{m}$  tall,  $65 \mu\text{m} \pm 3 \mu\text{m}$  tip diameter). The process was tuned to attain narrow tip diameter with protruding surface-level CNTs and a large-area contact with the PCB surface to benefit electrical and thermal conduction, resulting in conical shapes.

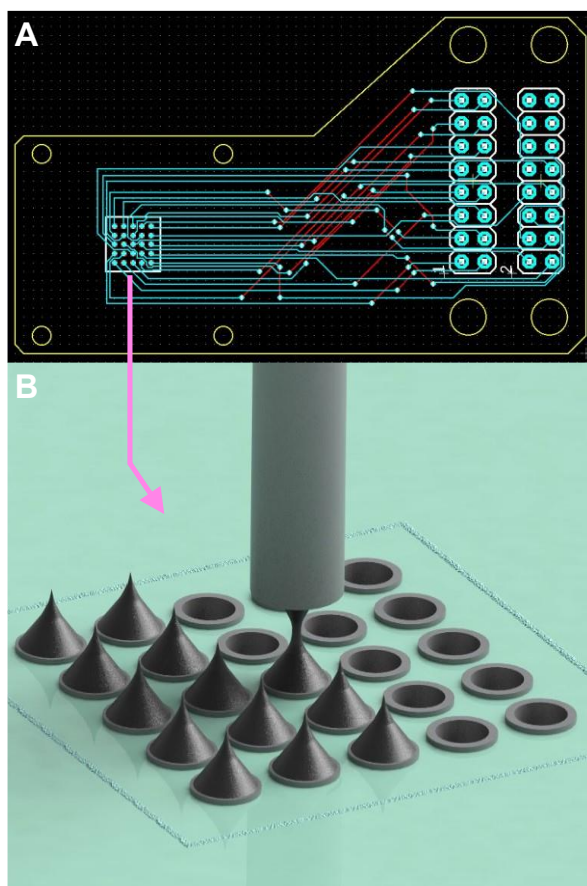


**Figure 9.3-1:** Printing of arrays of individually addressable field emitters. A) PCB wiring schematic. B) Rendering of point-by-point printing process from cylindrical printing nozzle; each emitter is extruded on top of a different PCB via, yielding an array of individually addressable field emitters.

### 9.3.2. CNT Ink Preparation

The deposited ink was tailored to fulfill competing specifications to create solid conical structures by extrusion of an ink with a high loading of CNTs and fine feature resolution. The resulting custom inks contain 13-15 wt% CNTs (CheapTubes, 10-20 nm diameter, 0.5-



2.0  $\mu\text{m}$  in length) in an aqueous dispersion stabilized by sodium deoxycholate (DOC) surfactant (15-17 wt%) and were prepared by gradual addition of a mixture of the dry CNTs and DOC to water followed by tip sonication at low power (Misonix XL-2020, power “2”) for 30 minutes until smooth. Finally, a small amount of pre-formulated ink with single-walled CNTs were added (0.10-0.15% final mass fraction in the ink; Coat\_E, OCSiAl) to improve solution ductility. This method builds on previous methods of ink production, using an understanding of the scalings of CNT-based rheology to tailor the formulations [35].

To avoid chemical curing or sintering steps, these concentrated inks were optimized to have moderate-to-high shear yield stresses at rest. Yield stress behavior mechanically enables the printing of objects with good feature fidelity [70]. For a field emission application, the presence of a yield stress also facilitates the formation of sharp, centered peaks during detachment of the ink from the printing nozzle due to the fluid filament breakup [294] (shown schematically in **Figure 9.3-1b**). After ink deposition, the yield stress counteracts gravity and Laplace pressure from the surface tension of the ink solvent to preserve printed tip features in stable form [71]. We compared printed arrays made from two inks with yield stresses of 250 and 610 Pa respectively having 13 and 15 wt% CNTs, to assess the impact on resolution resulting from small variations in ink production. Sub-100  $\mu\text{m}$  tips (**Figure 9.3-2**) were extruded with the 500  $\mu\text{m}$  nozzle. The high-concentration ink was used for most of the remaining study. Further, all inks exhibited shear-thinning rheology, allowing extrusion from fine nozzles despite high stresses exhibited at rest. The CNT ink material cost was \$6.63 per mL of ink, or \$0.00066 per emitter with volume of  $10^{-4}$  mL.

After printing, the solvent was removed by evaporation in ambient conditions. The high CNT content was required to prevent excessive shrinkage during drying, even though similar yield stress levels could have been achieved by using a smaller concentration of longer CNTs [36]. Inks with higher concentration could be produced with 18% CNT content, but could not be extruded without clogging. Altogether, this ink formulation facilitated the printing of short, freestanding structures (**Figure 9.3-3**), requiring neither polymeric fillers that would reduce electrical conductivity of the emitters, nor a curing step that could hinder PCB process compatibility.

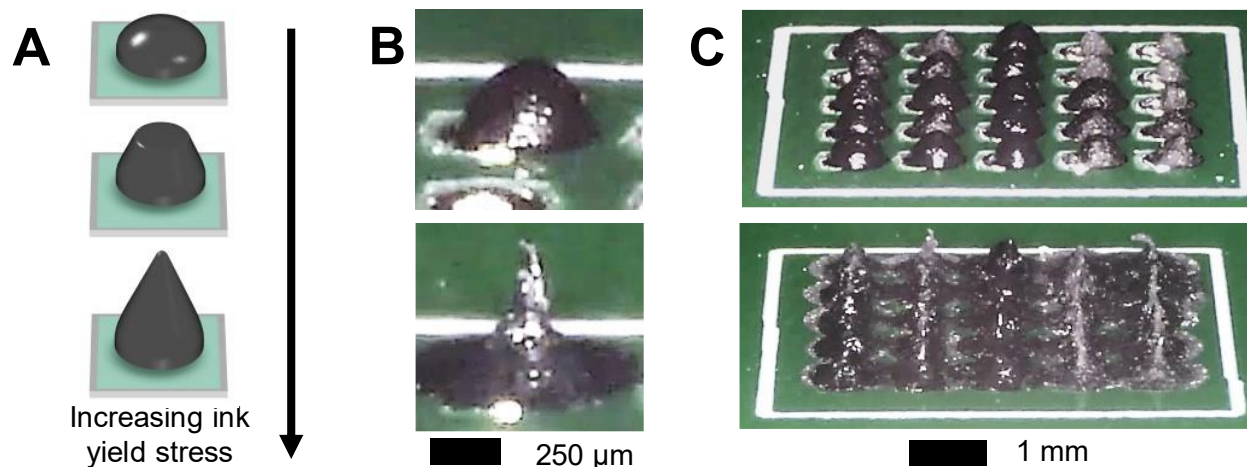


**Figure 9.3-2:** Effects of ink modulation. A) Schematic showing individual emitter geometry as affected by ink yield stress. B-C) Optical photographs of FEAs as affected by ink yield stress variation (top row 250 Pa, bottom row 610 Pa).

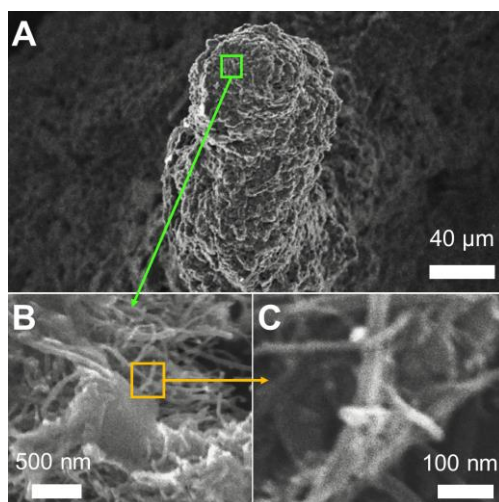


**Figure 9.3-3:** Scanning electron micrograph (SEM) views of a 3D-printed emitter. A) Overhead view, showing an as-printed tip diameter of  $\sim 65 \mu\text{m}$ , with far finer features derived from the CNT ink. B-C) CNT bundles protruding from emitter. The effective emission length scale from Fowler-Nordheim analysis is 4-7 nm per emitter, visually corresponding to protrusions on the multi-walled CNTs viewed in C.

#### 9.4. Field Emission Results

Electrical characterization in  $10^{-6}$  Torr vacuum of the 3D-printed FEAs in diode configuration (emitters, counter electrode) used a duo of Keithley 2657a power supplies (Keithley Instruments, Cleveland OH, USA). Emission results show a turn-on electric field of  $0.1 \text{ V}/\mu\text{m}$ , max current density of  $1 \text{ mA}/\text{cm}^2$ ,  $10 \mu\text{A}$  total emission current at  $1 \text{ V}/\mu\text{m}$ , and field enhancement factor  $\beta \approx 1 \times 10^5 \text{ cm}^{-1}$  (**Figure 9.4-1**), in line with previously demonstrated

results for CNT-based emitters [286]. Results are consistent for the full array and for three example individually addressed units, two on the array edges and one in the array center. Data follow the Fowler-Nordheim (FN) model [284], and standard FN analysis of the least-squares fitting of the data indicates that the emitters have 4-7 nm quantum tunneling features, potentially corresponding to single CNTs or portions of CNT sidewalls emitting from the top surfaces of the printed structures. In comparison, the emitter array made with the lower yield stress ink, forming mounds instead of peaks, exhibited approximately the same field enhancement factor  $\beta \approx 9 \times 10^4 \text{ cm}^{-1}$ , and turn-on field of  $0.1 \text{ V}/\mu\text{m}$ , but much lower max current density of  $0.02 \text{ mA}/\text{cm}^2$ , and much lower total emission current at  $1 \text{ V}/\mu\text{m}$  of  $0.2 \text{ }\mu\text{A}$  (**Figure 9.6-1**). When tested up to a higher maximum field of  $3 \text{ V}/\mu\text{m}$  they achieved the same current density and emission current as the peaked emitters at  $1 \text{ V}/\mu\text{m}$  but were destroyed in the process.

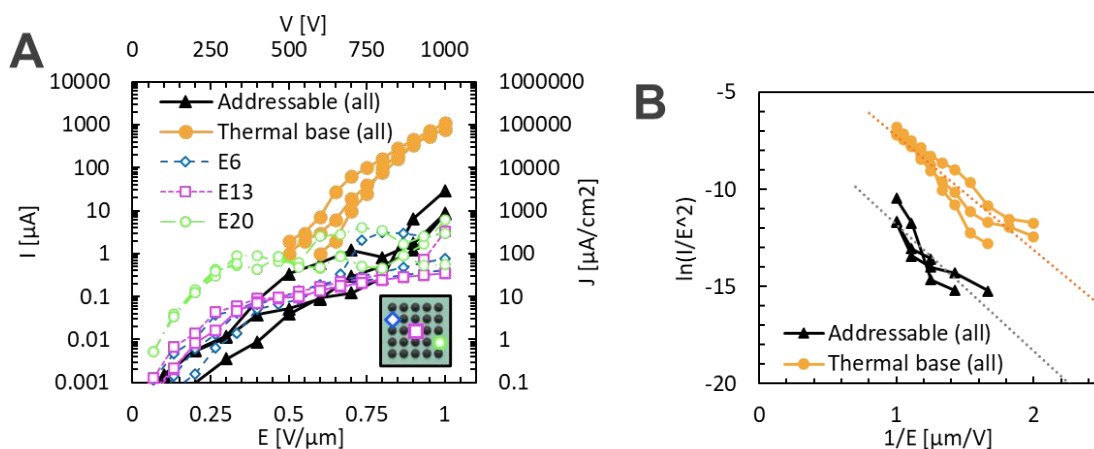


**Figure 9.4-1:** Emission data from an individually addressable FEA (“Addressable”) activated in bulk and a variant printed on a bulk copper substrate for heat dissipation (“Thermal base”). A) Direct emission current (left axis) and array current density (right axis) vs. nominal electric field strength (bottom axis) and applied bias voltage (top axis) for both bulk activation tests and for representative activations of two individual emitters, whose locations in the array are marked by colored shapes (inset). Data are shown for three voltage sweeping cycles per sample. B) Fowler-Nordheim plot for both bulk activation tests, from which field enhancement factors and activation areas were computed. Dotted lines show linear fits of  $\ln(I/E^2)$  vs  $1/E$ ; a linear fit implies Fowler-Nordheim model conformity.

Characterization of arrays of individually addressed emitters shows that the total emitted current scales with the number of emitters; individual emitters have a turn-on field of  $0.1 \text{ V}/\mu\text{m}$ ,  $\sim 0.4 \text{ }\mu\text{A}$  emission current at  $1 \text{ V}/\mu\text{m}$ , and  $\beta \approx 4 \times 10^5 \text{ cm}^{-1}$  field enhancement factor.

The same FEA structures printed onto a monolithic copper electrode show improved properties, with a higher turn-on field ( $0.5 \text{ V}/\mu\text{m}$ ), peak array current density ( $>100 \text{ mA}/\text{cm}^2$ ), total emission current of  $1000 \mu\text{A}$  at  $1 \text{ V}/\mu\text{m}$ , though a similar field enhancement factor ( $\beta \approx 2 \times 10^5 \text{ cm}^{-1}$ ), possibly due to more efficient heat dissipation and power delivery through the copper base. Poole-Frenkel dielectric breakdown was excluded from possibility by testing the devices in reverse polarity; no emission was observed when the bias voltage acting on the emitters was above the bias voltage of the counter electrode.

### 9.5. Discussion and Conclusion

The FEAs reported here demonstrate the potential to directly 3D print individually addressable field emission electron sources onto functional devices in an automated process. Benefitting from the compatibility of additive manufacturing with a variety of substrates, the proposed cathode technology has excellent relevance to industrial challenges. The reported devices meet state-of-the-art performance for CNT-based field emitters [240], [286] while enabling individual emitter addressability. This combination of features is a critical requirement to enable field uniformity correction in EPL [287], without which distortion of projected patterns occurs. Recorded performance herein immediately satisfies the expected emission current density of  $10\text{-}600 \mu\text{A}/\text{cm}^2$  for a commercial EPL system.

Further, the customizable deposition of emitters on arbitrary substrates has great utility for medical imaging, as integration with existing infrastructure can allow products to incorporate CNT inks directly. Controllable emission localization also enables high-precision X-ray imaging via phase contrast signal encoding in the emission pattern [293].

While existing cleanroom-made FEAs have excellent performance [295], [296], their cost of iteration and integration difficulty lead to 3D printing being a more sustainable approach for limited-scale production. Here, the instrument cost is under  $\$100,000$ , while total device fabrication time (including setup and calibration) is under 5 minutes. This enables vastly expedited development timeframes without continuing expenses associated with cleanroom usage.

No byproduct waste is produced during the printing process for the FEAs reported here besides residual ink, avoiding significant quantities of environmental pollutants and toxins released during subtractive processing of conventional devices, often made via etching in cleanroom lithography protocols. Most costs associated with hazard disposal are thus avoided.

Ongoing efforts focus on increasing emitter array density while sustaining the same per-emitter current, with a view towards leveraging other benefits of additive manufacturing (e.g., topological customization or use of non-planar base substrates) for obtaining new emission modalities. With additional process and ink refinement, emitter dimensions can become more precise, allowing for smaller-scale emitters and consequently higher packing density. More tailored manufacturing such as parallel dispensing [297] could create massively large-scale arrays, further reducing FEA fabrication costs and heralding the next generation of vacuum electron sources.

### 9.6. Appendix: Field emission properties of mound-like emitters

Field emission data is presented in **Figure 9.6-1** for emitter arrays with peaks printed onto PCBs and copper formed from ink with yield stress of 610 Pa, and emitter arrays with mound-like shapes formed from ink with yield stress of 250 Pa.

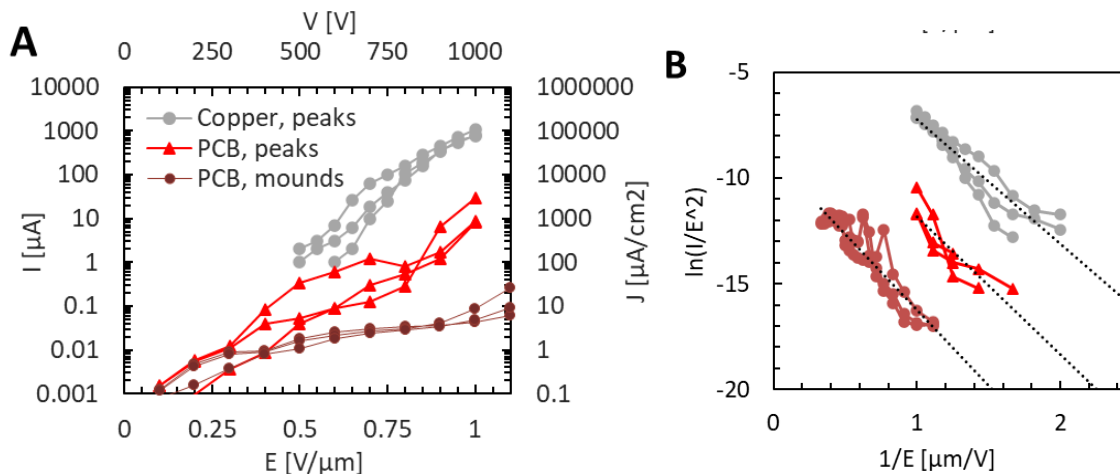


**Figure 9.6-1:** Emission data from CNT emitter arrays printed with peaked shape onto PCBs and a bulk copper substrate, and arrays with a mound shape printed onto PCBs. A) Direct emission current (left axis) and array current density (right axis) vs. nominal electric field strength (bottom axis) and applied bias voltage (top axis) for bulk activation tests. Data are shown for three voltage sweeping cycles per sample. B) Fowler-Nordheim plot for each test, from which field enhancement factors and activation areas were computed. Dotted lines show linear fits of  $\ln(I/E^2)$  vs  $1/E$ ; a linear fit implies Fowler-Nordheim model conformity.

---

***Part III:***

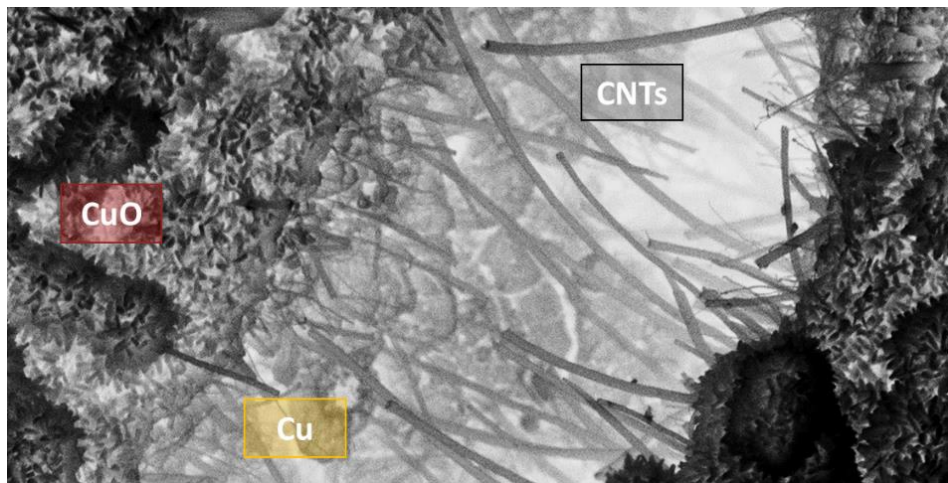
***Path to a Copper-Carbon Nanotube  
Composite***

---

---

## Chapter 10. Formation of a copper-CNT composite by electrowetting for improved electrical performance

---



Chapter Introduction Image: scanning electron micrograph of a rift in a Cu-CNT composite, like exploring a strange microscopic jungle

### 10.1. Abstract

In this chapter, a method is developed to enhance the conductivity of existing CNT structures using copper electrodeposition of a copper electrolyte solution onto a preformed CNT mesh. Input charge, the product of current and time, was identified as the key control parameter for Cu mass deposition, regardless of Cu location on surfaces or fully impregnating the CNT mesh. To gain insight into the progression of Cu morphology during

nucleation and growth, the electrical conductivity of the composite material was related to Cu mass loading, and images were taken at different time points in the process. CNT wettability was identified as a key parameter enabling homogeneous nucleation of metal. The electrolyte solutions were tuned to control the wetting behavior, thereby tuning nucleation location of Cu, which was validated by scanning electron micrographs and electron dispersion spectrographs of cross-sections of experimental specimens. CNT-copper composites were formed with final conductivity up to 2,000 kS/m (3% of pure Cu) for a lightweight composite with density less than 0.8 g/cm<sup>3</sup>, yielding a specific conductivity of 2,500 S.m<sup>2</sup>/kg. Finally, electrodeposition was combined with methods of printing from **Chapter 5** to create a CNT-Cu composite spiral inductor. This work provides the initial steps towards creation of fully-dense Cu-CNT structures in short times, and these results can advise process development and further generation of dense Cu-CNT composites.

## 10.2. Introduction

As electronics are driven towards progressively smaller scales and higher speeds, bulk metals such as copper are reaching their material limits, and the use of metal composites with ultraconductive nanomaterials, particularly CNTs, is becoming increasingly appealing to make fast, efficient devices with high electrical and thermal performance [31]. However, fully aligned, densely-packed CNT assemblies within metal networks are required to generate optimal wiring and electronic structures. Even small microstructural defects can cause large losses in mechanical strength and electrical/thermal transport [20], [51], which constrains the range of processing strategies that can be employed. To address this challenge, we have been using experimental techniques to integrate copper (Cu) with CNTs for applications in electronics, and focusing on the homogeneous nucleation of Cu within preformed CNT mats to use in additive manufacturing processes.

Cu/CNT composites have already been demonstrated in many forms [298], [299] but production of a fully-dense structure, rather than a core-shell structure with Cu cladding, universally relies on a multi-step process to pre-treat the CNT surface before depositing copper, adding complications and severely reducing process speed. Pretreatment is required because of the hydrophobic nature of CNT bundles and mats, which restricts deposition of metal directly from aqueous electrolyte solutions. In addition, favored pretreatments often add defects to the CNTs, increasing hydrophilicity at the cost of reducing conductivity. In this chapter, a new method is introduced to create a uniform Cu-



CNT composite from an isotropic CNT mat in single step electrodeposition using an electrolyte solution modified to have a marginally wetting contact angle on the CNT mat. First, the electrodeposition behavior of a standard copper sulfate (II) electrolyte onto CNT mats is described, with respect to input current, time, and overall charge. Next, this deposition is imaged to view Cu nucleation location and size. Further, wetting behavior is evaluated, and an electrolyte showing marginal wetting is introduced. Finally, this electrodeposition method is applied to a printed CNT spiral inductor. In the longer view, this material design effort underpins steps towards creating a fully integrated method of additive manufacturing to create printed electronics, especially those with radio-frequency functionality in GHz ranges and at elevated temperatures, in which CNTs show particularly appealing properties.

### 10.3. *Materials and Methods*

#### *Electrodeposition*

Electrodeposition was performed by placing electrodes in a bath onto a copper substrate and CNT buckypaper held on slides to have an even spacing and orientation relative to each other. A current-controlled DC power supply (Dr.meter) provided a constant current for a fixed amount of time. The typical recipe was selected to use 1M copper sulfate as a Cu source, 0.5M H<sub>2</sub>SO<sub>4</sub> to increase solution conductivity, 100 $\mu$ M PEG as an inhibitor, 50 $\mu$ M Janus Green B as a leveling agent, 20 $\mu$ M mercaptopropanesulfonic acid, MPSA as an accelerator, and 1mM NaCl as an aid to the accelerator, adapted from [300]. When methanol was added, it replaced a portion of the original solvent, water, leaving the molar concentrations of additives the same with respect to total solvent level.

#### *Characterizations*

Scanning electron microscopy (SEM) was performed on dried fibers without modification using a Zeiss Merlin High-resolution SEM. Electrical resistance was measured using an LCR meter with 4 terminal Kelvin clips (IM3536, Hioki) at room temperature (23-25 degrees C) and ambient humidity (23-52% RH).

### 10.4. *Controlling Cu-CNT material composition by electrodeposition*

The formation of Cu-CNT composites was studied using electrodeposition of copper into pre-existing CNT meshes called buckypaper, formed by vacuum filtration (**Figure 10.4-1**).

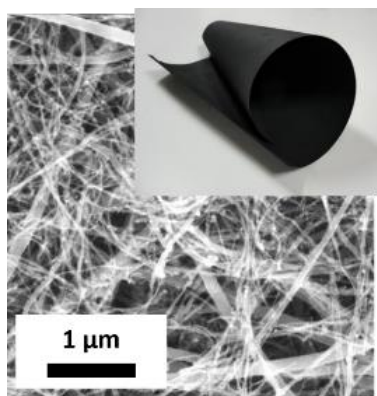


**Figure 10.4-1:** The base carbon nanotube substrate used for experiments is buckypaper which is a micro/nanoporous CNT mesh. This image shows a macro-scale photograph and a scanning electron micrograph of the buckypaper.

The experimental setup holds a buckypaper electrode parallel to a Cu electrode, both submerged in an electrolyte bath (**Figure 10.4-2**). As current is applied, Cu is deposited from the electrolyte solution and nucleates onto the CNTs in the buckypaper.

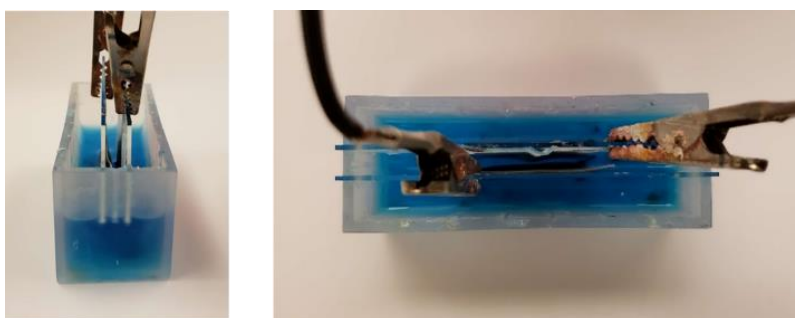


**Figure 10.4-2:** The system used for controlled electrodeposition coating onto CNTs uses small vessel to hold a glass slide with a CNT mesh parallel to a copper electrode while a controlled current is applied. The device measures 1 inch x 1 inch x 3 inches to match standard glass slide dimensions.

Higher applied current density (current per area) and longer time of application both caused greater Cu mass deposition and therefore conductivity of the final Cu-CNT composite (**Figure 10.4-3**). Although this dependence is multivariate, we applied various models to identify the key driving physics in the mass transfer and conductivity generation. A highly-aligned and dense CNT tape was also tested to observe process variations onto different base substrates, showing greater conductivity for lower total input charge, while images showed that this was due to directional nucleation on the highly-aligned CNT tape (**Figure 10.4-3**).

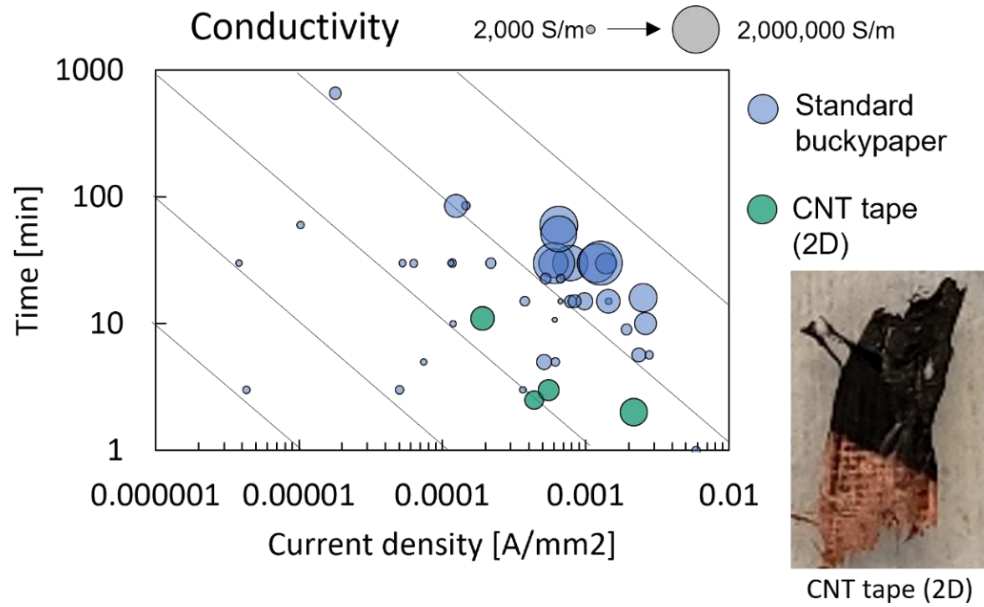


**Figure 10.4-3:** A conductivity map shows the influence of applied current density and time of application on the achieved conductivity of our Cu-CNT composite structures for buckypaper and for CNT tape.

This deposition is expected to follow the first law of electrolysis, in which the expected mass of copper deposited,  $m$ , is a well-described function of the inputted charge,  $z$ , time of current application  $t$ , molar mass of copper  $M_{Cu} = 63.5$  g/mol, Faradic efficiency  $\eta$ , and Faraday's constant  $F = 96,485$  C/mol:

$$m = \int_0^t \eta I(\tau) d\tau \frac{M_{Cu}}{Fz} \quad (1)$$

This equation describes the total mass deposition and deposition rate of copper onto CNT meshes and agrees with measured data directly, without fitting parameters (**Figure 10.4-4a-b**). A value of  $\eta = 1$  was used, indicating that this process is Faradaically efficient, meaning that all or nearly all input charge converts Cu ions into solid Cu without side reactions.

In addition, a large series of models were tested as predictors of conductivity of the composite, including percolation models for 2D and 3D percolation of metal materials. The equation for a metal foam was found to most accurately describe the physics of the process control of conductivity (Figure 10.4-3c), as a function of the observed conductivity  $\sigma$  the conductivity of pure copper  $\sigma_{Cu}$ , the density of copper in the composite  $\rho$ , the density of pure copper  $\rho_{Cu}$ , and an exponent  $n$  which for copper is 3:

$$\frac{\sigma}{\sigma_{Cu}} = \left( \frac{\rho}{\rho_{Cu}} \right)^n \quad (2)$$

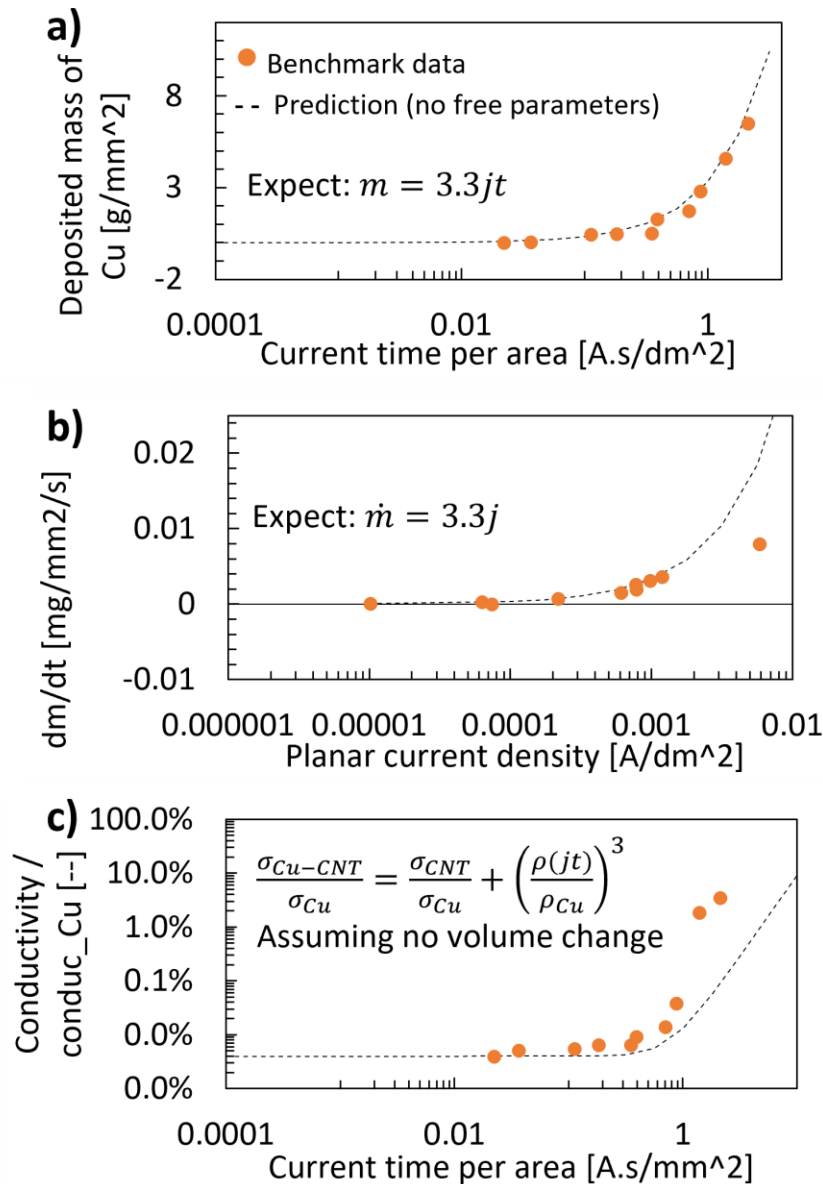


**Figure 10.4-4:** Process control in the system covers (a) copper mass deposition, (b) mass deposition rate, and (c) conductivity are explained using reduced variables to understand what may be tuned for the process control. Black dotted lines show predicted behavior with no fitting parameters using equations described in the text.

These equations together allowed a description and thereby control of the final conductivity of our Cu-CNT composites over three orders of magnitude increasing from the conductivity of the buckypaper of 2,000 S/m up to a composite conductivity of 2,000,000 S/m. In addition, composite density (at room temperature) was controlled over several orders of

magnitude from the density of the pure buckypaper of 0.3 g/cm<sup>3</sup> up to a density of about 0.8 g/cm<sup>3</sup> for the highly conductive composite, which is substantially less than the density of pure copper at 8.96 g/cm<sup>3</sup>. With appropriate control parameters, this allowed controlled and uniform nucleation of Cu onto the surface of CNT meshes (**Figure 10.5-2**).

### 10.5. Microscopic view and theory

As copper nucleation progresses, copper nucleate onto portions of CNT fibers, and progressively increase in density, eventually fusing into a bulk structure enclosing the CNT mesh (**Figure 10.5-1**). During this time, CNTs typically deposit into small, faceted structures with a distribution of sizes (**Figure 10.5-2**).

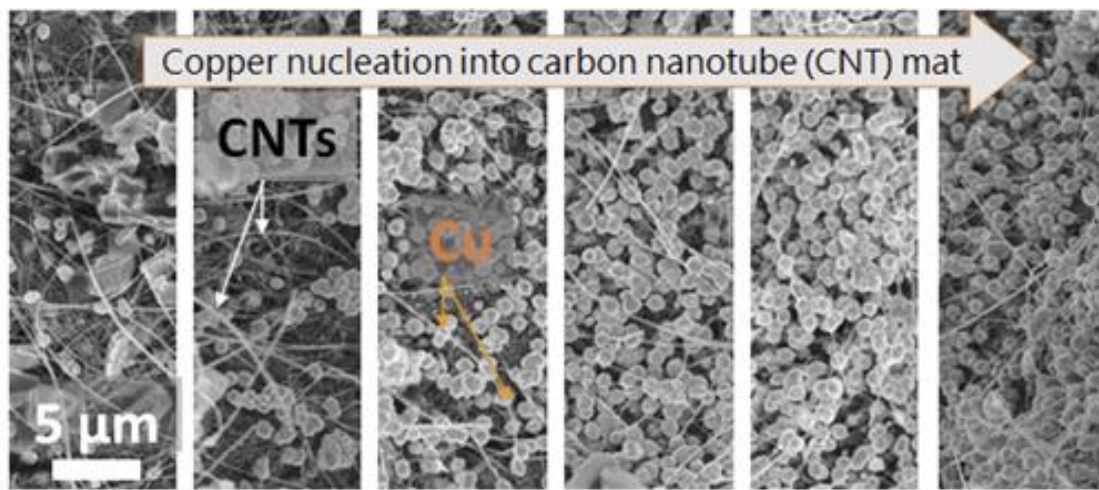


**Figure 10.5-1:** Overview of the process development allowing controlled composite generation, combination with printed CNT spiral structures, and anticipated combination with fully-embedded printed structures.

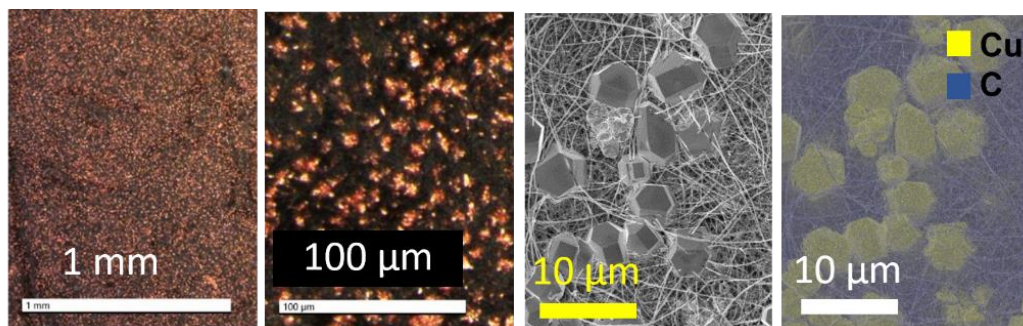


**Figure 10.5-2:** Uniform nucleation of Cu is possible onto these CNT sheets, shown by optical microscopy, scanning electron microscopy, and electron-dispersion spectroscopy to mark the elemental composition of materials studied, denoting copper (Cu) and carbon (C).

### 10.6. Tuning wettability of electrolyte solutions

Existing electrodeposition processes typically either form core-shell structures with Cu mostly external to the CNT structure [301], or require a long process using multiple solvents to incorporate Cu internal to the CNTs [299]. The major obstacle to uniform material synthesis is a poor wettability interaction between typical copper electrolyte solutions, which are aqueous, and carbon nanotube meshes, which are hydrophobic (**Figure 10.6-1**).

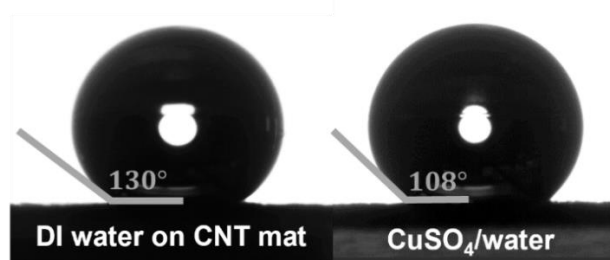


**Figure 10.6-1:** Electrolyte solutions on buckypaper meshes show hydrophobic behavior.

However, by modifying the electrolyte by adding small amounts of organic solvent (**Figure 10.6-2**), the contact angle was reduced sufficiently to allow for infiltration of a measured droplet of electrolyte into the CNT mesh pores. By altering the electrolyte in this way, a method was created that reduces what is typically a two-step process with a very slow first step (>24 hrs) into a single step process that is able to create homogeneously-filled Cu-CNT composites within 2 hours. This holds promise for progressing a similar process to a scalable method performed on the same timescales as are used in typical 3D printing.

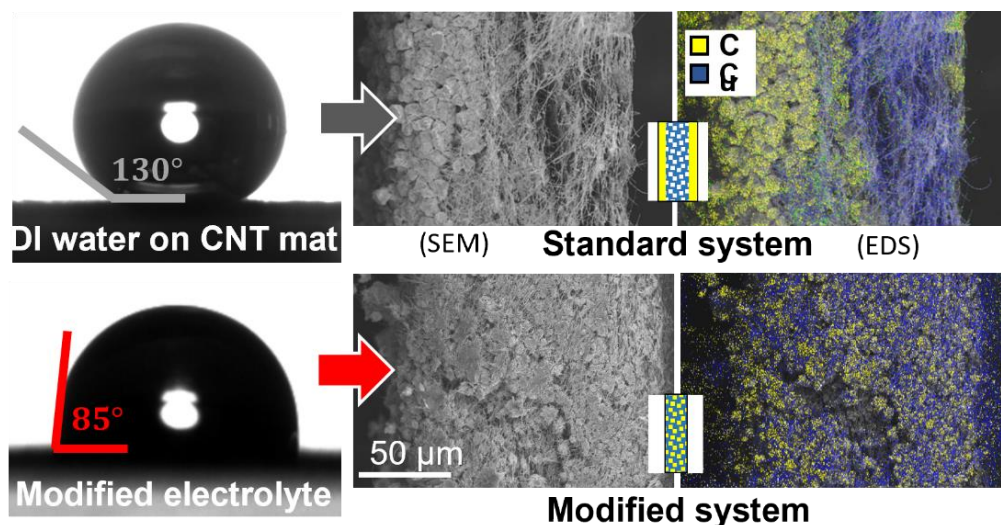


**Figure 10.6-2:** High contact angles caused copper to only deposit on the surface of structures, whereas a modified electrolyte allowed deposition homogeneously inside pores of the CNT mat. Various treatments to the deposited electrolyte control the apparent contact angle on the textured substrate, leading to marginal wetting behavior. As a direct result, electrodeposition forms Cu nuclei either only on the outer surfaces or throughout the CNT mat, as shown by scanning electron micrographs (SEM) and electron dispersion spectrographs (EDS) for each case.

### 10.6.1. Cu-CNT Percolation

The method of Cu nucleation and percolation was examined by comparing two cases. In the first case, nonwetting solutions cause formation of two-dimensional Cu overcoatings on the CNT mat, which percolate at lower volume fractions but ultimately fail to form a true composite. In the second case, marginally wetting solutions allow formation of fully three-dimensional Cu networks within the CNT mat. The limits of Cu penetration into dense initial CNT networks were imaged using electron dispersion spectrographs of cross-sections of experimental specimens (**Figure 10.6-2**). Comparing both approaches, conductivity percolation behavior was inspected. At higher concentrations, bulk conductivity measurements begin to discriminate between core-shell and homogeneous composites prepared via different deposition strategies. These are compared with models for conductivity including Hashin-Shtrikman bounds [302] which delineate thresholds for isotropic composite conductors, a fitted percolation model (with critical density 10% and scaling exponent 1.5), and the standard model for the conductivity of three-dimensional Cu foam, which scales as density ratio cubed and has no fitting parameters.

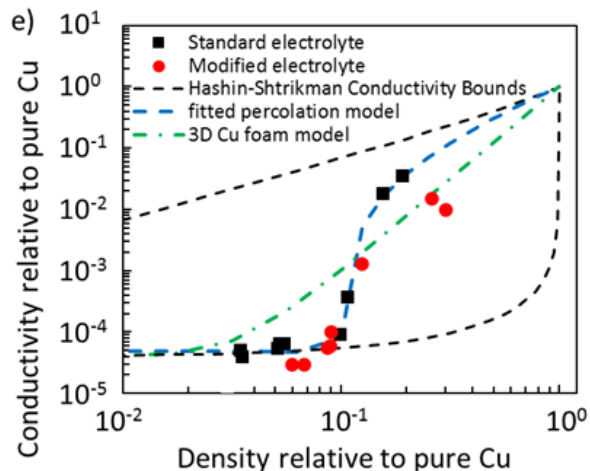


**Figure 10.6-3:** At higher concentrations, bulk conductivity measurements begin to discriminate between core-shell and homogeneous composites prepared via different deposition strategies. These are compared with models for conductivity including Hashin-Shtrikman bounds which delineate thresholds for isotropic composite conductors, a fitted percolation model (with critical density 10% and scaling exponent 1.5), and the standard model for the conductivity of three-dimensional Cu foam, which scales as density ratio cubed and has no fitting parameters.

### 10.7. Integration into planar spiral inductor

Finally, this composite material generation protocol was combined with the the printing process described in **Chapter 6**. Electrodeposition was applied to add Cu onto a two-dimensional (2D) spiral inductor printed from CNTs onto a 2D Kapton film (**Figure 10.7-1**). Making contact between an electrode and a single external point of the spiral, the Cu coats progressively onto the CNTs. By applying a sufficiently low deposition rate, the Cu was made to coat the entire span of the spiral structure with a continuous, bright metal layer without defects from too-high or too-low current.



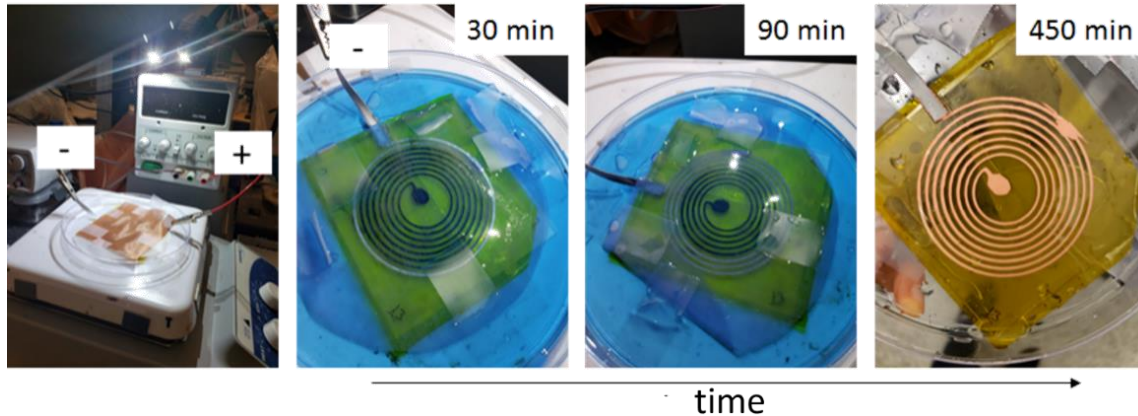


**Figure 10.7-1:** Time-series showing the coating of Cu onto a printed CNT planar Archimedes spiral inductor progressing from the outside to the center. A bright, continuous coating is formed.

### 10.8. Conclusions

In this chapter, the electrodeposition of copper onto a CNT mesh was characterized. Charge was identified as the key control parameter for Cu mass deposition. The electrical conductivity was related to Cu concentration to understand Cu morphology progression during nucleation. By understanding the role of CNT wettability for homogeneous nucleation of metal, CNT-copper composites were formed with final conductivity up to 2,000 kS/m (3% of pure Cu) for a lightweight composite with density less than 0.8 g/cm<sup>3</sup>, yielding a specific conductivity of 2,500 S.m<sup>2</sup>/kg. By controlling wetting behavior, the nucleation location of Cu was tunable, creating initial steps towards creation of fully-dense Cu-CNT structures in short times. Finally, electrodeposition was combined with methods of printing from **Chapter 5** to create a CNT-Cu composite spiral inductor. These results can advise process development and further generation of dense Cu-CNT composites.

---

## Chapter 11. Conclusions and Recommendations for Further Work

---

“There’s plenty of room at the bottom” – Richard Feynman [303]

### 11.1. Research summary

Manufacturing with nanostructured fluids promises to enable manufacturing of goods with advanced functional properties. This thesis began by developing an understanding of CNT-based ink rheology, to inform and coordinate with printing processes, in order to create functional items with particular emphasis on electrical properties (**Figure 11.1-1**).

In the beginning, **Part I** discussed the contributions of CNT concentration to rheological behavior and developed tools and methodologies for assessing rheology of these and similar materials. In **Chapter 2**, a summary of literature explored of the rheological behavior of the flow curves for steady shear of CNT inks, comparing CNTs of multiple lengths and diameters in superacids, water, and epoxy as solvents. Taking input from data measured here and found in literature, the development of yield stress as a function of concentration was a particular focus. Power law trends were given for the rheological values as a function of CNT concentration in the solvent, enabling calculation of fluid rheological behavior at different concentrations. Inks having a yield stress were observed to fall into concentrated or liquid crystalline regime based on their aspect ratio. Inks in the liquid crystalline regime, having longer CNTs, were found to develop similar levels of yield stress or modulus at 1/10

the concentration of inks in the concentrated regime. While modulus and failure strain were found to vary between samples, the power law dependence of the yield stress on concentration was consistently 2.7 for multiple datasets, though divided into the two individual regimes.

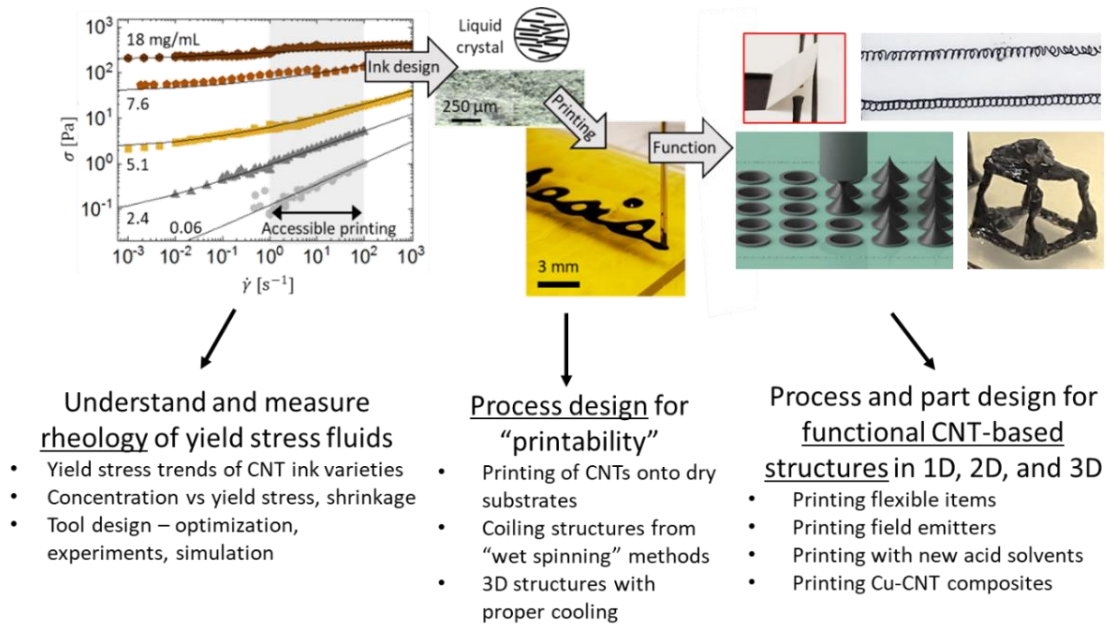


**Figure 11.1-1:** Thesis road map. Developing an understanding of CNT-based ink rheology, to inform and coordinate with printing processes to create functional items. Additional functional items not covered in this thesis are published elsewhere, most notably in [33].

In **Chapter 3**, a family of fractal vanes was introduced along with design and measurement rules to enable facile measurement of the rheology of yield stress fluids, including CNT inks and others, to prevent measurement anomalies including slip and shear history deformation resulting from sample loading, while retaining accurate measurements. Fabrication of the vanes by 3D printing enabled direct assessment of various vane designs, and equations were proposed and validated to extract material parameters from measured data. These equations were shown to give accurate data within 3% of reference data for sparse, 4-arm vanes through dense, 24-arm fractal vanes.. The torque-to-stress equation, combined with the considerations for good measurement embedded in the fractal design of the vane, may allow researchers to identify a bespoke design that addresses specific needs, and tune their own 3D-printed geometries to the specific rheology of the material of interest. Moreover, vanes made by 3D printing of

photopolymer are inexpensive, disposable, and chemically compatible with a wide range of solvents

In **Chapter 4**, another rheological measurement challenged was approached: studying the failure of composite layered disks in the form of Oreo cookies (“oreology”). Through a series of experiments with a laboratory rheometer used to hold whole Oreo cookies, it was determined that creme distribution upon cookie separation by torsional rotation is not a function of rate of rotation, creme “stuff” (*i.e.*, filling height  $H$ ) level, or flavor, but was mostly determined by the pre-existing level of adhesion between the cookie creme and each wafer, most likely set by details of their initial manufacturing. There was some amount of cookie-to-cookie and box-to-box variation in failure stress and strain. Apparent reflow of creme due to unknown causes had the most significant effect in altering failure type, allowing for improved creme-wafer bond and subsequent cohesive failure of the creme, splitting nearly evenly between the two wafers. To further enable measurements of similar materials, a 3D-printable “Oreometer” was introduced and validated, functioning using weights in the form of pennies to apply a known torque to a disk held within the Oreometer until the disk failed by adhesion or cohesion.

In **Part II**, the understanding of CNT ink rheology was used as a foundation to tailor CNT-based inks for extrusion printing, with application to flexible electronics, formation of extensible coils, and manufacturing of field emitters. This began with **Chapter 5**, which described the development and application of a series of aqueous CNT inks for use in direct-write printing of electronically functional features and devices. It was shown in detail how the properties of the ink, particularly concentration, determine the electrical conductivity of printed features, and the importance of related processing capabilities (feature size, production speed) for manufacturing success (*e.g.*, continuous lines). While the extrusion-based methods presented herein are best suited to localized deposition, the ink could readily be adapted to production-scale methods, such as gravure and screen-printing, that could readily handle and benefit from the rheological properties of yield-stress fluids.

In **Chapter 6**, a method was introduced to print the same CNT inks as in **Chapter 5** into a Newtonian viscous bath that precipitated carbon nanotubes from the extruded ink into linear fibers showing tailorable and high conductivity and coils showing high extensibility. Printed CNT threads in a strong antisolvent showed average conductivity of  $10^5$  S/m and average specific conductivity (conductivity per weight) of  $2 \times 10^3$  S m<sup>2</sup>/kg, comparable with

gold. The accessible printing regimes were analyzed, with particular focus on the speed of counter-diffusion of the ink solvent and the bath liquid, which allowed for tuning of fiber diameter, conductivity, and specific conductivity respectively over 1, 4, and 5 orders of magnitude. When the speed of solvent counter-diffusion is high, the conductivity of resulting threads was highest. When extrusion speed was also high, a coiling instability was observed which created threads with regular coil morphology, allowing for intricate designs despite a linear extrusion path. Resulting coils, once dried, could be fully removed from the bath and survived up to 50% strain with <1% change in conductivity or 170% linear extension with 20% change in conductivity. This methodology of immersed printing allowed simple printing of complex coil structures with potential application to circuitry and flexible interconnects.

In **Chapter 7**, a method of additive deposition was introduced to form individual freestanding CNT emitters with dense, vertically-aligned CNTs leveraging the design of an ink with high extensional viscosity. Deposited ink was held in tension between two pins while drying, creating the desired morphology. Field emission measurements validated state-of-the-art performance compared to extant CNT-based field emitters.

In **Chapter 8**, two methods for the automated printing of arrays of CNT-based field emitters were developed and compared. In the first method, a high concentration of short CNTs enabled the direct extrusion of “mound”-like emitters with a three-dimensional shape but rounded top. In the second method, an ink designed to have a very stable fluid thread under extension was printed and then multiple deposited drops were stretched simultaneously to make arrays. Both succeeded in forming arrays, and the second method showed approximately an order of magnitude improved performance due to the finer tip size, with some effect from CNT quality. However, the difficulty of the second process may impede application compared to other direct-printing methods, especially in areas for which additive manufacturing excels, such as over large or non-flat substrates.

In **Chapter 9**, field emitter arrays were printed by direct extrusion onto a printed circuit board. The ink from **Chapter 8** was further tailored to explore the effect of yield stress on the tip morphology and creating finer tip features even when using the simpler first printing method described in **Chapter 8**. Field emission tests demonstrated successful emission with properties on par with current CNT field emitters made by other methods, validating the potential of the method to directly 3D print individually addressable field emission electron sources onto functional devices in an automated process.

Finally, in **Part III**, Cu-CNT composites were developed to further enhance the manufacturing of electronic components with very high conductivity. In **Chapter 10**, a process for the electrodeposition of copper onto a CNT mesh was developed and the effect of input parameters on the conductivity and Cu nucleation morphology were characterized. Charge, as the product of electrical current and time, was identified as the key control parameter driving Cu mass deposition. The final electrical conductivity was related to Cu concentration to understand Cu morphology progression during nucleation. By understanding the role of CNT wettability for homogeneous nucleation of metal, CNT-copper composites were formed with final conductivity up to 2,000 kS/m (3% of pure Cu) for a lightweight composite with density less than 0.8 g/cm<sup>3</sup>, yielding a specific conductivity of 2,500 S.m<sup>2</sup>/kg. By controlling wetting behavior, the nucleation location of Cu was tunable, creating initial steps towards creation of fully-dense Cu-CNT structures in short times. Finally, electrodeposition was combined with methods of printing from **Chapter 5** to create a CNT-Cu spiral inductor. These results can advise process development and further generation of dense Cu-CNT composites which could serve as the foundational material for some next-generation electronics, particularly for low-weight, high-temperature, high-power, and high-frequency applications.

### *11.2. Synthesizing a perspective on ink design rules to create flexible vs freestanding structures*

Based on the characterization of shear rheology of CNT inks developed in **Chapter 2**, yield stress develops in CNT inks with increasing concentration according to one of two behaviors: growing within the concentrated regime or within the liquid crystalline regime (**Figure 11.2-1**). Based on this behavior, two inks were developed extensively in this thesis, one in each of the concentrated and liquid crystalline regimes.

For liquid crystalline inks, a long length and low concentration allowed printing of high-quality and high-conductivity, flexible traces that lost volume while drying, condensing to thin films on a surface (**Figure 11.2-2** and **Chapter 5**). Yield stress enabled the printing of continuous traces onto a variety of substrates, even those with mildly non-wetting behavior towards the inks for which solvent itself, water, would bead up and form discontinuous lines due to the influence of surface tension in the absence of yield stress.

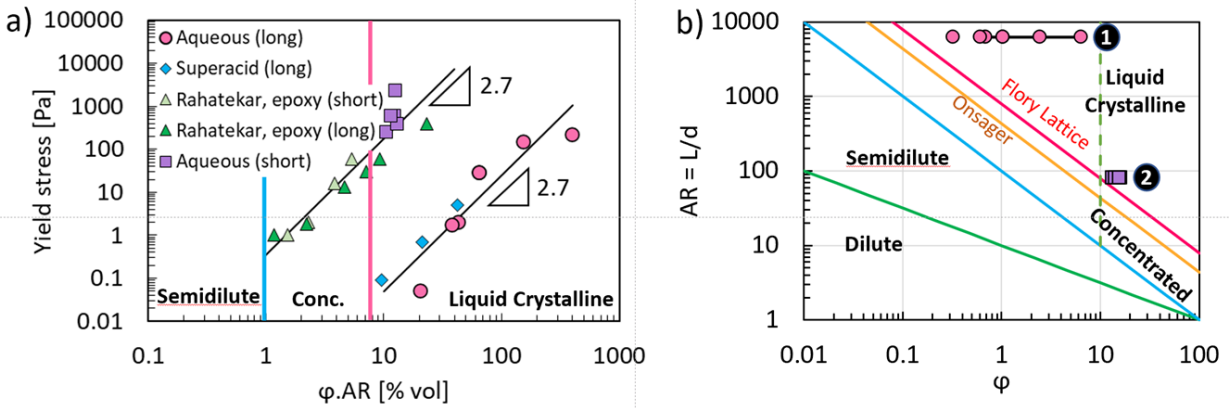


**Figure 11.2-1:** Scaling of yield stress and rheology design maps from **Chapter 2**.

However, for the printing of three-dimensional structures, a low-concentration ink would not be able to create freestanding structures due to shrinkage, and so a more concentrated ink was developed with somewhat high yield stress and substantially higher concentration, allowing printing of structures with tunable shapes from rounded profiles with moderate yield stress up to peaked cones with high yield stress (**Figure 11.2-2** and **Chapter 8**). This shape tunability finally allowed the production of useful field emitter arrays showing turn-on voltage and field enhancement factors on par with what has been achieved making field emitters from freestanding state-of-the-art wet solvent spun CNT fibers.

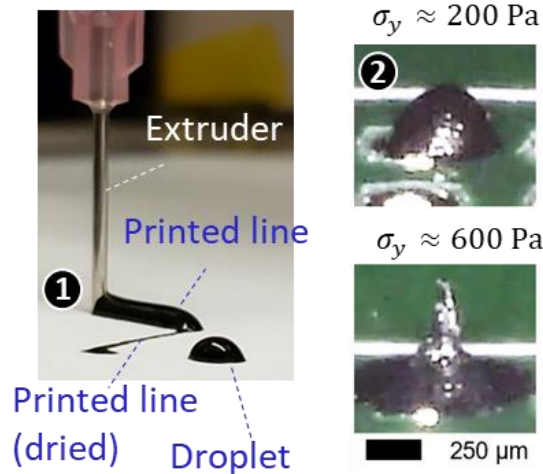


**Figure 11.2-2:** Printed CNT artifacts from **Chapter 5** keeping resolution during printing and then drying into thin films, and from **Chapter 8**, showing a large difference in morphology based on ink yield stress for drops deposited onto a PCB.

### 11.3. Recommendations for future work

“Always the beautiful answer who asks a more beautiful question.” e. e. cummings.

Despite the progress made in this thesis in developing initial inks and producing manufactured items, much remains to be done to fully enable widespread manufacturing of parts using CNTs as a main component of conducting elements, and much more development and exploration is ripe for new discoveries. Key areas of potential future development are in understanding the rheology of CNT-based inks, creating composite inks, in characterization of printed structures, and in use of printed CNTs for applications.

First, in the space of ink measurement, more needs to be understood about how rheology develops as a function of CNT concentration and type in order to predict and optimize formulations to increase conductivity without running into solubility limitations. In addition, modeling and measurement of the liquid-crystalline behavior in particular of CNT inks at high concentration could possibly give insight into how to print aligned CNT structures with nematic domains aligned from the printing process itself. In addition, thixotropy of CNT inks is poorly understood, and likely contributes to variations in properties when printing with the same process parameters.

Second, in the space of ink design, while CNT-in-solvent inks have been developed here, composite inks with additives hold promise to further improve the properties of printed items according to needs of specific applications in electronics, such as inductance or more precise field emission. With printed circuits, the addition of metal nanoparticles like nickel or iron would increase inductance, allowing printing of inductors from the base ink. In addition, when printing coiled structures, currently the coils make physical contact and interact. While some inductance is expected, it would also be expected to be lossy, and additional process design to create a core-shell structure with an insulating material encasing the conductive CNT core would be expected to greatly reduce the loss and allow straightforward printing of CNT-based inductors. Within the space of field emission, materials with low work function like gold or molybdenum nanoparticles would be expected to increase field emission. In addition, there is current uncertainty about the location of emission on the CNT structures, only that the emission area is predicted to be nanoscale on an emission tip that is micron-scale. Thus, including a small portion of functionalized CNTs or functionalizing the peaks of printed emitter structures could help designate emission locations more directly, and perhaps remove the necessity for separately formed emitters



but still allow creation of a system with a functional array by instead doping or functionalizing regions on buckypaper or a spincoated layer of CNTs to excite specific positions for field emission. Finally, guidelines drawn from the properties of yield stress fluids may apply more broadly to the design of solution-processable conductive inks.

Third, this thesis focused on the electrical conductivity of printed items, with some additional measurements of mechanical strength and field emission. Additional parameters of great interest would be ampacity (current carrying capacity), thermal conductivity and specific thermal conductivity, electrical and thermal properties at elevated temperatures, and electrical properties at high frequencies, in order to understand behavior and better select applications in which CNTs or CNT composites would be the material of choice. Within the Cu-CNT composite work, additional parameters that are most compelling for future investigation include additional characterization for higher Cu loading, measuring the electrical conductivity at high frequencies (1-50 GHz) and elevated temperatures (100-400°C), as well as the thermal conductivity and the coefficient of thermal expansion for different substrates. Within the 3D printing process, interrogating the minimum overall size limits and minimum surface roughness limits should also aid in assessing applications in high-performance printed electronics.

Forth, other and more fully integrated applications of printed devices can be considered. For example, with flexible electronics, full circuits could be developed including sensors and data storage and transmission, and such circuits could be created on already-3D topologies or topologies designed to bend into final form rather than stay generally planar. For another example, field emitters can be used for mass spectrometry, x-ray imaging, and electron projection lithography.

Manufacturing by 3D printing has already explosively altered the face of manufacturing in many industries and continues to grow seemingly without bound. Within electronics manufacturing, 3D printing is uniquely suited to enable further improvements to material fabrication and design by allowing, for example, printing of nanomaterials and composites not easily handled by other methods, creating materials with unique geometries such as lattices and thin strips to characterize unknown material properties, and the potential to extrusion-print materials with gradient properties for expedited material selection or for final applications. With the advent of machine learning combined with 3D printing, perhaps automation can enable both the design and the handling of even more complex inks. However, even if computers can take over and expedite more and more of currently

low-throughput empirical and iterative processes, it seems that, for the time being, the (human) operator will continue to have faster and better results by continuing to incorporate rational design into the process.

## Bibliography

- [1] H. A. De Volder MF, Tawfick SH, Baughman RH and M. F. L. De Volder, “Carbon nanotubes: present and future commercial applications.,” *Science.*, vol. 535, no. February, pp. 339(6119):535–9., 2013, doi: 10.1126/science.1222453.
- [2] P. E., M. D., W. Q., G. K., and D. H., “Thermal Conductance of an Individual Single-Wall Carbon Nanotube above Room Temperature,” *Nano Lett.*, vol. 6, p. 96, 2006, doi: 10.1021/nl052145f.
- [3] H. Dai, E. W. Wong, C. M. Liebert, and C. M. Lieber, “Probing Electrical Transport in Nanomaterials: Conductivity of Individual Carbon Nanotubes,” *Science (80-. )*, vol. 272, no. April, pp. 523–526, 1996, doi: 10.1126/science.272.5261.523.
- [4] P. Kim, L. Shi, A. Majumdar, and P. L. McEuen, “Thermal Transport Measurements of Individual Multiwalled Nanotubes,” *Phys. Rev. Lett.*, vol. 87, no. 21, p. 215502, 2001, doi: 10.1103/PhysRevLett.87.215502.
- [5] Q. Wang, J. Dai, W. Li, Z. Wei, and J. Jiang, “The effects of CNT alignment on electrical conductivity and mechanical properties of SWNT/epoxy nanocomposites,” *Compos. Sci. Technol.*, vol. 68, no. 7–8, pp. 1644–1648, 2008, doi: 10.1016/j.compscitech.2008.02.024.
- [6] A. M. Beese *et al.*, “Key factors limiting carbon nanotube yarn strength: Exploring processing-structure-property relationships,” *ACS Nano*, vol. 8, no. 11, pp. 11454–11466, 2014, doi: 10.1021/nn5045504.
- [7] R. J. Headrick *et al.*, “Structure–Property Relations in Carbon Nanotube Fibers by Downscaling Solution Processing,” *Adv. Mater.*, vol. 30, no. 9, pp. 1–8, 2018, doi: 10.1002/adma.201704482.
- [8] D. Pettit, “The Tyranny of the Rocket Equation,” *Crews and Expeditions*, 2012. [http://www.nasa.gov/mission\\_pages/station/expeditions/expedition30/tryanny.html](http://www.nasa.gov/mission_pages/station/expeditions/expedition30/tryanny.html).
- [9] L. Hall, “2015 NASA Technology Roadmaps,” no. July, 2015, [Online]. Available: <http://www.nasa.gov/offices/oct/home/roadmaps/index.html>.
- [10] D. E. Tsentelovich *et al.*, “Relationship of Extensional Viscosity and Liquid Crystalline Transition to Length Distribution in Carbon Nanotube Solutions,” *Macromolecules*, vol. 49, no. 2, pp. 681–689, 2016, doi: 10.1021/acs.macromol.5b02054.
- [11] T. A. Materials and M. Systems, “NASA Technology Roadmaps and Manufacturing,” no. July, 2015.

- [12] T. Kellner, “World’s First Plant to Print Jet Engine Nozzles in Mass Production,” *GE Reports*, 2014. <http://www.gereports.com/post/91763815095/worlds-first-plant-to-print-jet-engine-nozzles-in/>.
- [13] J. Harbaugh, “Space Station 3-D Printer Builds Ratchet Wrench To Complete First Phase of Operations,” 2014. .
- [14] M. Gannon, “3D Printer Could Transform Moon Dirt Into Lunar Base,” 2012. <http://www.space.com/18694-moon-dirt-3d-printing-lunar-base.html>.
- [15] C. E. Owens, A. J. Hart, and G. H. McKinley, “Improved rheometry of yield stress fluids using bespoke fractal 3D printed vanes,” *J. Rheol. (N. Y. N. Y.)*, vol. 64, no. 3, pp. 643–662, May 2020, doi: 10.1122/1.5132340.
- [16] C. E. Owens, M. R. Fan, A. J. Hart, and G. H. McKinley, “ On Oreology, the fracture and flow of ‘milk’s favorite cookie ® ’ ,” *Phys. Fluids*, vol. 34, no. 4, p. 043107, 2022, doi: 10.1063/5.0085362.
- [17] C. E. Owens *et al.*, “Flexible Electronics: Substrate-Versatile Direct-Write Printing of Carbon Nanotube-Based Flexible Conductors, Circuits, and Sensors (Adv. Funct. Mater. 25/2021),” *Adv. Funct. Mater.*, vol. 31, no. 25, p. 2170181, 2021, doi: 10.1002/adfm.202170181.
- [18] C. Penu, G.-H. Hu, A. Fernandez, P. Marchal, and L. Choplin, “Rheological and electrical percolation thresholds of carbon nanotube/polymer nanocomposites,” *Polym. Eng. Sci.*, vol. 52, no. 10, pp. 2173–2181, Oct. 2012, doi: 10.1002/pen.23162.
- [19] X. Wei, M. Naraghi, and H. D. Espinosa, “Optimal length scales emerging from shear load transfer in natural materials: Application to carbon-based nanocomposite design,” *ACS Nano*, vol. 6, no. 3, pp. 2333–2344, 2012, doi: 10.1021/nn204506d.
- [20] N. Behabtu *et al.*, “Strong, light, multifunctional fibers of carbon nanotubes with ultrahigh conductivity,” *Science (80-. )*, vol. 339, no. 6116, pp. 182–186, Jan. 2013, doi: 10.1126/science.1228061.
- [21] K. R. Jinkins *et al.*, “Aligned 2D carbon nanotube liquid crystals for wafer-scale electronics,” *Sci. Adv.*, vol. 7, no. 37, pp. 1–12, 2021, doi: 10.1126/sciadv.abh0640.
- [22] J. H. Kim *et al.*, “Three-Dimensional Printing of Highly Conductive Carbon Nanotube Microarchitectures with Fluid Ink,” *ACS Nano*, vol. 10, no. 9, pp. 8879–8887, Sep. 2016, doi: 10.1021/acsnano.6b04771.
- [23] G. Postiglione, G. Natale, G. Griffini, M. Levi, and S. Turri, “Conductive 3D microstructures by direct 3D printing of polymer/carbon nanotube nanocomposites via

liquid deposition modeling,” *Compos. Part A Appl. Sci. Manuf.*, vol. 76, pp. 110–114, 2015, doi: 10.1016/j.compositesa.2015.05.014.

[24] G. C. Pidcock and M. In Het Panhuis, “Extrusion printing of flexible electrically conducting carbon nanotube networks,” *Adv. Funct. Mater.*, vol. 22, no. 22, pp. 4790–4800, 2012, doi: 10.1002/adfm.201200724.

[25] K. Gnanasekaran *et al.*, “3D printing of CNT- and graphene-based conductive polymer nanocomposites by fused deposition modeling,” *Appl. Mater. Today*, vol. 9, pp. 21–28, 2017, doi: 10.1016/j.apmt.2017.04.003.

[26] C. J. Hohimer, G. Petrossian, A. Ameli, C. Mo, and P. Pötschke, “Electrical conductivity and piezoresistive response of 3D printed thermoplastic polyurethane/multiwalled carbon nanotube composites,” *Behav. Mech. Multifunct. Mater. Compos. XII*, no. March 2018, p. 15, Mar. 2018, doi: 10.1117/12.2296774.

[27] K. Chiou, S. Byun, J. Kim, and J. Huang, “Additive-free carbon nanotube dispersions, pastes, gels, and doughs in cresols,” *Proc. Natl. Acad. Sci.*, vol. 115, no. 22, pp. 5703–5708, 2018, doi: 10.1073/pnas.1800298115.

[28] P. L. McEuen and J. Park, “Electron Transport in Single-Walled Carbon Nanotubes,” *MRS Bull.*, vol. 29, no. 4, pp. 272–275, Apr. 2004, doi: 10.1557/mrs2004.79.

[29] A. Lekawa-Raus, J. Patmore, L. Kurzepa, J. Bulmer, and K. Koziol, “Electrical properties of carbon nanotube based fibers and their future use in electrical wiring,” *Adv. Funct. Mater.*, vol. 24, no. 24, pp. 3661–3682, 2014, doi: 10.1002/adfm.201303716.

[30] V. A. Davis *et al.*, “True solutions of single-walled carbon nanotubes for assembly into macroscopic materials,” *Nat. Nanotechnol.*, vol. 4, no. 12, pp. 830–834, 2009, doi: 10.1038/nnano.2009.302.

[31] L. W. Taylor *et al.*, “Improved properties, increased production, and the path to broad adoption of carbon nanotube fibers,” *Carbon N. Y.*, vol. 171, pp. 689–694, 2021, doi: 10.1016/j.carbon.2020.07.058.

[32] R. J. Headrick, “Novel solution processing and characterization of aligned carbon nanotube materials for rapid composition-property relationship determination and additive manufacturing,” Rice University, 2018.

[33] R. J. Headrick *et al.*, “Versatile acid solvents for pristine carbon nanotube assembly,” *Sci. Adv.*, vol. 8, no. 17, pp. 1–9, 2022, doi: 10.1126/sciadv.abm3285.

- [34] L. Maillaud *et al.*, “Highly Concentrated Aqueous Dispersions of Carbon Nanotubes for Flexible and Conductive Fibers,” *Ind. Eng. Chem. Res.*, vol. 57, no. 10, pp. 3554–3560, 2018, doi: 10.1021/acs.iecr.7b03973.
- [35] C. E. Owens *et al.*, “Substrate-Versatile Direct-Write Printing of Carbon Nanotube-Based Flexible Conductors, Circuits, and Sensors,” *Adv. Funct. Mater. Recent. Accept.*, 2021, doi: adfm.202100245R1.
- [36] S. S. Rahatekar, K. K. Koziol, S. R. Kline, E. K. Hobbie, J. W. Gilman, and A. H. Windle, “Length-dependent mechanics of carbon-nanotube networks,” *Adv. Mater.*, vol. 21, no. 8, pp. 874–878, 2009, doi: 10.1002/adma.200802670.
- [37] V. A. Davis *et al.*, “Phase behavior and rheology of SWNTs in superacids,” *Macromolecules*, vol. 37, no. 1, pp. 154–160, 2004, doi: 10.1021/ma0352328.
- [38] E. K. Hobbie, “Shear rheology of carbon nanotube suspensions,” *Rheol. Acta*, vol. 49, no. 4, pp. 323–334, 2010, doi: 10.1007/s00397-009-0422-4.
- [39] F. Mirri *et al.*, “High-Performance Carbon Nanotube Transparent Conductive Films by Scalable Dip Coating,” *ACS Nano*, vol. 6, no. 11, pp. 9737–9744, 2012, doi: 10.1021/nn303201g.
- [40] F. Mirri *et al.*, “Lightweight, Flexible, High-Performance Carbon Nanotube Cables Made by Scalable Flow Coating,” *ACS Appl. Mater. Interfaces*, vol. 8, no. 7, pp. 4903–4910, 2016, doi: 10.1021/acsami.5b11600.
- [41] S. Zhang and S. Kumar, “Carbon nanotubes as liquid crystals,” *Small*, vol. 4, no. 9, pp. 1270–1283, 2008, doi: 10.1002/smll.200700082.
- [42] C. Qiao, G. Chen, J. Zhang, and J. Yao, “Structure and rheological properties of cellulose nanocrystals suspension,” *Food Hydrocoll.*, vol. 55, pp. 19–25, Apr. 2016, doi: 10.1016/j.foodhyd.2015.11.005.
- [43] U. T. Reinhardt, E. L. M. de Groot, G. G. Fuller, and W.-M. Kulicke, “Rheo-optical characterization (flow-birefringence and flow-dichroism) of the Tobacco Mosaic Virus,” *Macromol. Chem. Phys.*, vol. 196, no. 1, pp. 63–74, Jan. 1995, doi: 10.1002/macp.1995.021960103.
- [44] D. Tanner, J. A. Fitzgerald, and B. R. Phillips, “The Kevlar Story--an Advanced Materials Case Study,” *Angew. Chemie Int. Ed. English*, vol. 28, no. 5, pp. 649–654, May 1989, doi: 10.1002/anie.198906491.

- [45] E. G. Chatzi and J. L. Koenig, "Morphology and Structure of Kevlar Fibers: A Review," *Polym. Plast. Technol. Eng.*, vol. 26, no. 3–4, pp. 229–270, Sep. 1987, doi: 10.1080/03602558708071938.
- [46] B. Dan, G. C. Irvin, and M. Pasquali, "Continuous and scalable fabrication of transparent conducting carbon nanotube films," *ACS Nano*, vol. 3, no. 4, pp. 835–843, 2009, doi: 10.1021/nn8008307.
- [47] W. W. Graessley, "Polymer chain dimensions and the dependence of viscoelastic properties on concentration, molecular weight and solvent power," *Polymer (Guildf.)*, vol. 21, no. 3, pp. 258–262, 1980, doi: 10.1016/0032-3861(80)90266-9.
- [48] M. Doi and S. F. Edwards, *The Theory of Polymer Dynamics*. 1986.
- [49] V. Skákalová, U. Dettlaff-Weglikowska, and S. Roth, "Electrical and mechanical properties of nanocomposites of single wall carbon nanotubes with PMMA," *Synth. Met.*, vol. 152, no. 1–3, pp. 349–352, 2005, doi: 10.1016/j.synthmet.2005.07.291.
- [50] G. L. Goh, S. Agarwala, and W. Y. Yeong, "Directed and On-Demand Alignment of Carbon Nanotube: A Review toward 3D Printing of Electronics," *Adv. Mater. Interfaces*, vol. 6, no. 4, 2019, doi: 10.1002/admi.201801318.
- [51] D. E. Tsentelovich *et al.*, "Influence of Carbon Nanotube Characteristics on Macroscopic Fiber Properties," *ACS Appl. Mater. Interfaces*, vol. 9, no. 41, pp. 36189–36198, 2017, doi: 10.1021/acsami.7b10968.
- [52] S. K. Kang *et al.*, "Relationship between field emission property and composition of carbon nanotube paste for large area cold cathode," *J. Vac. Sci. Technol. B Microelectron. Nanom. Struct.*, vol. 22, no. 3, p. 1345, 2004, doi: 10.1116/1.1667514.
- [53] J. H. Ha, S. E. Lee, and S. H. Park, "Effect of dispersion by three-roll milling on electrical properties and filler length of carbon nanotube composites," *Materials (Basel)*, vol. 12, no. 23, pp. 10–17, 2019, doi: 10.3390/ma122333823.
- [54] Y. Y. Huang and E. M. Terentjev, "Dispersion of carbon nanotubes: Mixing, sonication, stabilization, and composite properties," *Polymers (Basel)*, vol. 4, no. 1, pp. 275–295, 2012, doi: 10.3390/polym4010275.
- [55] J. Stegen, "Mechanics of carbon nanotube scission under sonication," *J. Chem. Phys.*, vol. 140, no. 24, 2014, doi: 10.1063/1.4884823.
- [56] E. Varrla *et al.*, "Turbulence-assisted shear exfoliation of graphene using household detergent and a kitchen blender," *Nanoscale*, vol. 6, no. 20, pp. 11810–11819, 2014, doi: 10.1039/c4nr03560g.

- [57] M. Yi and Z. Shen, “Kitchen blender for producing high-quality few-layer graphene,” *Carbon N. Y.*, vol. 78, pp. 622–626, 2014, doi: 10.1016/j.carbon.2014.07.035.
- [58] B. Kumanek, T. Wasiak, G. Stando, P. Stando, D. Łukowiec, and D. Janas, “Simple method to improve electrical conductivity of films made from single-walled carbon nanotubes,” *Nanomaterials*, vol. 9, no. 8, pp. 1–11, 2019, doi: 10.3390/nano9081113.
- [59] W. K. A. Ma, F. Chinesta, A. Ammar, and M. R. Mackley, “Rheological modeling of carbon nanotube aggregate suspensions,” *J. Rheol. (N. Y. N. Y.)*, vol. 52, no. 6, pp. 1311–1330, 2008, doi: 10.1122/1.2982932.
- [60] A. A. Kolesnikova, Y. S. Eremin, and A. M. Grekhov, “Time-stability dispersion of carbon nanotubes in chloroform,” *Phys. Procedia*, vol. 72, pp. 51–55, 2015, doi: 10.1016/j.phpro.2015.09.015.
- [61] H. T. Ham, Y. S. Choi, and I. J. Chung, “An explanation of dispersion states of single-walled carbon nanotubes in solvents and aqueous surfactant solutions using solubility parameters,” *J. Colloid Interface Sci.*, vol. 286, no. 1, pp. 216–223, 2005, doi: 10.1016/j.jcis.2005.01.002.
- [62] C. Pramanik, J. R. Gissinger, S. Kumar, and H. Heinz, “Carbon Nanotube Dispersion in Solvents and Polymer Solutions: Mechanisms, Assembly, and Preferences,” *ACS Nano*, vol. 11, no. 12, pp. 12805–12816, 2017, doi: 10.1021/acsnano.7b07684.
- [63] L. Liang *et al.*, “High-efficiency dispersion and sorting of single-walled carbon nanotubes: Via non-covalent interactions,” *J. Mater. Chem. C*, vol. 5, no. 44, pp. 11339–11368, 2017, doi: 10.1039/c7tc04390b.
- [64] Y.-G. Tao, W. K. den Otter, and W. J. Briels, “Kayaking and Wagging of Rods in Shear Flow,” *Phys. Rev. Lett.*, vol. 95, no. 23, p. 237802, Dec. 2005, doi: 10.1103/PhysRevLett.95.237802.
- [65] A. W. K. Ma, M. R. Mackley, and S. S. Rahatekar, “Experimental observation on the flow-induced assembly of Carbon nanotube suspensions to form helical bands,” *Rheol. Acta*, vol. 46, no. 7, pp. 979–987, 2007, doi: 10.1007/s00397-007-0183-x.
- [66] W. H. Herschel and R. Bulkley, “Konsistenzmessungen von Gummi-Benzollosungen,” *Colloid Polym. Sci.*, vol. 39, no. 4, pp. 291–300, 1926.
- [67] N. Fakhri, D. A. Tsybouski, L. Cagnet, R. B. Weisman, and M. Pasquali, “Diameter-dependent bending dynamics of single-walled carbon nanotubes in liquids,” *Proc. Natl. Acad. Sci.*, vol. 106, no. 34, pp. 14219–14223, Aug. 2009, doi: 10.1073/pnas.0904148106.



- [68] A. W. K. Ma, K. M. Yearsley, F. Chinesta, and M. R. MacKley, “A review of the microstructure and rheology of carbon nanotube suspensions,” *Proc. Inst. Mech. Eng. Part N J. Nanoeng. Nanosyst.*, vol. 222, no. 3–4, pp. 71–94, 2008, doi: 10.1243/17403499JNN153.
- [69] S. S. L. Chan, R. M. Pennings, L. Edwards, and G. V Franks, “3D printing of clay for decorative architectural applications: Effect of solids volume fraction on rheology and printability,” *Addit. Manuf.*, vol. 35, no. April, p. 101335, 2020, doi: 10.1016/j.addma.2020.101335.
- [70] M. Milazzo *et al.*, “3D Printability of Silk/Hydroxyapatite Composites for Microprosthetic Applications,” *ACS Biomater. Sci. Eng.*, 2022, doi: 10.1021/acsbiomaterials.2c01357.
- [71] A. M’Barki, L. Bocquet, and A. Stevenson, “Linking Rheology and Printability for Dense and Strong Ceramics by Direct Ink Writing,” *Sci. Rep.*, vol. 7, no. 1, pp. 1–10, 2017, doi: 10.1038/s41598-017-06115-0.
- [72] P. Coussot, “Yield stress fluid flows: A review of experimental data,” *J. Nonnewton. Fluid Mech.*, vol. 211, pp. 31–49, 2014, doi: 10.1016/j.jnnfm.2014.05.006.
- [73] Y. M. Joshi and G. Petekidis, “Yield stress fluids and ageing,” *Rheol. Acta*, pp. 1–29, 2018, doi: 10.1007/s00397-018-1096-6.
- [74] D. Bonn, M. M. Denn, L. Berthier, T. Divoux, and S. Manneville, “Yield stress materials in soft condensed matter,” *Rev. Mod. Phys.*, vol. 89, no. 3, pp. 1–40, 2017, doi: 10.1103/RevModPhys.89.035005.
- [75] M. Dinkgreve, M. Fazilati, M. M. Denn, and D. Bonn, “Carbopol: From a simple to a thixotropic yield stress fluid,” *J. Rheol. (N. Y. N. Y.)*, vol. 62, no. 3, pp. 773–780, 2018, doi: 10.1122/1.5016034.
- [76] P. C. F. Møller, J. Mewis, and D. Bonn, “Yield stress and thixotropy: On the difficulty of measuring yield stresses in practice,” *Soft Matter*, vol. 2, no. 4, pp. 274–283, 2006, doi: 10.1039/b517840a.
- [77] H. A. Barnes and Q. D. Nguyen, “Rotating vane rheometry—a review,” *J. Nonnewton. Fluid Mech.*, vol. 98, no. 1, pp. 1–14, 2001, doi: 10.1016/S0377-0257(01)00095-7.
- [78] P. Coussot, L. Tocquer, C. Lanos, and G. Ovarlez, “Macroscopic vs. local rheology of yield stress fluids,” *J. Nonnewton. Fluid Mech.*, vol. 158, no. 1–3, pp. 85–90, 2009, doi: 10.1016/j.jnnfm.2008.08.003.

- [79] T. Divoux, D. Tamarii, C. Barentin, and S. Manneville, “Transient shear banding in a simple yield stress fluid,” *Phys. Rev. Lett.*, vol. 104, no. 20, pp. 1–4, 2010, doi: 10.1103/PhysRevLett.104.208301.
- [80] C. F. Ferraris *et al.*, “Role of Rheology in Achieving Successful Concrete Performance,” *Concr. Int.*, vol. 39, no. 6, pp. 43–51, 2017.
- [81] Q. D. Nguyen and D. V. Boger, “Yield Stress Measurement for Concentrated Suspensions,” *J. Rheol. (N. Y. N. Y.)*, vol. 27, no. 4, pp. 321–349, 1983, doi: 10.1122/1.549709.
- [82] C. R. Daubert, J. A. Tkachuk, and V. D. Truong, “Quantitative measurement of food spreadability using the vane method,” *J. Texture Stud.*, vol. 29, no. 4, pp. 427–435, 1998, doi: 10.1111/j.1745-4603.1998.tb00814.x.
- [83] V. D. Truong, C. R. Daubert, M. A. Drake, and S. R. Baxter, “Vane rheometry for textural characterization of Cheddar cheeses: Correlation with other instrumental and sensory measurements,” *LWT - Food Sci. Technol.*, vol. 35, no. 4, pp. 305–314, 2002, doi: 10.1006/fstl.2001.0872.
- [84] H. S. Melito and C. R. Daubert, “Rheological Innovations for Characterizing Food Material Properties,” *Annu. Rev. Food Sci. Technol.*, vol. 2, no. 1, pp. 153–179, 2012, doi: 10.1146/annurev-food-022510-133626.
- [85] H. Bui, “The application of rheology in the development of cosmetic products,” in *Society of Rheology Annual Meeting*, 2019, p. PG18.
- [86] M. Kogan, L. Ducloué, J. Goyon, X. Chateau, O. Pitois, and G. Ovarlez, “Mixtures of foam and paste: Suspensions of bubbles in yield stress fluids,” *Rheol. Acta*, vol. 52, no. 3, pp. 237–253, 2013, doi: 10.1007/s00397-013-0677-7.
- [87] P. Wei, H. Leng, Q. Chen, R. C. Advincula, and E. B. Pentzer, “Reprocessable 3D-Printed Conductive Elastomeric Composite Foams for Strain and Gas Sensing,” *ACS Appl. Polym. Mater.*, vol. 1, no. 4, pp. 885–892, 2019, doi: 10.1021/acsapm.9b00118.
- [88] E.-J. Courtial *et al.*, “Silicone rheological behavior modification for 3D printing: evaluation of yield stress impact on printed object properties,” *Addit. Manuf.*, vol. 28, pp. 50–57, 2019, doi: 10.1016/j.addma.2019.04.006.
- [89] J. T. Muth, D. M. Vogt, R. L. Truby, D. B. Kolesky, R. J. Wood, and J. A. Lewis, “Embedded 3D Printing of Strain Sensors within Highly Stretchable Elastomers,” pp. 6307–6312, 2014, doi: 10.1002/adma.201400334.

- [90] A. K. Grosskopf, R. L. Truby, H. Kim, A. Perazzo, J. A. Lewis, and H. A. Stone, “Viscoplastic Matrix Materials for Embedded 3D Printing,” *ACS Appl. Mater. Interfaces*, vol. 10, no. 27, pp. 23353–23361, 2018, doi: 10.1021/acsami.7b19818.
- [91] R. Moreno, “Colloidal processing of ceramics and composites,” *Adv. Appl. Ceram.*, vol. 111, no. 5–6, pp. 246–253, 2012, doi: 10.1179/1743676111Y.0000000075.
- [92] Y. Qian and S. Kawashima, “Distinguishing dynamic and static yield stress of fresh cement mortars through thixotropy,” *Cem. Concr. Compos.*, vol. 86, pp. 288–296, 2018, doi: 10.1016/j.cemconcomp.2017.11.019.
- [93] R. G. Larson and Y. Wei, “A Review of Thixotropy and its Rheological Modeling,” *J. Rheol. (N. Y. N. Y.)*, vol. 63, pp. 477–501, 2019.
- [94] C. J. Dimitriou and G. H. McKinley, “A comprehensive constitutive law for waxy crude oil: A thixotropic yield stress fluid,” *Soft Matter*, vol. 10, no. 35, pp. 6619–6644, 2014, doi: 10.1039/c4sm00578c.
- [95] S. M. Fielding, P. Sollich, and M. E. Cates, “Ageing and Rheology in Soft Materials,” *J. Rheol. (N. Y. N. Y.)*, vol. 323, no. 2, pp. 323–369, 1999, doi: 10.1122/1.551088.
- [96] Q. D. Nguyen and D. V. Boger, “Characterization of yield stress fluids with concentric cylinder viscometers,” *Rheol. Acta*, vol. 26, no. 6, pp. 508–515, 1987, doi: 10.1007/BF01333734.
- [97] C. J. Dimitriou, R. H. Ewoldt, and G. H. McKinley, “Describing and prescribing the constitutive response of yield stress fluids using large amplitude oscillatory shear stress (LAOStress),” *J. Rheol. (N. Y. N. Y.)*, vol. 57, no. 1, pp. 27–70, 2013, doi: 10.1122/1.4754023.
- [98] J. Yoon and C. El Mohtar, “Disturbance effect on time-dependent yield stress measurement of bentonite suspensions,” *Geotech. Test. J.*, vol. 36, no. 1, pp. 78–87, 2013, doi: 10.1520/GTJ20120082.
- [99] X. D. Zhang, D. W. Giles, V. H. Barocas, K. Yasunaga, and C. W. Macosko, “Measurement of foam modulus via a vane rheometer,” *J. Rheol. (N. Y. N. Y.)*, vol. 42, no. 4, pp. 871–889, 2002, doi: 10.1122/1.550906.
- [100] J. Patarin, H. Galliard, A. Magnin, and B. Goldschmidt, “Vane and plate-plate rheometry of cheeses under oscillations and large strains: A comparative study and experimental conditions analysis,” *Int. Dairy J.*, vol. 38, pp. 24–30, 2014.
- [101] Q. D. Nguyen, T. Akroyd, D. C. De Kee, and L. Zhu, “Yield stress measurements in suspensions: an inter-laboratory study,” *Korea-Australia Rheol. J.*, vol. 18, no. 1, pp. 15–24, 2006.

- [102] C. Atkinson and J. D. Sherwood, “The Torque on a Rotating n-Bladed Vane in a Newtonian Fluid or Linear Elastic Medium,” *Proc. R. Soc. A Math. Phys. Eng. Sci.*, vol. 438, no. 1902, pp. 183–196, 1992, doi: 10.1098/rspa.1992.0101.
- [103] C. Baravian, A. Lalante, and A. Parker, “Vane rheometry with a large, finite gap,” *Appl. Rheol.*, vol. 12, no. 2, pp. 81–87, 2002, doi: 10.3933/ApplRheol-12-81.
- [104] H. A. Barnes and J. O. Carnali, “The vane-in-cup as a novel rheometer geometry for shear thinning and thixotropic materials,” *J. Rheol. (N. Y. N. Y.)*, vol. 34, no. 6, pp. 841–866, 1990, doi: 10.1122/1.550103.
- [105] M. Keentok, J. F. Milthorpe, and E. O’Donovan, “On the shearing zone around rotating vanes in plastic liquids: theory and experiment,” *J. Nonnewton. Fluid Mech.*, vol. 17, no. 1, pp. 23–35, 1985, doi: 10.1016/0377-0257(85)80003-3.
- [106] G. Ovarlez, F. Mahaut, F. Bertrand, and X. Chateau, “Flows and heterogeneities with a vane tool: Magnetic resonance imaging measurements,” *J. Rheol. (N. Y. N. Y.)*, vol. 55, no. 2, pp. 197–223, 2011, doi: 10.1122/1.3526349.
- [107] E. Gutierrez-Barranco, L. Parras, C. del Pino, and F. J. Rubio-Hernandez, “Flow visualizations in a rotating vane rheometer,” in *Perspectives in Fundamental and Applied Rheology*, no. January, 2013, pp. 401–406.
- [108] J. D. Sherwood and G. H. Meeten, “The use of the vane to measure the shear modulus of linear elastic solids,” *J. Nonnewton. Fluid Mech.*, vol. 41, no. 1–2, pp. 101–118, 1991, doi: 10.1016/0377-0257(91)87037-X.
- [109] A. Potanin, “3D simulations of the flow of thixotropic fluids, in large-gap Couette and vane-cup geometries,” *J. Nonnewton. Fluid Mech.*, vol. 165, no. 5–6, pp. 299–312, 2010, doi: 10.1016/j.jnnfm.2010.01.004.
- [110] P. V. Liddell and D. V. Boger, “Yield stress measurements with the vane,” *J. Nonnewton. Fluid Mech.*, vol. 63, no. 2–3, pp. 235–261, 1996, doi: 10.1016/0377-0257(95)01421-7.
- [111] G. H. Meeten and J. D. Sherwood, “Vane techniques for shear-sensitive and wall-slipping fluids,” in *Theoretical and Applied Rheology*, 1992, pp. 935–937.
- [112] D. Feys, R. Verhoeven, and G. De Schutter, “Evaluation of time independent rheological models applicable to fresh self-compacting concrete,” *Appl. Rheol.*, vol. 17, no. 5, pp. 1–10, 2007.

- [113] N. Pashias, D. V. Boger, J. Summers, and D. J. Glenister, “A fifty cent rheometer for yield stress measurement,” *J. Rheol. (N. Y. N. Y.)*, vol. 40, no. 6, pp. 1179–1189, 2002, doi: 10.1122/1.550780.
- [114] D. T. Fisher, S. A. Clayton, D. V. Boger, and P. J. Scales, “The bucket rheometer for shear stress-shear rate measurement of industrial suspensions,” *J. Rheol. (N. Y. N. Y.)*, vol. 51, no. 5, pp. 821–831, 2007, doi: 10.1122/1.2750657.
- [115] M. O. Chevrel, A. J. L. L. Harris, M. R. James, L. Calabrò, L. Gurioli, and H. Pinkerton, “The viscosity of pāhoehoe lava: In situ syn-eruptive measurements from Kilauea, Hawaii,” *Earth Planet. Sci. Lett.*, vol. 493, pp. 161–171, 2018, doi: 10.1016/j.epsl.2018.04.028.
- [116] H. Pinkerton and R. S. J. Sparks, “Field measurements of the rheology of lava,” *Nature*, vol. 276, no. November, pp. 383–385, 1978.
- [117] D. A. Bikos and T. G. Mason, “Customizable tool geometries by additive manufacturing for mechanical rheometry of soft matter,” *J. Rheol. (N. Y. N. Y.)*, vol. 60, no. 6, pp. 1257–1267, 2016, doi: 10.1122/1.4963802.
- [118] S. Raayai, “Geometry Mediated Drag Reduction Using Riblets and Wrinkled Surface Textures,” Massachusetts Institute of Technology, 2018.
- [119] T. D. Ngo, A. Kashani, G. Imbalzano, K. T. Q. Nguyen, and D. Hui, “Additive manufacturing (3D printing): A review of materials, methods, applications and challenges,” *Compos. Part B Eng.*, vol. 143, pp. 172–196, 2018.
- [120] A. J. Hart, *Additive Manufacturing for Innovative Design and Production*. MIT xPRO, 2018.
- [121] P. Coussot, *Rheometry of Pastes, Suspensions, and Granular Materials*. Hoboken, New Jersey: John Wiley & Sons, 2005.
- [122] N. J. Balmforth, I. A. Frigaard, and G. Ovarlez, “Yielding to Stress: Recent Developments in Viscoplastic Fluid Mechanics,” *Annu. Rev. Fluid Mech.*, vol. 46, no. 1, pp. 121–146, 2013, doi: 10.1146/annurev-fluid-010313-141424.
- [123] P. Saramito, “A new constitutive equation for elastoviscoplastic fluid flows,” *J. Nonnewton. Fluid Mech.*, vol. 145, no. 1, pp. 1–14, 2007, doi: 10.1016/j.jnnfm.2007.04.004.
- [124] P. Saramito, “A new elastoviscoplastic model based on the Herschel-Bulkley viscoplastic model,” *J. Nonnewton. Fluid Mech.*, vol. 158, no. 1–3, pp. 154–161, 2009, doi: 10.1016/j.jnnfm.2008.12.001.

- [125] P. Coussot, H. Tabuteau, X. Chateau, L. Tocquer, and G. Ovarlez, “Aging and solid or liquid behavior in pastes,” *J. Rheol. (N. Y. N. Y.)*, vol. 50, no. 6, pp. 975–994, 2006, doi: 10.1122/1.2337259.
- [126] E. F. Medina-Bañuelos, B. M. Marín-Santibáñez, J. Pérez-González, and D. M. Kalyon, “Rheo-PIV analysis of the vane in cup flow of a viscoplastic microgel,” *J. Rheol. (N. Y. N. Y.)*, vol. 63, no. 6, pp. 905–915, 2019, doi: 10.1122/1.5118900.
- [127] C. W. Macosko, “Rheology Principles, Measurements, and Applications,” New York: Wiley-VCH, Inc., 1994, pp. 190–193.
- [128] C. Ozalp, A. Pinarbasi, and B. Sahin, “Experimental measurement of flow past cavities of different shapes,” *Exp. Therm. Fluid Sci.*, vol. 34, no. 5, pp. 505–515, 2010, doi: 10.1016/j.expthermflusci.2009.11.003.
- [129] G. B. West, J. H. Brown, and B. J. Enquist, “The fourth dimension of life: Fractal geometry and allometric scaling of organisms,” *Science (80-. )*, vol. 284, no. 5420, pp. 1677–1679, 1999, doi: 10.1126/science.284.5420.1677.
- [130] D. M. Warme, “Spanning trees in hypergraphs with applications to Steiner trees,” *ProQuest Diss. Theses*, no. May, p. 122, 1998, [Online]. Available: <https://search.proquest.com/docview/304460440?accountid=188395>.
- [131] S. Kalpakjian and S. R. Schmid, *Manufacturing Engineering and Technology*, 7th ed. Pearson, 2013.
- [132] FormLabs, “Materials Data Sheet: Photopolymer Resin for Form 1+ and Form 2,” 2017. doi: 10.1016/j.biortech.2012.09.095.
- [133] D. Bourell *et al.*, “Materials for additive manufacturing,” *CIRP Ann. - Manuf. Technol.*, vol. 66, no. 2, pp. 659–681, 2017, doi: 10.1016/j.cirp.2017.05.009.
- [134] C. E. Owens and A. J. Hart, “High-precision modular microfluidics by micromilling of interlocking injection-molded blocks,” *Lab Chip*, vol. 18, no. 6, pp. 890–901, 2018, doi: 10.1039/c7lc00951h.
- [135] TA Instruments, “Discovery Hybrid Rheometer,” pp. 3–6, 2016.
- [136] G. Benmouffok-Benbelkacem, F. Caton, C. Baravian, and S. Skali-Lami, “Non-linear viscoelasticity and temporal behavior of typical yield stress fluids: Carbopol, Xanthan and Ketchup,” *Rheol. Acta*, vol. 49, no. 3, pp. 305–314, 2010, doi: 10.1007/s00397-010-0430-4.
- [137] E. Chaparian and I. A. Frigaard, “Cloaking: Particles in a yield-stress fluid,” *J. Nonnewton. Fluid Mech.*, vol. 243, pp. 47–55, 2017, doi: 10.1016/j.jnnfm.2017.03.004.

- [138] J. A. Goshawk, D. M. Binding, D. B. Kell, and R. Goodacre, “Rheological phenomena occurring during the shearing flow of mayonnaise,” *J. Rheol. (N. Y. N. Y.)*, vol. 42, no. 6, pp. 1537–1553, 1998, doi: 10.1122/1.550967.
- [139] L. Ma and G. V. Barbosa-Canovas, “Rheological Characterization of Mayonnaise. Part II: Flow and Viscoelastic Properties at Different Oil and Xanthan Gum Concentrations,” *J. Food Eng.*, vol. 25, pp. 409–425, 1994, doi: 10.11777/j.issn1000-3304.2014.14030.
- [140] L. Ma and G. V. Barbosa-Canovas, “Rheological Characterization of Mayonnaise. Part I: Slippage at Different Oil and Xanthan Gum Concentrations,” *J. Food Eng.*, vol. 25, pp. 397–408, 1995, doi: 10.11777/j.issn1000-3304.2014.14030.
- [141] B. Keshavarz, T. Divoux, S. Manneville, and G. H. McKinley, “Nonlinear Viscoelasticity and Generalized Failure Criterion for Polymer Gels,” *ACS Macro Lett.*, vol. 6, no. 7, pp. 663–667, 2017, doi: 10.1021/acsmacrolett.7b00213.
- [142] A. Jaishankar and G. H. McKinley, “Power-law rheology in the bulk and at the interface: quasi-properties and fractional constitutive equations Author for correspondence :,” *Proc. R. Soc. A*, vol. 469, no. 2149, 2013.
- [143] R. L. Bagley and P. J. Torvik, “On the Fractional Calculus Model of Viscoelastic Behavior,” *J. Rheol. (N. Y. N. Y.)*, vol. 30, no. 1, pp. 133–155, 1986, doi: 10.1122/1.549887.
- [144] T. S.-K. Ng and G. H. McKinley, “Power law gels at finite strains: The nonlinear rheology of gluten gels Published by the The Society of Rheology Power law gels at finite strains: The nonlinear rheology,” vol. 417, no. 2008, 2017, doi: 10.1122/1.2828018.
- [145] Y. Wei, M. J. Solomon, and R. G. Larson, “Letter to the Editor: Modeling the nonmonotonic time-dependence of viscosity bifurcation in thixotropic yield-stress fluids,” *J. Rheol. (N. Y. N. Y.)*, vol. 63, no. 4, pp. 673–675, 2019, doi: 10.1122/1.5098485.
- [146] F. Y. Fan *et al.*, “Polysulfide flow batteries enabled by percolating nanoscale conductor networks,” *Nano Lett.*, vol. 14, no. 4, pp. 2210–2218, 2014, doi: 10.1021/nl500740t.
- [147] K. C. Smith, Y.-M. Chiang, and W. Craig Carter, “Maximizing Energetic Efficiency in Flow Batteries Utilizing Non-Newtonian Fluids,” *J. Electrochem. Soc.*, vol. 161, no. 4, pp. A486–A496, 2014, doi: 10.1149/2.011404jes.
- [148] T. S. Wei *et al.*, “Biphasic Electrode Suspensions for Li-Ion Semi-solid Flow Cells with High Energy Density, Fast Charge Transport, and Low-Dissipation Flow,” *Adv. Energy Mater.*, vol. 5, no. 15, pp. 1–7, 2015, doi: 10.1002/aenm.201500535.

- [149] B. Derakhshandeh, S. G. Hatzikiriakos, and C. P. J. Bennington, “Rheology of pulp suspensions using ultrasonic Doppler velocimetry,” *Rheol. Acta*, vol. 49, no. 11, pp. 1127–1140, 2010, doi: 10.1007/s00397-010-0485-2.
- [150] R. B. Bird, R. C. Armstrong, and O. Hassager, *Dynamics of Polymeric Liquids*. Wiley, 1987.
- [151] A. J. T. M. Mathijssen, M. Lisicki, V. N. Prakash, and E. J. L. Mossige, “Culinary fluid mechanics and other currents in food science,” pp. 1–76, 2022, [Online]. Available: <http://arxiv.org/abs/2201.12128>.
- [152] A. Ghanbari, Z. Mousavi, M. C. Heuzey, G. S. Patience, and P. J. Carreau, “Experimental methods in chemical engineering: Rheometry,” *Can. J. Chem. Eng.*, vol. 98, no. 7, pp. 1456–1470, 2020, doi: 10.1002/cjce.23749.
- [153] T. J. Faber, A. Jaishankar, and G. H. McKinley, “Describing the firmness, springiness and rubberiness of food gels using fractional calculus. Part II: Measurements on semi-hard cheese,” *Food Hydrocoll.*, vol. 62, pp. 325–339, 2017, doi: 10.1016/j.foodhyd.2016.06.038.
- [154] E. Blanco *et al.*, “Conching chocolate is a prototypical transition from frictionally jammed solid to flowable suspension with maximal solid content,” *Proc. Natl. Acad. Sci. U. S. A.*, vol. 116, no. 21, pp. 10303–10308, 2019, doi: 10.1073/pnas.1901858116.
- [155] J. R. Stokes, M. W. Boehm, and S. K. Baier, “Oral processing, texture and mouthfeel: From rheology to tribology and beyond,” *Curr. Opin. Colloid Interface Sci.*, vol. 18, no. 4, pp. 349–359, 2013, doi: 10.1016/j.cocis.2013.04.010.
- [156] M. A. Via, M. Baechle, A. Stephan, T. A. Vilgis, and M. P. Clausen, “Microscopic characterization of fatty liver-based emulsions: Bridging microstructure and texture in foie gras and pâté,” *Phys. Fluids*, vol. 33, no. 11, 2021, doi: 10.1063/5.0070998.
- [157] F. Ronda, S. Pérez-Quirce, and M. Villanueva, “Rheological Properties of Gluten-Free Bread Doughs: Relationship With Bread Quality,” in *Advances in Food Rheology and Its Applications*, Elsevier, 2017, pp. 297–334.
- [158] H. S. Joyner *et al.*, “Development of starch texture rheological maps through empirical modeling of starch swelling behavior,” *Food Hydrocoll.*, vol. 120, p. 106920, Nov. 2021, doi: 10.1016/j.foodhyd.2021.106920.
- [159] S. Cikrikci, M. Yucekutlu, B. Mert, and M. H. Oztop, “Physical characterization of low-calorie chocolate formulations,” *J. Food Meas. Charact.*, vol. 11, no. 1, pp. 41–49, Mar. 2017, doi: 10.1007/s11694-016-9369-1.



- [160] E. O. Afoakwa, A. Paterson, and M. Fowler, “Factors influencing rheological and textural qualities in chocolate – a review,” *Trends Food Sci. Technol.*, vol. 18, no. 6, pp. 290–298, Jun. 2007, doi: 10.1016/j.tifs.2007.02.002.
- [161] P. Bertsch, L. Savorani, and P. Fischer, “Rheology of Swiss Cheese Fondue,” *ACS Omega*, vol. 4, no. 1, pp. 1103–1109, Jan. 2019, doi: 10.1021/acsomega.8b02424.
- [162] C. C. Berton-Carabin, L. Sagis, and K. Schroën, “Formation, Structure, and Functionality of Interfacial Layers in Food Emulsions,” *Annu. Rev. Food Sci. Technol.*, vol. 9, no. 1, pp. 551–587, Mar. 2018, doi: 10.1146/annurev-food-030117-012405.
- [163] E. E. Ehrichs, H. M. Jaeger, G. S. Karczmar, J. B. Knight, V. Y. Kuperman, and S. R. Nagel, “Granular Convection Observed by Magnetic Resonance Imaging,” *Science (80-. )*, vol. 267, no. 5204, pp. 1632–1634, Mar. 1995, doi: 10.1126/science.267.5204.1632.
- [164] M. H. Tunick and D. L. Van Hekken, “Torsion Gelometry of Cheese,” *J. Dairy Sci.*, vol. 85, no. 11, pp. 2743–2749, Nov. 2002, doi: 10.3168/jds.S0022-0302(02)74361-0.
- [165] L. Fisher, “Physics takes the biscuit,” *Nature*, vol. 397, no. 6719, p. 469, 1999, doi: 10.1038/17203.
- [166] P. Zhao *et al.*, “Multiphysics analysis for unusual heat convection in microwave heating liquid,” *AIP Adv.*, vol. 10, no. 8, p. 085201, Aug. 2020, doi: 10.1063/5.0013295.
- [167] M. Geri, B. Keshavarz, G. H. McKinley, and J. W. M. Bush, “Thermal delay of drop coalescence,” *J. Fluid Mech.*, vol. 833, p. R3, Dec. 2017, doi: 10.1017/jfm.2017.686.
- [168] J. Han, “A Study on the Coffee Spilling Phenomena in the Low Impulse Regime,” *Achiev. Life Sci.*, vol. 10, no. 1, pp. 87–101, Jun. 2016, doi: 10.1016/j.als.2016.05.009.
- [169] H. Ockendon and J. R. Ockendon, “How to Mitigate Sloshing,” *SIAM Rev.*, vol. 59, no. 4, pp. 905–911, Jan. 2017, doi: 10.1137/16M1077787.
- [170] T. Seimiya and T. Seimiya, “Revisiting the ‘pearl string’ in draining soap bubble film first witnessed by Sir James Dewar some 100 years ago: A note of analyses for the phenomena with related findings,” *Phys. Fluids*, vol. 33, no. 10, 2021, doi: 10.1063/5.0059830.
- [171] E. Wolfson, “Aerospace engineers found a way to predict with 100% accuracy where the cream ends up when you twist an Oreo,” *Quartz*, October, 2016.
- [172] F. Bergström, “Behind The Scenes In The Oreo Factory,” *Youtube*, 2016. <https://youtu.be/HlZmDxcbpWw?t=193> (accessed Oct. 25, 2021).

- [173] M. Leturia, M. Benali, S. Lagarde, I. Ronga, and K. Saleh, “Characterization of flow properties of cohesive powders: A comparative study of traditional and new testing methods,” *Powder Technol.*, vol. 253, pp. 406–423, 2014, doi: 10.1016/j.powtec.2013.11.045.
- [174] Y. Forterre and O. Pouliquen, “Flows of dense granular media,” *Annu. Rev. Fluid Mech.*, vol. 40, pp. 1–24, 2008, doi: 10.1146/annurev.fluid.40.111406.102142.
- [175] H. Ko and D. L. Hu, “The physics of tossing fried rice,” *J. R. Soc. Interface*, vol. 17, no. 163, p. 20190622, Feb. 2020, doi: 10.1098/rsif.2019.0622.
- [176] M. Tennenbaum, Z. Liu, D. Hu, and A. Fernandez-Nieves, “Mechanics of fire ant aggregations,” *Nat. Mater.*, vol. 15, no. 1, pp. 54–59, Jan. 2016, doi: 10.1038/nmat4450.
- [177] K. M. Baumer *et al.*, “Visualizing 3D imagery by mouth using candy-like models,” *Sci. Adv.*, vol. 7, no. 22, May 2021, doi: 10.1126/sciadv.abh0691.
- [178] M. Ozawa, L. Berthier, G. Biroli, A. Rosso, and G. Tarjus, “Random critical point separates brittle and ductile yielding transitions in amorphous materials,” *Proc. Natl. Acad. Sci.*, vol. 115, no. 26, pp. 6656–6661, Jun. 2018, doi: 10.1073/pnas.1806156115.
- [179] H. J. Barlow, J. O. Cochran, and S. M. Fielding, “Ductile and Brittle Yielding in Thermal and Athermal Amorphous Materials,” *Phys. Rev. Lett.*, vol. 125, no. 16, p. 168003, 2020, doi: 10.1103/physrevlett.125.168003.
- [180] E. J. Hemingway and S. M. Fielding, “Edge fracture instability in sheared complex fluids: Onset criterion and possible mitigation strategy,” *J. Rheol. (N. Y. N. Y.)*, vol. 63, no. 5, pp. 735–750, Sep. 2019, doi: 10.1122/1.5095717.
- [181] R. I. Tanner and M. Keentok, “Shear Fracture in Cone-Plate Rheometry,” *J. Rheol. (N. Y. N. Y.)*, vol. 27, no. 1, pp. 47–57, Feb. 1983, doi: 10.1122/1.549698.
- [182] S. T. Chan *et al.*, “Torsional fracture of viscoelastic liquid bridges,” *Proc. Natl. Acad. Sci. U. S. A.*, vol. 118, no. 24, 2021, doi: 10.1073/pnas.2104790118.
- [183] M. Fonte, L. Reis, F. Romeiro, B. Li, and M. Freitas, “The effect of steady torsion on fatigue crack growth in shafts,” *Int. J. Fatigue*, vol. 28, no. 5–6, pp. 609–617, May 2006, doi: 10.1016/j.ijfatigue.2005.06.051.
- [184] P. Coussot, Q. D. Nguyen, H. T. Huynh, and D. Bonn, “Avalanche Behavior in Yield Stress Fluids,” *Phys. Rev. Lett.*, vol. 88, no. 17, 2002, doi: 10.1103/PhysRevLett.88.175501.
- [185] J. M. Pearce, “Emerging Business Models for Open Source Hardware,” *J. Open Hardw.*, vol. 1, no. 1, Mar. 2017, doi: 10.5334/joh.4.
- [186] J. S. Cybulski, J. Clements, and M. Prakash, “Foldscope: Origami-based paper microscope,” *PLoS One*, vol. 9, no. 6, 2014, doi: 10.1371/journal.pone.0098781.

- [187] M. S. Bhamla, B. Benson, C. Chai, G. Katsikis, A. Johri, and M. Prakash, “Hand-powered ultralow-cost paper centrifuge,” *Nat. Biomed. Eng.*, vol. 1, no. 1, pp. 1–7, 2017, doi: 10.1038/s41551-016-0009.
- [188] B. E. Vos, E. B. Blesa, and T. Betz, “Designing a High-Resolution, LEGO-Based Microscope for an Educational Setting,” *Biophys.*, vol. 2, no. 3, pp. 29–40, 2021, doi: 10.35459/tbp.2021.000191.
- [189] F. Quercioli, B. Tiribilli, A. Mannoni, and S. Acciai, “Optomechanics with LEGO,” *Appl. Opt.*, vol. 37, no. 16, p. 3408, Jun. 1998, doi: 10.1364/AO.37.003408.
- [190] A. K. Au, W. Huynh, L. F. Horowitz, and A. Folch, “3D-Printed Microfluidics,” *Angew. Chemie - Int. Ed.*, vol. 55, no. 12, pp. 3862–3881, 2016, doi: 10.1002/anie.201504382.
- [191] Z. Fahimi, C. P. Broedersz, T. H. S. van Kempen, D. Florea, G. W. M. Peters, and H. M. Wyss, “A new approach for calculating the true stress response from large amplitude oscillatory shear (LAOS) measurements using parallel plates,” *Rheol. Acta*, vol. 53, no. 1, pp. 75–83, 2014, doi: 10.1007/s00397-013-0738-y.
- [192] “Human Performance Capabilities.” [Online]. Available: <https://msis.jsc.nasa.gov/sections/section04.htm>.
- [193] A. Alghooneh, S. M. A. Razavi, and S. Kasapis, “Classification of hydrocolloids based on small amplitude oscillatory shear, large amplitude oscillatory shear, and textural properties,” *J. Texture Stud.*, vol. 50, no. 6, pp. 520–538, 2019, doi: 10.1111/jtxs.12459.
- [194] S. L. Breidinger and J. F. Steffe, “Texture Map of Cream Cheese,” *J. Food Sci.*, vol. 66, no. 3, pp. 453–456, Apr. 2001, doi: 10.1111/j.1365-2621.2001.tb16128.x.
- [195] G. P. Citerne, P. J. Carreau, and M. Moan, “Rheological properties of peanut butter,” *Rheol. Acta*, vol. 40, no. 1, pp. 86–96, 2001, doi: 10.1007/s003970000120.
- [196] M. Perreira and E. Payne, “Oreos high school experiment: Double and Mega Stuff filling doesn’t add up,” *CNN*, Aug. 2013.
- [197] R. Budynas and K. Nisbett, *Shigley’s Mechanical Engineering Design*, 9th ed. McGraw Hill, 2014.
- [198] G. van Zyl and A. Al-Sahli, “Failure analysis of conveyor pulley shaft,” *Case Stud. Eng. Fail. Anal.*, vol. 1, no. 2, pp. 144–155, Apr. 2013, doi: 10.1016/j.csefa.2013.04.011.
- [199] A. H. Committee, “ASM Handbook,” *Fractography*, vol. 12, 1987.
- [200] P. Coussot, Q. D. Nguyen, H. T. Huynh, and D. Bonn, “Viscosity bifurcation in thixotropic, yielding fluids,” *J. Rheol. (N. Y. N. Y.)*, vol. 46, no. 3, pp. 573–589, 2002, doi: 10.1122/1.1459447.

- [201] M. Fenstermaker, "How to avoid soggy cookies: The optimal dunking time," *The Utah Statesman*, 2016. <https://usustatesman.com/how-to-avoid-soggy-cookies-the-optimal-dunking-time/> (accessed Nov. 02, 2022).
- [202] W. T. Medina, A. A. de la Llera, J. L. Condori, and J. M. Aguilera, "Physical Properties and Microstructural Changes during Soaking of Individual Corn and Quinoa Breakfast Flakes," *J. Food Sci.*, vol. 76, no. 3, pp. E254–E265, Apr. 2011, doi: 10.1111/j.1750-3841.2011.02054.x.
- [203] "Printed Electronics: Global Markets to 2022," 2018. [Online]. Available: <https://www.bccresearch.com/>.
- [204] A. Kamyshny and S. Magdassi, "Conductive nanomaterials for 2D and 3D printed flexible electronics," *Chem. Soc. Rev.*, vol. 48, no. 6, pp. 1712–1740, 2019, doi: 10.1039/c8cs00738a.
- [205] S. Azoubel and S. Magdassi, "Controlling Adhesion Properties of SWCNT–PET Films Prepared by Wet Deposition," *ACS Appl. Mater. Interfaces*, vol. 6, no. 12, pp. 9265–9271, Jun. 2014, doi: 10.1021/am501488p.
- [206] B. Zhou *et al.*, "Interfacial adhesion enhanced flexible polycarbonate/carbon nanotubes transparent conductive film for vapor sensing," *Compos. Commun.*, vol. 15, pp. 80–86, Oct. 2019, doi: 10.1016/j.coco.2019.06.012.
- [207] T. Altalhi, T. Kumeria, A. Santos, and D. Losic, "Synthesis of well-organised carbon nanotube membranes from non-degradable plastic bags with tuneable molecular transport: Towards nanotechnological recycling," *Carbon N. Y.*, vol. 63, pp. 423–433, Nov. 2013, doi: 10.1016/j.carbon.2013.07.003.
- [208] B. Vigolo, C. Coulon, M. Maugey, C. Zakri, and P. Poulin, "Fluid dynamics: An experimental approach to the percolation of sticky nanotubes," *Science (80-. )*, vol. 309, no. 5736, pp. 920–923, 2005, doi: 10.1126/science.1112835.
- [209] W. Bauhofer and J. Z. Kovacs, "A review and analysis of electrical percolation in carbon nanotube polymer composites," *Compos. Sci. Technol.*, vol. 69, no. 10, pp. 1486–1498, 2009, doi: 10.1016/j.compscitech.2008.06.018.
- [210] Y. F. Liu, M. H. Tsai, Y. F. Pai, and W. S. Hwang, "Control of droplet formation by operating waveform for inks with various viscosities in piezoelectric inkjet printing," *Appl. Phys. A Mater. Sci. Process.*, vol. 111, no. 2, pp. 509–516, 2013, doi: 10.1007/s00339-013-7569-7.

- [211] S. Azoubel, S. Shemesh, and S. Magdassi, “Flexible electroluminescent device with inkjet-printed carbon nanotube electrodes,” *Nanotechnology*, vol. 23, no. 34, 2012, doi: 10.1088/0957-4484/23/34/344003.
- [212] B. G. Compton and J. A. Lewis, “3D-Printing of Lightweight Cellular Composites,” *Adv. Mater.*, vol. 26, no. 34, pp. 5930–5935, Sep. 2014, doi: 10.1002/adma.201401804.
- [213] J. N. Rodriguez, C. Zhu, E. B. Duoss, T. S. Wilson, C. M. Spadaccini, and J. P. Lewicki, “Shape-morphing composites with designed micro-architectures,” *Sci. Rep.*, vol. 6, no. 1, p. 27933, Jun. 2016, doi: 10.1038/srep27933.
- [214] V. H. M. Mouser, F. P. W. Melchels, J. Visser, W. J. A. Dhert, D. Gawlitta, and J. Malda, “Yield stress determines bioprintability of hydrogels based on gelatin-methacryloyl and gellan gum for cartilage bioprinting,” *Biofabrication*, vol. 8, no. 3, 2016, doi: 10.1088/1758-5090/8/3/035003.
- [215] Y. Weng, M. Li, M. J. Tan, and S. Qian, “Design 3D printing cementitious materials via Fuller Thompson theory and Marson-Percy model,” *Constr. Build. Mater.*, vol. 163, pp. 600–610, 2018, doi: 10.1016/j.conbuildmat.2017.12.112.
- [216] C. Xu and N. Willenbacher, “How rheological properties affect fine-line screen printing of pastes: a combined rheological and high-speed video imaging study,” *J. Coatings Technol. Res.*, vol. 15, no. 6, pp. 1401–1412, 2018, doi: 10.1007/s11998-018-0091-2.
- [217] G. J. Donley, W. W. Hyde, S. A. Rogers, and F. Nettekheim, “Yielding and recovery of conductive pastes for screen printing,” *Rheol. Acta*, vol. 58, no. 6–7, pp. 361–382, 2019, doi: 10.1007/s00397-019-01148-w.
- [218] Y. Jin, W. Chai, and Y. Huang, “Printability study of hydrogel solution extrusion in nanoclay yield-stress bath during printing-then-gelation biofabrication,” *Mater. Sci. Eng. C*, vol. 80, pp. 313–325, 2017, doi: 10.1016/j.msec.2017.05.144.
- [219] D. H. Kim and J. A. Rogers, “Stretchable electronics: Materials strategies and devices,” *Adv. Mater.*, vol. 20, no. 24, pp. 4887–4892, 2008, doi: 10.1002/adma.200801788.
- [220] D.-H. Kim *et al.*, “Stretchable and Foldable Silicon Integrated Circuits,” *Science (80-. )*, vol. 320, no. 5875, pp. 507–511, Apr. 2008, doi: 10.1126/science.1154367.
- [221] Y. Sun and J. A. Rogers, “Structural forms of single crystal semiconductor nanoribbons for high-performance stretchable electronics,” *J. Mater. Chem.*, vol. 17, no. 9, p. 832, 2007, doi: 10.1039/b614793c.

- [222] A. C. Siegel, S. T. Phillips, M. D. Dickey, N. Lu, Z. Suo, and G. M. Whitesides, “Foldable printed circuit boards on paper substrates,” *Adv. Funct. Mater.*, vol. 20, no. 1, pp. 28–35, 2010, doi: 10.1002/adfm.200901363.
- [223] B. Weigl, G. Domingo, P. LaBarre, and J. Gerlach, “Towards non- and minimally instrumented, microfluidics-based diagnostic devices,” *Lab Chip*, vol. 8, no. 12, pp. 1999–2014, 2008, doi: 10.1039/b811314a.
- [224] S. S. Das, S. Kar, S. Dawn, P. Saha, and S. Chakraborty, “Electrokinetic Trapping of Microparticles Using Paper-and-Pencil Microfluidics,” *Phys. Rev. Appl.*, Nov. 2019, doi: 10.1103/PhysRevApplied.12.054017.
- [225] L. Yang, R. Zhang, D. Staiculescu, C. P. Wong, and M. M. Tentzeris, “A novel conformal RFID-enabled module utilizing inkjet-printed antennas and carbon nanotubes for gas-detection applications,” *IEEE Antennas Wirel. Propag. Lett.*, vol. 8, pp. 653–656, 2009, doi: 10.1109/LAWP.2009.2024104.
- [226] M. Weng *et al.*, “Multiresponsive Bidirectional Bending Actuators Fabricated by a Pencil-on-Paper Method,” *Adv. Funct. Mater.*, vol. 26, no. 40, pp. 7244–7253, Oct. 2016, doi: 10.1002/adfm.201602772.
- [227] A. Yakoh, S. Chaiyo, W. Siangproh, and O. Chailapakul, “3D Capillary-Driven Paper-Based Sequential Microfluidic Device for Electrochemical Sensing Applications,” *ACS Sensors*, vol. 4, no. 5, pp. 1211–1221, May 2019, doi: 10.1021/acssensors.8b01574.
- [228] E. Svanholm, “Printability and Ink-Coating Interactions in Inkjet Printing,” Karlstad University, 2007.
- [229] Z. Lei and P. Wu, “A highly transparent and ultra-stretchable conductor with stable conductivity during large deformation,” *Nat. Commun.*, vol. 10, no. 1, pp. 1–9, 2019, doi: 10.1038/s41467-019-11364-w.
- [230] S. Iijima and T. Ichihashi, “Single-shell carbon nanotubes of 1-nm diameter,” *Nature*, no. 3, pp. 603–605, 1993, doi: 363603a0.
- [231] J. Chen, S. Wei, and H. Xie, “A Brief Introduction of Carbon Nanotubes: History, Synthesis, and Properties,” *J. Phys. Conf. Ser.*, vol. 1948, no. 1, 2021, doi: 10.1088/1742-6596/1948/1/012184.
- [232] P. Parnian, “A Short Review on: Recent Advances in the Use of Carbon Nanotubes in Additive Manufacturing of Polymer Matrix Composites,” *Macromol. Symp.*, vol. 405, no. 1, pp. 1–4, 2022, doi: 10.1002/masy.202100339.

- [233] I. A. Perales-Martinez and L. F. Velásquez-García, “Fully 3D-printed carbon nanotube field emission electron sources with in-plane gate electrode,” *Nanotechnology*, vol. 30, no. 49, 2019, doi: 10.1088/1361-6528/ab3d17.
- [234] S. Jiang, P.-X. Hou, C. Liu, and H.-M. Cheng, “High-performance single-wall carbon nanotube transparent conductive films,” *J. Mater. Sci. Technol.*, vol. 35, no. 11, pp. 2447–2462, Nov. 2019, doi: 10.1016/j.jmst.2019.07.011.
- [235] E. Amram Bengio *et al.*, “High efficiency carbon nanotube thread antennas,” *Appl. Phys. Lett.*, vol. 111, no. 16, 2017, doi: 10.1063/1.4991822.
- [236] E. Amram Bengio *et al.*, “Carbon nanotube thin film patch antennas for wireless communications,” *Appl. Phys. Lett.*, vol. 114, no. 20, 2019, doi: 10.1063/1.5093327.
- [237] F. Vitale, S. R. Summerson, B. Aazhang, C. Kemere, and M. Pasquali, “Neural stimulation and recording with bidirectional, soft carbon nanotube fiber microelectrodes,” *ACS Nano*, vol. 9, no. 4, pp. 4465–4474, 2015, doi: 10.1021/acsnano.5b01060.
- [238] W. M. Tsang *et al.*, “Insect-machine interface: A carbon nanotube-enhanced flexible neural probe,” *J. Neurosci. Methods*, vol. 204, no. 2, pp. 355–365, 2012, doi: 10.1016/j.jneumeth.2011.11.026.
- [239] F. F. Dall’Agnol, T. A. de Assis, S. B. Fairchild, J. Ludwick, G. Tripathi, and M. Cahay, “Looped carbon nanotube fibers as cathodes with giant field enhancement factors,” *Appl. Phys. Lett.*, vol. 117, no. 25, p. 253101, Dec. 2020, doi: 10.1063/5.0030100.
- [240] S. B. Fairchild *et al.*, “Carbon Nanotube Fiber Field Emission Array Cathodes,” *IEEE Trans. Plasma Sci.*, vol. 47, no. 5, pp. 2032–2038, 2019, doi: 10.1109/TPS.2019.2900219.
- [241] X. Zhang, W. Lu, G. Zhou, and Q. Li, “Understanding the Mechanical and Conductive Properties of Carbon Nanotube Fibers for Smart Electronics,” *Adv. Mater.*, vol. 32, no. 5, pp. 1–21, 2020, doi: 10.1002/adma.201902028.
- [242] S. Ling, Z. Qin, C. Li, W. Huang, D. L. Kaplan, and M. J. Buehler, “Polymorphic regenerated silk fibers assembled through bioinspired spinning,” *Nat. Commun.*, vol. 8, no. 1, 2017, doi: 10.1038/s41467-017-00613-5.
- [243] Y. Jang, S. M. Kim, G. M. Spinks, and S. J. Kim, “Carbon Nanotube Yarn for Fiber-Shaped Electrical Sensors, Actuators, and Energy Storage for Smart Systems,” *Adv. Mater.*, vol. 32, no. 5, pp. 1–14, 2020, doi: 10.1002/adma.201902670.

- [244] F. Iervolino, A. Bonessa, G. Foti, M. Levi, and R. Suriano, “Additive Manufacturing of Electrically Conductive Nanocomposites Filled with Carbon Nanotubes,” *Adv. Eng. Mater.*, vol. 24, no. 12, pp. 1–11, 2022, doi: 10.1002/adem.202200947.
- [245] F. Liu *et al.*, “Additive Manufacturing of Stretchable Multi-Walled Carbon Nanotubes/Thermoplastic Polyurethanes Conducting Polymers for Strain Sensing,” *3D Print. Addit. Manuf.*, vol. 00, no. 00, pp. 1–11, 2022, doi: 10.1089/3dp.2022.0223.
- [246] O. Kanoun, A. Bouhamed, R. Ramalingame, J. R. Bautista-Quijano, D. Rajendran, and A. Al-Hamry, “Review on Conductive Polymer/CNTs Nanocomposites Based Flexible and Stretchable Strain and Pressure Sensors,” *Sensors*, vol. 21, no. 2, pp. 1–29, 2021, doi: 10.3390/s21020341.
- [247] V. A. Davis, “Anisotropic Nanomaterial Liquid Crystals: From Fiber Spinning to Additive Manufacturing,” *Langmuir*, 2022, doi: 10.1021/acs.langmuir.2c03519.
- [248] T. Bhattacharjee *et al.*, “Writing in the granular gel medium,” no. September, pp. 1–7, 2015.
- [249] C. S. O’Bryan *et al.*, “Three-dimensional printing with sacrificial materials for soft matter manufacturing,” *MRS Bull.*, vol. 42, no. 8, pp. 571–577, 2017, doi: 10.1557/mrs.2017.167.
- [250] F. K. Oppong and J. R. de Bruyn, “Diffusion of microscopic tracer particles in a yield-stress fluid,” *J. Nonnewton. Fluid Mech.*, vol. 142, no. 1–3, pp. 104–111, 2007, doi: 10.1016/j.jnnfm.2006.05.008.
- [251] H. Yuk and X. Zhao, “A New 3D Printing Strategy by Harnessing Deformation, Instability, and Fracture of Viscoelastic Inks,” *Adv. Mater.*, vol. 30, no. 6, pp. 1–8, 2018, doi: 10.1002/adma.201704028.
- [252] L. Zhang, Q. Wang, Y. C. Liu, and L. Z. Zhang, “On the mutual diffusion properties of ethanol-water mixtures,” *J. Chem. Phys.*, vol. 125, no. 10, 2006, doi: 10.1063/1.2244547.
- [253] G. D’Errico, O. Ortona, F. Capuano, and V. Vitagliano, “Diffusion coefficients for the binary system glycerol + water at 25 °C. a velocity correlation study,” *J. Chem. Eng. Data*, vol. 49, no. 6, pp. 1665–1670, 2004, doi: 10.1021/je049917u.
- [254] “Deoxycholic acid,” *ChemBK*. [https://www.chembk.com/en/chem/Deoxycholic acid](https://www.chembk.com/en/chem/Deoxycholic%20acid).
- [255] E. Jambon-Puillet, M. R. Piéchaud, and P. T. Brun, “Elastic amplification of the Rayleigh–Taylor instability in solidifying melts,” *Proc. Natl. Acad. Sci. U. S. A.*, vol. 118, no. 10, pp. 1–6, 2021, doi: 10.1073/pnas.2020701118.



- [256] A. Z. Nelson, B. Kundukad, W. K. Wong, S. A. Khan, and P. S. Doyle, “Embedded droplet printing in yield-stress fluids,” *Proc. Natl. Acad. Sci. U. S. A.*, vol. 117, no. 11, pp. 5671–5679, 2020, doi: 10.1073/pnas.1919363117.
- [257] L. Palangetic, N. K. Reddy, S. Srinivasan, R. E. Cohen, G. H. McKinley, and C. Clasen, “Dispersity and spinnability: Why highly polydisperse polymer solutions are desirable for electrospinning,” *Polym. (United Kingdom)*, vol. 55, no. 19, pp. 4920–4931, 2014, doi: 10.1016/j.polymer.2014.07.047.
- [258] C. Mercader *et al.*, “Kinetics of fiber solidification,” *Proc. Natl. Acad. Sci.*, vol. 107, no. 43, pp. 18331–18335, 2010, doi: 10.1073/pnas.1003302107.
- [259] P. T. Brun, N. M. Ribe, and B. Audoly, “A numerical investigation of the fluid mechanical sewing machine,” *Phys. Fluids*, vol. 24, no. 4, 2012, doi: 10.1063/1.3703316.
- [260] J. S. Bulmer, A. Kaniyoor, and J. A. Elliott, “A Meta-Analysis of Conductive and Strong Carbon Nanotube Materials,” *Adv. Mater.*, vol. 33, no. 36, 2021, doi: 10.1002/adma.202008432.
- [261] M. Miao, “Electrical conductivity of pure carbon nanotube yarns,” *Carbon N. Y.*, vol. 49, no. 12, pp. 3755–3761, 2011, doi: 10.1016/j.carbon.2011.05.008.
- [262] N. M. Ribe, J. R. Lister, and S. Chiu-Webster, “Stability of a dragged viscous thread: Onset of  $\theta$  stitching” in a fluid-mechanical ‘sewing machine,” *Phys. Fluids*, vol. 18, no. 12, 2006, doi: 10.1063/1.2409617.
- [263] L. Mahadevan, W. S. W. S. Ryu, and A. D. T. A. D. T. Samuel, “Fluid ‘rope trick’ investigated,” *Nature*, vol. 392, no. 2, p. 140, Mar. 1998, [Online]. Available: <http://dx.doi.org/10.1038/32321>.
- [264] Y. Rahmani, M. Habibi, A. Javadi, and D. Bonn, “Coiling of yield stress fluids,” *Phys. Rev. E - Stat. Nonlinear, Soft Matter Phys.*, vol. 83, no. 5, pp. 1–4, 2011, doi: 10.1103/PhysRevE.83.056327.
- [265] A. Javadi, “Drops and jets of complex fluids,” 2013.
- [266] L. Mahadevan and J. B. Keller, “Coiling of flexible ropes,” *Proc. R. Soc. London. Ser. A Math. Phys. Eng. Sci.*, vol. 452, no. 1950, pp. 1679–1694, Dec. 1996, doi: 10.1098/rspa.1996.0089.
- [267] S. Zou, D. Therriault, and F. P. Gosselin, “Failure mechanisms of coiling fibers with sacrificial bonds made by instability-assisted fused deposition modeling,” *Soft Matter*, vol. 14, no. 48, pp. 9777–9785, 2018, doi: 10.1039/c8sm01589a.

- [268] P. T. Brun *et al.*, “The molten glass sewing machine,” *Philos. Trans. R. Soc. A Math. Phys. Eng. Sci.*, vol. 375, no. 2093, 2017, doi: 10.1098/rsta.2016.0156.
- [269] H. Y. Kim, M. Lee, K. J. Park, S. Kim, and L. Mahadevan, “Nanopottery: Coiling of electrospun polymer nanofibers,” *Nano Lett.*, vol. 10, no. 6, pp. 2138–2140, 2010, doi: 10.1021/nl100824d.
- [270] Z. Huang *et al.*, “Three-dimensional integrated stretchable electronics,” *Nat. Electron.*, vol. 1, no. 8, pp. 473–480, 2018, doi: 10.1038/s41928-018-0116-y.
- [271] H. M. Manohara, R. Toda, R. H. Lin, A. Liao, M. J. Bronikowski, and P. H. Siegel, “Carbon nanotube bundle array cold cathodes for THz vacuum tube sources,” *J. Infrared, Millimeter, Terahertz Waves*, vol. 30, no. 12, pp. 1338–1350, 2009, doi: 10.1007/s10762-009-9547-x.
- [272] N. S. Xu and S. E. Huq, “Novel cold cathode materials and applications,” *Mater. Sci. Eng. R Reports*, vol. 48, no. 2–5, pp. 47–189, 2005, doi: 10.1016/j.mser.2004.12.001.
- [273] J.-M. M. Bonard, K. A. Dean, B. F. Coll, and C. Klinke, “Field emission of individual carbon nanotubes in the scanning electron microscope,” *Phys. Rev. Lett.*, vol. 89, no. 19, p. 89, 2002, doi: 10.1103/PhysRevLett.89.197602.
- [274] C. M. Collins, R. J. Parmee, W. I. Milne, and M. T. Cole, “High Performance Field Emitters,” *Adv. Sci.*, vol. 3, no. 5, p. 1500318, May 2016, doi: 10.1002/advs.201500318.
- [275] S. B. Fairchild *et al.*, “Morphology dependent field emission of acid-spun carbon nanotube fibers,” *Nanotechnology*, vol. 26, no. 10, 2015, doi: 10.1088/0957-4484/26/10/105706.
- [276] I. A. Perales-Martinez and L. F. Velásquez-García, “Fully 3D-printed carbon nanotube field emission electron sources with in-plane gate electrode,” *Nanotechnology*, vol. 30, no. 49, 2019, doi: 10.1088/1361-6528/ab3d17.
- [277] J. M. Connelly, W. W. Tang, J. R. Harris, and K. L. Jensen, “Demonstration of 3-D-Printed Field-Emission Cathodes,” *IEEE Trans. Plasma Sci.*, vol. 47, no. 9, pp. 4292–4300, Sep. 2019, doi: 10.1109/TPS.2019.2931819.
- [278] C. E. Owens, G. H. McKinley, and A. J. Hart, “3D printing by tailored extrusion of carbon nanotube inks,” 2019, [Online]. Available: <https://ui.adsabs.harvard.edu/abs/2019APS..MARV49009O/abstract>.
- [279] A. W. K. K. Ma, F. Chinesta, T. Tuladhar, and M. R. Mackley, “Filament stretching of carbon nanotube suspensions,” *Rheol. Acta*, vol. 47, no. 4, pp. 447–457, 2008, doi: 10.1007/s00397-007-0247-y.

- [280] R. H. Fowler and L. Nordheim, “Electron emission in intense electric fields,” *Proc. R. Soc. London. Ser. A, Contain. Pap. a Math. Phys. Character*, vol. 119, no. 781, pp. 173–181, May 1928, doi: 10.1098/rspa.1928.0091.
- [281] S. B. Fairchild *et al.*, “Carbon Nanotube Fiber Field Emission Array Cathodes,” *IEEE Trans. Plasma Sci.*, vol. 47, no. 5, pp. 2032–2038, 2019, doi: 10.1109/TPS.2019.2900219.
- [282] A. Kyritsakis and J. P. Xanthakis, “Derivation of a generalized Fowler–Nordheim equation for nanoscopic field-emitters,” *Proc. R. Soc. A Math. Phys. Eng. Sci.*, vol. 471, no. 2174, p. 20140811, Feb. 2015, doi: 10.1098/rspa.2014.0811.
- [283] A. Chatziafratis and J. P. Xanthakis, “Field emission from a nanometric paraboloidal emitter,” *J. Electron Spectros. Relat. Phenomena*, vol. 241, p. 146871, May 2020, doi: 10.1016/j.elspec.2019.06.003.
- [284] R. G. Forbes, “Development of a simple quantitative test for lack of field emission orthodoxy,” *Proc. R. Soc. A Math. Phys. Eng. Sci.*, vol. 469, no. 2158, p. 20130271, Oct. 2013, doi: 10.1098/rspa.2013.0271.
- [285] J. Chen, B. Yang, X. Liu, J. Yang, L. Cui, and X. Yan, “Large field emission current and density from robust carbon nanotube cathodes for continuous and pulsed electron sources,” *Sci. China Mater.*, vol. 60, no. 4, pp. 335–342, 2017, doi: 10.1007/s40843-016-9016-5.
- [286] C. E. Owens *et al.*, “Pointwise fabrication and fluidic shaping of carbon nanotube field emitters,” *Submitted*.
- [287] M. Esashi, A. Kojima, N. Ikegami, H. Miyaguchi, and N. Koshida, “Development of massively parallel electron beam direct write lithography using active-matrix nanocrystalline-silicon electron emitter arrays,” *Microsystems Nanoeng.*, vol. 1, no. 0, pp. 1–8, 2015, doi: 10.1038/micronano.2015.29.
- [288] C. E. Owens *et al.*, “Pointwise Fabrication and Fluidic Shaping of Carbon Nanotube Field Emitters,” *IEEE Transducers*, no. June, pp. 21–24, 2021.
- [289] L. F. Velaásquez-García, B. L. P. Gassend, and A. I. Akinwande, “CNT-based MEMS/NEMS gas ionizers for portable mass spectrometry applications,” *J. Microelectromechanical Syst.*, vol. 19, no. 3, pp. 484–493, 2010, doi: 10.1109/JMEMS.2010.2045639.
- [290] A. A. Fomani, A. I. Akinwande, and L. F. Velásquez-García, “Resilient, nanostructured, high-current, and low-voltage neutralizers for electric propulsion of small

- spacecraft in low earth orbit,” *J. Phys. Conf. Ser.*, vol. 476, no. 1, pp. 1–6, 2013, doi: 10.1088/1742-6596/476/1/012014.
- [291] S. B. Fairchild *et al.*, “Field emission cathodes made from knitted carbon nanotube fiber fabrics,” *J. Appl. Phys.*, vol. 133, no. 9, 2023, doi: 10.1063/5.0123120.
- [292] A. Kachkine and L. F. Velasquez-Garcia, “Densely Packed, Additively Manufactured, In-Plane Gated Carbon Nanotube Field Emission Electron Sources,” *2022 21st Int. Conf. Micro Nanotechnol. Power Gener. Energy Convers. Appl. PowerMEMS 2022*, no. December, pp. 38–41, 2022, doi: 10.1109/PowerMEMS56853.2022.10007579.
- [293] R. Gupta, L. F. Velasquez-Garcia, R. Lanza, B. K. P. Horn, and A. I. Akinwande, “Method for Coded-Source Phase Contrast X-Ray Imaging,” US 10 , 045 , 752 B2, 2018.
- [294] Q. Barral, G. Ovarlez, X. Chateau, J. Boujlel, B. Rabideau, and P. Coussot, “Adhesion of yield stress fluids,” *Soft Matter*, vol. 6, no. 6, pp. 1343–1351, 2010, doi: 10.1039/b922162j.
- [295] S. Cheng, F. A. Hill, E. V. Heubel, and L. F. Velasquez-Garcia, “Low-bremsstrahlung X-ray source using a low-voltage high-current-density nanostructured field emission cathode and a transmission anode for markerless soft tissue imaging,” *J. Microelectromechanical Syst.*, vol. 24, no. 2, pp. 373–383, 2015, doi: 10.1109/JMEMS.2014.2332176.
- [296] A. Basu, M. E. Swanwick, A. A. Fomani, and L. F. Velásquez-García, “A portable x-ray source with a nanostructured Pt-coated silicon field emission cathode for absorption imaging of low-Z materials,” *J. Phys. D. Appl. Phys.*, vol. 48, no. 22, p. 225501, 2015, doi: 10.1088/0022-3727/48/22/225501.
- [297] S. G. M. Uzel, R. D. Weeks, M. Eriksson, D. Kokkinis, and J. A. Lewis, “Multimaterial Multinozzle Adaptive 3D Printing of Soft Materials,” *Adv. Mater. Technol.*, vol. 7, no. 8, pp. 1–10, 2022, doi: 10.1002/admt.202101710.
- [298] C. Subramaniam *et al.*, “One hundred fold increase in current carrying capacity in a carbon nanotube-copper composite,” *Nat. Commun.*, vol. 4, pp. 1–7, 2013, doi: 10.1038/ncomms3202.
- [299] C. Subramaniam *et al.*, “Carbon nanotube-copper exhibiting metal-like thermal conductivity and silicon-like thermal expansion for efficient cooling of electronics,” *Nanoscale*, vol. 6, no. 5, pp. 2669–2674, 2014, doi: 10.1039/c3nr05290g.

- [300] N. Lazarus, S. S. Bedair, S. H. Hawasli, M. J. Kim, B. J. Wiley, and G. L. Smith, “Selective Electroplating for 3D-Printed Electronics,” *Adv. Mater. Technol.*, vol. 4, no. 8, 2019, doi: 10.1002/admt.201900126.
- [301] P. M. Hannula *et al.*, “Observations of copper deposition on functionalized carbon nanotube films,” *Electrochim. Acta*, vol. 232, pp. 495–504, 2017, doi: 10.1016/j.electacta.2017.03.006.
- [302] S. Torquato, *Random Heterogeneous Materials: Microstructure and Macroscopic Properties*. New York, NY: Springer Science & Business Media, 2002.
- [303] W. G. Eberhard and W. T. Wcislo, “Plenty of room at the bottom?,” *Am. Sci.*, vol. 100, no. 3, pp. 226–233, 2012, doi: 10.1511/2012.96.226.